



UNIVERSITY OF
BIRMINGHAM

ASTEROSEISMIC INFERENCE ON A POPULATION SCALE:
FROM DETECTION TO INTERNAL PROPERTIES

by

EMILY HATT

A thesis submitted to the University of Birmingham for the degree of
DOCTOR OF PHILOSOPHY

Sun, Stars and Exoplanets
School of Physics and Astronomy
College of Engineering and Physical Sciences
University of Birmingham
April 2024

© Copyright by EMILY HATT, 2024

All Rights Reserved

Abstract

A painter should begin every canvas with a wash of black, because all things in nature are dark except where exposed by the light.

- Leonardo Da Vinci

Stars give off light which enables the evolution of intelligent life and gives it access to information about the universe it inhabits. Despite their importance, our understanding of the inner workings of these objects is still far from complete. This thesis is dedicated to the only probe capable of providing observational information about the deep interiors of stars, asteroseismology, the study of stellar oscillations. In the following I will study the solar-like oscillator, in which sound waves are excited and subsequently trapped, manifesting in pulsations. Alongside probing the conditions in the interior of a star, observations of these oscillations provide accurate and precise constraints on fundamental stellar parameters. Asteroseismic measurements of stellar masses, radii, and ages have advanced several fields outside of stellar astrophysics, including exoplanet research and the study of the history of the Milky Way. In this thesis, I will cover a range of asteroseismic analyses, from detecting the presence of solar-like oscillations to exploiting the pulsations to measure the properties of stellar cores.

After a brief introduction to stellar evolution and an overview of the basics of asteroseismic analysis, I will present three works. The first introduces an automated pipeline we designed to detect solar-like oscillations using measurements of stellar flux as a function of time. This pipeline is then applied to data collected by NASA's TESS mission for over 200,000 stars, generating a catalogue of thousands of solar-like oscillators. The next work looks to the future of

asteroseismology, presenting predictions for the proposed HAYDN space telescope. The mission would exploit solar-like oscillators in stellar clusters to answer some of the most pressing open questions in stellar astrophysics and the history of the Milky Way. Two features of stellar evolution that could be investigated are core rotation and core magnetic fields. I comment on the potential for using HAYDN to make asteroseismic inferences on these properties and evaluate potential detection biases. Finally, I present the first large catalogue of asteroseismic probes of core rotation and magnetism in real stars observed by *Kepler*. In this catalogue I identify a bimodality in the distribution of core rotation rates which has not yet been replicated by stellar models and has implications for our understanding of angular momentum transport in stars.

Asteroseismology has provided us with tools to investigate stars in unprecedented levels of detail. To fully exploit this information to better our understanding of stellar evolution, we require larger and more complete catalogues of seismic parameters. In this thesis I build upon this, both introducing new methods to assist asteroseismic analysis in large datasets and reporting thousands of new measurements from the most fundamental detections to probes of the deep interiors of stars. The future of the field will see missions like ESA's PLATO providing even more data amenable to asteroseismic analysis, making the tools and results detailed here a crucial chapter in the ongoing asteroseismic story.

Dedicated to my mum and dad.

Acknowledgements

This thesis was made possible by the excellent guidance of both my supervisor, Prof. William Chaplin, and Dr. Martin Nielsen who have provided excellent support throughout my PhD. I am very proud to have been supervised by two such excellent researchers. I must also thank Prof. Andrea Miglio, my secondary supervisor who first piqued my interest in asteroseismology during my undergraduate degree. Finally I would like to thank Dr. Guy Davies for all the discussions both in and out of CICO meetings, I am very grateful to have been included in your research group.

It has been my pleasure to work for The Sun, Stars, and Exoplanets Group at the University of Birmingham, which continues to provide a productive, nurturing, and thoroughly enjoyable environment under the care of Prof. Amaury Triaud. Another key member of the group is Louise Barden, our group secretary, and ardent supporter. Lou's role in the group goes far beyond the job title, as an excellent listener and caring source of support. I am lucky enough to call my colleagues good friends, all of whom are both talented scientists and warm, funny, and accepting people. Special thanks to Alex and Emma, who made me feel at home in the group since the beginning of my PhD. The group has also recently benefited massively from the addition of Dr. Amalie Stockholm, who somehow manages to support everyone who comes to her for help as if they were her first priority. If I end up as half the researcher and colleague, I'd call my career a success. The biggest thanks to Owen, who has been a patient and supportive partner. Thank you for listening even when it didn't make sense.

Finally, I would never have attempted a PhD without my parents. Both of whom are hard workers and high achievers, instilling in me the drive to try even when a task seems impossible. Thank you for being you.

Contents

Abstract	i
Acknowledgements	v
Contents	vii
List of Figures	xiii
List of Tables	xxiii
1 Introduction	1
1.1 Evolution of Low-mass Stars	4
1.1.1 Oscillations in Low-mass Stars	8
1.2 Stellar Rotation and Magnetic Fields	9
1.2.1 Rotation	10
1.2.2 Magnetic Fields	15
1.3 Solar-Like Oscillations	17
1.3.1 Overview of the Data	18
1.3.2 General Properties of Solar-like Oscillations	20
1.3.3 Pressure, Gravity and Mixed Modes	21
1.3.4 Asymptotic Equations of Solar-Like Oscillations	24
1.3.5 Magnetism, Rotation and Asteroseismology	25
1.3.6 Solar-Like Oscillations and Stellar Evolution	28

1.4	Summary	32
2	Asteroseismic Data	33
2.1	Frequency Analysis	34
2.1.1	Fourier Transforms	34
2.1.2	The Lomb-Scargle Periodogram	36
2.1.3	Stellar signals in the Frequency Domain	37
2.2	Stellar Properties	45
2.2.1	Model Independent Property Recovery	45
2.2.2	Model Dependent Property Recovery	46
2.3	Sources of Asteroseismic Data	47
2.3.1	<i>Kepler</i>	48
2.3.2	TESS	49
2.3.3	PLATO	51
2.4	Summary	51
3	Detecting Oscillations	53
3.1	Automated Detection	54
3.1.1	Null Hypothesis (H_0) tests	55
3.1.2	Alternative Hypothesis (H_1) Testing	56
3.1.3	Asteroseismic Applications of Bayesian Model Fitting	57
3.2	A New Pipeline	59
3.2.1	Data Pre-Conditioning	60
3.2.2	Power Excess Test	60
3.2.3	Repeating Pattern Test	65
3.2.4	Validation and Performance	68
3.3	Summary	74
4	TESS Catalogue	75
4.1	Introduction	75

4.2	Target selection	78
4.3	Data selection	79
4.4	Detection of solar-like oscillators	81
4.4.1	Literature Sample	85
4.4.2	Asteroseismic Target List	86
4.4.3	Large Sample	86
4.4.4	20-second cadence	87
4.5	Global asteroseismic parameters	87
4.5.1	Literature Sample	92
4.5.2	Asteroseismic Target List	92
4.5.3	Large Sample	94
4.5.4	20-second cadence	96
4.6	Conclusions	98
	Appendices	100
4.A	Additional plots	100
	5 Predictions for HAYDN	103
5.1	NGC 6397	105
5.2	Introduction	105
5.3	Simulations	108
5.3.1	Stellar Parameters	108
5.3.2	Simulated Lightcurves	111
5.3.3	Properties of The Unperturbed Oscillations	112
5.3.4	Properties of the noise	115
5.3.5	Observation duration and Gaps	115
5.4	Detection Metrics	116
5.4.1	The Presence of Oscillations	116
5.4.2	$l = 0, 2$ Mode Frequency Recovery	117

5.5	Results in Unperturbed Spectra	120
5.5.1	Detection of Oscillations	120
5.5.2	Results: $l = 0,2$ recovery	123
5.6	Rotation and Magnetism	124
5.6.1	Simulated Mode Frequencies with Core Rotation	126
5.6.2	Simulated Mode Frequencies with Core Magnetism	127
5.6.3	$l= 1$ Mode Recovery	128
5.6.4	Results: Rotation Recovery	130
5.6.5	Results: Magnetic Recovery	133
5.7	Conclusions	134
6	Rotation and Magnetism	137
6.1	Introduction	137
6.2	Survey Methodology	140
6.2.1	Target Selection	140
6.2.2	Data pre-processing	142
6.2.3	Estimating the $l=1$ model parameters	144
6.3	Results	154
6.3.1	Rotational splitting	154
6.3.2	Magnetic Parameters	155
6.4	Discussion	158
6.4.1	Rotation and stellar mass	158
6.4.2	Magnetic Perturbations and Stellar Properties	161
6.5	Limitations	166
6.6	Conclusions	167
Appendices		168
6.A	Injection Recovery	168
6.B	Literature Comparisons	168

6.B.1	G-mode asymptotics	168
6.C	Example Corner Plots	170
7	Conclusions and Future Work	173
References		177

List of Figures

1.1	HR-diagram showing the evolutionary tracks of stars of mass $1M_{\odot}$, 1.5_{\odot} and $2M_{\odot}$ at solar metallicity. For each track, the location of the main sequence is identified by the label ‘MS’, the subgiant branch by ‘SG’ and the red giant branch by ‘RGB’.	5
1.2	Illustrative diagram showing the refraction and reflection of an acoustic wave as it travels from a point on the surface radially inward and then outward to be reflected at another point.	8
1.3	Surface rotation rates as a function of stellar mass for stars in 8 stellar clusters. The youngest cluster is plotted in the top left and the oldest cluster in the bottom right. Periods appear randomly distributed in the youngest cluster, as the age increases stars start join a track in mass-period space. There-in, the higher mass stars converge to shorter periods than the lower mass stars. Figure 2 in Irwin et al. (2009)	11
1.4	Asteroseismically inferred core rotation periods as a function of stellar radius shown as scatter points. Lines show various predictions for the core period as a function of radius according to different prescriptions for angular momentum transport. In green is a simple treatment, with rotation considered in shells and the total angular momentum is conserved. The model in purple includes rotational instabilities. In red is a model with a core magnetic field in the radiative core. Black line shows the surface period. Figure 2 from (Cantiello et al., 2014).	12

1.5 Example of the spectrum of a subgiant solar-like oscillator observed by <i>Kepler</i> (KIC6442183). The signature of granulation, white noise and the shape of the mode envelope are indicated by a dashed, dotted and continuous line respectively. The inset axis shows a zoom in around the mode envelope, showing a number of Lorentzian peaks associated with individual mode frequencies.	19
1.6 Examples of spherical harmonics for angular degrees (ℓ) 0 and 1 and the associated azimuthal orders (m). Red indicates a minima, and blue a maxima.	21
1.7 Signal-to-noise spectrum for three stars observed by <i>Kepler</i> (KIC6106415, KIC6442183 and KIC6035199 respectively). Evolutionary phase increases downward, such that the third panel is the most evolved star.	29
1.8 Propagation diagrams for a model of a $1.15M_{\odot}$ star at solar metallicity in three different evolutionary phases. The Brunt-Väisälä frequency and dipole Lamb frequency is shown. Shaded regions are those with $\nu^2 < N^2$ (identified with g-mode frequencies) and $\nu^2 > S_1^2$ (identified with p-mode frequencies).	30
2.1 Model for the contribution of a single pulse in the lightcurve attributed to granulation. The real signal is modelled as the sum of a number of these peaks, which randomly appear.	38
2.2 Smoothed spectra for 3 stars at different evolutionary phases. The characteristic timescale of granulation increases with decreasing ν_{\max} , such that the frequency at which the granulation profile has a knee decreases.	39
2.3 Signal-to-noise spectrum of the solar-like oscillator KIC6442183 observed by <i>Kepler</i> . The dotted line represents the Gaussian function used to describe the p-mode envelope. The large frequency separation $\Delta\nu$ is marked with an arrow. The inset shows a zoom around three individual modes with angular degree $\ell = 0, 1$ and 2	40

2.4	Visibility as a function of angular degree according to Ballot et al. (2011). Values are calculated using atmospheric models for the limb darkening of a star with $T_{\text{eff}} = 5800\text{K}$ and $\log g = 4.5\text{dex}$ at solar metallicity. The maximum of this function is at $\ell = 1$	43
2.5	Simulated mode profiles in a dipole multiplet containing rotational perturbation only at three different inclinations. The first panel is for the star observed pole-on, and in the third the star is viewed equator on.	44
2.6	Simulated mode profiles for a dipole multiplet in a star at intermediate inclination (45°). In the left hand panel the profile is shown with rotational splitting only, while on the right we show rotational and magnetic splitting	44
2.7	ν_{max} as a function of T_{eff} for solar-like oscillators observed by <i>Kepler</i> . Measurements are taken from Yu et al. (2018a) and Serenelli et al. (2017). The <i>Kepler</i> long cadence Nyquist frequency is marked by a black dotted line. Three evolutionary tracks are shown for stars at solar metallicity with masses 1.0, 1.5 and $2.0M_\odot$ generated by MIST (Choi et al., 2016).	50
3.1	Spectrum of KIC6442183 observed by <i>Kepler</i> . Black solid line represents a fit of Equation 2.9 to the data, dotted line is the approximation calculated via a moving median filter.	61
3.2	Example of the likelihoods output from the power excess test in a star observed by TESS. The top panel shows the log-likelihoods for the H0 and H1 hypotheses. The bottom panel is the signal-to-noise spectrum.	64
3.3	Main panel shows the two dimensional autocorrelation function for the star in Figure 3.2. The peak identified with the true value of $\Delta\nu$ and ν_{max} is identified by the black cross. Dotted lines show the range in τ that is summed over for each test frequency. The panels at the top and on the left are the collapsed autocorrelation function over test frequency and lag respectively.	67

3.4 Luminosity as a function of effective temperature for solar-like oscillators observed by <i>Kepler</i> , and those in the TESS test set. The <i>Kepler</i> sample is in orange, consisting of 16,000 solar-like oscillators Serenelli et al. (according to 2017), Lund et al. (2017), and Yu et al. (2018a). The remaining scatter points are those in our TESS short cadence test set. The background is a histogram of a random draw of Gaia stars for comparison purposes. The top and right-hand panels are one dimensional histograms of the distributions in luminosity and effective temperature in the two sets. Reproduction of Figure 1 from Nielsen et al. (2023)	71
3.5 Left frame shows the true positive versus false positive rates for varying thresholds on the power excess and repeating pattern tests. Each curve corresponds to a single power excess threshold, with every point on the line being a single repeating pattern threshold. The false positive and true positive rates for stars passing these thresholds in either one module (labelled 'Either') or two modules (labelled 'Both') are plotted on the x and y axes. Panels to the right show the accuracy of the pipeline at each combination of thresholds. The top panel is for responses in either module, and the bottom for responses in both modules. Scatter points mark the maximum accuracy. Reproduction of figure 7 in Nielsen et al. (2023)	73
4.1 2MASS K_S magnitude and predicted ν_{\max} for stars observed in 120-second cadence with a detection probability exceeding 10% (grey). The targets that we identified as solar-like oscillators are marked in blue.	83
4.2 Left: Distribution of T_{eff} for targets used in the testing set of 400 oscillators from N22 compared to those in the catalogue reported here. Right: Distribution with 2MASS K_S magnitude	85

4.3	Mean simulated collapsed ACF as a function of $\Delta\nu$ for filtered white noise (top panel). Colours represent time series of different lengths, with one sector in black, four in blue, nine in green, and twelve in magenta. Pale lines show the predictions for each length according to Eq. 4.2. Variance on the simulated collapsed ACF presented in the top panel (bottom panel).	90
4.4	Asteroseismic HR diagram for stars in all samples (main panel, orange circles). Effective temperatures have been drawn from the TIC in all cases, to maintain consistency. Contour lines represent measurements from <i>Kepler</i> data reported in Yu et al. (2018b), Lund et al. (2017), and Serenelli et al. (2017), with effective temperatures from GDR2. The horizontal dashed line represents the <i>Kepler</i> long-cadence Nyquist frequency. Three stellar tracks at masses 1.0, 1.5, and 2.0 M_\odot generated by MIST (Choi et al., 2016) are shown in grey. The distributions in T_{eff} and ν_{max} are shown in the bottom and right panels, respectively. Here, the catalogue is split into the ATL set in turquoise and the Large Sample in pink (dashed), with the <i>Kepler</i> distribution shown in black.	91
4.5	Comparison of the global asteroseismic parameters measured by our algorithm to those reported in the literature. Stars are coloured by the number of modules in which they produce a flag; pink for a single module, brown for two modules, and an open grey marker for none. Triangles represent stars for which no uncertainty on ν_{max} was reported in the literature. Targets λ^2 For, ν Ind, and HD212771, which are discussed in the text, are marked with a diamond, circle, and square, respectively. The left and right panels show the fractional difference between the values of ν_{max} and $\Delta\nu$ as measured by the algorithm vs literature value, respectively.	93

4.6 $\Delta\nu$ as a function of ν_{\max} measured by the algorithm for validated solar-like oscillators from the ATL set (main panel). Stars producing flags in only one module are shown in pink, and those producing flags in both modules are shown in brown. Triangles mark stars that were likely misclassified as solar-like oscillators. Targets TIC381975502 and TIC271701447, which are discussed in the text, have been marked with a diamond and circle. The dotted black line shows Eq. 4.1. Additional panels show the fractional uncertainties on $\Delta\nu$ and ν_{\max}	95
4.7 Prior ν_{\max} ($\nu_{\max,\text{prior}}$) vs measured values in short cadence targets. The dashed blue line represents the 1-1 line.	97
4.8 $\Delta\nu$ vs ν_{\max} for validated solar-like oscillators from the 20-second cadence set. Stars producing flags in only one module are shown in pink, and those producing flags in both are in plotted in brown.	98
4.A.1 $\Delta\nu$ as a function of ν_{\max} for targets in the final catalogue in brown. Values that were removed after manual identification are shown as open circles.	101
5.1 HR diagram for selected stars from simulation. The full set of stars output from TRILEGAL is shown in the empty scatter points. Filled points are the solar-like oscillators selected for this work. The black dotted line marks the location of the red-edge of the δ Scuti instability strip. Accordingly, stars in the red shaded region are unlikely to host solar-like oscillations. The background colour shows the distribution of luminosity and temperature in a random draw from Gaia.	110
5.2 HR diagram for the simulated population of NGC 6397 showing detection results made with year-long lightcurves. Right: Points coloured by the maximum of the PE merit function in a given spectrum. Left: Points coloured by the maximum of the RP merit function in a given spectrum. Dashed horizontal line marks the maximum ν_{\max} of stars reliably recovered by the PE module. The dotted dashed line is the same for the RP module.	119

5.3	Number of stars with PE or RP merit functions exceeding thresholds as a function of observation length.	121
5.4	Global asteroseismic parameters ν_{\max} (top panel) and $\Delta\nu$ (bottom panel) measured by the detection pipeline as a function of the values from the stellar models. Black dotted line is the one-to-one line.	122
5.5	Recovery of $\ell = 0$ and 2 frequencies according to the mean difference between model and measured frequencies. Successful recoveries are defined as those in which the average difference between the model and measured mode frequencies is less than the average uncertainty reported by pbjam. The top panel shows the fraction of stars in which $\ell = 0$ or 2 modes are recovered as a function of ν_{\max} . Fractions are calculated in bins in ν_{\max} with a width of 20 μ Hz. For reference, the distribution in ν_{\max} of all of the stars in which we detect the presence of oscillations is included in the bottom panel.	123
5.6	Rotational splitting as a function of surface gravity for stars reported in Deheuvels et al. (2014) and Gehan et al. (2018a) and Triana et al. (2017). Squares represent core rotation rates, circles for envelope rotation rates. Line shows the log-linear fit to the data of Deheuvels et al. (2014) and Triana et al. (2017). . . .	127
5.7	Spectrum of the star used to test fitting perturbed $\ell = 1$ modes. Insert is the region in which we fit the perturbed dipole modes. Grey dotted lines show the true values of the $m = 0$ frequencies.	129
5.8	Recovery of rotational splitting for $0.1 \mu\text{Hz} < \delta\nu_{\text{core}} < 1.0 \mu\text{Hz}$. Panels in the top row show the posterior on the difference between the model and measured values of $\delta\nu_{\text{rot},n}$ for each value of $\delta\nu_{\text{core}}$. Annotations are included with the value of $\delta\nu_{\text{core}}$ in μHz . Panels on the bottom row show the number of modes in which we measure $ \delta\nu_{\text{rot},n,\text{measure}} - \delta\nu_{\text{rot},n,\text{modell}} < 3\sigma$	131
5.9	As in Figure 5.8, but with $1.1 \mu\text{Hz} < \delta\nu_{\text{core}} < 2.0 \mu\text{Hz}$	132
5.10	As in Figure 5.8, but with $2.1 \mu\text{Hz} < \delta\nu_{\text{core}} < 3.0 \mu\text{Hz}$	132

5.11 Diagnostic plots for the recovery of magnetically perturbed modes. Plots in the left-hand column are the average difference in the model and measured frequencies as a fraction of the measurement uncertainty, $\sigma(\nu_{\text{fit}})$. From top to bottom these are for perturbations with $a = -0.5, 0$ and 1 . Plots in the right hand panel are in the same order in a . These panels show the recovery of the asymmetry parameter, δ_{asym} . Empty circles are the true value.	136
6.1 ν_{max} and T_{eff} values for the selected sample (pink) compared to those from the catalogue by Yu et al. (2018a) (green). For reference we show the MIST (Choi et al., 2016; Dotter, 2016) evolutionary tracks for $1 M_{\odot}$, $1.5 M_{\odot}$, $2 M_{\odot}$, and $2.5 M_{\odot}$ stars at $[\text{Fe}/\text{H}] = -0.25$ which approximately corresponds to the median metallicity of the selected sample, as reported in table 2 of Yu et al. (2018a).	141
6.2 Stretched échelle power diagrams for two red giants showing characteristic features of rotation and magnetism. (a): KIC 10006097, showing symmetric rotational splitting. (b): KIC 8684542, from the sample of Li et al. (2022a), showing pronounced asymmetric rotational splitting indicative of core magnetism. The power spectrum indicates excess power along the g-mode ridges that do not correspond to identified and fitted modes in, e.g., their Fig. 3.	147
6.3 Distribution of summed power across ridges defined by $\delta\nu_{\text{rot}} = 0$, $\delta\nu_{\text{mag}} = 0$ and $a = -0.5$ for a white noise spectrum stretched according to the asymptotic parameters of KIC10006097	150
6.4 Left panel: Inverse of the 2-dimensional H0 likelihood space for $\delta\nu_{\text{mag}}$ and $\delta\nu_{\text{rot}}$. Two stars are shown, KIC 8684542 and KIC10006097. Right panel: Inverse of the 2-dimensional H0 likelihood space for $\delta\nu_{\text{mag}}$ and a for KIC 8684542 and KIC 10006097.	151
6.5 Core rotational splitting from the template matching technique versus those reported in G18. Black dotted lines show the 1-1 relation $\pm 0.05 \mu\text{Hz}$	153

6.6 Left panel: Magnetic splitting, $\delta\nu_{\text{mag}}$, measured using summed power versus that reported in L23. Black dotted lines are the 1-1 relation $\pm 0.05\mu\text{Hz}$. Right panel: Topology parameter, a , measured using summed power versus that reported in L23. Black dotted line is the 1-1 relation.	154
6.7 Distribution of $\delta\nu_{\text{rot}}$ in three mass ranges. Values of $\delta\nu_{\text{rot}}$ are those reported here, supplemented by values from G18 with $\nu_{\text{max}} < 150\mu\text{Hz}$. The black curves show are a KDE of the distribution. Black dotted lines mark the locations of the two peaks identified in the lowest mass set to guide the eye.	156
6.8 Fractional difference in $\delta\nu_{\text{rot}}$ measured here and reported in G18 as a function of $\delta\nu_{\text{mag}}$	157
6.9 Distributions of magnetic parameters. Histograms are built using 100 draws from the posterior for each of the 302 stars. Top panel: Distribution of $\delta\nu_{\text{mag}}$. Middle panel: Distribution of δ_{asym} . Bottom panel: Distribution of a	159
6.10 Distribution of $\delta\nu_{\text{rot}}$ as a function of stellar mass for the combined set of stars reported here and in G18. The left-most panel shows just the measurements reported in this work. In the center panel we fold in measurements from G18. The Black contours in the right hand panel are a kernel density estimate (KDE) highlighting the bimodality.	160
6.11 Distribution of $\delta\nu_{\text{rot}}$ reported in G18 (grey edgecolor) and here (black edgecolor) for stars in 3 different N ranges. The left-most panel is targets with $N < 7$, the middle panel has targets in the range $7 < N < 11$. The right-most is stars with $N > 11$. Black dotted lines are at $\delta\nu_{\text{rot}} = 0.32 \mu\text{Hz}$ and $0.47 \mu\text{Hz}$. Histograms on the right show the distribution in the stars with $N < 7$ in pink and with $N > 11$ in green.	161
6.12 Left panel: $\delta\nu_{\text{mag}}$ as a function of stellar mass. Right panel: Best fitting $\sqrt{\langle B_r^2 \rangle}$ as a function of stellar mass.	164

6.13 Best fitting $\sqrt{\langle B_r^2 \rangle}$ as a function of mixed mode density, \mathcal{N} . Stars with $\delta\nu_{\text{mag}} - 2\sigma(\delta\nu_{\text{mag}}) > 0$ are shown in orange. The remaining measurements are in grey. Blue diamonds show values reported in L23 for stars that do not appear in this work.	165
6.B.1 Corner plot showing the distribution of the asymptotic parameters, rotational splitting and magnetic parameters across all 302 stars.	169
6.B.2 Left: Difference in period spacing measured here and reported in V16. Right: Difference in q measured here and reported in M17.	170
6.C.1 Corner plot of the asymptotic parameters of KIC11515377.	171
6.C.2 Corner plot of the asymptotic parameters of KIC7018212.	172

List of Tables

4.1	Global asteroseismic parameters of stars in the literature sample.	80
4.2	Catalogue of seismic parameters for detected solar-like oscillators. The full table is available in online materials. Quantities RP and PE track which modules the target produced a detection in. Flag is ‘SB9’ for targets in the <i>Ninth Catalogue of Spectroscopic Binary Orbits</i> (Pourbaix et al., 2004) and ‘PH’ for targets which are confirmed planet hosts according to NASA’s Exoplanet Archive.	84
4.3	Detection counts in each sample. ‘Double’ refers to cases where the star flagged a detection in both the power excess and repeating pattern modules. ‘Single’ refers to cases where the star flagged in one module only.	87
4.4	Parameters for Eq. 4.2 and 4.3.	89
5.1	Proposed set of specifications for the HAYDN mission, used to generate expected noise levels.	108
5.2	Exponents used in Equation 5.3 for stars on the red giant branch and the main sequence. Exponents for stars on the main sequence are from a manipulation of the equations in Kjeldsen et al. (1995). These are the result of a combination of theoretically derived scaling relations and fits to model stars and observational data. There-in error bars are not listed on the exponents of the fits. Exponents for red giants were determined via a fit to measurements from the Yu et al. (2018c) catalogue.	113
5.3	Parameters for Equation 5.5, according to Ball et al. (2018).	114

5.4	Number of stars exceeding detection thresholds in the PE and RP modules for various lightcurve lengths.	121
5.5	Priors used in the fit of the perturbed dipole mode frequencies.	130
6.A.1	Values of the asymptotic parameters used to construct a mock spectrum for KIC8684542.	168

Chapter 1

Introduction

From the first measurements of distance to another galaxy made by Edwin Hubble (Hubble, 1925; Hubble, 1926) to the recent exploration of exoplanets, some of the most fundamental questions in astrophysics have been answered via observations of starlight. Any study using this information to make physical inferences must, therefore, have a good understanding of the object producing the light. Stars are not static, they evolve as they age, undergoing various physical changes that influence their observable properties. Until very recently, stellar astrophysics (the field dedicated to understanding these changes) remained broadly theoretical, observationally limited to the properties of the surface layers of stars. This era ended with the advent of **asteroseismology**, to which this thesis is dedicated, which finally provided the means to probe the internal structures of stars.

The first book laying out the detailed fundamentals of stellar evolution was published by Sir Arthur Eddington (Eddington, 1926). From 1926 until the 1960s many of the physical principles of stellar evolution could not be observationally challenged. This was a direct result of the opaque nature of stars, which only become transparent to photons in a thin shell (0.1% by radius in the Sun) near the surface, known as the photosphere. Given photons are the main transmitter of information from distant stars to us observers, on face value it would appear we have no direct probe sensitive to depths below a few fractional percent. This was taken as true until the 1960s, when Leighton et al. (1962) reported the discovery of oscillations in Doppler

measurements of the solar surface. Subsequent work demonstrated the dominant period of these oscillations is ≈ 5 mins and they do not just occur on the surface, rather the whole Sun pulsates (Claverie et al., 1979).

The oscillations Leighton observed are excited by convection in a thin layer near the surface of the solar convective envelope. The turbulent motion associated with this process generates sound waves which travel through the body of the Sun, being refracted as they do so. The waves continue on their paths until they re-emerge at the surface, and the sharp drop in density results in reflection. The incoming reflected wave and outgoing refracted wave interfere, producing trapped standing waves. As a result, the Sun pulsates (or oscillates), periodically expanding and contracting.

The waves which form the modes propagate in regions far below the photosphere, where they are encoded with information about the properties of the gas. Therefore, measurements of their frequencies, lifetimes and amplitudes can be used to make inference on the internal workings of the Sun. A new field of stellar astrophysics emerged on this principle, which today we call **helioseismology**. The advent of helioseismology revolutionized solar physics, providing measurements of the sound speed profile in the Sun alongside many other fundamental properties like the rotational profile below the photosphere (see the reviews of Howe, 2009; Basu, 2016; Buldgen et al., 2019).

Helioseismic analysis uses observations of the pulsations of the Sun to infer its fundamental properties. As it happens, the Sun is far from the only star which oscillates. The natural next question is whether we can apply helioseismic methods to other stars. This question is the basis of research in the field of **asteroseismology**. Broadly, we classify pulsating stars into one of two categories, defined by the manner in which the observable oscillations are excited. So-called classical oscillators host pulsations that are excited by heat engines, whereas solar-like oscillators host pulsations excited by turbulence from convection. This thesis will focus on stars in the latter category. Not all solar-like oscillators are in the same phase of their lives as the Sun. Indeed, the vast majority of stars in which we have detected this class of oscillation are much more evolved. This highlights the greatest success of asteroseismology, as a tool to study not

only the current internal state of stars like the Sun, but the way in which they evolve.

As helioseismology revolutionized solar physics, asteroseismology revolutionized stellar physics. The most basic asteroseismic analysis can provide tight constraints on fundamental stellar properties like mass and radius (which can be determined with a precision on the order of a few percent), while more detailed work includes the measurement of properties deep within the body of a star. Examples of mechanisms that asteroseismology alone can probe include rotation and magnetism near stellar cores. Aside from stellar physics for stellar physics sake, these improvements have crucial implications for many other fields of research, including the study of exoplanets (which benefit from measurements of fundamental stellar properties) and the history of The Milky Way (which requires the stellar ages that asteroseismology can provide).

Observing campaigns (or missions) releasing data suitable for asteroseismic analysis have been rapidly increasing their output in recent years. We now have the data required to deploy asteroseismic techniques on hundreds of thousands of stars. Current tools must be adapted to the demands of this "big data", prioritizing automation over manually intensive methods. With these adaptations in place, it is the perfect time to make population-based inferences on asteroseismically inferred stellar properties. This thesis is dedicated to that task, going from automating the detection of solar-like oscillators in large datasets to making population scale inference on the properties of stellar cores using asteroseismology.

The thesis is structured as follows, in Chapter 1, I will briefly cover the aspects of stellar evolution required to understand the following work, and highlight the processes I will later investigate. This will include an overview of the theory of stellar oscillations. In Chapter 2, I will cover the necessary aspects of data analysis utilized by asteroseismologists and how we exploit them to detect solar-like oscillations. I will introduce a pipeline that Dr. Martin Nielsen and I developed for automating the process of detection in Chapter 3. Chapter 4 applies this detection algorithm to a large dataset, and is adapted from a paper I published. In Chapter 5, I will discuss the potential for asteroseismic studies of stellar clusters, and present some predictions for the total detection yields for a candidate cluster. Finally, in Chapter 6, I will go beyond detection, and detail a pipeline I generated for the measurement of core rotation and core

magnetic fields using asteroseismic techniques. I will also present the results of the application of this method to hundreds of stars.

Given the wealth of data we still have to explore, the field of asteroseismology is still in its infancy. In this thesis I will demonstrate this, by greatly expanding the number of stars to which we can apply asteroseismic techniques. Additionally, I will demonstrate how the currently available data can be used to open a window on the core properties of hundreds of stars. Finally, I will look to the future, making predictions for a proposed asteroseismic specific observing mission.

1.1 A General Overview of the Evolution of Low-mass Stars

All stars begin their lives as clouds of interstellar gas which have become unstable to gravitational collapse. This gas cloud will eventually evolve into a stable star, which will then undergo a series of evolutionary processes significantly changing its properties. Historically, we have studied these changes in the context of the stellar luminosity and temperature. Stars were initially classified by placing observational proxies of the former as a function of the latter on what is known as a **Hertzprung-Russell diagram** (HR diagram). We access information about luminosity and temperature via measurements of the photons a star gives off, the stellar flux. While the total flux is a function of luminosity, its wavelength dependence carries information about temperature. We use this to define the **effective temperature**, the temperature of a perfect blackbody producing the same flux-wavelength dependence.

An example HR diagram is shown in Figure 1.1, showing the paths taken by stars of three different initial masses. I have limited these tracks to show only the phases of evolution that will be important for this work; **The main sequence (MS)**, **subgiant branch (SGB)** and **red giant branch (RGB)**. Briefly, stars begin their lives on the main sequence, burning hydrogen to helium at their cores. Once the hydrogen fuel has been exhausted at their cores, they join the subgiant branch and then the red giant branch, where hydrogen burning continues in a shell about the inert core. Subsequent evolution will involve the burning of progressively heavier elements.

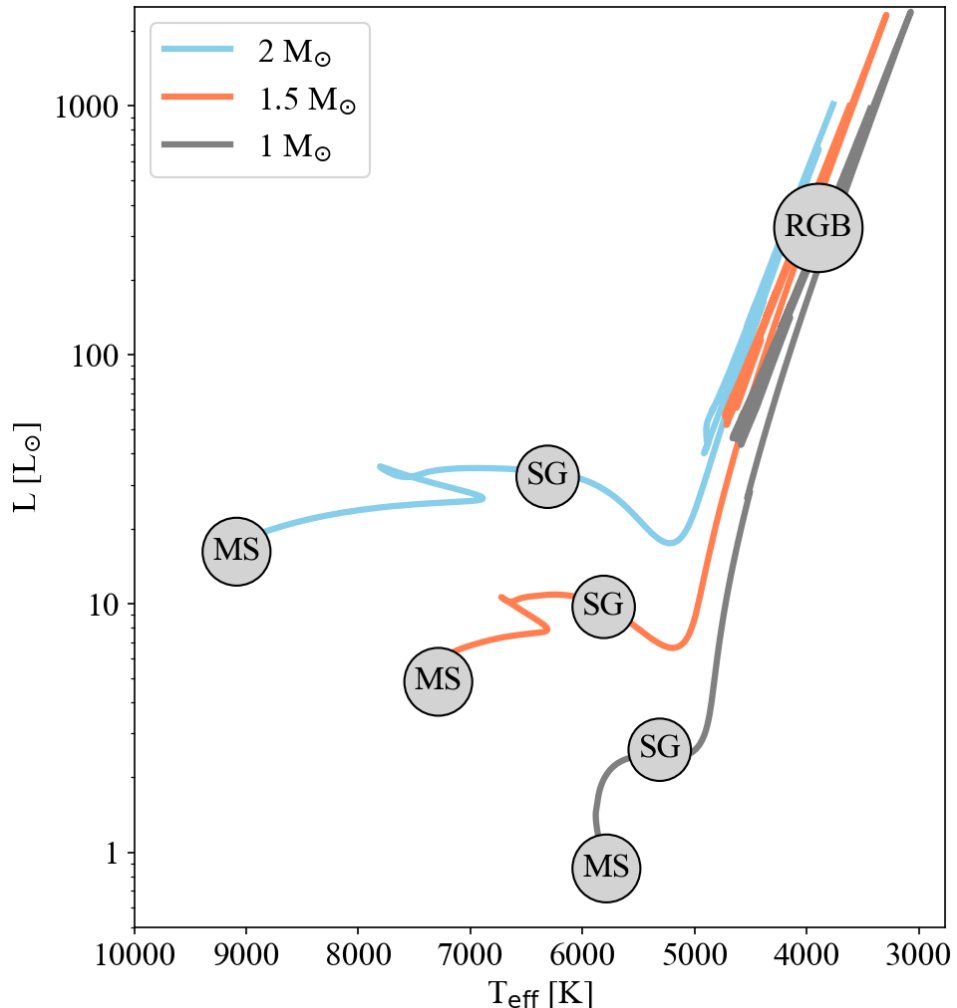


Figure 1.1: HR-diagram showing the evolutionary tracks of stars of mass $1M_{\odot}$, 1.5_{\odot} and $2M_{\odot}$ at solar metallicity. For each track, the location of the main sequence is identified by the label ‘MS’, the subgiant branch by ‘SG’ and the red giant branch by ‘RGB’.

The path which a star takes while it traverses the HR diagram depends crucially on the way in which energy is transported. Largely, stars transport energy via two processes: radiation and convection. In the case of the former, the net flow of energy is a result of the way in which photons interact with the gas. The latter involves the upward movement of hot gas, and downward movement of cool gas. Should a bubble of gas be displaced upwards into a region in which the gas is less dense, it will survive and continue to rise if the element is in pressure equilibrium with its surroundings. According to the ideal gas law, this would imply the temperature in the bubble of gas must be higher than that in the surrounding plasma. These conditions are met in regions in which the temperature gradient in the ambient gas is a more rapidly decreasing function of radius than the adiabatic temperature gradient. Once the pressure equilibrium is disrupted, the bubble dissolves, depositing its thermal energy to the surrounding plasma. A sinking bubble of gas must be denser than the surroundings, implying it is cooler. The movement of relatively hot gas upward, and relatively cool gas downward produces a net flow of thermal energy outward.

For a predominantly radiative star, the relation between luminosity and effective temperature is a function of opacity, a measure of how much energy is required to heat the gas by 1K. Gas is under different conditions in stars of varied mass, such that the opacity is dominated by distinct processes. For example, where the density of free electrons is very high, the opacity is dominated by electron scattering. This requires the gas to be fully ionised, and as such only occurs in the hottest stars, which are predominantly high mass. On the other hand, the luminosity for a fully convective star is essentially independent of mass and scales only with temperature. This causes stars to evolve along a single line in the HR-diagram, known as the Hayashi track. On the Hayashi track, luminosity decreases with increasing temperature. In the following I will use this context to discuss the evolution of a typical solar-like oscillator.

For a gas cloud to collapse we require that it has gravitational energy exceeding approximately twice its thermal energy. This implies hotter clouds of gas must be higher mass to be unstable to collapse. These high mass clouds are the progenitors of high mass stars, and so more massive stars begin their lives at hotter temperatures. Due to their large radii, even the hottest proto-stars are cool in a stellar physics context. This causes high opacities, which result in larger ambient

temperature gradients, making the gas unstable to convection. Accordingly, the cloud follows the Hayashi track on the HR diagram and decreases in luminosity as it heats up.

Once the gas becomes dense enough at the core of the proto-star, hydrogen begins to fuse, releasing enough nuclear energy to support the cloud against contraction. We label the period in a star's life when core hydrogen burning is occurring as the **main sequence** (see MS label on figure 1.1). The luminosity and temperature of the new star increase during this phase, the change being much less significant than it was during the pre-main-sequence. For stars with masses $> 0.25M_{\odot}$, the outer layers of the star meet the required conditions for convection. This convective envelope decreases in thickness with increasing mass, such that for a star of mass $0.4M_{\odot}$ at solar metallicity the base of the zone sits at 40% of the radius, compared to 70% in the Sun (van Saders et al., 2012). Stars with masses in the range $1.1M_{\odot} \lesssim M_* \lesssim 1.5M_{\odot}$ host two convection zones, both in the outer envelope and in the stellar core. Should the mass exceed $\approx 1.5M_{\odot}$, surface convection will not occur (Kippenhahn et al., 1994).

After a period of time, the hydrogen fuel will be exhausted in the core. However, the temperature in a shell outside of the resulting inert core will have become sufficiently high to enable hydrogen fusion. The burning produces more inert helium, increasing the mass of the core and causes it to contract. In a process that is still not well understood, the presence of shell burning leads to an expansion of the outer layers of the star, decreasing the temperature at the surface. At this point, most of the star is radiative such that the decrease in temperature leads to a decrease in luminosity. We call this phase of the lifecycle of a star the **subgiant branch**. Given the timescales associated with gravitational contraction are much shorter than those of nuclear burning, core contraction during the subgiant branch is rapid when compared to the timescales of evolution on the main-sequence.

As the temperature of the star continues to drop, the outer convection shell deepens until the star is primarily convective in nature and joins the Hayashi track, marked by a sharp increase in luminosity. This phase is called the **red giant branch**. The outer layers continue to expand, decreasing the temperature and increasing the luminosity until the core is dense and hot enough for helium fusion to begin. This causes the core to expand, such that the outer layers contract

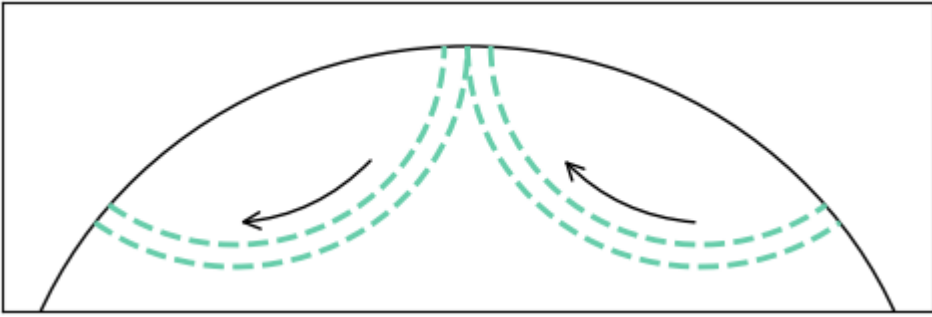


Figure 1.2: Illustrative diagram showing the refraction and reflection of an acoustic wave as it travels from a point on the surface radially inward and then outward to be reflected at another point.

and the star reverses its path on the HR diagram.

1.1.1 Oscillations in Low-mass Stars

We have identified that convection occurs in the outer envelopes of low-mass stars on the main-sequence ($M_* \lesssim 1.5M_\odot$) and in stars on the subgiant and red giant branches. This outer envelope crucially influences the dynamics of the entire star, acting as the birth place of solar-like oscillations. As gas in the outer envelope undergoes turbulent motion, sound waves are generated. These waves propagate through the body of the star, before being refracted back toward the surface where they are eventually reflected. An illustration showing this refraction and reflection can be seen in Figure 1.2. The ingoing and outgoing waves interfere with each other and create trapped standing modes of oscillation, which cause the star to periodically expand and contract at characteristic frequencies.

As we will see in detail in Section 1.3, the frequencies at which a solar-like oscillator will pulsate are dependent on the properties of the gas in which they propagate. On the population scale, this causes differences in the periods of oscillation for stars with different masses, radii and effective temperatures. This enables us to use observations of solar-like oscillations to measure these fundamental properties in field stars, which would otherwise be very poorly constrained. Aside from bulk stellar parameters, the frequencies of the solar-like oscillations are impacted by internal properties, such that they can be used to study conditions deep below

the stellar photosphere to which all other traditional observations are blind. Two mechanisms which asteroseismology is uniquely situated to study are magnetism and rotation, which have a measurable impact on solar-like oscillations (which will be discussed in Section 1.3.5). Thus far I have discussed stars in the absence of these phenomena, in the following section I will address the ways in which they impact stellar evolution, and detail the current observations.

1.2 Stellar Rotation and Magnetic Fields

Rotation (primarily non-solid-body rotation) impacts the manner in which different chemical elements are transported through the body of a star. The associated mixing processes can provide the core with additional hydrogen fuel and dredge burnt helium up to the surface (see Maeder et al., 2012, for a review). The increase in hydrogen in the core increases the main sequence lifetime of a star when compared to the non-rotating case (Meynet et al., 2000). It has also been shown that the increased helium in the surface layers substantially changes the stellar luminosity, a result of the decrease in opacity (Meynet et al., 2000; Maeder et al., 2010; Eggenberger et al., 2021). Therefore, attempts to predict the observable properties of a star without considering rotation are inherently flawed. Despite the clear requirement for a good understanding of stellar rotation to accurately model a star, the details of how stars rotate in reality are still not well understood. As I will discuss in Section 1.2.1, classical observational data is limited in sensitivity to just the surface layers, and there is little reason to assume all stars rotate as solid bodies. To fully understand how rotation impacts stellar evolution, we must observationally probe deeper into the interior. Asteroseismology is the only technique capable of making such measurements.

The surfaces of low-mass stars are observed to spin-down as they evolve on the main sequence (Kraft, 1967; Skumanich, 1972; Barnes, 2003; Barnes, 2007; Irwin et al., 2009). As we will see in section 1.2.2, this is the result of magnetism in the upper layers. Accordingly, the most accurate stellar model should account for both rotation and magnetism. Akin to rotation, observations of magnetic fields are primarily limited to the surface layers (see section 1.2.2).

However, the presence of a magnetic field below the outer convective envelope could lead to coupling across the stellar radius influencing the transport of angular momentum through the body of the star (Mestel et al., 1987; Charbonneau et al., 1993; Maeder et al., 2014). Again, only asteroseismology can produce observations of magnetic fields in these regions.

In the following sections I will give a brief overview of the ways in which we expect the rotation of a star to evolve from the main sequence to the red giant branch. These theories will be compared to current observations. I will then discuss the leading theories regarding stellar magnetic fields and the limits of current observations.

1.2.1 Rotation

Theory

The host of dynamical processes occurring in a star as it evolves make predicting rotation difficult. Stars inherit the angular momentum of the cloud from which they form, which is then conserved as the gas contracts, spinning the star up. A common assumption is that the fully convective pre-main sequence star rotates as a solid-body (Amard et al., 2019). This is interrupted by the appearance of radiative zones, and the star begins to experience radial differential rotation. After the main sequence, the stellar core contracts while the envelope expands. To locally conserve angular momentum, this implies that the core must spin up, while the envelope spins down.

Including a full treatment of stellar rotation when modelling evolution is difficult given the number of mechanisms that can alter the transport of angular momentum. These include the motion of convective elements and solar-like oscillations. Magnetic fields are also capable of altering the rotational profile of a star by enhancing the coupling between layers. Indeed, even a weak field can enforce rigid body rotation (Mestel et al., 1987).

Observations

Stellar rotation is most commonly measured using one of two techniques (see Bouvier, 2013, for a review), Doppler broadening of absorption lines and starspot monitoring, which I will briefly

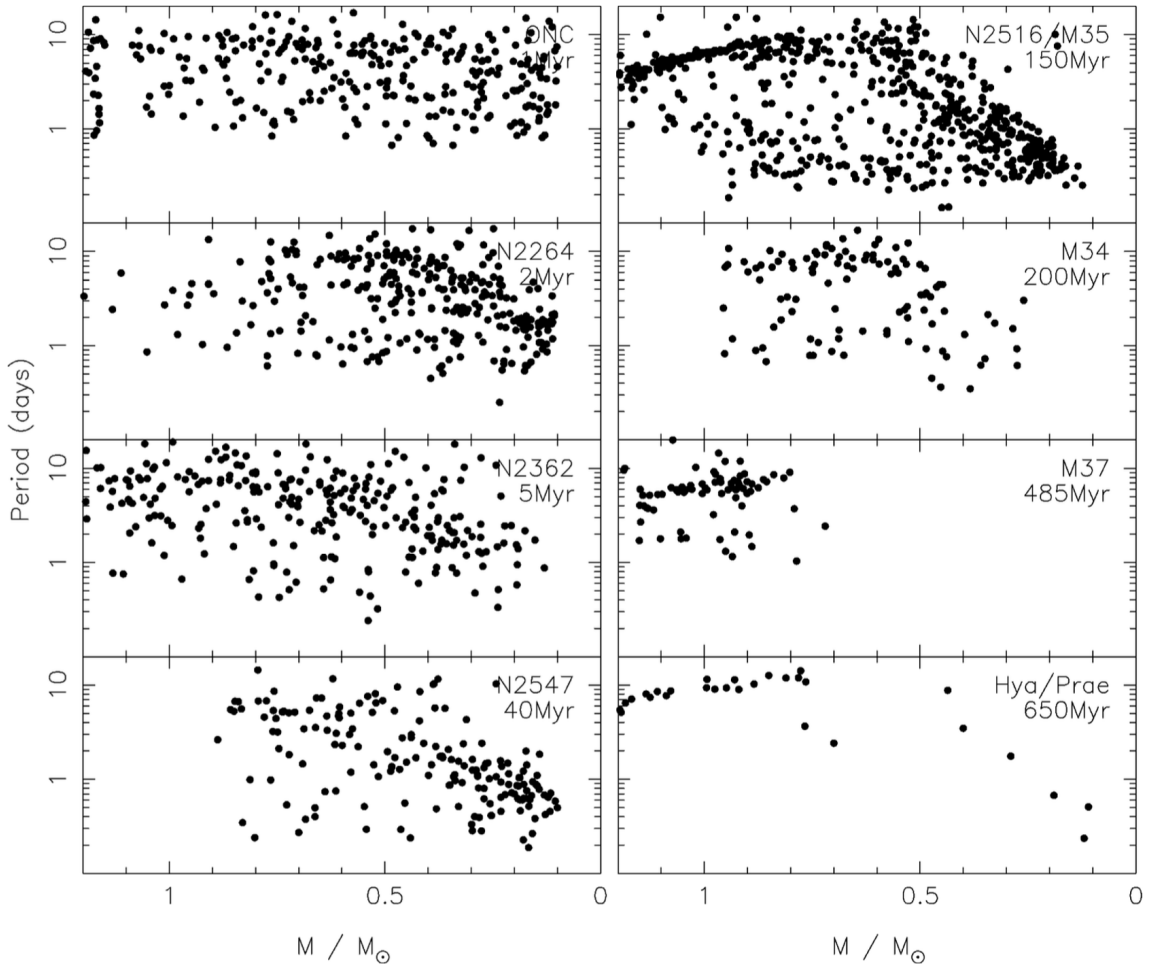


Figure 1.3: Surface rotation rates as a function of stellar mass for stars in 8 stellar clusters. The youngest cluster is plotted in the top left and the oldest cluster in the bottom right. Periods appear randomly distributed in the youngest cluster, as the age increases stars start join a track in mass-period space. There-in, the higher mass stars converge to shorter periods than the lower mass stars. Figure 2 in Irwin et al. (2009)

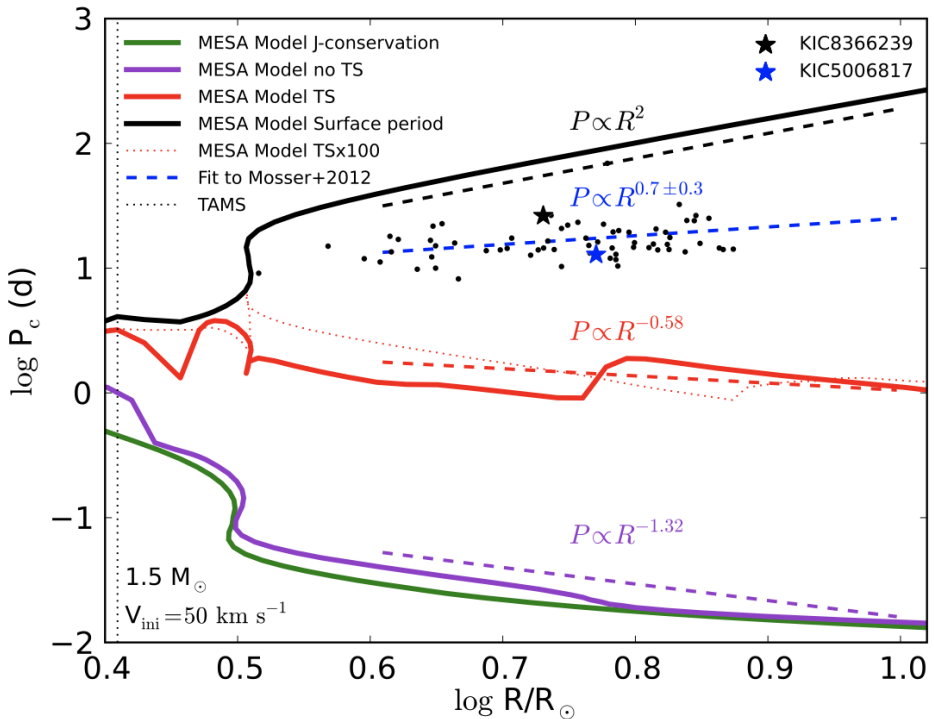


Figure 1.4: Asteroseismically inferred core rotation periods as a function of stellar radius shown as scatter points. Lines show various predictions for the core period as a function of radius according to different prescriptions for angular momentum transport. In green is a simple treatment, with rotation considered in shells and the total angular momentum is conserved. The model in purple includes rotational instabilities. In red is a model with a core magnetic field in the radiative core. Black line shows the surface period. Figure 2 from (Cantiello et al., 2014).

cover in the following.

One limb of a rotating star has velocity along the line of sight toward the observer, while the other has velocity in the opposite direction. Therefore, the light from one side of the observed disk will be blue shifted while the other is red shifted. This broadens absorption lines in the spectrum of a star, with the degree of broadening being dependent on how rapidly a star is spinning. As the absorption features originate in the stellar photosphere measurements of Doppler broadening are only sensitive to rotation in the surface layers, and cannot provide information about the radial profile within the star.

Photometric measurements can also be used to measure surface rotation. This is done via the monitoring of starspots, locally dimmer regions on the stellar surface caused by strong magnetic fields. These magnetic fields suppress convection, preventing hot gas from moving upwards such that the area is locally cooler and therefore dimmer. The magnetic fields are frozen-in to the gas, meaning that starspots rotate with the star. The periodic dimming of the star as a spot rotates onto and off of the observable disk is thus a direct measure of the stellar rotation period. The magnetism manifesting in starspots acts only in the surface layers of the star, and again the probe is not sensitive to the rotation below the outer convection zone.

Measurements of surface rotation periods have been made for thousands of stars, which lead to the identification of a decrease in the surface rotation rate of main-sequence stars as they age. The effect can be seen in Figure 1.3, which shows the rotational periods as a function of stellar mass for stars in stellar clusters at different ages (Irwin et al., 2009). In the youngest bin, all stars are on the pre-main sequence, and rotation rates are randomly distributed. As the age increases, stars start to join the main sequence, and begin to converge to a track in period-mass space. By 150 Myrs, almost all stars with masses $\gtrsim 0.7M_{\odot}$ have joined this track. The average period on the track decreases with stellar mass, such that higher mass stars are rotating more rapidly. These stars exhaust their core hydrogen supply faster than their lower mass counterparts, implying that the degree to which a star spins down depends on how long it spends on the main sequence.

The spin down exemplified in Figure 1.3 is the result of a phenomenon known as the stellar wind. Stars with mass $\lesssim 1.5M_{\odot}$ host convective envelopes which generate magnetic fields.

These fields throw off gas near the surface of the star. The gas remains coupled to the star out to the radius at which the magnetic tension is no longer high enough to resist the coriolis force. The effective increase in radius slows the stellar spin, converging to the observed sequence. It was found that this process produces rotation rates that can be approximated by a simple power law on the main sequence age ($\Omega \propto t^{-1/2}$) known as the Skumanich relation (Skumanich, 1972). High mass stars without convective envelopes are not spun down by stellar winds, and thus rotate much more rapidly on the main sequence.

Classical measurements of rotational period can only provide information about the surface layers. Although the assumption of solid-body rotation is sometimes made to simplify stellar modelling, in reality we know that it is likely not a true reflection of the interior of a star. Fortunately, the frequencies of the oscillations of a rotating star differ from a non-rotating reference, such that we can make asteroseismic measurements of rotation. I will discuss this in greater depth in section 1.3.5. Helioseismic measurements of rotation have been made down to depths of $\approx 50\%$ of the solar radius. These have shown that solar rotation varies with both radius and latitude in the outer convection zone, but converges to a solid body profile in the radiative zone (Howe et al., 2000).

As solar-like oscillators evolve, the observed frequencies become increasingly sensitive to regions near the core (a full discussion will be given in Section 1.3). This has enabled asteroseismic measurements of core rotation in hundreds of red giants, highlighting a major shortcoming in our understanding of stellar rotation. Rates are orders of magnitude slower than those that would be predicted from traditional models of angular momentum transport (Eggenberger et al., 2012; Eggenberger et al., 2017; Ceillier et al., 2013; Marques et al., 2013; Spada et al., 2016; Ouazzani et al., 2017; Fuller et al., 2019; Mombarg, 2023). Additionally, the rates remain remarkably consistent across the entire red giant branch, despite the core contraction. This is shown in Figure 1.4, which is Figure 2 in Cantiello et al. (2014). There-in the authors compare the observed distribution of rotation rates with those predicted by various theories. Marked in green is the simplest case, where rotation is considered in shells and the total angular momentum is conserved. The other predictions include terms that can transport

angular momentum from the core to the envelope, reducing the core rotational period. The authors considered mechanisms associated with rotational instabilities (purple) and a magnetic field generated in the radiative core (red lines). Although none of the predictions can replicate the observations, it is important to note the model including a magnetic field gets the closest.

Asteroseismology has confirmed that the surfaces of red giants rotate slowly. However, the rates are so slow that actually measuring the surface rotation rate (rather than putting upper limits on the possible value) is difficult. Currently we have only seismically inferred the surface rotation of a few tens of evolved stars (Deheuvels et al., 2014; Triana et al., 2017). Akin to the core rotation, which remains fairly constant across the entire red giant branch, the surface rotation also appears remarkably consistent despite the rapidly expanding outer layers. Unlike main sequence stars, classical measurements of the surface rotation of evolved stars are limited. The signature in Doppler broadening is often on the order of the measurement uncertainty. Additionally, evolved stars are not very magnetically active, such that starspot monitoring is not frequently successful.

1.2.2 Magnetic Fields

Theory

As we have seen, magnetic fields have both an observable impact on surface rotation and are theorised to be influential on core rotation rates. However, the evolution of magnetic fields in stars is a topic of much debate. Indeed, we currently lack a unified theory capable of predicting the properties of the magnetic field we should expect to observe in a star of given type. In theory, magnetic fields in the interstellar medium should ‘freeze-in’ to a protostar as it collapses. It is possible for certain field geometries to remain stable through subsequent evolution onto the main sequence. After a star has inherited a field from the interstellar medium, there are several mechanisms by which it may transform this initial field from one configuration to another, destroying the original field architecture.

The mechanism which is best understood is the fluid dynamo, which is believed to generate

the magnetic field in the outer layers of the Sun (Parker, 1955; Babcock, 1961). In such a process the star starts with an initial seed field which is distorted by the currents induced by the shear or turbulent motion of conducting gas. This alters the field structure and supports it against ohmic decay. The ingredients are clear, an initial seed field and shear or turbulent motion. These conditions are met in convection zones. Accordingly, we expect magnetic fields in fully convective pre-main sequence stars alongside the outer envelopes of low mass stars on the main sequence and potentially the convective cores of intermediate mass stars on the main sequence. It is possible for a field originally driven in a convection zone to remain stable over the timescales associated with stellar evolution. This would allow for the existence of magnetic fields in radiative zones. They are labelled as ‘fossil fields’ given they are no longer being actively regenerated.

Finally, the Spruit-Tayler dynamo (Spruit, 2002; Fuller et al., 2019) allows for the generation of a dynamo in stably stratified regions. In this scenario, differential rotation creates instabilities in the magnetic field which result in dynamo action. In this way differential rotation acts as a replacement for convection in the traditional solar dynamo. This could produce fields near the cores of evolved stars, releasing the requirement that such a field be ‘fossil’ in nature.

Observations

For stars on the main sequence, the primary method of detecting fields is spectropolarimetry, exploiting the Zeeman splitting of spectral lines. Given this effect is limited to the regions where the absorption is occurring, it is only sensitive to magnetic fields in the outer layers of the star. Measurements using spectropolarimetry on solar-type stars have shown that faster rotators generally have stronger field strengths (Reiners et al., 2022). Spectropolarimetric studies of A and B-type main sequence stars have revealed magnetic fields with strengths in the range of a few hundred to tens of kG in $\approx 10\%$ of the studied sample (Power et al., 2008). These stars have radiative envelopes which cannot be supporting a solar dynamo.

The strength of a field generated by a solar dynamo scales with surface rotation such that small average field strengths are expected in red giants (with slow surface rotation). However,

starspots (implying stronger field strengths) have been observed in a small fraction of giants. In a sample of over 4000 giants observed by *Kepler*, Gaulme et al. (2020) found an occurrence rate for spot modulation of 8%. Beyond the red giant branch, strong magnetic fields are also observed in $\approx 10\%$ of white dwarfs (Liebert et al., 2003) and, although an occurrence rate is not known, have also been observed in neutron stars. The ‘fossil field’ theory is the leading explanation as to why there are magnetic fields in these radiative stars.

Assuming the magnetic fields in white dwarfs and neutron stars are the fossil remnants of a field generated earlier in the stellar lifecycle, we should expect some red giants to have buried magnetic fields, close to the core. Asteroseismology provides the only probe sensitive to conditions in these regions. Much like rotation, magnetic fields perturb mode frequencies, as we will see in Section 1.3.5. Methods to exploit this phenomena to measure the properties of such fields in red giants have only just become operable. Indeed, the first catalogue of asteroseismically inferred magnetic fields in the cores of red giants was made in 2022, with a set of 3 stars (Li et al., 2022a). There-in, the authors identified magnetic fields with strengths in the range of 30-100kG. Subsequently, asteroseismology has been used to identify magnetic fields in the cores of 21 red giants (Deheuvels et al., 2023; Li et al., 2023).

With the relevant aspects of stellar evolution covered, I will now describe the properties of solar-like oscillators. I will cover the general properties of the oscillations, give a basic overview of the theory and discuss the ways in which the pulsations evolve with the star. This will be extended in Chapter 2, where-in I will provide additional details about how we use asteroseismic data to make inferences about stellar properties.

1.3 Fundamentals of Solar-Like Oscillations

Asteroseismology is the study of stellar pulsations, which are broadly excited by one of two mechanisms - convection or a heat engine. Thus far we have discussed the former mechanism, which generates solar-like oscillations. The latter mechanism generates a class of stars known as classical oscillators, which will not be the focus of this work. As we previously discussed,

solar-like oscillators require only the existence of an outer convection zone in which sound waves are being produced. Therefore, we can expect such oscillations in low mass stars on the main sequence and in all subgiants and red giants.

Solar-like oscillations are encoded with information about the gas in which they propagate. Basic measurements of their properties enables precise inference on a star's mass and radius, parameters which can usually only be effectively constrained for the brightest stars, or in stars in eclipsing binary systems. More detailed analysis can reveal information about internal properties that are completely inaccessible to other observational probes, such as how the star is rotating below the photosphere and whether a magnetic field is present outside of the convective envelope. In the following, I will detail some fundamentals of the theory of solar-like oscillations, and how the pulsations depend on both the global stellar properties and the conditions in the stellar interior.

1.3.1 Overview of the Data

Almost all asteroseismic analysis is done in the frequency domain. The data of interest is the frequency power spectrum associated with measurements of either the stellar flux as a function of time (which we call a lightcurve), or temporal variations in the velocity of the surface. In this thesis I will only use the former. I will start by discussing an example power spectrum as a means of introducing the important parameters, before providing an overview of the theory of solar-like oscillations. In Chapter 2 I will build on this to give a much more detailed review of the data.

An example spectrum for a subgiant solar-like oscillator observed by NASA's *Kepler* mission (Borucki et al., 2010) is shown in Figure 1.5. The shape of this power spectrum (and those of all solar-likes) can be described using the combined signature of a handful of phenomena. Power at the lowest frequencies (below $\approx 10 \mu\text{Hz}$ in Figure 1.5) is identified with the signature of instrumental drift alongside contributions from rotation and activity. In the intermediate regime (below $\approx 500 \mu\text{Hz}$ in Figure 1.5) the signal is dominated by a process known as *granulation*. This is the observable imprint of convection, as cells of gas move upward, radiate energy as

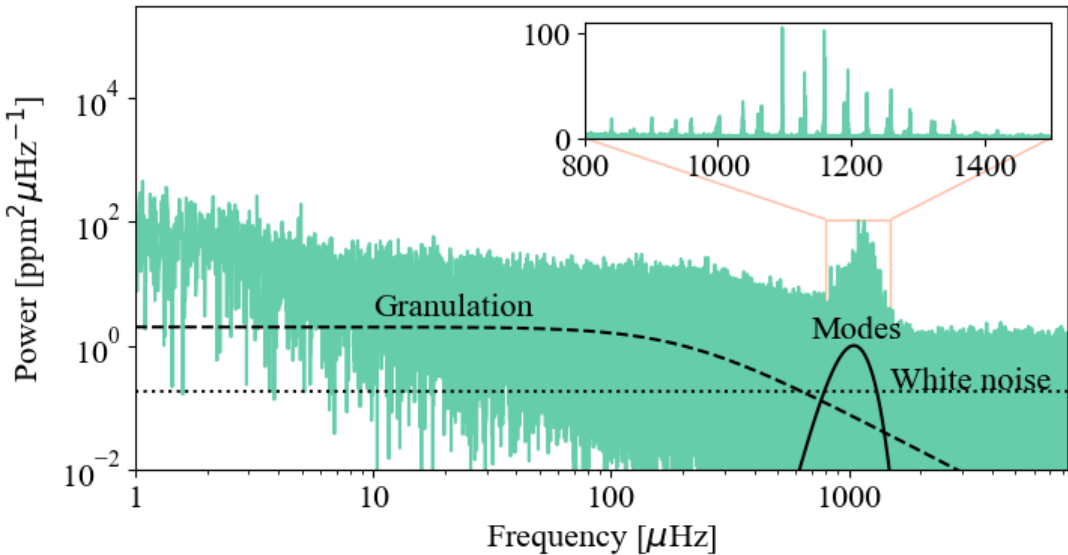


Figure 1.5: Example of the spectrum of a subgiant solar-like oscillator observed by *Kepler* (KIC6442183). The signature of granulation, white noise and the shape of the mode envelope are indicated by a dashed, dotted and continuous line respectively. The inset axis shows a zoom in around the mode envelope, showing a number of Lorentzian peaks associated with individual mode frequencies.

heat and sink. Granulation is described by either one (as exemplified by the black dashed line in Figure 1.5) or multiple Harvey profiles (Harvey, 1985a), the parameters of which are dependent on the physical properties of the star (see Chapter 2). Solar-like oscillation appear at frequencies above the characteristic frequency of granulation. A single mode can be approximated by a Lorentzian peak in the power spectral density (see the inset in Figure 1.5), with height modulated by an approximately Gaussian function (the continuous black line in Figure 1.5). We call the frequency at which this Gaussian function is a maximum the frequency at maximum power, ν_{\max} . Individual mode frequencies appear at regular intervals in frequency, which we parameterize using the large frequency separation $\Delta\nu$. Both ν_{\max} and $\Delta\nu$ will be discussed in greater detail in the following section. Finally, shot noise associated with the instrument used to make the observations dominates at the highest frequencies. This produces a flat offset (as shown by the black dotted line in Figure 1.5).

1.3.2 General Properties of Solar-like Oscillations

The modes of oscillation that we observe in the Sun are trapped sound waves, and are thus referred to as pressure or p-modes. The maximum frequency which a sound wave can have before it is no longer reflected at the surface of a star is referred to as the acoustic cut-off frequency (ν_{ac}). Brown et al. (1991) argued that the range in frequency in which we observe p-modes should scale with ν_{ac} . That is, $\nu_{\text{max}} \propto \nu_{\text{ac}}$. This leads to a scaling with stellar surface properties that goes as,

$$\nu_{\text{max}} \propto \nu_{\text{ac}} \propto g T_{\text{eff}}^{-0.5}, \quad (1.1)$$

where g is the surface gravity and T_{eff} is the effective temperature. Indeed, a significant body of observational evidence has confirmed this scaling to be broadly accurate (e.g. Stello et al., 2008; Chaplin et al., 2011a; Coelho et al., 2015).

Given we are observing standing sound waves, modes should be separated by a near-constant spacing in frequency. To calculate an approximate dependence of this separation on stellar properties, consider simplifying the star to an open-ended 1D pipe with length L . In this case we observe overtones at frequencies $\nu_n = (n + 1)c/2L$, where c is the sound speed in the gas. Therefore, the separation between modes of successive overtone is $\nu_{n+1} - \nu_n = c/2L$. In our star, the appropriate length scale is the stellar radius (R_*), and so we expect modes to be separated in frequency by,

$$\Delta\nu = \left[2 \int_0^{R_*} \frac{dr}{c_*} \right]^{-1}, \quad (1.2)$$

where c_* is the sound speed. We refer to this spacing as the large frequency separation. We can calculate an approximation for the sound speed in the star by assuming the ideal gas law, such that the sound speed scales with the square root of the ratio of the gas pressure (P) to the density (ρ), $c_* \propto \sqrt{P_*/\rho_*}$. Using this in Equation 1.2 and combining it with the equation for hydrostatic equilibrium, $P/R_* \propto M_*\rho_*/R^2$ allows us to identify $\Delta\nu$ as a proxy for stellar density,

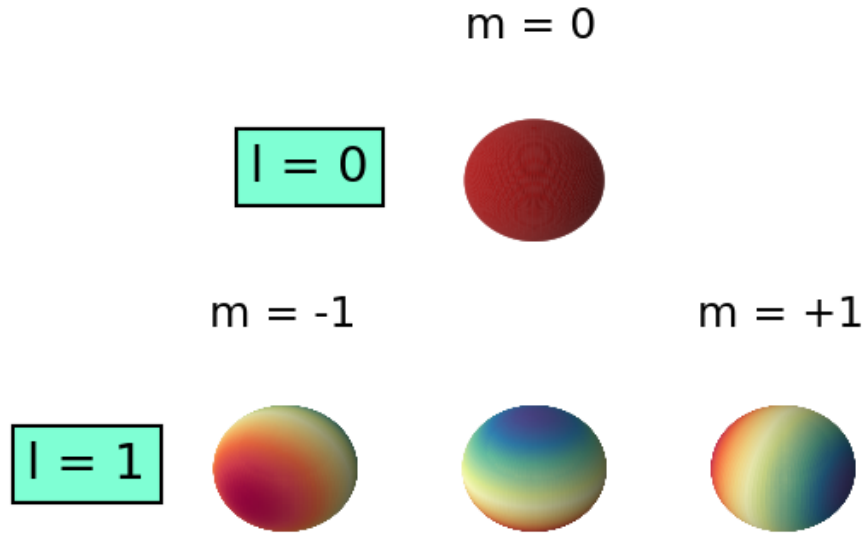


Figure 1.6: Examples of spherical harmonics for angular degrees (ℓ) 0 and 1 and the associated azimuthal orders (m). Red indicates a minima, and blue a maxima.

$$\Delta\nu \propto \sqrt{\rho_*}, \quad (1.3)$$

Again, there is a large observational body of evidence confirming the relation (Ulrich, 1986; White et al., 2011b; Guggenberger et al., 2016; Guggenberger et al., 2017).

Thus far I have discussed some general properties of the p-mode oscillations of a solar-like oscillator. However, $\Delta\nu$ and ν_{\max} only carry information about the bulk properties of the star. Individual modes, on the other hand, reveal more detailed structural information. In the following section I will discuss how the frequencies of these modes can be approximated, and in the process introduce two additional types of pulsation; gravity and mixed modes.

1.3.3 Pressure, Gravity and Mixed Modes

The frequencies at which a star can pulsate arise as the solution to a number of differential equations and associated boundary conditions. To compute these we assume stellar oscillations can be described using spherical harmonics (see Figure 1.6), such that each mode is associated with three parameters, the radial order (n), the angular degree (ℓ) and the azimuthal order (m).

The radial order specifies the number of nodes in the radial direction. The angular degree represents the number of nodes on the surface of the star, such that the number of regions contracting and expanding increases with increasing ℓ . We call modes with $\ell = 0$ radial modes, $\ell = 1$ dipole modes, $\ell = 2$ quadrupole, and so on. Finally, the azimuthal order denotes the number of nodes passing through the stellar equator. For a given angular degree m can vary between $-\ell$ and ℓ , such that there will be $2\ell + 1$ values of m for each ℓ . In the case of a non-rotating star, the direction in which an oscillation is travelling is of no consequence, given the spherical symmetry. As such, the frequencies of all of the azimuthal orders for a given combination of n and ℓ are identical. However, departures from spherical symmetry will change this, lifting the degeneracy. In the following we will discuss the symmetric case, and I will extend this analysis to include non-symmetric terms in Section 1.3.5.

In this framework, several simplifying assumptions are applied to the equations of stellar oscillations and a second-order differential equation is derived,

$$\frac{d^2\xi_r}{dr^2} = \frac{\omega^2}{c_s^2} \left(1 - \frac{N^2}{\omega^2}\right) \left(\frac{S_\ell^2}{\omega^2} - 1\right) \xi_r, \quad (1.4)$$

where ξ_r is the radial component of the displacement associated with a given mode and ω the angular frequency. Importantly, the eigenvalues at which this equation has oscillatory solutions can be sorted into two ‘flavours’, defined by the Lamb frequency, S_ℓ , and the Brunt Väisällä frequency, N .

The Lamb frequency is associated with pressure modes (acoustic or p-modes), which are trapped sound waves. It is defined as,

$$S_\ell^2 = \frac{\ell(\ell+1)c_s^2}{r^2}, \quad (1.5)$$

where $c_s = \sqrt{\Gamma_1 P / \rho}$. The Lamb frequency increases with depth, which (for most of the stellar body) is due to the increase in sound speed. Close to the core, the term in $1/r^2$ dominates.

The Brunt Väisällä frequency defines a type of mode which we have not yet encountered, the gravity mode (buoyancy or g-mode). In the absence of convection, should an element of gas

be displaced from its equilibrium position to a region where the gas is less dense, gravity will restore it to its original position. The frequencies of the associated modes are defined by N ,

$$N^2 = g \left(\frac{1}{\Gamma_1 P} \frac{dP}{dr} - \frac{1}{\rho} \frac{d\rho}{dr} \right), \quad (1.6)$$

where Γ_1 is the adiabatic exponent. The Brunt-Väisällä frequency has a strong dependence on the density gradient. Regions where this gradient is large and positive, where heavier material is sitting on top of lighter material, have negative N^2 . Positive values of N^2 occur where the density gradient is negative. This gradient is maximum in regions where nuclear burning has occurred, meaning heavier burnt material sits below the lighter unburnt material.

P-modes are those having $\omega^2 > S_\ell^2$ and $\omega^2 > N^2$. On the other hand, g-modes have $\omega^2 < S_\ell^2$ and $\omega^2 < N^2$. There is a slight caveat here, in that g-modes with $\ell = 0$ cannot exist, given they cannot provide the required horizontal displacement. In the intermediate regime (i.e $N^2 < \omega^2 < S_\ell^2$) solutions to the oscillation equation are not oscillatory in nature, i.e. this defines evanescent regions. Given S_ℓ decreases from core to surface, regions close to the surface support p-modes with a greater range in frequency than regions nearer to the stellar core. Modes with lower angular degrees have a lower Lamb frequency throughout the body of the star, as is clear by the ℓ dependence on S_ℓ . As such, a p-mode with lower angular degree will generally propagate further into the star. Additionally, N^2 is only positive in regions with radiative stratification, such that the outer convection zone cannot support g-modes. Being trapped deep within the body of a star means that g-modes have very little impact on the observable properties of solar-like oscillators. That is, they have very little influence on the total stellar flux, making them very difficult to detect.

In the Sun, the frequencies at which p-modes are excited to an observable degree are sufficiently distinct from g-mode frequencies, such that the two modes do not influence each-other to any significant degree. However, should a star support g-modes at frequencies near those of the observable p-modes the two types can couple causing a third observable ‘flavour’ of oscillation, the mixed-mode. Akin to coupling two springs, the frequencies of the mixed-modes are no longer that of the pure g- or p-mode, instead they sit at intermediate values.

1.3.4 Asymptotic Equations of Solar-Like Oscillations

Taking limits on equation 1.4 allows us to determine some simple relations approximating the frequencies of solar-like oscillations. We call these asymptotic expressions, and they are commonly used to model the spectra of solar-like oscillators.

Pressure Modes

The high frequency limit, $\omega^2 \gg N^2$, defines the asymptotic relation for p-modes,

$$\nu_{n,\ell}^p \approx \Delta\nu(n_p + \ell/2 + \epsilon_p) - \delta\nu_{0,\ell}, \quad (1.7)$$

where ϵ_p is a phase offset which depends on the boundary conditions in the region in which p-modes propagate. The small frequency separation, $\delta\nu_{0,\ell}$, describes the difference in frequency between radial and non-radial modes whose order, n , differs by unity.

Gravity Modes

Taking low frequency limit, $\omega^2 \ll S_\ell^2$, we obtain the asymptotic relation for g-modes,

$$\frac{1}{\nu_{n,\ell}^g} \approx \Delta\Pi_\ell(n_g + \epsilon_g). \quad (1.8)$$

There-in, modes are spaced with an approximately constant separation in period, rather than frequency. We call this the period spacing, $\Delta\Pi_\ell$, which depends on the integral of the Brunt-Väisällä frequency in the region in which a g-mode is trapped. The offset ϵ_g is associated with the boundary conditions in the g-mode cavity.

Mixed Modes

Mixed modes occur where the frequencies of g-modes and p-modes approach eachother. Asymptotic analysis involves matching solutions across the p-mode and g-mode cavities. The resulting relation defines the mixed mode frequencies as a function of the pure g and p-mode frequencies and a coupling term, q ,

$$\nu_{n,l}^{mm} = \nu_{n_p,\ell}^p + \frac{\Delta\nu}{\pi} \arctan \left[q \tan \pi \left(\frac{1}{\Delta\Pi_\ell} \nu_{n,\ell}^{mm} - \epsilon_g \right) \right] \quad (1.9)$$

Inherent in the derivation of these relations is the assumption that stars are spherically symmetric. Accordingly, the azimuthal order, m , does not appear in the asymptotic expressions. However, there are mechanisms that can break this spherical symmetry, such that the asymptotic relations must be modified. I will discuss these cases in the following section.

1.3.5 Magnetism, Rotation and Asteroseismology

In Section 1.2 we discussed the importance of rotation and magnetic fields in the context of stellar evolution. Thus far, I have not addressed how these phenomena impact stellar oscillations. In fact, both mechanisms can break the spherical symmetry that was assumed in the preceding section. This lifts the degeneracy between modes of different m , such that where once we would have a single peak in the power spectrum per n, ℓ , we now have multiple components. We refer to collections having the same n and ℓ as multiplets.

As we shall see, both magnetism and rotation introduce perturbations to mode frequencies. In this context, an important property of modes is their inertia,

$$I_{n,\ell} = \int_V \rho \vec{\xi}_{n,\ell} \cdot \vec{\xi}_{n,\ell} d^3\vec{r}, \quad (1.10)$$

which can be identified with the amount of mass that is affiliated with a given pulsation. As gravity modes propagate in regions close to the stellar core, where the density is high, they have much higher inertia than pressure modes. We use the mode inertia to define the parameter ζ , which quantifies whether a mixed mode has properties dominated by the underlying pure g-mode or the pure p-mode,

$$\zeta = \frac{I_{\text{core}}}{I}. \quad (1.11)$$

The mode inertia in the core, I_{core} , is equivalent to the total mode inertia, I for a pure g-mode,

such that ζ is unity. Pure p-modes, on the other hand, do not propagate in the core and thus $\zeta = 0$.

Rotation

The rotation rates associated with solar-like oscillators are slow enough that the resulting shift to frequencies is taken as a perturbation to the reference, non-rotating case. This produces mode frequencies that are approximated as $\nu_{n,\ell,m} = \nu_{n,\ell} + \delta\nu_{n,\ell,m,\text{rot}}$, where $\delta\nu_{n,\ell,m,\text{rot}} \ll \nu_{n,\ell}$. The perturbation depends on the properties of the rotation in the regions in which a given mode is sensitive. We parameterise this using a **rotational kernel**, $K_{n,\ell,m}$, which quantifies the interaction between a mode and the rotational profile. This results in the definition,

$$\delta\nu_{n,\ell,m,\text{rot}} = m \int_0^R \int_0^\pi K_{n,\ell,m}(r, \theta) \frac{\Omega(r, \theta)}{2\pi} dr d\theta, \quad (1.12)$$

where $\Omega(r, \theta)$ is the stellar rotation. According to Equation 1.12, modes are perturbed proportionally to m , resulting in frequencies that are symmetric about the $m = 0$ mode. For a given multiplet we can measure $\delta\nu_{n,\ell,m,\text{rot}}$ by the difference in frequency between modes of $m = +m'$ and $m = -m'$, such that we refer to the quantity as the **rotational splitting**. Measurements of $\delta\nu_{n,\ell,m}$ can be used to invert for the stellar rotation profile, if $K_{n,\ell,m}$ is known.

In main sequence stars, we only observe pressure modes (see the discussion in Section 1.3.6). The associated rotational kernels all probe similar locations close to the stellar surface. In evolved stars, however, we observe mixed modes (see Section 1.3.6). Here, kernels have sensitivity much closer to the stellar core. Accordingly, observations of rotationally split mixed modes can provide measurements of core rotation, a parameter which is impossible to access using any other technique. In practise, we assume that the stellar rotational profile varies in radius only, such that we have $\Omega(r)$. For evolved stars, we assume the core has very different rotational properties to the envelope, and decompose the splitting into components from the two distinct regions,

$$\delta\nu_{n,\ell,m,\text{rot}} = \beta_{\text{core},\ell} \left\langle \frac{\Omega_{\text{core}}}{2\pi} \right\rangle_{\text{core}} + \beta_{\text{env},\ell} \left\langle \frac{\Omega_{\text{env}}}{2\pi} \right\rangle_{\text{env}}. \quad (1.13)$$

For dipole modes, $\beta_{\text{core},1} = \zeta/2$ and $\beta_{\text{env},1} = (1 - \zeta)$ (Goupil et al., 2013).

Magnetism

Magnetism both affects the structure of mode cavities and alters the oscillation equations via the introduction of the Lorentz force. Again, the effect is frequently treated as a perturbation to a reference, non-magnetic star. Accordingly, the frequencies (ignoring rotation) can be written $\nu_{n,\ell,m} = \nu_{n,\ell} + \delta\nu_{n,\ell,m,\text{mag}}$, with $\delta\nu_{n,\ell,m,\text{mag}} \ll \nu_{n,\ell,m}$. The value of $\delta\nu_{n,\ell,m,\text{mag}}$ depends on the perturbation due to the Lorentz force,

$$\delta F_L = \frac{1}{4\pi} [(\nabla \wedge \mathbf{B}) \wedge \delta\mathbf{B} + (\nabla \wedge \delta\mathbf{B}) \wedge \mathbf{B}], \quad (1.14)$$

where \mathbf{B} is the stellar magnetic field with perturbation given by $\delta\mathbf{B} = \nabla \wedge (\xi \wedge \mathbf{B})$, with ξ as the displacement of the oscillation eigenvector. The resulting frequency shift is then calculated via,

$$\delta\nu_{n,\ell,m} = -\frac{\langle \xi_{n,\ell,m}, \delta F_L / \rho \rangle}{4\pi \langle \xi_{n,\ell,m}, \xi_{n,\ell,m} \rangle}, \quad (1.15)$$

where $\langle \xi, \alpha \rangle = \int_V \rho (\xi^* \cdot \alpha) dV$. As Equation 1.14 is crucially dependent on the curl of the field, the resulting magnetic splitting depends on the geometry of \mathbf{B} . Unlike rotation, modes of the same absolute value of the azimuthal order ($|m|$) are perturbed equally. Additionally, magnetic fields can (depending on the geometry of the field) induce shifts to the $m = 0$ modes. The shifts on these modes need not be equal to those on modes with $m \neq 0$, such that the resulting multiplet can have an asymmetric appearance in frequency. Similar to rotation, whether a magnetic field will affect the observed oscillations depends on where it is localised compared to the mode propagation cavities. Oscillations in stars on the main sequence are only sensitive to magnetic fields in the outer envelope, while oscillations in evolved stars can probe magnetic fields buried closer to the stellar core.

Using perturbed mixed-mode frequencies in solar-like oscillators is the only method currently

capable of probing core magnetic fields, but analysis has only recently been applied to real data. Li et al. (2022a) derived the relation between the magnetic field and the perturbations to mixed mode frequencies in the case of an axisymmetric field. They found for dipole mixed modes (denoted mm in superscript),

$$\delta\nu_{m=0,\text{mag}}^{mm} = \zeta(1-a)\nu_B, \quad (1.16)$$

and

$$\delta\nu_{m=\pm 1,\text{mag}}^{mm} = \zeta(1+a/2)\nu_B, \quad (1.17)$$

where a contains the dependence on the topology of the field. The parameter ν_B scales with the radial magnetic field strength (B_r) as $\nu_B \propto \langle B_r^2 \rangle / r^3$, where the average is calculated in a region near the hydrogen burning shell. Accordingly, the signature of a magnetic field in the core of an evolved star can be identified with asymmetrically split multiplets, with a frequency dependence $1/\nu^3$.

1.3.6 Solar-Like Oscillations and Stellar Evolution

Mode frequencies are sensitive to stellar structure, such that the frequencies of evolved stars differ significantly from those in stars on the main sequence. The spectra of three stars at different evolutionary phases is shown in figure 1.7. There-in we have replaced power spectral density with signal-to-noise, S/N. This is the observed power with contributions from instrumental drift, rotation, granulation and white noise removed.

We may visualise the way in which modes evolve by using what's known as a propagation diagram. This shows S_ℓ^2 and N^2 as a function of radius. Figure 1.8 shows such diagrams for a stellar model with mass $1.15M_\odot$ in three different evolutionary phases (ages 1.4, 7 and 7.5 Gyr respectively). There-in I have chosen to plot the Lamb frequency for dipole modes, S_1 . I will use this to discuss the general properties of oscillations in solar-like oscillators on the main sequence, subgiant branch and red giant branch.

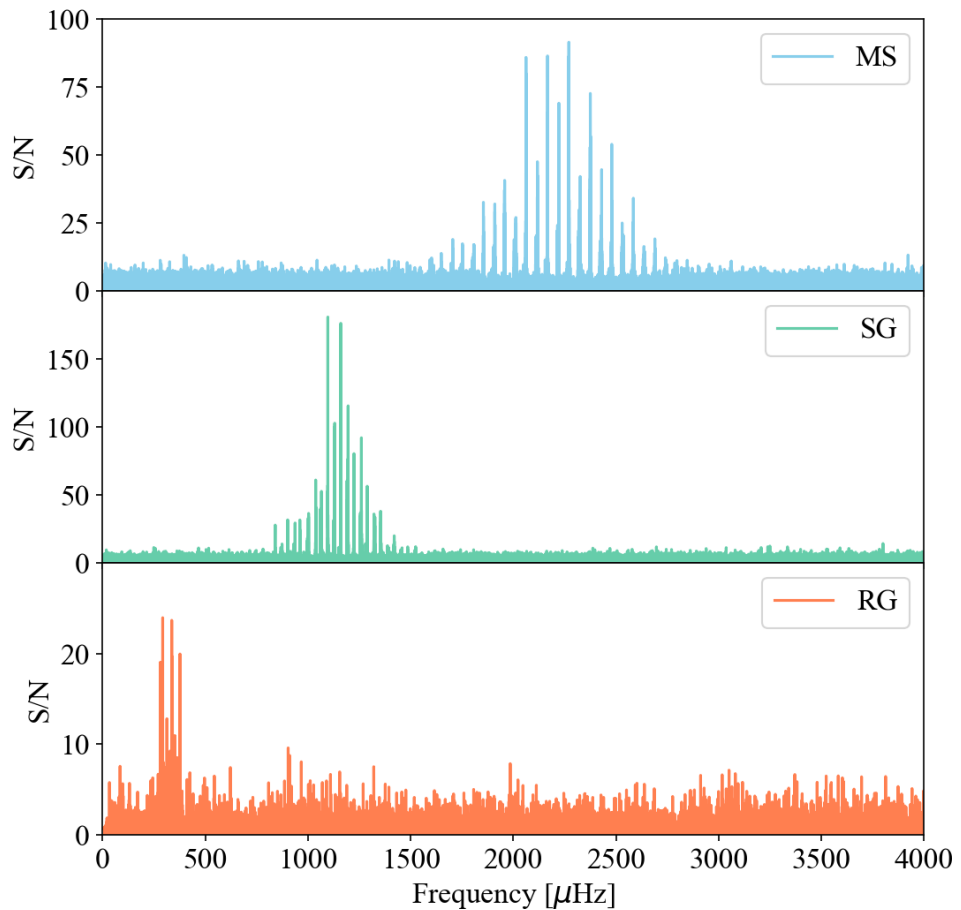


Figure 1.7: Signal-to-noise spectrum for three stars observed by *Kepler* (KIC6106415, KIC6442183 and KIC6035199 respectively). Evolutionary phase increases downward, such that the third panel is the most evolved star.

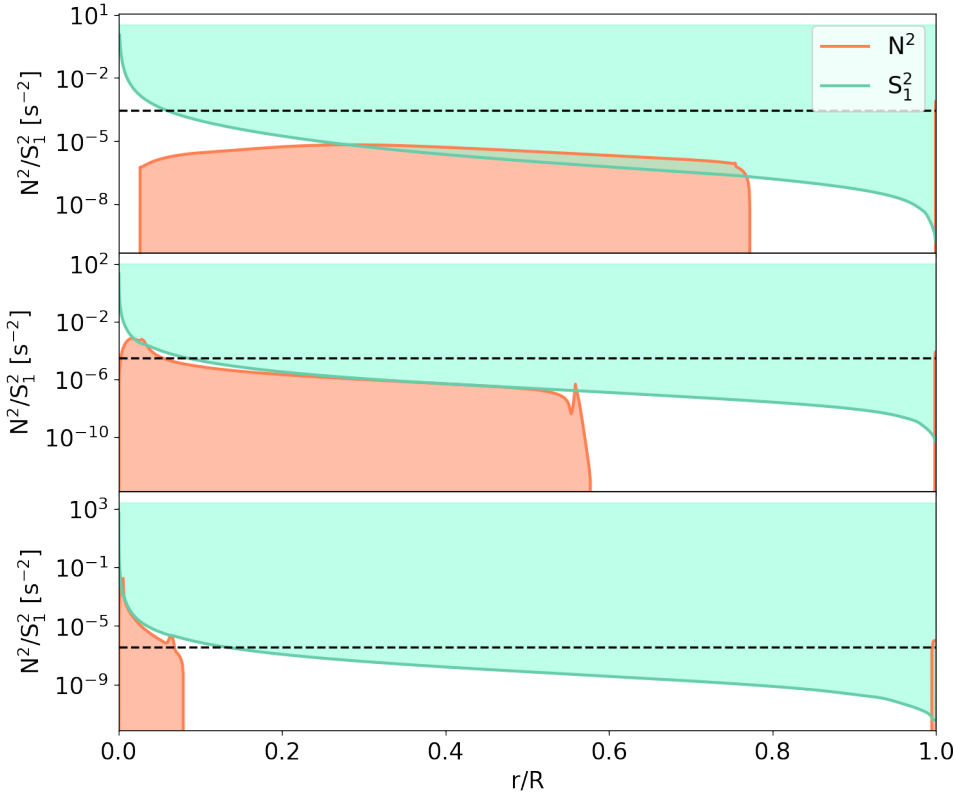


Figure 1.8: Propagation diagrams for a model of a $1.15M_{\odot}$ star at solar metallicity in three different evolutionary phases. The Brunt-Väisälä frequency and dipole Lamb frequency is shown. Shaded regions are those with $\nu^2 < N^2$ (identified with g-mode frequencies) and $\nu^2 > S_1^2$ (identified with p-mode frequencies).

Solar-like Oscillations in the Sun and main sequence Stars

The value of ν_{\max} scales with g and T_{eff} , such that stars on the main sequence oscillate at the highest frequencies (typically a few thousand μHz). An example of an observed spectrum for a star on the main sequence is shown in the top panel of Figure 1.7.

The top panel of Figure 1.8 is that of a model on the main sequence, where ν_{\max} has been plotted as a black dotted line. The star supports dipole p-modes at frequencies about ν_{\max} from the surface down to a depth of $\approx 10\%$ of the total radius. However, ν_{\max}^2 is significantly larger than N^2 throughout the star. As such, the star will not host any g-modes in the frequency range at which we would expect to observe p-modes. Given a spectrum of pure p-modes is described by Equation 1.7, stars on the main-sequence can be identified by mode envelopes that appear very regular, with modes appearing at intervals of $\Delta\nu$. This can be seen in Figure 1.7.

Evolved Solar-like Oscillators

As a star evolves off of the main sequence, its radius significantly increases. This leads to a decrease in ν_{\max} , which drops from a few thousand μHz towards a few tens of μHz on the red giant branch. The middle and lower panel on 1.7 show an observed subgiant spectrum and red giant spectrum respectively. The profile of N^2 also changes significantly as a star evolves off of the main sequence, as can be seen in the middle panel in Figure 1.8. This is the same model star discussed in Section 1.3.6, but on the subgiant branch. The process of nuclear burning has established a negative density gradient in the core resulting in a peak in the Brunt-Väisälä frequency. At radii smaller than $\approx 10\%$ of the total radius, N^2 exceeds ν_{\max}^2 . G-modes will now be supported at frequencies close to the frequencies of the observed p-modes and mixed modes emerge (see section 1.3.3).

The degree to which a mode is coupled (parameterized by q in equation 1.9), and accordingly the extent to which a mixed mode is perturbed from the pure p-mode or g-mode frequency, is a function of the size of the evanescent zone separating the two mode cavities. Given the p-mode cavity extends further into the star for modes of low ℓ , the impact of mode mixing decreases with increasing ℓ .

For a subgiant star, the g-mode density is such that, generally, mixed modes emerge as a single pure p-mode coupling to a single pure g-mode. Given g-modes are spaced inversely in frequency, the appearance of mixed modes disrupts the simple comb-like pattern observed in main sequence stars. Aside from the appearance of these modes, $\Delta\nu$ decreases in response to the decrease in the bulk stellar density in the subgiant phase. The resulting spectrum of a subgiant is thus both less regular and presents a much denser collection of peaks. This can be seen in the example spectrum in the middle panel of Figure 1.7.

The decrease in $\Delta\nu$ and ν_{\max} continues as a star evolves up the red giant branch. The maximum value of N^2 also increases, such that more g-modes emerge per $\Delta\nu$. This results in multiple g-modes coupling to a single p-mode and an increase in the density of mixed modes. As such, red giants can have spectra with very complex appearance, which is exemplified in the final panel of Figure 1.7.

1.4 Summary

Thus far we have seen that stellar evolution is a complex process, and for many years our theoretical understanding has been hampered by a lack of observations of properties below the photosphere. Solar-like oscillations, however, are sensitive to these regions and encoded with detailed information about their host. The global asteroseismic parameters, $\Delta\nu$ and ν_{\max} , are dependent on the bulk properties mass, radius and effective temperature. As we shall see in Chapter 2, this enables us to invert $\Delta\nu$ and ν_{\max} to measure mass and radius to extraordinary precision. Additionally, given the evolution of the oscillations as a star traverses the HR diagram, even a brief glimpse at the spectrum of a solar-like oscillator can give invaluable insight into the evolutionary status of the observed star.

We have seen that solar-like oscillations come in three ‘flavours’, pressure modes, gravity modes and mixed-modes. The former are the most readily observable, given they propagate primarily in regions close to the stellar surface. Gravity modes, however, are trapped deep within the body of the star, near the core, meaning they have very little impact on the net variability of the stellar flux. Mixed-modes emerge in evolved stars, where the frequencies of the observable pressure modes and the low amplitude gravity modes are close enough that the two types can couple. The resulting coupled modes share characteristics of the modes that produced them, such that they have much larger amplitude than pure g-modes whilst still containing information about the properties of the stellar core. We have also seen that the frequencies of solar-like oscillations are affected by rotation and magnetism. Accordingly, mixed-modes can be used to measure the properties of these mechanisms near the stellar core, in regions which cannot be probed by any other observational technique.

With the basic physical principles covered, in the next chapter I will discuss asteroseismic analysis in more detail. I will describe how power spectra are calculated, and the data that is used to do so. I will also give a much more detailed overview of how the observable properties of the oscillations are modelled, and the relations between the parameters of these models and the stellar properties.

Chapter 2

A Crash Course in Asteroseismic Data

Solar-like oscillations cause stars to expand and contract, heating and cooling as they do so. This change in temperature propagates to periodic changes in luminosity, modulating an observed lightcurve. Assuming we observe the star for long enough to properly sample these flux variations, we can use the data to measure various properties of the oscillations. The most basic analyses exploit the global parameters $\Delta\nu$ and ν_{\max} which, as we have seen in Chapter 1.3, provide information about the bulk density, effective temperature and surface gravity of the star. The individual mode frequencies contain even more detailed information about the stellar body, with the potential to measure properties such as stellar rotation and magnetism (see Section 1.3.5).

Most asteroseismic analysis is done in the frequency domain, as solar-like oscillations are not coherent. In the following Chapter I will introduce the techniques we use to translate between time and frequency. I will then go on to give a detailed description of the power spectra of solar-like oscillators, and how they vary with stellar fundamental properties. The relations I discuss will underpin the analysis presented in the following Chapters. I will cover the two main methods used to make inference on the physical parameters of solar-like oscillators via their observed properties. Finally I will describe the two current observing missions which are crucial to the work in this thesis.

2.1 Frequency Analysis

2.1.1 Fourier Transforms

The analysis of solar-like oscillations usually begins with a conversion between the time and frequency domains. This can be achieved via a Fourier transform, which represents how much of a function can be described by periodic signals with different frequencies. It is defined as,

$$X(\nu) = \frac{1}{\sqrt{2\pi}} \int_{-\infty}^{+\infty} x(t) e^{-i2\pi\nu t} dt, \quad (2.1)$$

where $X(\nu)$ and $x(t)$ are the signal in the frequency and time domain respectively. To directly apply this transform we require knowledge of the continuous function, $x(t)$. In our real data we have to take measurements at specific times, such that we can never truly observe $x(t)$. Instead we observe N instances of the continuous function at integer multiples (j) of the sampling cadence (Δt). These observations are made for a total observing time, T , and the observed signal is thus,

$$x_{\text{obs}}(t) = \sum_{n=-\infty}^{+\infty} x(t) \delta(t - j\Delta t) \Pi\left(\frac{t}{T}\right), \quad (2.2)$$

where the delta function ($\delta(t - j\Delta t)$) describes the sampling, and the rectangular function ($\Pi(\frac{t}{T})$) is known as a **window function**, defining the duration over which our observations were made.

Taking the Fourier transform of $x_{\text{obs}}(t)$ we arrive at,

$$X_{\text{obs}}(\nu) = \sum_{n=0}^N x(n\Delta t) e^{-i2\pi\nu n\Delta t}, \quad (2.3)$$

where N is the total number of observations. Given we cannot numerically compute $X_{\text{obs}}(\nu)$ for continuous ν , we now need to define a set of frequencies on which to evaluate the Fourier transform. Accordingly we define the sampled Fourier transform $X_k = X_{\text{obs}}(k\Delta_\nu)$, where k is an integer and Δ_ν is the **frequency resolution**.

The most appropriate frequency resolution can be identified with the properties of the window

function, $\Pi(\frac{t}{T})$. Taking the Fourier transform of the product of two functions (here our sampled observations of $x(t)$ and $\Pi(\frac{t}{T})$) involves calculating the convolution of the Fourier transforms of the two functions independently. The Fourier transform of the rectangular function is a sinc function, with width given by the inverse of the width of the rectangle. For our observation that width is $T = N\Delta t$. Accordingly, $X_{\text{obs}}(\nu)$ will be correlated at frequencies separated by less than $1/N\Delta t$. Therefore, the natural choice for the frequency resolution is,

$$\Delta_\nu = \frac{1}{N\Delta t}. \quad (2.4)$$

Substituting this resolution into Equation 2.3 with $\nu = k\Delta_\nu$, we arrive at,

$$X_k = \sum_{n=0}^N x(n\Delta t) e^{\frac{-i2\pi kn}{N}}. \quad (2.5)$$

This is just the definition of the **discrete Fourier transform**.

The maximum frequency at which we evaluate Equation 2.5 must also be defined. In practise this is usually set at the **Nyquist frequency**, the maximum frequency that can be uniquely identified in a dataset with sampling rate Δt . The Nyquist frequency is related to the properties of the observed data by

$$\nu_{\text{Nyq}} = \frac{1}{2\Delta t}. \quad (2.6)$$

This is simply stating that we cannot make unambiguous inference on periodic signals that are sampled less than twice over the period of the variability (i.e. the minimum period is $2\Delta t$). Oscillations in the Sun have been measured with periods as short as ≈ 3 mins, implying we require observations with a sampling rates on the order of 1 mins. This constraint is relaxed for more evolved stars, which oscillate with longer periods. A low-luminosity red giant, for example, may only require sampling every 30 mins.

Finally, we must appreciate that we are not making instantaneous flux measurements, instead we are collecting total flux over an observation cadence and then summing it. In reality the representation of sampling in time as a set of delta functions is not accurate. Instead we must multiply the true underlying signal by another set of rectangular functions with a width at the

cadence of the observations. As previously discussed, this results in the signal in the frequency domain being modulated by a sinc function, this time with width $1/\Delta t$,

$$\eta(\nu) = \text{sinc}(\pi\nu\Delta t) = \text{sinc}\left[\frac{\pi}{2}\frac{\nu}{\nu_{\text{Nyq}}}\right], \quad (2.7)$$

and the amplitude of the signal drops off as we approach the Nyquist frequency. We call this **apodization**. Given the associated decrease in amplitude, it is preferable to try to design observations such that the mode frequencies are some distance from the Nyquist frequency.

To determine how much of the observed signal is described by oscillatory components at different frequencies we calculate the power spectral density (or PSD). This removes the phase dependence and complex components,

$$P(k) = |X_k|^2. \quad (2.8)$$

Statistics of the Power Spectral Density

In order to determine whether the peak in a PSD is significant, we need a good understanding of the statistics describing the noise. The data relevant to this thesis will be measurements of stellar flux, so that the noise in the time domain is that associated with photon counting. Given the large numbers of photons we sum over, we assume our flux measurements are distributed according to a Gaussian (or a normal distribution), with a standard deviation determined by the specifics of a given instrument. The real and imaginary components of the Fourier transform of such a variable are also independently Gaussian distributed. Accordingly, calculating $P(k)$ involves summing two independently distributed, squared, random variables. The resulting distribution is χ^2 2 degrees of freedom (dof) (Woodard, 1984; Appourchaux et al., 1998).

2.1.2 The Lomb-Scargle Periodogram

The algorithm frequently used to calculate the discrete Fourier transform is known as a fast Fourier transform. This is derived under the assumption that the signal is sampled on a regular

grid. This is not necessarily the case for real-world observations, which are interrupted by, for example, telescope repointing, signal loss due to cosmic rays and data downlinking. Where regular sampling produces a predictable aliasing of peaks in the power spectrum, irregular sampling produces aliases that are specific to the irregularity, giving the power spectrum the appearance of random noise. It is thus harder to establish a peak associated with solar-like oscillations. The Lomb-Scargle Periodogram (LSP, Lomb, 1976; Scargle, 1982) was designed to overcome this challenge. In essence, at each frequency the sinusoidal function representing the minimum χ^2 goodness-of-fit is calculated, and a periodogram is constructed using the amplitude of that function. Accordingly, the resulting LSP is distributed according to χ^2 2 dof statistics. The spurious peaks associated with the aliasing of a true signal are reduced in the LSP versus the discrete fourier transform, making the signature of actual oscillation on a star easier to identify.

2.1.3 Stellar signals in the Frequency Domain

In Section 1.3, I briefly covered the different signals contributing to the spectrum of a solar-like oscillator. In the following section I will provide a much more detailed overview of how these features are described in the PSD, and how they vary with stellar properties. The resulting relations will be used throughout the rest of this thesis.

Granulation

Granulation is the direct observable product of convection in the near surface layers. In the convective envelope, hot plasma rises in currents, reaching the surface and radiating heat, which contributes to the stellar luminosity and thus the observed flux. We model the response in the lightcurve as a superposition of peaks which randomly, instantaneously appear and then exponentially decay. An example of a single peak in such a model is shown in Figure 2.1. Assuming these peaks have a characteristic amplitude σ_c and timescale τ_c the response in the frequency domain would be,

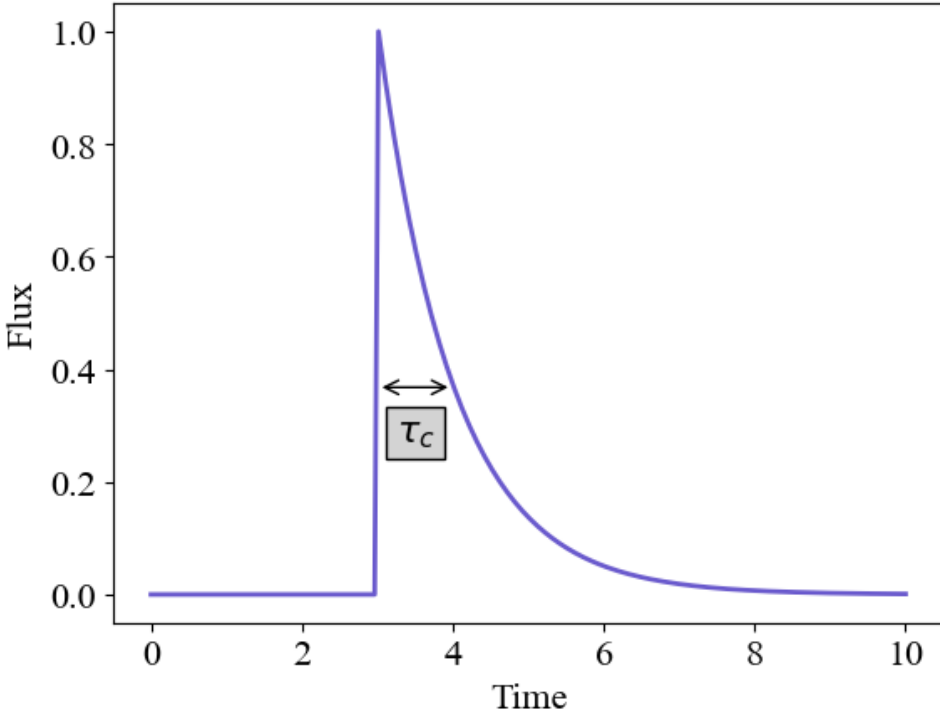


Figure 2.1: Model for the contribution of a single pulse in the lightcurve attributed to granulation. The real signal is modelled as the sum of a number of these peaks, which randomly appear.

$$P_c(\nu) = \frac{4\sigma_c^2 \tau_c}{1 + (2\pi\nu\tau_c)^2}. \quad (2.9)$$

Modelling the peaks as undergoing exponential growth, rather than instantaneous appearance gives a similar response, albeit with the exponent of two in the denominator changing to a 4. Harvey laws (Harvey, 1985a) like Equation 2.9 are commonly used to fit the granulation signal in real data, with the exact choice of exponent in the denominator varying between 2 and 4 depending on the author (Mathur et al., 2011; Kallinger et al., 2014a; Lund et al., 2017).

The convective properties of a star depend on its fundamental properties, like mass and effective temperature. The acoustic cut off frequency (see Section 1.3) depends on the pressure scale height in the convection zone, a parameter which controls the properties of convective elements. Therefore, both σ_c and τ_c should have some dependence on the acoustic cut-off frequency, and accordingly should scale with ν_{\max} . Indeed, Kjeldsen et al. (2011) showed that,

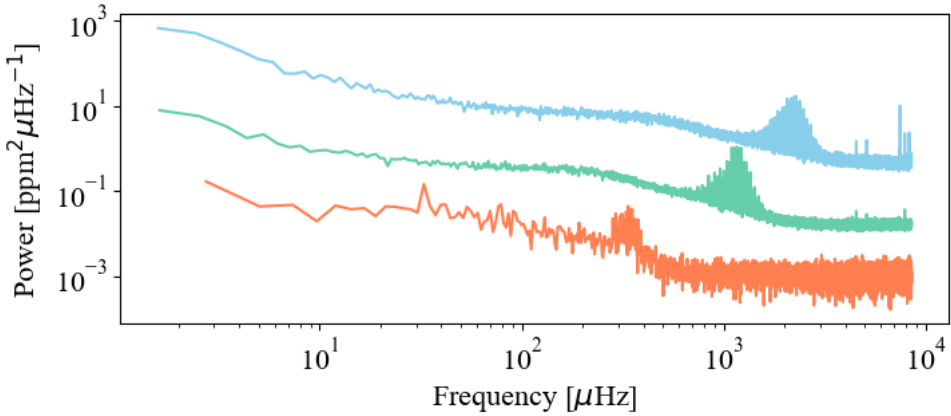


Figure 2.2: Smoothed spectra for 3 stars at different evolutionary phases. The characteristic timescale of granulation increases with decreasing ν_{\max} , such that the frequency at which the granulation profile has a knee decreases.

$$\tau_c \propto \frac{1}{\nu_{\max}} \quad (2.10)$$

and

$$\sigma_c \propto \sqrt{\frac{L^2}{M^3 T_{\text{eff}}^{5.5}}} \nu_{\max}, \quad (2.11)$$

where L is the stellar luminosity and M is the stellar mass. An example of the spectra of three stars with different ν_{\max} is shown in Figure 2.2, highlighting the dependence of τ_c on ν_{\max} .

Mode Envelope

The mode envelope of a solar-like oscillator observed by *Kepler* is shown in Figure 2.3. The total power due to the oscillations appears to be modulated by a smoothly varying function in frequency, which is commonly modelled as a Gaussian centered on the parameter ν_{\max} (Lefebvre et al., 2008; Lund et al., 2017). That is, if we smooth the observed power over $\Delta\nu$ (averaging over the sharp Lorentzian peaks), we would find we could describe the resulting smoothed spectrum by,

$$H_{\text{gau}}(\nu) = H_{\text{env}} \exp \frac{-(\nu - \nu_{\max})^2}{2\sigma_{\text{env}}^2}, \quad (2.12)$$

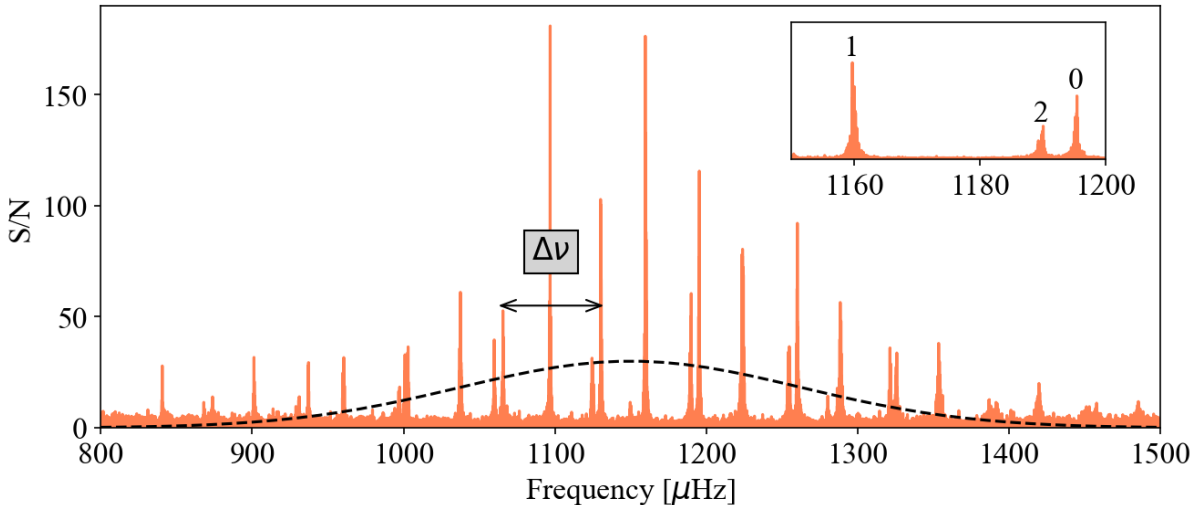


Figure 2.3: Signal-to-noise spectrum of the solar-like oscillator KIC6442183 observed by *Kepler*. The dotted line represents the Gaussian function used to describe the p-mode envelope. The large frequency separation $\Delta\nu$ is marked with an arrow. The inset shows a zoom around three individual modes with angular degree $\ell = 0, 1$ and 2 .

with $\sigma_{\text{env}} = \Gamma_{\text{env}}/2\sqrt{2\ln 2}$. We can relate the envelope height (H_{env}) to the properties of the modes by defining the amplitude of a notional $\ell = 0$ p-mode at ν_{max} , A_{max} . The smoothed power in a section of the spectrum centered on ν_{max} with width $\Delta\nu$ would then be,

$$H_{\text{env}} = \frac{A_{\text{max}}^2 \zeta}{2\Delta\nu}. \quad (2.13)$$

Here ζ accounts for the fact that modes of different ℓ have different heights (see the insert in Figure 2.3, the derivation of ζ will be discussed further in Section 2.1.3). We can use Equation 2.13 to relate the observed height of the envelope to the properties of the modes, which depend on the physical properties of the star.

The exact dependence of A_{max} on the properties of the star is complex, and is still an ongoing area of research (Samadi et al., 2005; Samadi et al., 2007; Houdek, 2006). A simplified analysis assuming adiabaticity and approximating the star as a polytrope predicts the amplitude as observed by a specific instrument should be given by scaling relations of the form,

$$A_{\text{max}} \propto \left(\frac{L}{M}\right)^s T_{\text{eff}}^{-(r-1+\alpha_{\text{bol}})}, \quad (2.14)$$

(Kjeldsen et al., 1995; Basu et al., 2017b), where the values of the positive scalars s and r are obtained empirically. The term α_{bol} is required to describe the wavelength response of the observing instrument. Although the exact choice of s and r likely varies between stars of different evolutionary status, the general rule is that mode amplitudes increase as a star evolves from the main sequence to the red giant branch.

Equation 2.14 has been shown to over-predict amplitudes in the hottest solar-like oscillators. The degree of suppression has been approximated using the empirically derived β correction (Chaplin et al., 2011b),

$$\beta = 1 - \exp \frac{-(T_{\text{red}} - T_{\text{eff}})}{1250}, \quad (2.15)$$

where T_{red} is the temperature of the red-edge of the δ -Scuti instability strip, which marks the approximate transition between stars that do and do not host outer convective envelopes. This scales with luminosity approximately as $T_{\text{red}} \propto L^{0.093}$ (Houdek et al., 1999).

The envelope width, Γ_{env} is dependent on the efficiency of mode excitation, and a simple theoretical derivation of the dependence on stellar parameters does not currently exist. Empirically, however, it has been shown to scale with ν_{max} according to,

$$\Gamma_{\text{env}}(\nu_{\text{max}}) = \begin{cases} 0.66 \left(\frac{\nu_{\text{max}}}{\mu\text{Hz}} \right)^{0.88}, & T_{\text{eff}} \leq 5600 \\ 0.66 \left(\frac{\nu_{\text{max}}}{\mu\text{Hz}} \right)^{0.88} (1 + 6 \times 10^{-4} (T_{\text{eff}} - T_{\text{eff},\odot})), & T_{\text{eff}} > 5600 \end{cases}$$

(Mosser et al., 2012a; Lund et al., 2017). That is, the width of the mode envelope decreases as a star evolves.

Properties of Individual Modes

The inset in Figure 2.3 shows the spectra of three individual modes, labelled by their angular degree. Treating solar-like oscillations as randomly driven, damped, harmonic oscillations would imply modes should appear in the PSD as Lorentzians (Basu et al., 2017b). The Lorentzian function is defined as,

$$P(\nu) = \frac{h_{n,\ell,m}}{1 + 4/\Gamma_{n,\ell,m}^2 (\nu - \nu_{n,\ell,m})^2}, \quad (2.16)$$

where $h_{n,\ell,m}$ is the height and $\Gamma_{n,\ell,m}$ is the width of a mode at frequency $\nu_{n,\ell,m}$.

Aside from the intrinsic properties of a given mode, observed amplitudes are also dependent on geometric effects. For stars other than the sun, we observe the flux averaged over the stellar disk. As ℓ increases, this involves taking the average of a large number of nodes and anti-nodes, resulting in smaller net fluctuations. Therefore, for solar-like oscillators, almost all asteroseismic analysis is restricted to the study of modes with $\ell = 0 - 3$. In addition to the geometry of the pulsations, we must also consider the impact of **limb darkening**. This describes how the observed stellar flux varies with the distance from the center of the disk. We observe a star is brightest at the center, becoming progressively fainter with increasing radius. This is the result of the decrease in the optical depth as our line of sight through the star gets progressively shorter, and probes regions of decreased gas density. Limb darkening generally decreases the amplitudes of modes with low ℓ compared to high ℓ , mitigating some of the cancellation.

The net effect of the geometric cancellation and limb darkening is parameterized in the **visibility function**, S_ℓ , which corrects the amplitudes in the time domain (Dziembowski, 1977; Gizon et al., 2003; Ballot et al., 2011). This is then squared, to represent the power as seen in the frequency domain and normalized to the visibility of a radial mode, $(S_\ell/S_0)^2$. The sum of these visibilities gives the value of ζ , used in Equation 2.13. An example of the normalised mode visibility is shown as a function of angular degree in Figure 2.4. The maximum of this curve corresponds to dipolar modes, as the best trade off between geometric cancellation and limb darkening.

As discussed in Section 1.3, rotation and magnetism break the degeneracy between frequencies of different azimuthal order. Accordingly, where we would have observed a single peak for a given n, ℓ in a non-rotating and/or non-magnetic star, we now observe multiple. The amplitudes of the modes in these multiplets are dependent on the stellar inclination, i (Gizon et al., 2003). Taking the example of dipolar modes, those with $m = 0$ have a nodal line at the equator, such that observations made pole on minimize the cancellation between expanding

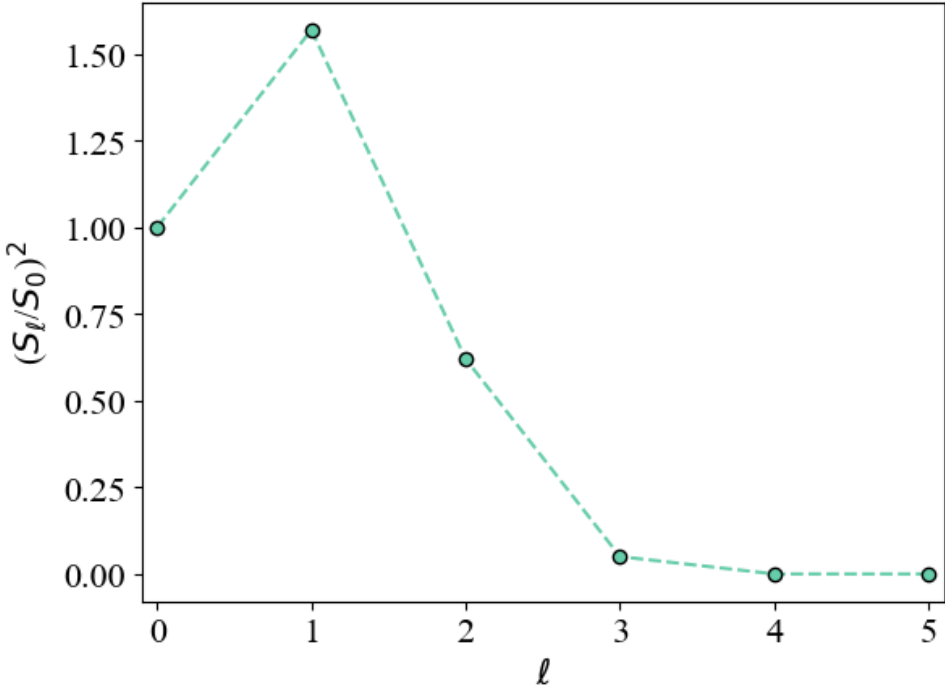


Figure 2.4: Visibility as a function of angular degree according to Ballot et al. (2011). Values are calculated using atmospheric models for the limb darkening of a star with $T_{\text{eff}} = 5800\text{K}$ and $\log g = 4.5\text{dex}$ at solar metallicity. The maximum of this function is at $\ell = 1$.

and contracting regions and the modes are readily observable. On the other hand, modes with $m \pm 1$ have nodal lines crossing the poles, such that observations made pole on maximize the cancellation. Accordingly, it is not possible to observe $\ell = 1, m \pm 1$ modes for a star with $i = 0^\circ$. Similarly, $\ell = 1, m = 0$ components are only observable at $i < 90^\circ$, with amplitudes progressively decreasing with increasing inclination. An example of the distribution in power for a simulated dipole multiplet observed at three different inclination angles can be seen in Figure 2.5. There-in I have normalised each multiplet to have the same maximum height.

In the presence of rotation only, modes are perturbed by a frequency proportional to m , such that the resulting distribution in power is symmetric about the $m = 0$ profile. Magnetism, on the other hand, causes shifts to all components of a multiplet. The scale of this shift (generally) differs among components with different absolute values of m (Prat et al., 2019; Bugnet et al., 2021; Mathis et al., 2021; Li et al., 2022a). That is, $\delta\nu_{\text{mag},m=\pm 1} \neq \delta\nu_{\text{mag},m=0}$ (see Section 1.2.2). This results in multiplets which are no longer symmetric about a central component. An example of such a distribution is shown in Figure 2.6.

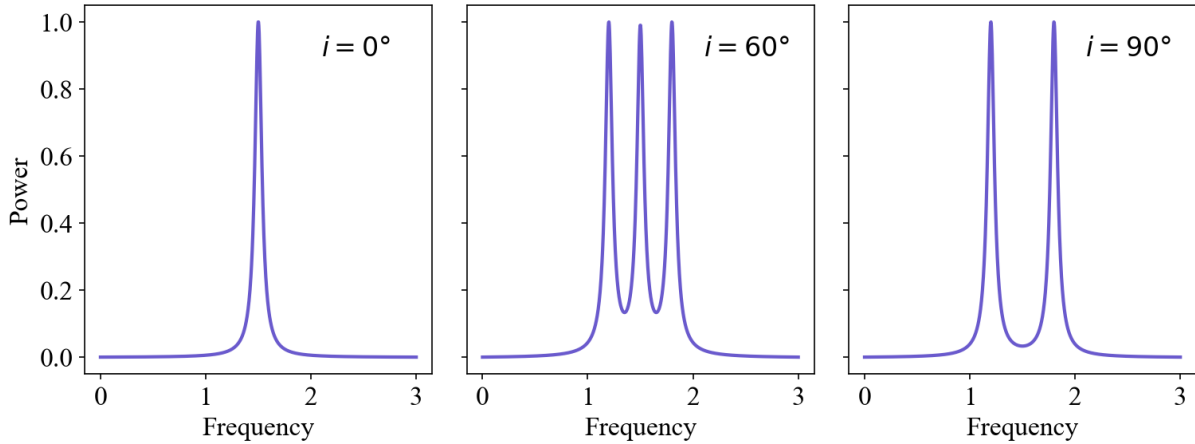


Figure 2.5: Simulated mode profiles in a dipole multiplet containing rotational perturbation only at three different inclinations. The first panel is for the star observed pole-on, and in the third the star is viewed equator on.

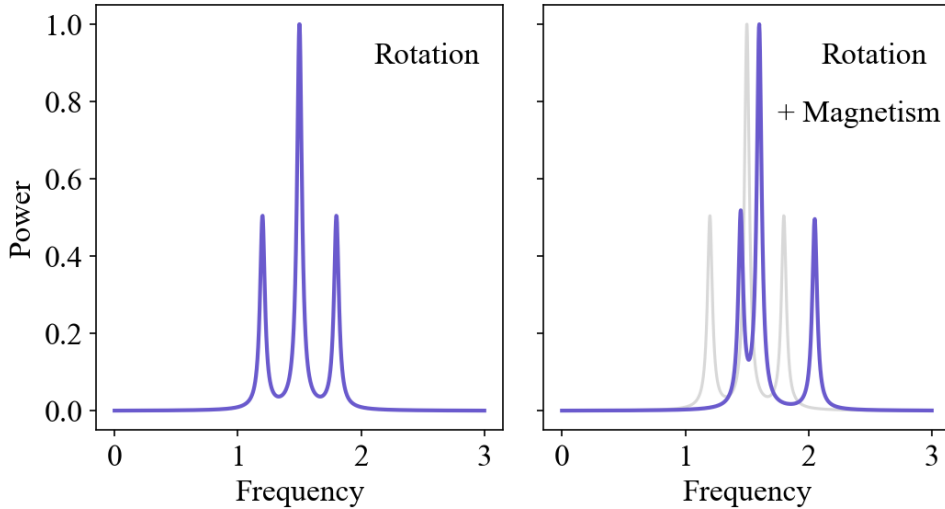


Figure 2.6: Simulated mode profiles for a dipole multiplet in a star at intermediate inclination (45°). In the left hand panel the profile is shown with rotational splitting only, while on the right we show rotational and magnetic splitting

2.2 Asteroseismic Observables to Stellar Properties

Thus far, we have seen the ways in which the frequencies and amplitudes of solar-like oscillations are dependent on the physical properties of the star. In the following section I will detail how we can use measurements of the asteroseismic parameters to invert for stellar properties. Methods of doing so can be broadly divided into two domains. Those requiring **stellar models**, and those that are model independent.

2.2.1 Model Independent Property Recovery

The most fundamental observable asteroseismic parameters required to describe a solar-like oscillator are ν_{\max} and $\Delta\nu$, which capture the basic properties of the oscillations. They are fairly simple to interpret and the easiest values to measure in the power spectrum of a solar-like oscillator. The pair share dependencies on stellar mass and radius. Accordingly, with an independent measurement of T_{eff} , ν_{\max} and $\Delta\nu$ can be combined to give mass (M) and radius (R),

$$\frac{M}{M_{\odot}} = \left(\frac{\nu_{\max}}{\nu_{\max,\odot}} \right)^3 \left(\frac{\Delta\nu}{\Delta\nu_{\odot}} \right)^{-4} \left(\frac{T_{\text{eff}}}{T_{\text{eff},\odot}} \right)^{1.5}, \quad (2.17)$$

$$\frac{R}{R_{\odot}} = \left(\frac{\nu_{\max}}{\nu_{\max,\odot}} \right) \left(\frac{\Delta\nu}{\Delta\nu_{\odot}} \right)^{-2} \left(\frac{T_{\text{eff}}}{T_{\text{eff},\odot}} \right)^{0.5}. \quad (2.18)$$

We call this method of determining stellar properties the ‘direct method’ (Brown et al., 1991; Kjeldsen et al., 1995). Typical fractional uncertainties on ν_{\max} , $\Delta\nu$ and T_{eff} are on the order of 1%, propagating to fractional uncertainties on mass of the order of 10%. Indeed, Mathur et al. (2012) achieved a median precision of 9% on mass derived via Equation 2.17 for a sample of 22 high signal to noise targets using a month of *Kepler* data. Given the smaller exponents on Equation 2.18, the uncertainties on radii are smaller. Mathur et al. (2012) report a median precision of 3% on radius for their sample of stars.

The accuracy of the direct method has been extensively studied. Comparing the masses and

radii measured using traditional techniques to their seismic equivalents has shown the scaling relation derived values are systematically overestimated. To account for the bias in the scaling relations, several corrections to Equations 2.17 and 2.18 have been suggested (White et al., 2011b; Miglio et al., 2012; Sharma et al., 2016), which are generally dependent on effective temperature or metallicity. Gaulme et al. (2016) studied 10 red giants in eclipsing binaries, comparing the masses and radii calculated via radial velocities and eclipse photometry to those determined by asteroseismic scaling relations (including corrections according to Mosser et al., 2013). They found that on average the overestimation on radius was approximately 5% and on mass was approximately 15%.

2.2.2 Model Dependent Property Recovery

Direct application of Equations 2.17 and 2.18 assumes that for a star of given mass and radius all values of effective temperature are equally valid. Thus, an erroneous measurement of the latter will influence the derived stellar properties. Additionally, the base scaling relations for ν_{\max} and $\Delta\nu$ are approximations and not exact. Indeed, it is now well established that they should contain some additional metallicity dependence (Rodrigues et al., 2017; Li et al., 2022b).

To obtain results that fold in our understanding of stellar evolution theory we require **stellar models**. For a set of simulated stars with different initial properties (frequently initial masses and metallicities), predictions are made for the evolution of the star at discrete points in its lifecycle. From the associated fundamental properties, the expected observable parameters can then be calculated. Each set of such properties (fundamental and observable) is referred to as a single stellar model. Thousands to hundreds of thousands of these models are combined to produce a grid. Inference is made on the fundamental properties of an observed star by assigning a likelihood to each model in the grid according to the similarity between the model and real observables. Given we cannot make grids with infinitely fine resolution, such techniques often involve interpolating between grid points.

Alongside traditional observables like effective temperature and magnitude, mode frequencies can be simulated for comparison with observations. This increases the computational

expense, and is not always necessary, given model values of ν_{\max} and $\Delta\nu$ can be calculated directly from mass, radius and temperature. Stellar masses and radii calculated in this manner are more precise than those inferred using scaling relations. For a set of 66 stars, Silva Aguirre et al. (2017) distributed measurements of individual mode frequencies, effective temperatures and metallicities to a number of stellar modelling teams and found average uncertainties of 4% and 2% on mass and radius respectively. In a set of 87 stars Chaplin et al. (2014) performed a similar exercise but only used $\Delta\nu$, ν_{\max} , metallicity and effective temperature. They found that grid-based modelling could achieve average uncertainties of 5.4% on mass and 2.2% on radius when including metallicity in their set of observables. In addition, other physical parameters can be fit for in this manner. Stellar ages are generally in high demand, given they are notoriously difficult to determine using traditional techniques. Grid-based modelling with asteroseismic observables can lead to uncertainties on ages of order 10% (Silva Aguirre et al., 2017).

2.3 Sources of Asteroseismic Data

Requirements for observations suitable for the recovery of solar-like oscillations are primarily related to total duration and cadence. Stars on the main-sequence oscillate at the highest frequencies, with ν_{\max} values in the mHz range (Lund et al., 2017). For a suitable Nyquist frequency, this requires cadences of the order of minutes (see Section 2.1.1). Additionally, mode widths can be as small as a fraction of a μ Hz in the most evolved solar-like oscillators (Yu et al., 2018b). To resolve the associated Lorentzian profiles, we require observations with lengths on the order of weeks to months rather than days. In the least evolved stars, amplitudes are on the order of parts per million (ppm), which again requires observations largely on the order of weeks to months, which are broadly uninterrupted. Although these requirements can be met by a few ground based observatories for the brightest solar-like oscillators, large catalogues of measurements were only made possible by the space-based missions CoRoT (Baglin et al., 2006), *Kepler* (Borucki et al., 2010) and TESS (Ricker et al., 2014).

2.3.1 *Kepler*

The NASA *Kepler* mission launched in 2009, with the main aim of detecting Earth-sized exoplanets orbiting in the habitable zones of their hosts via the transit method¹. The same patch of sky was observed for 4-years, ending with the failure of a reaction wheel. During the 4-year observing run, the telescope required periodic rolls to align solar panels, meaning the observations were split into ≈ 90 day ‘quarters’. Each quarter saw the release of lightcurves of two types, referred to as long and short cadence data. In total, $\approx 200,000$ stars were observed in long cadence, in which measurements were read out every ≈ 29.4 minutes. This sampling means that the resulting lightcurves have a Nyquist frequency of $\approx 277\mu\text{Hz}$. A smaller selection of targets were observed in short cadence, with images produced every 58.85 seconds, resulting in a Nyquist frequency of $8333\mu\text{Hz}$. In a given quarter, only 512 stars could be observed in short-cadence. Accordingly these slots were preferentially retained for the cool, main-sequence stars that were most likely to meet the aims of the mission.

The total number of solar-like oscillators identified and analysed using *Kepler* data numbers over 16,000 (Lund et al., 2017; Serenelli et al., 2017; Yu et al., 2018a). Given ν_{\max} scales with the temperature and radius of the star (see Equation 1.1), we can make a seismic analogy to the HR diagram with ν_{\max} as a function of T_{eff} . Figure 2.7 shows the resulting plot for the >16,000 solar-like oscillators identified using *Kepler* data (Serenelli et al., 2017; Yu et al., 2018a). From the perspective of cataloguing solar-like oscillators, two features are notable on this plot. Firstly, the number of solar-like oscillators detected on the red giant branch significantly outweighs the number on the main sequence. Secondly, there is a clear divide between the two regimes with a decrease in the density of detections around $\approx 300\mu\text{Hz}$. These features are the product of both the *Kepler* observing strategy and the dependence of mode heights on stellar properties. As previously discussed, most of the data collected by *Kepler* was done so in long cadence. Given the maximum detectable frequency in this data is $\approx 277\mu\text{Hz}$, it is not appropriate for targets that have not yet joined the red giant branch (see Figure 2.7). Detections in less evolved solar-like

¹The transit method detects the presence of an exoplanet by the relative decrease in stellar flux that occurs while the planet crosses in front of the star, relative to the observer

oscillators could only be made in the smaller number of stars observed in short cadence. This compounds with the fact that the amplitude of solar-like oscillations scales approximately with L/M (Kjeldsen et al., 1995), such that the average signal to noise for main sequence oscillations is much lower than that of their evolved counterparts. Although subgiants are more luminous, and thus have higher mode amplitudes, they were not prioritized for observation. This was because the main aim of the mission was the detection of small planets via the transit technique. A small planet would produce a larger transit when orbiting a less luminous star, so short cadence observations were prioritized for stars on the main sequence. The resulting sampling of the HR diagram is such that red giants are the best represented, followed by main sequence stars with subgiants as the least populous group. Such a disjoint coverage of the HR diagram impacts asteroseismic inference on the evolution of stellar properties.

2.3.2 TESS

The *Kepler* mission was succeeded by NASA’s Transiting Exoplanet Survey Satellite (TESS), launching in 2018. Rather than observing a single field of view for the duration of the mission, TESS observes millions of stars across the sky. To do so, the sky is split into 26 rectangular segments which are each observed for ≈ 27.5 days before the pointing changes. The nominal mission had a duration of 2 years, with 13 sectors in the southern hemisphere observed during the first year and the remaining 13 in the northern hemisphere observed in the second year. At time of writing, TESS has been observing for 5 years, such that most targets will have been observed for at least 2 sectors (≈ 2 months). A small number (relative to the total target list) of stars have been observed for a year or more. This is the result of the segmented approach, as sectors overlap at the poles in regions known as the Continuous Viewing Zones.

The mission prioritized observing brighter stars than those observed by *Kepler*, with the distribution in 2MASS K-band magnitude for TESS targets peaking at ≈ 9 , compared to ≈ 14 for *Kepler*. Again, lightcurves are available at multiple cadences, varying from 30 minutes to 20 seconds. All stars are observed in the longest cadence, thereafter target lists decrease in size with decreasing cadence. Indeed, 20 second cadence data is only available for 1,000 stars per

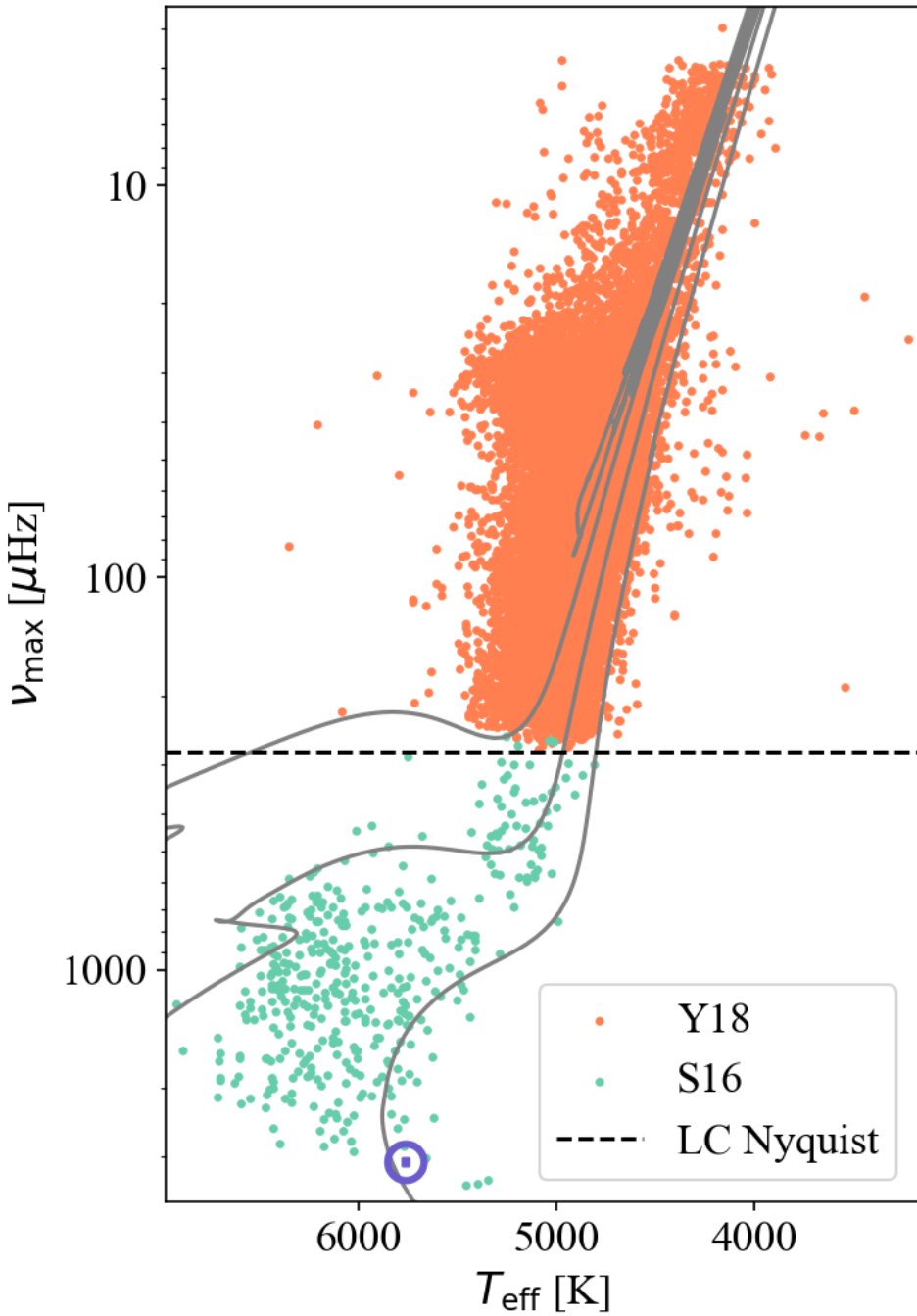


Figure 2.7: ν_{\max} as a function of T_{eff} for solar-like oscillators observed by *Kepler*. Measurements are taken from Yu et al. (2018a) and Serenelli et al. (2017). The *Kepler* long cadence Nyquist frequency is marked by a black dotted line. Three evolutionary tracks are shown for stars at solar metallicity with masses $1.0, 1.5$ and $2.0 M_{\odot}$ generated by MIST (Choi et al., 2016).

sector.

2.3.3 PLATO

The next space mission expected to provide significant contributions to asteroseismology is The PLAnetary Transits and Oscillations of stars (PLATO) mission (Rauer et al., 2014), funded by ESA and set to launch in 2026. Like TESS and *Kepler*, the main aim of PLATO is the detection of terrestrial planets via transits in stellar lightcurves. Although asteroseismology for the sake of studying stellar internal properties is not the main aim of the mission, it will be used as a crucial method to determine the properties of host stars. Observations are scheduled for a nominal period of 4 years, observing two fields for two years each. Targets will be observed in various cadences, varying from 25 seconds, to 600 seconds.

2.4 Summary

In this chapter, I have given a detailed review of the properties of the power spectrum of a solar-like oscillator. We began at an overview of the construction of a power spectrum from measurements of stellar flux as a function of time. We identified the most important features of these spectra in the context of asteroseismic analysis, namely the Nyquist frequency, frequency resolution and the apodization of the signal. I then described how solar-like oscillations appear in the power spectral density, and how their observable properties depend on fundamental stellar properties. We then exploited this to demonstrate how measurements of the features in the power spectrum can be used to invert for the properties of the star. Finally, I described three notable observing missions, *Kepler*, TESS and PLATO.

Asteroseismic analysis of solar-like oscillations is uniquely powerful in its ability to give excellent constraints on bulk stellar properties, like mass and radius, in addition to inference on mechanisms like rotation and magnetism occurring below the photosphere. To fully exploit these features, it is of prime interest that we maximise the number of stars in which we have detected solar-like oscillations. In terms of the quantity of observations, no other mission comes

close to the output of TESS. However, having so much data is both a blessing and a curse, as it is no longer possible to manually search for solar-like oscillations. In the following chapter I will address this issue by introducing a pipeline we designed to detect solar-like oscillations in large datasets.

Chapter 3

Detecting Oscillations

As discussed in Chapter 2, NASA’s TESS mission monitors millions of stars (Ricker et al., 2014) making it an invaluable resource in the search for solar-like oscillators. Manually vetting this data to identify solar-like oscillators would be an impractical task. Therefore, it is crucial we automate as much of the recovery process as possible. Given we know that solar-oscillations require an outer convection zone, which is only present for stars in certain regions of the HR-diagram, measurements of luminosity and effective temperature can give us a feel for whether a star is likely to be a solar-like oscillator or not. However, whether oscillations will be detectable depends on the ratio of the signal amplitude to the telescope specific noise and the total duration of the observations among many other details that are not related to the fundamental properties of the star. For a mission like TESS, a simple cut based on luminosity and temperature would return hundreds of thousands of stars (Stassun et al., 2019), a large percentage of which would likely not display any detectable signature of solar-like oscillations.

Aside from constructing a simple true or false flag, the significance of a detection is useful in determining the information that can be extracted from an observed oscillation spectrum. That is, measurements of $\Delta\nu$ and ν_{\max} may be possible even in the low S/N domain. Individual mode frequencies, however, require more favourable conditions. It is, therefore, of prime importance that we can assign a significance to the stars labelled as detections.

In the following chapter I will introduce methods of establishing the significance of peaks in the power spectrum, and how we can identify these with solar-like oscillations. Using these principles, I will discuss the detection algorithm that we created to automate the recovery of solar-like oscillations in large datasets. That work was the joint effort of Dr. Martin Nielsen and myself and resulted in the publication of two papers, a method paper (Nielsen et al., 2022a) and the results of the application of the pipeline (Hatt et al., 2023, see section 4). The following chapter details the work published in the former paper. For that publication the roles which I was solely responsible for included experimenting with the background removal method, creating the testing set of stars and determining the true and false positive rates in that set. I then applied the pipeline to hundreds of thousands of lightcurves collected by TESS, producing the first catalogue of solar-like oscillators detected in TESS short cadence data (see Chapter 4).

3.1 Automating Identification of Solar-like Oscillations

Much of the following work relies on the application of **Bayesian statistics** (Bayes et al., 1763), a formalism for describing the probability that a hypothesis is supported by observations of some type. In practise, we use Bayesian statistics to determine whether data can be described by a model with a set of parameters. The four key components of Bayesian analysis are the *prior probability*, *likelihood*, *evidence* and *posterior probability*. In the following, I will use H to denote the hypothesis, I for prior information and D for data.

The *prior probability*, $P(H|I)$, encapsulates the beliefs we have about the model parameters before ‘seeing’ the data. These can be entirely physically motivated, or inspired by independent studies. As a simple example, I may be trying to measure the age of a star given some data. In the absence of any other information, I could place a prior on this parameter that would allow the age to vary from a few tens of thousands of years, to the age of the universe.

The *likelihood*, $P(D|H, I)$, represents the probability of observing the data given a set of model parameters. This is calculated by assuming some likelihood function, which quantifies

how likely it would be to observe a given datapoint assuming the model is true. The appropriate likelihood function depends on the statistical properties of a given dataset.

The *evidence*, $P(D|I)$, is the probability of observing the data given any hypothesis, which involves summing the likelihoods of all possible hypotheses. It is required for normalisation, but usually requires integration over a very large parameter space. In the example of aging a star, we would have to establish the likelihood of every age in the prior range and sum. Many Bayesian methods are designed such that this calculation is not required.

These parameters are then combined to calculate the *posterior probability*, $P(H|D, I)$, the probability that a certain model accurately represents the data. The posterior probability is calculated via Bayes' theorem, which has that,

$$P(H|D, I) = \frac{P(H|I)P(D|H, I)}{P(D|I)}. \quad (3.1)$$

The best fitting model maximises this posterior probability.

In the following section, our hypotheses will be that detectable modes either are present (the H1 hypothesis) or are not present (the H0 hypothesis) in a given spectrum (this being the data, D). Using the assumption that the data can be described by one of these cases, I will outline how to establish the posterior probability that the H1 hypothesis is true.

3.1.1 Null Hypothesis (H0) tests

The null (or H0) hypothesis states that the data can be described by just observational noise. For the asteroseismic analysis in this thesis, we work with measurements of stellar flux as a function of time. We approximate these measurements as normally distributed, independent, random variables. Each element in the associated power spectrum is the sum of the squared real and imaginary components of the Fourier transform of this data. Both values are normally distributed, with variance given by that in the time domain. Such a sum is known to follow a χ^2 distribution with 2 degrees of freedom (Woodard, 1984; Appourchaux et al., 1998). The

associated probability density function is given by,

$$f(x) = \frac{\exp -x/2}{2}. \quad (3.2)$$

This defines the H0 likelihood function, describing the probability we would observe power, x , in a given bin according to the null hypothesis.

Rather than causing excesses in power in individual bins in the spectrum, solar-like oscillations produce additional power spread across a range in frequency. Accordingly, we may want to search for regions in a spectrum where the H0 likelihood is consistently low. This can be achieved by investigating the power summed across N bins. In this case, the total summed power is distributed according to a χ^2 distribution with $2N$ degrees of freedom. The probability density function is modified to,

$$f(x, N) = \frac{x^{N-1} \exp -x/2}{2^N \Gamma(N)}. \quad (3.3)$$

Applying this equation to automate detection would involve dividing the spectrum into several segments (or windows), and calculating the H0 likelihood in each. The widths of these windows would be informed by the predicted width of a mode envelope, Γ_{env} . Windows with low H0 likelihood could then be flagged as potentially containing a mode envelope.

The H0 likelihood alone (without calculating the posterior probability) could be used to reduce the list of potential solar-like oscillators by removing spectra consisting of just white noise. However, there are a host of phenomena which can cause excesses in power which are not related to photon noise. Non-solar-like periodic signals include those caused by eclipsing binaries, transits and classical pulsations. An H0 test could not discern these cases, resulting in false positives.

3.1.2 Alternative Hypothesis (H1) Testing

To minimize the number of false positives, an H1 test allows us to include expectations about the features specific to solar-like oscillations. Assuming solar-like oscillations are present, basic

information about the star in question allows us to predict the total power we should observe in N bins. The observed power would then be distributed about this prediction according to Equation 3.3. Accordingly, the likelihood that the observed power excess (s_ν) is consistent with the signature of solar-like oscillations (s_{pred}) is given by $f(s_\nu/s_{\text{pred},\nu}, N)$. We can inform $s_{\text{pred},\nu}$ via a combination of theoretical predictions and observations. These will be discussed in Section 3.2.2.

Now that we have the likelihood for each of our competing hypotheses, we can calculate the posterior probability on the H1 hypothesis, thus determining whether the data supports the presence of solar-like oscillations. The evidence is the sum of the probabilities of H1 and H0,

$$P(D|I) = \underbrace{P(H0|I)P(H0|D, I)}_{\text{Probability of H0}} + \underbrace{P(H1|I)P(H1|D, I)}_{\text{Probability of H1}}. \quad (3.4)$$

Given we have assumed that one of the two hypotheses must be true, we also have that $P(H0|I) + P(H1|I) = 1$. Substituting these terms into Bayes' theorem (Equation 3.1) we have that the posterior probability for the H1 hypothesis is,

$$P(H1|D, I) = \frac{P(H1|I)P(s_\nu, s_{\text{pred},\nu}, N|H1)}{(1 - P(H1|I))P(s_\nu \geq s'_\nu, N|H0) + P(H1|I)P(s_\nu, s_{\text{pred},\nu}, N|H1)}, \quad (3.5)$$

and a star with $P(H1|D, I) > 0.5$ can be labelled as likely presenting detectable solar-like oscillations.

3.1.3 Asteroseismic Applications of Bayesian Model Fitting

Once solar-like oscillations have been detected in a spectrum, the following analysis will be to measure some property or properties of the identified modes. Generally, this involves fitting one of two classes of models. Either we are interested in the asymptotic properties of the modes, that is the parameters in Equation 1.7 or Equation 1.8, or we are interested in the individual Lorentzian profiles themselves. The underlying machinery enabling the determination of these parameters in a Bayesian manner is the same as that informing our H0 and H1 tests. However,

the likelihoods for these tests were functions of a maximum of two parameters, s_ν and $s_{\text{pred},\nu}$. Models describing the spectrum in more detail can be functions of a large number of parameters, such that the problem of determining which model best describes the data becomes increasingly computationally expensive.

To fit our model we take the hypothesis, H , that the selected model determined by a set of parameters (Θ) describes the data. We then calculate the posterior probability for a given set Θ via Equation 3.1. This posterior distribution has dimensions equal to the number of parameters in the model. To make inference on the best fitting values of individual parameters, however, we require the posterior distribution on each parameter independently. This is calculated from the full space by integrating over all parameters but the one of interest. For the example of a model described by $\Theta = (\alpha, \beta)$, the posterior probability of α would be given by,

$$P(\alpha|D) = \int P(\alpha, \beta|D) d\beta, \quad (3.6)$$

which we refer to as a marginalised posterior probability.

Calculating marginalised posterior probabilities requires the computation of integrals over the large number of, often correlated, parameters. Evaluating the evidence is subject to the same problem. Both calculations are commonly analytically impossible and must be done numerically. However, as the number of parameters in a given model increases, the number of grid points required to effectively approximate the posterior distribution becomes intractable. Therefore, we instead explore the posterior distribution using *sampling algorithms*. There-in, we draw samples from the posterior using one of a number of stochastic algorithms. One such algorithm, frequently used due to its simplicity, is the Markov Chain Monte Carlo (MCMC) method (Metropolis et al., 1953).

The MCMC algorithm is an iterative process, deploying one or more *walkers* to explore the posterior space. Walkers are initialized with a set of parameters, which are used to calculate discrete values of the posterior. A new set of parameters is then drawn, using a proposal distribution centered on the current parameter set. The posterior is evaluated for this new set, and the parameters are accepted as a new position with a probability given by the ratio of the new

to old posterior probability. In this way, walkers will converge to the true underlying posterior distribution, with most of the walkers concentrated in areas of high posterior probability and fewer in regions of low posterior probability. Given steps are taken based on the ratio of posterior values, the evidence cancels and is not required.

3.2 A New Pipeline For Automating the Detection of Solar-like Oscillators

We now have the tools required to define tests determining whether solar-like oscillations are present in a power spectrum. This machinery is exploited in the pipeline I developed in collaboration with Dr. Martin Nielsen, which is capable of recovering solar-like oscillators in large datasets. Our aim was to apply this pipeline to TESS short cadence data, hoping to populate the sparsely sampled subgiant regime (see Section 2.3.1). The work resulted in two publications, one describing the method (Nielsen et al., 2022a) and the other the results of its application to data (Hatt et al., 2023, see section 4). This section covers the details published in the method paper.

Alongside evaluating the posterior probability that oscillations are present via identification of power excesses consistent with our expectations, we also included a test searching for the presence of a regularity in the lightcurve associated with sound waves crossing the star. These function as two separate modules, the **power excess module** (PE module/test) and the **repeating pattern module** (RP module/test). The modules are used to produce functions that represent the significance of a detection of the associated feature as a function of frequency, which we call **merit functions**. To label the result of the tests as positive or negative (i.e. oscillations either detected or not detected) then requires isolating cases where the merit functions exceed some threshold.

3.2.1 Data Pre-Conditioning

The following tests are searching for signatures unique to solar-like oscillations. Other contributions to the spectrum of a solar-like oscillator include the additional power from instrumental drifts, activity, granulation and white noise (see Chapter 2). Given we are not interested in these phenomena, we call the resulting combined frequency response the *background*. The signal to noise in a given frequency bin (i) is thus defined as

$$\text{SNR}_i = \frac{P_i}{B_i}, \quad (3.7)$$

where P_i is the total observed power and B_i is the power from the background terms. Functionally, B_i is described by the combination of the Harvey law for granulation plus a flat white noise term (see Section 1.3). In practise, we could calculate this by fitting a model to the data. However, this is computationally expensive to evaluate for a large number of stars. Additionally, the presence of a yet undetected mode envelope could bias the results. Instead we employ a so-called ‘moving average’, which amounts to binning the data over the peaks associated with both the noise realisation and the excess caused by the modes. We use a moving median, which takes the median value of the power in a series of bins in frequency. Given the background consists of a rapidly varying signal at low-frequency and a slowly varying signal at high frequency, bins are spaced linearly in log-frequency. An example of the resulting approximation can be seen in Figure 3.1, where we see that the difference between the moving median background (dotted black line) and the result of a fit to the background (black line) is slight.

3.2.2 Power Excess Test

As discussed in Section 3.1, we can calculate the posterior probability for the hypothesis that solar-like oscillations are detectable in a spectrum by evaluating Equation 3.5. There-in we replace s_ν and $s_{\text{pred},\nu}$ with the SNR. Calculation then requires knowledge of $\text{SNR}_{\text{pred},i}$. We are also required to set a window in which to sum the observed power, which should capture the

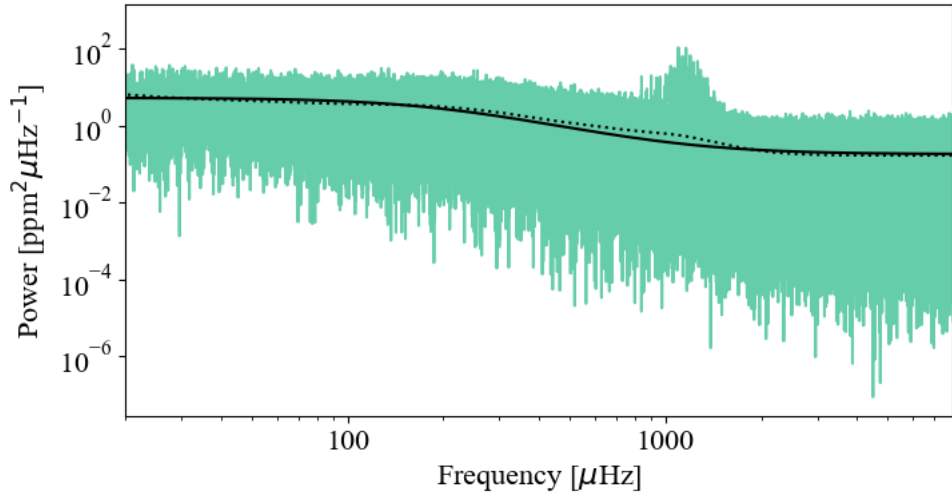


Figure 3.1: Spectrum of KIC6442183 observed by *Kepler*. Black solid line represents a fit of Equation 2.9 to the data, dotted line is the approximation calculated via a moving median filter.

entire envelope to ensure we correctly compare to predictions. This would involve summing power in the range $\nu_{\max} - \Gamma_{\text{env}} < \nu < \nu_{\max} + \Gamma_{\text{env}}$. In the fully automated approach, we cannot apriori set ν_{\max} . Therefore, we must define a set of windows that we should like to test ahead of doing any analysis. In the following we label the central frequencies of the selected segments as $\{\nu_0, \nu_1, \dots, \nu_i, \dots, \nu_n\}$.

The width of a window at test frequency ν_i is set by the predicted width of a mode envelope at $\nu_{\max} = \nu_i$. As discussed in Section 2.1.3, there is no theoretically rigorous prediction for how this parameter should scale with stellar properties. Instead we use the empirically derived scaling,

$$\Gamma_{\text{env}}(\nu_{\max}) = \begin{cases} 0.66 \left(\frac{\nu_{\max}}{\mu\text{Hz}} \right)^{0.88}, & T_{\text{eff}} \leq 5600 \\ 0.66 \left(\frac{\nu_{\max}}{\mu\text{Hz}} \right)^{0.88} (1 + 6 \times 10^{-4}(T_{\text{eff}} - T_{\text{eff},\odot})), & T_{\text{eff}} > 5600 \end{cases}$$

where $T_{\text{eff},\odot} = 5777\text{K}$ (Mosser et al., 2012a; Lund et al., 2017). The width of a window at ν_i is thus $\Gamma_{\text{env}}(\nu_i)$ ($\Gamma_{\text{env},i}$), such that the number of bins we are summing in a spectrum with frequency resolution Δ_ν is given by $N_{\text{env},i} = \Gamma_{\text{env},i}/\Delta_\nu$.

The predicted power in a p-mode envelope centered on ν_i can be estimated using Equations 1.1, 2.13 and 2.14. The exponents of Equation 2.14 were given by Kjeldsen et al. (1995),

$$A_{\max} = A_{\max,\odot} \beta \left(\frac{L}{L_\odot} \right) \left(\frac{M}{M_\odot} \right)^{-1} \left(\frac{T_{\text{eff}}}{T_{\text{eff},\odot}} \right)^{-2}. \quad (3.8)$$

The stellar mass (M) is replaced by ν_{\max} given that,

$$\nu_{\max} = \left(\frac{M}{M_\odot} \right) \left(\frac{R}{R_\odot} \right)^{-2} \left(\frac{T_{\text{eff}}}{T_{\text{eff},\odot}} \right)^{-1/2}. \quad (3.9)$$

We then use the Stefan Boltzmann law, $L \propto R^2 T_{\text{eff}}^4$, to replace the dependence on luminosity (L) and radius (R) with T_{eff} . This results in $A_{\max} \propto \beta T_{\text{eff}}^{1.5} \nu_{\max}^{-1}$. This is substituted into the equation relating the height of the envelope to A_{\max} (Equation 2.13). This relation has dependence on the large frequency separation, $\Delta\nu$, which is replaced with ν_{\max} using the approximation $\Delta\nu \propto \nu_{\max}^\alpha$ such that we arrive at,

$$H_{\text{env}} = H_{\text{env},\odot} \eta^2 D^2 \beta^2 \left(\frac{\nu_{\max}}{\nu_{\max,\odot}} \right)^{-(2+\alpha)} \left(\frac{T_{\text{eff}}}{T_{\text{eff},\odot}} \right)^3. \quad (3.10)$$

We have added η^2 to account for the apodization of the signal, as discussed in Section 2.1.1. Additionally, flux from other stars in the target aperture will reduce the total SNR. The parameter D accounts for this, defined as the ratio of the target flux to the total measured flux in the aperture. Estimates of D are available for TESS targets as a part of the TESS input catalogue (TIC). We determined the exponent α via a fit to observations. Using the combined catalogues of White et al. (2011a), Silva Aguirre et al. (2015), Serenelli et al. (2017), Lund et al. (2017), and Yu et al. (2018a) we found the best fitting value was $\alpha = 0.791$.

Finally, we use H_{env} evaluated with $\nu_{\max} = \nu_i$ ($H_{\text{env},i}$), $\Gamma_{\text{env},i}$ and ν_i to evaluate the expected height of the Gaussian envelope as a function of ν (Equation 2.12). We then only require an independent constraint on T_{eff} . The value of $\text{SNR}_{\text{pred},i}$ is calculated as

$$\text{SNR}_{\text{pred},i} = \sum_{N_{\text{env},i}} \frac{H_{\text{gauss},i}}{B_i}, \quad (3.11)$$

The observed signal to noise in the envelope is,

$$\text{SNR}_i = \sum_{N_{\text{env},i}} \frac{P_{\text{obs},i}}{B_i}. \quad (3.12)$$

These predicted and observed values are then used to evaluate the H0 and H1 likelihood according to $\chi^2 / 2N_{\text{env},i}$ degrees of freedom statistics. That is,

$$\mathcal{L}_i(\text{SNR}_i | H0, N_{\text{env},i}) = \frac{1}{2^{N_{\text{env}}} \Gamma(N_{\text{env}})} (\text{SNR}_i)^{N_{\text{env}}-1} \exp\left(-\frac{1}{2} \text{SNR}_i\right), \quad (3.13)$$

and

$$\mathcal{L}_i(\text{SNR}_i | H1, N_{\text{env},i}) = \frac{1}{2^{N_{\text{env},i}} \Gamma(N_{\text{env},i})} \left(\frac{\text{SNR}_i}{\text{SNR}_{\text{pred},i}}\right)^{N_{\text{env},i}-1} \exp\left(-\frac{1}{2} \frac{\text{SNR}_i}{\text{SNR}_{\text{pred},i}}\right). \quad (3.14)$$

An example power spectrum of a solar-like oscillator observed by TESS and the corresponding PE likelihoods is shown in Figure 3.2.

Priors

We define two priors for use with the power excess module. Firstly, we note that at high frequency, H_{env} tends towards small values. Accordingly the H1 likelihood will be high at high frequency, even in spectra lacking a clear envelope. This can be accounted for by demanding that our signal exceeds some false alarm probability. That is, for frequency ν_i , we calculate the SNR required to generate a H0 probability above some threshold, $\text{SNR}_{\text{thresh}}$. The prior then becomes the probability that the predicted envelope at ν_i would produce a signal in excess of this threshold,

$$P_{T,i} = \int_{R_i}^{\infty} \frac{\exp(-R_i)}{\Gamma(N)} R_i^{(N-1)} dR \quad (3.15)$$

, where $R_i = \sum_{N_{\text{env}}} \text{SNR}_{\text{thresh},i} / \text{SNR}_{\text{pred},i}$.

Additionally, large observing campaigns like Gaia (Perryman et al., 2001) and 2MASS mean that effective temperatures from colour photometry are far from the only independent

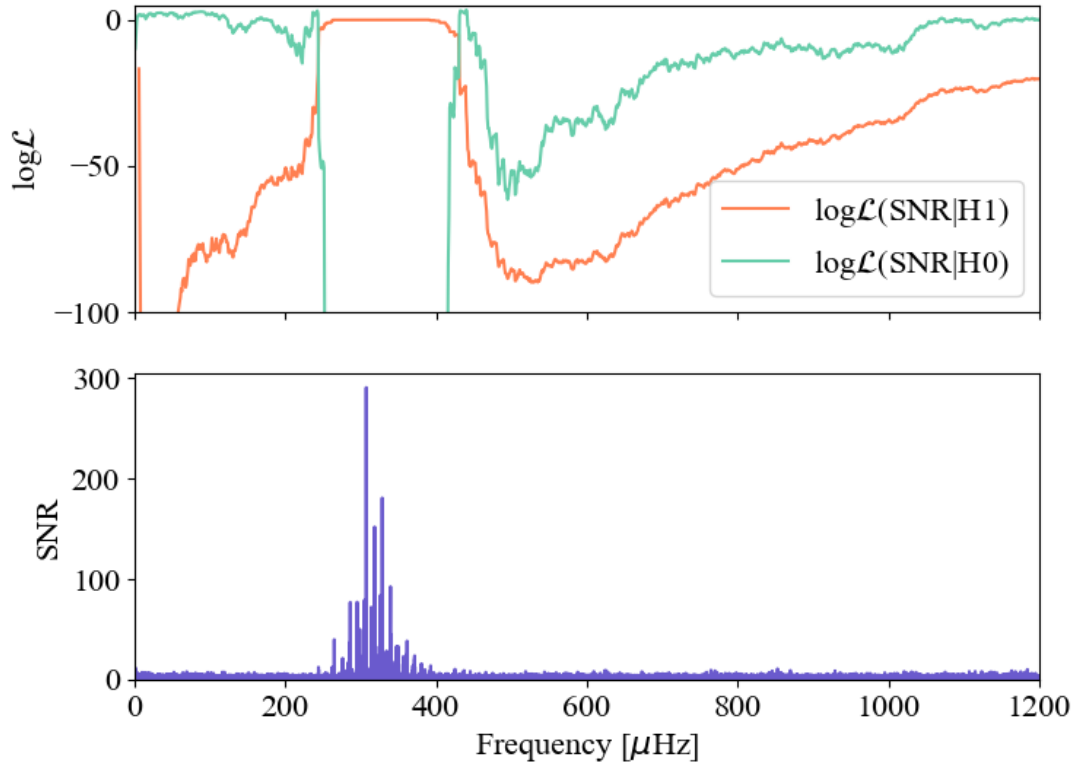


Figure 3.2: Example of the likelihoods output from the power excess test in a star observed by TESS. The top panel shows the log-likelihoods for the H0 and H1 hypotheses. The bottom panel is the signal-to-noise spectrum.

observational constraint available. Given an apparent magnitude and distance estimate we can calculate an approximate stellar luminosity, which can be translated to a radius when combined with effective temperature. These parameters are used to estimate ν_{\max} by manipulating Equation 1.1 and using the scaling with $\Delta\nu$,

$$\tilde{\nu}_{\max} = \nu_{\max,\odot} \left(\frac{R}{R_{\odot}} \right)^{\frac{0.5}{0.5-\alpha}} \left(\frac{T_{\text{eff}}}{T_{\text{eff},\odot}} \right)^{\frac{-0.25}{0.5-\alpha}}, \quad (3.16)$$

where again we use $\alpha = 0.791$. Excesses of power occurring outside of a sensible range in frequency (according to $\tilde{\nu}_{\max}$) are penalised via setting a log-normal prior,

$$P_{\nu_{\max},i} = \exp \frac{-\log(\nu_i/\tilde{\nu}_{\max})^2}{2\sigma_{\nu_{\max}}^2}. \quad (3.17)$$

Comparing this predicted value to the observed values in *Kepler* data reported in Yu et al. (2018a) and Lund et al. (2017), we found $\sigma_{\nu_{\max}} = 0.5$ captured the scatter of the residuals. We then define the prior on H1 as,

$$P_{\text{H1},i} = 0.5 P_{\text{T},i} P_{\nu_{\max},i}, \quad (3.18)$$

from which $P_{\text{H0},i}$ can be calculated given $P_{\text{H0},i} + P_{\text{H1},i} = 1$. The resulting merit function is given by the posterior probability on H1, normalised to be between 0 and 1 in every bin.

3.2.3 Repeating Pattern Test

A wave emitted at some point near the upper turning point of acoustic oscillations will travel across the star before it meets the surface at an opposing point, perturbs it and contributes to the observed flux. This induces correlations in the lightcurve separated by the time it takes for a sound wave to cross the stellar diameter (the acoustic radius). Recall from Section 1.3, the inverse of this time is also the definition of $\Delta\nu$. This led Roxburgh et al. (2006) to identify a measurement of the timescale of the correlation as a means to determine the large frequency separation. There-in the authors suggest using the **autocorrelation function** (ACF), which represents the degree of correlation between a function, $f(x)$, and the same function translated

by some amount, u ,

$$\text{ACF}(u) = \int_{-\infty}^{+\infty} f(x)f^*(x-u)dx. \quad (3.19)$$

The ACF has been used to measure the value of $\Delta\nu$ in a number of works (Mosser et al., 2009b; Hekker et al., 2009; Mosser et al., 2010; Tian et al., 2014). Given we should not expect large peaks in the ACF of a white noise lightcurve, we identify it as an additional mechanism to establish whether solar-like oscillations are present at all. That is, given a description of the statistical properties of the ACF of a white noise spectrum, we may infer another H0 probability.

Importantly, the ACF of the lightcurve and its power spectrum are Fourier pairs, such that the inverse Fourier transform of the latter returns the former. Therefore, for every frequency that we tested in the PE module we calculate

$$\text{ACF}_i(\tau) = \int_0^{\nu_{\text{Nyq}}} \text{SNR}(\nu)W_i(\nu) \exp(i2\pi\nu\tau)d\nu, \quad (3.20)$$

where τ is the lag in time (our proxy for $1/\Delta\nu$) and $W_i(\nu)$ is band-pass filter, defined to select the range in frequency consistent with the width of an envelope centered on $\nu_{\max} = \nu_i$. Mosser et al. (2009a) suggest the use of a Hanning filter, which approximates the shape of the envelope. Accordingly, we define our set of filters as

$$W_i = \begin{cases} 0.5 \left(1 - \cos\left(\frac{2\pi(\nu - \nu_i)}{N_{\text{env},i}}\right)\right), & |\nu - \nu_i| \leq \Gamma_{\text{env},i}/2 \\ 0 & |\nu - \nu_i| > \Gamma_{\text{env},i}/2. \end{cases}$$

For each test frequency, ν_i , we then have the autocorrelation as a function of lag, τ , such that the full space is a two-dimensional map. We label the associated matrix \mathbf{G} , with elements $G_{i,k}$. The contribution of each element to the observed flux is established by taking the squared, absolute value, $|G_{i,k}|^2$. For a solar-like oscillator, there will be a peak in this 2d distribution at $\tau \approx 1/\Delta\nu$ and $\nu_i \approx \nu_{\max}$. An example of the 2d space for the solar-like oscillator in Figure 3.2 is shown in Figure 3.3.

To establish a detection metric as a function of test frequency (such that it is analogous with

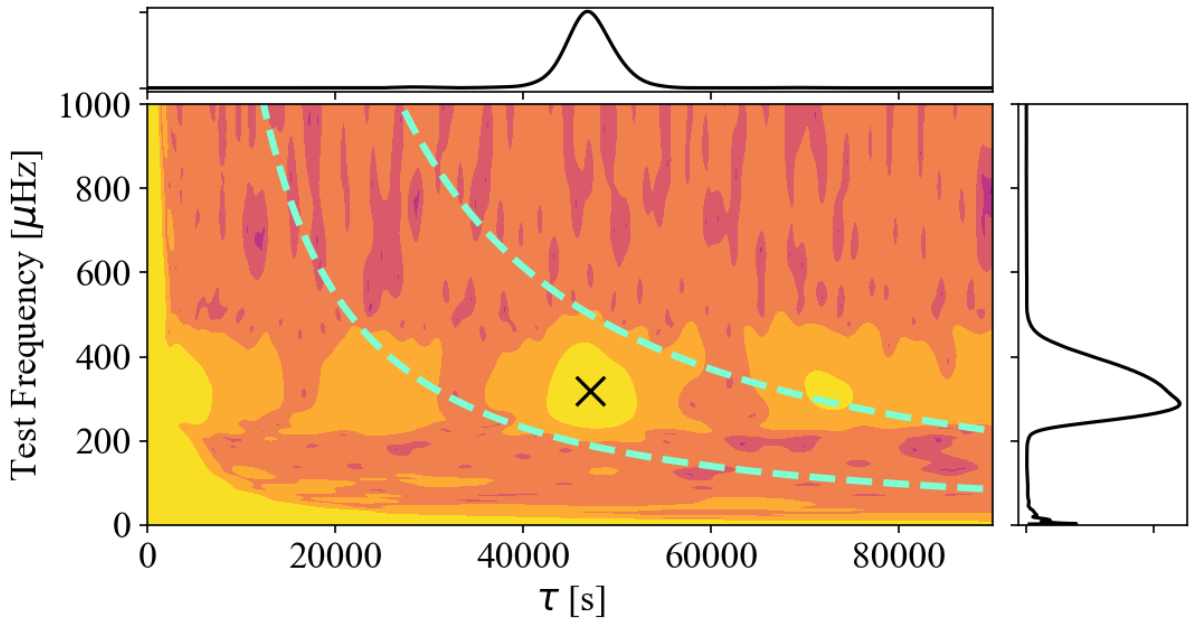


Figure 3.3: Main panel shows the two dimensional autocorrelation function for the star in Figure 3.2. The peak identified with the true value of $\Delta\nu$ and ν_{\max} is identified by the black cross. Dotted lines show the range in τ that is summed over for each test frequency. The panels at the top and on the left are the collapsed autocorrelation function over test frequency and lag respectively.

the metric from the PE test) we need to marginalise over τ . We also note that the ACF evaluated at $\tau = 0$ is just the total squared power, so we normalise to this value,

$$r_i = \frac{1}{N_{\tau,i}} \sum_{N_{\tau,i}} \frac{|G_{i,k}|^2}{|G_{i,0}|^2}, \quad (3.21)$$

where $N_{\tau,i}$ is the bins in τ over which we perform the sum. To limit this range we exploit the scaling $\Delta\nu \propto \nu_{\max}^\alpha$, again with $\alpha = 0.791$. To capture the possible range in τ for this choice of exponent we sum over $u\Delta_T/\widetilde{\Delta\nu_i} < \tau < u^{-1}\Delta_T/\widetilde{\Delta\nu_i}$, where $\widetilde{\Delta\nu_i}$ is determined via the scaling relation and u is set to $10^{0.2}$. The range in τ included in the sum is shown in Figure 3.3, with the resulting ACF marginalised over each axis shown in the top and right hand panels.

To establish the statistics of the filtered, collapsed autocorrelation function we used simulations. We generated 10,000 realisations of lightcurves of pure white noise, calculating r_i for each. The resulting distribution of r_i was well approximated by a Γ distribution with probability

density function

$$f(x; \alpha, \beta) = \frac{x^{\alpha-1} \exp{-(\beta x)} \beta^\alpha}{\Gamma(\alpha)}, \quad (3.22)$$

with $\alpha = \mu^2 / \sigma^2$ and $\beta = \mu / \sigma^2$. Empirically, we found that μ scaled with the number of bins included in the calculation according to

$$\mu = \frac{3}{2} \frac{1}{N_{\text{env},i} N_{\tau,i}}. \quad (3.23)$$

The variance was well approximated by,

$$\sigma_i^2 \approx \frac{\mu_i^2}{N_{\text{env},i}} \left(1 + \frac{N_{\text{T}}}{N_{\tau,i}} \right). \quad (3.24)$$

These are used to calculate the H0 likelihood, according to

$$P(r_i|H0) = \frac{r_i^{\alpha-1} \exp{-(\beta r_i)} \beta^\alpha}{\Gamma(\alpha)}. \quad (3.25)$$

The merit function is then the inverse of this likelihood, normalised to be between 0 and 1 in every bin.

3.2.4 Validation and Performance

Thus far I have described how the power excess and repeating pattern tests are used to generate merit functions. To label positive and negative detections we require sensible thresholds on these functions. In theory, excursions above a merit function of 0.5 would identify a spectrum as more likely to have detectable solar-like oscillations than not. However, we have taken the simplifying assumption that spectra contain power that is either consistent with solar-like oscillations or white noise. In reality, other phenomena can cause large excesses in power, which could result in false positives. Therefore, the optimal thresholds require tuning to real data.

The optimal thresholds should minimize the number of false positives whilst maximizing the number of true positives. Given the two tests are searching for different properties, causes of false positives will differ, meaning the thresholds need not be identical. In addition, we should

identify whether requiring the star to pass both tests (2 flag response) or just a single test (1 flag response) produces the best result. To answer these questions, we exploited a test set of data collected by the TESS mission.

Target and Data Selection

To calculate the true and false positive rates associated with different parameters, we required a set of spectra with solar-like oscillations and a set of spectra where-in we cannot identify solar-like oscillations. Given our aim is to apply the pipeline to a large number TESS short-cadence lightcurves, we drew our testing set from a small subset of these data. For the targets that we selected, power spectra were calculated using the detrended 120 second cadence lightcurves from the TESS Science Processing Operations Center (SPOC) pipeline (Jenkins et al., 2016). This data includes gaps which can be up to a year in length for stars observed in the nominal mission and then again in the extended mission. These gaps cause correlations in the power spectrum, and can reduce the signal to noise of modes of oscillation (García et al., 2014; Bedding et al., 2022a). We tested leaving these gaps untreated and removing them by shifting timestamps. We found that applying the latter approach for gaps larger than ≈ 50 days reduced the number of false positives and so employed this strategy. We used the open source package `Lightkurve` to download and process the lightcurves (Lightkurve Collaboration et al., 2018), calculating the power spectrum via a Lomb-Scargle periodogram.

Constructing a list of solar-like oscillators prior to completing the pipeline required manual identification. At time of this work, TESS had observed over 200,000 stars in 120 second cadence. The majority of these stars were unlikely to show detectable signatures of solar-like oscillations. Accordingly, a random draw on the full target list would have to be extensive to produce a large enough testing set. Fortunately, predictions for the targets that would be the best candidates for asteroseismic analysis were calculated pre-mission by Schofield et al. (2019). Exploiting similar machinery to that underpinning our power excess test, the authors calculated the probability that stars in the TESS input catalogue would show detectable signatures of solar-like oscillations. The work focused on targets oscillating at frequencies above the *Kepler* long

cadence cut off, enforcing a minimum predicted ν_{\max} of $240\mu\text{Hz}$. Additionally, stars that are likely to be classical oscillators were removed. This was achieved via a temperature dependent upper limit on luminosity, marking the location of the δ Scuti instability strip. In total, they produced a catalogue of 25,000 stars with detection probabilities $> 5\%$. Of these, 11,220 had been observed in 120 second cadence at time of work. From this list I identified 400 clear solar-like oscillators. From the larger set in which I could not identify oscillations, I drew another 400 stars, weighted by their effective temperature such that they produced the same distribution in T_{eff} as their oscillating counterparts. The combined test set is shown in Figure 3.4 alongside the set of *Kepler* solar-like oscillators (according to Serenelli et al., 2017; Lund et al., 2017; Yu et al., 2018a).

The power excess module requires input values of stellar radius and effective temperature for use in calculating SNR_{pred} and the prior on ν_{\max} . We drew T_{eff} values from version 8 of the TESS input catalogue (TIC; Stassun et al., 2019). For stellar radius we used a combination of parallaxes from GDR2 (Gaia Collaboration et al., 2018) to calculate distance, apparent magnitudes from 2MASS and a set of bolometric corrections to calculate an approximate luminosity. We then used this luminosity and the TIC T_{eff} to invert the Stefan-Boltzmann law for R . The bolometric corrections were calculated via a polynomial fit as a function of T_{eff} to the simulated parameters of the STAGGER grid (Magic et al., 2013).

Results

For single and double flag detections separately, we tested varying the threshold on each module independently, using 100 values between 0 and 1. We then calculated the true positive (TP)¹, true negative (TN)², false positive (FP)³ and false negative (FN)⁴ rates for each combination of power excess and repeating pattern threshold. The percentage of the sample which is correctly labelled is known as the accuracy,

¹Fraction of the oscillator set correctly identified as detections

²Fraction of the non-oscillator set labelled as non-detections

³Fraction of the non-oscillator set incorrectly identified as detections

⁴Fraction of oscillator set labelled as non-detections

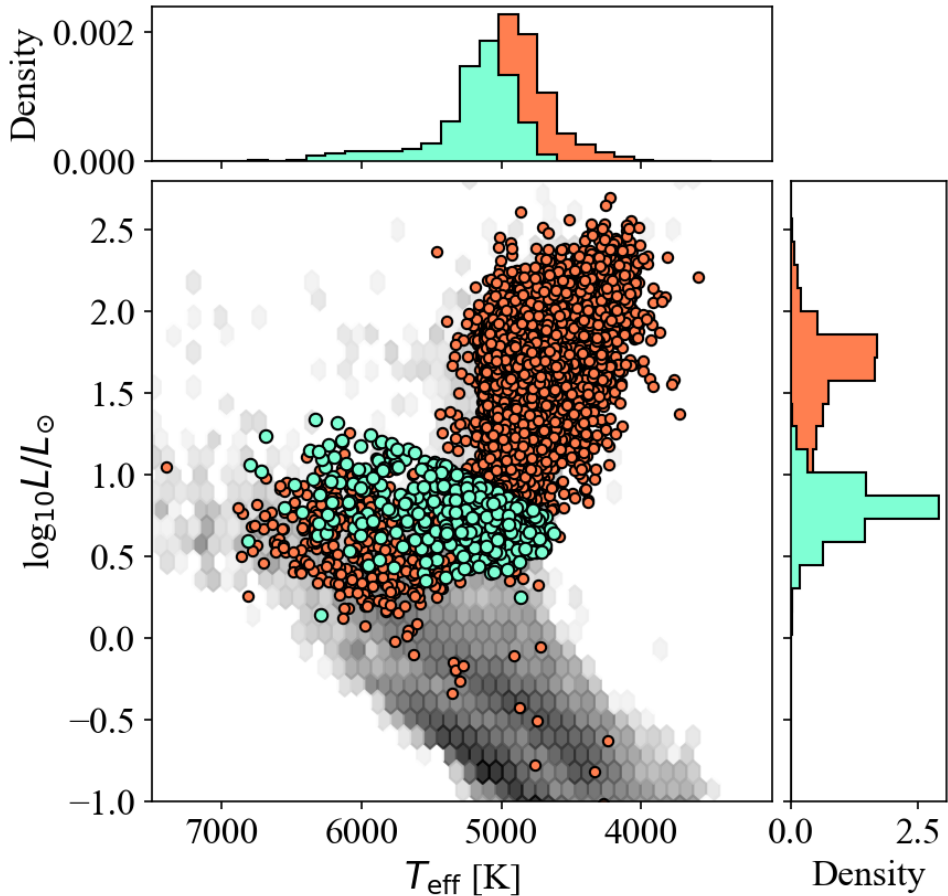


Figure 3.4: Luminosity as a function of effective temperature for solar-like oscillators observed by *Kepler*, and those in the TESS test set. The *Kepler* sample is in orange, consisting of 16,000 solar-like oscillators Serenelli et al. (according to 2017), Lund et al. (2017), and Yu et al. (2018a). The remaining scatter points are those in our TESS short cadence test set. The background is a histogram of a random draw of Gaia stars for comparison purposes. The top and right-hand panels are one dimensional histograms of the distributions in luminosity and effective temperature in the two sets. Reproduction of Figure 1 from Nielsen et al. (2023)

$$\text{accuracy} = \frac{\text{TP} + \text{TN}}{\text{TP} + \text{TN} + \text{FP} + \text{FN}}. \quad (3.26)$$

We used this to identify the most effective set of thresholds.

Figure 3.5 shows the TP rate as a function of the FP rate for the tested configurations of the pipeline. That is, each curve corresponds to a single power excess threshold, with each point on the line associated with a single repeating pattern threshold. Maximum accuracy corresponds to the ‘knee’ of such a curve, and is marked for the single and double flag scenarios. The maximum accuracy we achieved was 93.2%, corresponding to asking for a single module response with thresholds of 0.77 and 0.73 on the power excess and repeating pattern modules respectively. Asking for a double module response reduced the number of both true positives and false positives, such that for a given pair of thresholds the overall accuracy is lower. The maximum accuracy for double module responses was 91.5%, achieved with much lower thresholds (0.4 and 0.03 for power excess and repeating pattern respectively).

False positives included a signal with a period of 4-minutes that produced a single large peak in power. This was discussed in the TESS Data Release Notes for sector 5 as ‘black flutter’ (a periodic change in the mean black level affecting two cameras, Fausnaugh et al. (2019)). Additionally, 23 stars identified as false positives showed marginal detections in both the PE and RP module at frequencies consistent with the predictions in the prior. In these cases, we could not identify some other source of the signature. Although these cases were from the non-oscillator testing set, they may in reality be solar-like oscillators with very low SNR, such that manual identification was not possible.

Generally, false negatives were the result of incorrect predictions of either ν_{\max} or the signal-to-noise of the theoretical envelope. Although the prior on ν_{\max} was conservative, large offsets in the apparent magnitude, distance or effective temperature could result in the prior exploring the incorrect range in frequency. The parameters controlling the predicted signal-to-noise are T_{eff} and D . We used values of D from the TIC, which were calculated pre-mission, assuming a common width on the point spread function. As such, they may have been underestimated for stars in the vicinity of the brightest targets. However, the average magnitude in the 24 false

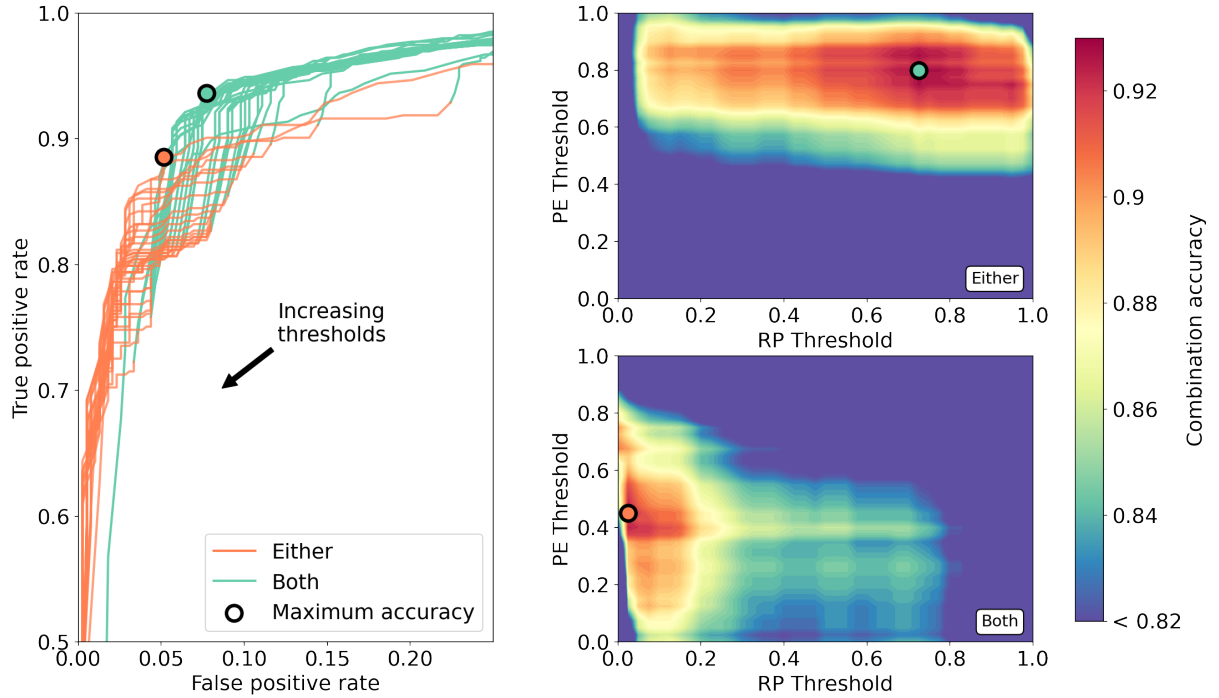


Figure 3.5: Left frame shows the true positive versus false positive rates for varying thresholds on the power excess and repeating pattern tests. Each curve corresponds to a single power excess threshold, with every point on the line being a single repeating pattern threshold. The false positive and true positive rates for stars passing these thresholds in either one module (labelled 'Either') or two modules (labelled 'Both') are plotted on the x and y axes. Panels to the right show the accuracy of the pipeline at each combination of thresholds. The top panel is for responses in either module, and the bottom for responses in both modules. Scatter points mark the maximum accuracy. Reproduction of figure 7 in Nielsen et al. (2023).

negatives that do not pass the PE threshold is higher, not lower, than the population average (7.07 versus 6.64). In the absence of issues with SNR_{pred} , a false negative could also be the result of an unexpected reduction in the observed SNR. This could result from the way in which we close large gaps in the lightcurves. Where a star was observed first in the nominal and then later in the extended mission, the resulting lightcurve has a gap of a year in length. We removed these by shifting timestamps, which we found reduced the false positive rate significantly. However, the method reduces the SNR of long-lived modes have lifetimes of similar length to the gap.

3.3 Summary

In this chapter I have introduced a pipeline that we developed to automate the detection of solar-like oscillations in large data sets. The algorithm takes in a lightcurve and converts it to a power spectrum, on which it runs two detection tests. These modules search for unique signatures of solar-like oscillations; The power excess associated with the mode envelope, and the correlation in the lightcurve associated with sound waves crossing the star.

By exploiting a testing set of 400 oscillators and non-oscillators identified in TESS 120 second cadence data, we determined the pipeline can achieve an accuracy of 93.2%. We identified the causes of false positives include instrumental effects that produce large peaks in the power spectrum, and errors in the independent measures of temperature and radius used to inform the predictions in the power excess test. Although we listed the combination of thresholds that maximised the accuracy of the algorithm, we note that different thresholds can be selected that will prioritize either minimizing false positives or false negatives, depending on the use case.

In the following chapter, I will detail the results of the application of the pipeline to a much larger set of TESS data. Additionally, I will exploit the likelihoods to make measurements of the global seismic parameters (ν_{max} and $\Delta\nu$) in the stars in which we make a detection.

Chapter 4

A Catalogue of Solar-Like Oscillators Observed by TESS

This chapter is a reformatted version of Hatt et al. (2023), for which I am responsible for all of the text and work. The paper has been kept in its entirety, such that there is some repetition of Chapter 3 in Section 4.4. The work was accepted and is published in *Astronomy & Astrophysics*, Volume 669.

4.1 Introduction

Asteroseismology, the study of the intrinsic oscillations of stars, has revealed the physical properties of thousands of stars to high precision (e.g. Metcalfe et al., 2014; Lebreton et al., 2014; Lagarde et al., 2015; Serenelli et al., 2017; Yu et al., 2018b; Yıldız et al., 2019). Solar-like oscillators, wherein modes are excited and damped by the turbulent motion of gas in the outer convection zone, have been of particular interest due to the host of identifiable overtones present in their oscillation power spectra. The spectra of these stars can be characterized via two global parameters, the large frequency separation ($\Delta\nu$) and the frequency at maximum power (ν_{\max}). The first describes the regular frequency interval separating overtone modes of a given angular degree. The second refers to the central frequency of the Gaussian-like envelope describing the

visible power excess caused by the modes. These two parameters are the most readily available in the spectrum of a solar-like oscillator and, when combined with an independent measure of effective surface temperature (T_{eff}), can be exploited to determine the mass and radius of a star to within a few percent (Silva Aguirre et al., 2012; Huber et al., 2012; Guggenberger et al., 2016; Gaulme et al., 2016; Yıldız et al., 2016; Li et al., 2021; Mathur et al., 2022).

With the only requirement for the excitation of modes being the presence of an outer convection zone, solar-like oscillations have been observed in stars on the main sequence (e.g. Chaplin et al., 2014), in the subgiant phase (e.g. Appourchaux et al., 2012a; Mathur et al., 2022) and on the red giant branch (e.g. Bedding et al., 2010; Yu et al., 2018b; Çelik Orhan et al., 2021). As a given star evolves through these phases, structural changes will affect the properties of the oscillations. The least evolved stars oscillate at a few thousand μHz . This decreases as the star evolves off the main-sequence, dropping to below $\sim 100 \mu\text{Hz}$ on the red giant branch. Despite the large coverage of the Hertzsprung-Russell (HR) diagram, current catalogues are disjoint in evolutionary state. Detections are dominated by a large number of red giants and a much smaller set of main-sequence stars, with the subgiant phase only sparsely sampled. Although a decrease in numbers is expected during this phase, given their rapid evolution, observational constraints have magnified the discrepancy.

Relying predominantly on space-based photometry means that observations of solar-like oscillators are mostly limited to data collected by a handful of missions. Of these, the *Kepler* (Borucki et al., 2010) mission provides the longest time series for a large number of available targets. Observing the same patch of sky for four years, the mission monitored approximately 196,000 targets (e.g. Huber et al., 2014). Data were collected in two modes, long and short cadence, with the associated sampling rates corresponding to Nyquist frequency limits of 283 μHz and 8496 μHz , respectively. The short cadence data span the full range in frequency where solar-like oscillations are located. However, due to telemetry constraints, the number of targets observed in the longer cadence greatly outnumbered those in short. Of the total observed targets, only a few thousand were selected for short cadence (Thompson et al., 2016). Therefore, of the tens of thousands of solar-like oscillators detected using *Kepler* data, the vast majority are more

evolved stars (Stello et al., 2013; Hekker et al., 2011; Yu et al., 2018b).

Although sparse in comparison, detections of solar-like oscillators were made in the short cadence data (Chaplin et al., 2011a). Due to the reduced capacity for these observations, these slots were reserved for targets most suited to the main aims of the mission: the detection of exoplanets via the transit method. This led to the preferential selection of cool main-sequence stars (Batalha et al., 2010). The combination of the selection criteria for the short cadence observations and the Nyquist frequency in the long-cadence data resulted in the asteroseismic yield lacking a significant number of subgiant stars. The largest list of these stars was constructed by Li et al. (2020) and numbers only 50 subgiants.

The TESS mission (Ricker et al., 2014) launched in 2018 and has been surveying the majority of the sky, providing an extensive database of potential solar-like oscillators. The nominal mission lasted two years, and observations continue during the first extended mission, which concluded observing in September of 2022. To maximise the sky coverage, observations are made in sectors with an average length of 27.4 days. Most targets are captured in one or two sectors, while a small number of stars are located where the sectors overlap at the ecliptic poles (known as the Continuous Viewing Zones). Similarly to *Kepler*, the majority of the stars monitored by TESS in the nominal mission were observed at 30-minute cadence (referred to as full-frame images, or FFIs), corresponding to a Nyquist frequency of $278 \mu\text{Hz}$. Currently, the largest systematic searches for solar-like oscillators have been performed with observations at this cadence, and they were therefore restricted to the more evolved stars (Hon et al., 2021; Mackereth et al., 2021; Stello et al., 2022). Shorter cadences are available for a smaller set of targets, with the nominal mission including a 120-second integration time (double the *Kepler* short cadence). The extended mission introduced 20-second data for a reduced target list while the FFI cadence was shortened to 10 minutes. With Nyquist frequencies of $4167 \mu\text{Hz}$ and $25000 \mu\text{Hz}$, respectively, the 120-second and 20-second cadence data allow us to detect solar-like oscillations in less evolved solar-like oscillators.

To this end, we used 120-second and 20-second TESS data to search for oscillations in stars observed during Sectors 1 to 46. Starting with a smaller set of targets that were identified as

the most likely to oscillate above the 30-minute FFI Nyquist frequency (Schofield et al., 2019), we have identified 400 candidate solar-like oscillators by eye. These were used to optimise a detection algorithm presented in Nielsen et al. (2022a) (henceforth referred to as N22). We then passed the remaining stars observed during the aforementioned sectors to this tuned pipeline. Although the main aim of this work is to construct a list of solar-like oscillators, we found that we could exploit the probability distributions calculated by the algorithm to measure the global properties (ν_{\max} and $\Delta\nu$). Therefore, we provide these values for the majority of the detected solar-like oscillators.

4.2 Target selection

The full list of targets observed in 120-second cadence by TESS exceeds 300,000. The Asteroseismic Target List (ATL, Schofield et al., 2019) gives some indication of which stars are most likely to be solar-like oscillators prior to running the algorithm. By separating this sample from the full set of 120-second cadence targets, we can loosen detection constraints whilst keeping the required manual validation to manageable levels. To distinguish the stars in the ATL from the remaining targets observed in 120-second cadence, we refer to the latter sample as ‘the Large Sample’.

The ATL was constructed prior to the launch of TESS to provide a prioritised list of targets most likely to yield detections of solar-like oscillations (Schofield et al., 2019; see also Fausnaugh et al., 2021; Godoy-Rivera et al., 2021). Aimed at 120-second cadence data, the list was restricted to stars that would oscillate above the 30-minute FFI Nyquist frequency. To select targets, the authors employed asteroseismic scaling relations for ν_{\max} (Campante et al., 2016). This allowed them to locate stars in the TESS field of view that were predicted to have $\nu_{\max} > 240 \mu\text{Hz}$. Calculating the expected power excess caused by the modes, the authors estimated the probability that the oscillations would be detectable. Only targets with a probability of at least 5% of making a detection were retained, which constituted $\approx 25,000$ targets. Of these, 11,220 had been observed at the time of this work. In the following analysis, values of parallax and T_{eff}

(required by the detection algorithm) were taken from the ATL. The ATL used parallaxes from Gaia data release 2 (GDR2; Gaia Collaboration et al., 2018), supplemented at bright magnitudes with values from the eXtended Hipparcos Catalogue (XHIP; Anderson et al., 2012). Effective temperatures in the ATL were computed from a polynomial in dereddened (B-V) colour, using coefficients according to Torres (2010).

The Large Sample consists of the remaining 120-second cadence targets. We selected stars brighter than 11th magnitude in 2MASS K_S magnitude, and used T_{eff} from the TESS Input Catalogue (TIC; Stassun et al., 2019) to restrict to the range $4500\text{K} < T_{\text{eff}} < 6500\text{K}$. This includes the typical ranges in T_{eff} of stars from the main sequence to the red giant branch, and removes stars that are likely too faint for modes to be visible (Stello et al., 2017). In this set, we analysed light curves for 255,089 stars. We applied the same cuts to all of the targets observed in 20-second cadence, which yielded light curves for 6157 stars. Parallaxes for both sets were again drawn from GDR2.

For reference, we also identified targets with a published detection of solar-like oscillations and some measure of the global asteroseismic parameters. A set of 13 such stars was produced, which is shown in Table 4.1 and referred to in the following as the ‘literature sample’. We prioritized targets oscillating at frequencies above the *Kepler* long-cadence Nyquist as per the main aim of the catalogue. Parallaxes and effective temperatures were drawn from GDR2.

4.3 Data selection

We used detrended light curves produced by the TESS Science Processing Operations Center (SPOC) pipeline (Jenkins et al., 2016), which carries out the simple aperture photometry and removes instrumental trends. We used light curves recorded in 120-second cadence, except when 20-second data were available. In the literature sample, we used 120-second cadence light curves for all but three stars (γ Pav, π Men and α Men), where we used 20-second cadence light curves. We used the open source package Lightkurve (Lightkurve Collaboration et al., 2018) to stitch sectors together, and remove flux values exceeding 5σ .

Name	TIC	ν_{max} (μHz)	$\Delta\nu$ (μHz)	Source
HD 19916	200723869	1188 ± 40	61.4 ± 1.5	TESS 120-second ¹
HD 222416	441462736	430 ± 18	28.94 ± 0.15	TESS 120-second ²
λ^2 For	122555698	≈ 1280	69.76 ± 0.23	TESS 120-second ³
HD 212771	12723961	226.6 ± 9.4	16.25 ± 0.19	TESS 30-minute FFI ⁴
HD 222076	325178933	203.0 ± 3.6	15.60 ± 0.13	TESS 120-second ⁵
94 Aqr	214664574	875 ± 12	50.2 ± 0.4	TESS 120-second ⁶
γ Pav	265488188	2693 ± 95	119.9 ± 1.0	TESS 20-second ⁷
π Men	261136679	2599 ± 69	116.7 ± 1.1	TESS 20-second ⁷
ν Ind	317019578		25.08 ± 0.10	TESS 120-second ⁸
β Hyi	267211065	≈ 1000	57.24 ± 0.16	HARPS and UCLES, WIRE ⁹
μ Ara	362661163	≈ 2000	89.68 ± 0.19	HARPS ¹⁰
μ Her	460067868	1216 ± 11	64.2 ± 0.2	SONG ¹¹
α Men	141810080	3134 ± 440	140 ± 2	TESS 20-second ¹²

Table 4.1: Global asteroseismic parameters of stars in the literature sample.

References. ¹ Addison et al. (2021) ² Huber et al. (2019) ³ Nielsen et al. (2020)⁴ Campante et al. (2019) ⁵ Jiang et al. (2020) ⁶ Metcalfe et al. (2020)⁷ Huber et al. (2022) ⁸ Chaplin et al. (2020) ⁹ Bedding et al. (2007), Karoff et al. (2007) ¹⁰ Bouchy et al. (2005) ¹¹ Grundahl et al. (2017) ¹² Chontos et al. (2021)

As TESS observes in 27.4 day sectors, there are gaps present in the light curves. During the nominal mission, the northern and southern hemispheres were each observed for 13 sectors, amounting to a total two-year observing run. The extended mission returned to the southern hemisphere, meaning that the light curves of some targets contain year-long gaps. Both leaving the gaps and methods to fill the gaps (e.g. linear interpolation; Stello et al., 2015) introduce strong correlations between frequency bins. Assuming mode lifetimes follow the relation given by Appourchaux et al. (2012b) (see also Lund et al., 2017), at $T_{\text{eff}} = 5000\text{K}$, we expect mode lifetimes on the order of weeks. Therefore, if a star is observed in the nominal mission and then a year later in the extended, we expect that the modes have been re-excited so that the variability in the time series is no longer correlated. Hence we removed the gap in the data by shifting the time stamps. As in N22, gaps larger than 50 days were treated in this way. Gap closing in this manner is not the optimal approach and does alter the line profiles, which would impact measurements of individual frequencies, as was discussed in Bedding et al. (2022b). However, as noted in N22, the inclusion of gaps significantly increased the false-positive rate (see N22 Fig. A.1), necessitating closing the gaps for our detection tests. Furthermore, we report only

the global seismic parameters, and do not measure individual frequencies. We then used the `Lightkurve` package to produce a power density spectrum via the ‘fast’ Lomb-Scargle method (Lomb, 1976; Scargle, 1982; Press et al., 1989).

4.4 Detection of solar-like oscillators

In the following section, we briefly review the methods used in the detection algorithm of N22 before we discuss the detections made in each set of targets. The detection test consists of two modules, which exploit different properties of solar-like oscillators:

1. **Power excess test:** The first module uses the power spectral density of the time series.

Given the assumption that the noise in each frequency bin follows a χ^2 distribution with 2 degrees of freedom, the probability that only noise is present in a given bin is calculated (the H_0 probability). The probability that an envelope is present is then computed via a prediction of the expected power in a hypothetical envelope centred on each frequency bin (the H_1 probability). The prediction is calculated via the methods of Chaplin et al. (2011b) and Schofield et al. (2019), requiring T_{eff} . Prior information on ν_{max} is used, guided by parallax and 2MASS K_S -band magnitude.

2. **Large separation test:** The second module looks for the signature of the regularly spaced overtones. This is achieved using the methods described in Mosser et al. (2009a), who used the autocorrelation function (ACF) of the time series. A band-pass filter is placed on the power spectrum at a test frequency and the ACF of this filtered time series is calculated via an inverse Fourier transform. Repeating this for other test frequencies, we produce a 2D ACF in test frequency (a proxy for ν_{max}) and lag (related to the large frequency separation via $\tau = 1/\Delta\nu$). This 2D map is collapsed along the lag axis to produce a 1D distribution in frequency. To evaluate whether the probability the observed collapsed ACF is inconsistent with noise, N22 approximated the response due to noise by a Γ distribution.

Using 400 solar-like oscillators and non-detections manually identified from the ATL, N22 established the performance of the pipeline for a range of detection thresholds. They found that

the pipeline was able to attain a true-positive rate of 94.7% and a false-positive rate of 8.2% when asking for a response in at least one of the two modules¹.

In the following sections, we discuss the detections made in the four samples via this algorithm (see Table 4.2). All of the reported solar-like oscillators have been manually vetted to check for false positives. We retained only targets in which we are confident we have identified the presence of oscillations, prioritizing a reduced false-positive rate over maximising the yield. This may cause an under-representation of targets with a very low signal-to-noise ratio. A breakdown of the total counts, and which sample they belong to, can be seen in Table 4.3. Cross-referencing with NASA’s Exoplanet Archive ², we found that 28 of the stars in our catalogue are confirmed planet hosts. The majority of these stars have not yet been studied asteroseismically. Asteroseismic inferences on these targets are reserved for an upcoming work. We also cross-referenced with the *Ninth Catalogue of Spectroscopic Binary Orbits* of Pourbaix et al. (SB9; 2004), discovering 25 stars are components in spectroscopic binary systems.

Fig. 4.1 shows the value of 2MASS K_S magnitude against the predicted value of ν_{\max} . In grey we show targets observed in 120-second cadence with a detection probability greater than 10% using the methods described by Chaplin et al. (2011b) and Schofield et al. (2019). The gap in the grey population starting at $K_S \approx 4$ is present in the full sample of short cadence targets and is not enforced by the probability cut, which only places upper limits on ν_{\max} and magnitude. This is likely the result of the TESS target selection process, which consists of selecting stars from a number of lists including cool dwarfs, known planet hosts, bright stars, hot subdwarfs, and guest investigator targets (Stassun et al., 2018; Stassun et al., 2019). We did not detect solar-like oscillations in any targets with $\nu_{\max} < 5 \mu\text{Hz}$, regardless of magnitude. As discussed in N22, the predicted mode amplitude used in the power excess module included the observed decrease near the red edge of the δ Scuti instability strip. This was done via a factor that depends on ν_{\max} and T_{eff} , so that at a given temperature, amplitudes decrease as a function of frequency (Chaplin et al., 2011b). The correction was calibrated using main-sequence stars

¹This is achieved when taking a threshold of 0.77 on the power excess module and 0.73 on the frequency spacing module.

²<https://exoplanetarchive.ipac.caltech.edu>

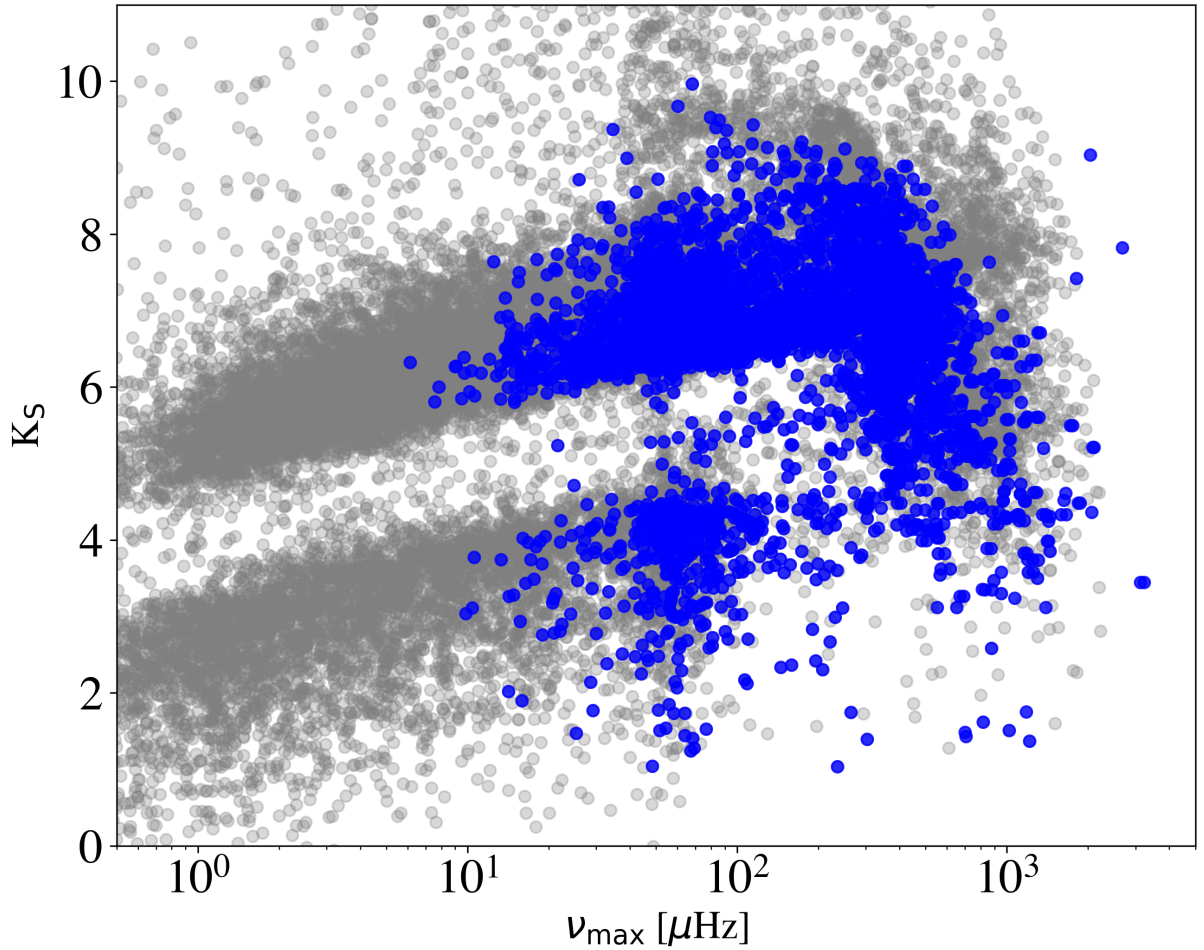


Figure 4.1: 2MASS K_S magnitude and predicted ν_{\max} for stars observed in 120-second cadence with a detection probability exceeding 10% (grey). The targets that we identified as solar-like oscillators are marked in blue.

and therefore may not be appropriate for the most evolved targets. At $T_{\text{eff}} = 4800\text{K}$, the factor decreases to approximately zero at frequencies below $5 \mu\text{Hz}$, which suppresses detections in the power excess module. In addition, from the approximate relation between ν_{\max} and $\Delta\nu$ (Stello et al., 2009, see Eq. 4.1) at a ν_{\max} of $5 \mu\text{Hz}$, we would expect $\Delta\nu$ to be below $1 \mu\text{Hz}$. This is approaching the resolution in a single sector of TESS data ($0.4 \mu\text{Hz}$). Therefore, detections in the repeating pattern module are also increasingly unlikely.

TICID	No. Sectors	RP	PE	ν_{\max} (μHz)	$\sigma(\nu_{\max})$ (μHz)	$\Delta\nu$ (μHz)	$\sigma(\Delta\nu)$ (μHz)	sample	Flag
270536913	1		1	368.24	11.22	24.17	0.35	120-sec	–
286507416	3		1	238.42	2.17	17.93	0.08	120-sec	–
142275448	2		1	523.65	14.99	32.05	0.25	120-sec	–
181655818	2		1	427.37	6.99	26.51	0.25	120-sec	–
394151928	3		1	285.34	12.86	21.55	0.17	120-sec	–
71109681	2		1	216.30	3.60	16.89	0.12	120-sec	–
47067158	3		1	375.80	7.54	24.23	0.36	120-sec	SB9
141201954	1		1	253.72	4.83	18.38	0.18	120-sec	–
301558151	2		1	483.88	4.09	29.26	0.19	120-sec	–
178199266	3		1	210.91	9.32	16.70	0.12	120-sec	–

Table 4.2: Catalogue of seismic parameters for detected solar-like oscillators. The full table is available in online materials. Quantities RP and PE track which modules the target produced a detection in. Flag is ‘SB9’ for targets in the *Ninth Catalogue of Spectroscopic Binary Orbits* (Pourbaix et al., 2004) and ‘PH’ for targets which are confirmed planet hosts according to NASA’s Exoplanet Archive.

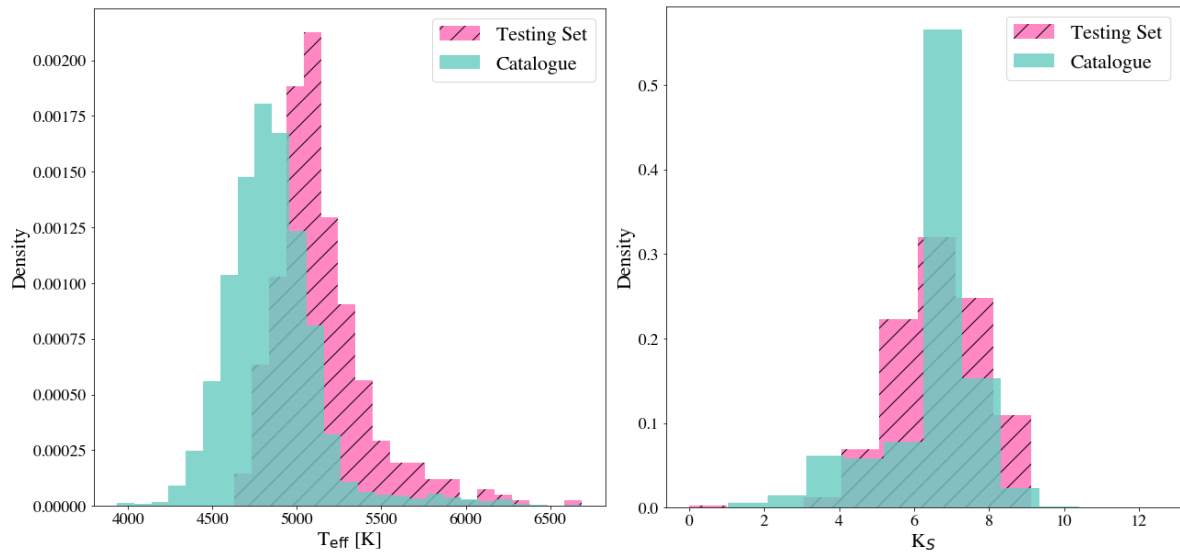


Figure 4.2: Left: Distribution of T_{eff} for targets used in the testing set of 400 oscillators from N22 compared to those in the catalogue reported here. Right: Distribution with 2MASS K_s magnitude

4.4.1 Literature Sample

Of the 13 solar-like oscillators drawn from the literature, the algorithm flagged a detection in both modules for 11 stars. μ Ara produced a response in the power excess module, but not the repeating pattern. Oscillations in this star have thus far only been detected in Doppler velocity (Bouchy et al., 2005). As the signal from granulation is lower relative to the modes in velocity measurements than in photometry (Basu et al., 2017a), the single-module response is likely just an effect of the decreased signal-to-noise ratio. The remaining star, HD19916, did not produce a flag in either module. Although oscillations in HD19916 have been detected in TESS 120-second cadence data, the authors note that a custom aperture had to be used, expanding to include more of the stellar flux (Addison et al., 2021). To maintain consistency with the rest of our catalogue, we did not mimic this approach. We note that the stars with detections reported in 20-second data (γ Pav, π Men, and α Men) produced flags in both modules. However, when we use the available 120-second data for the same stars, one is not detected at all (π Men) and the others are only detected in the power excess module, despite oscillating at frequencies well below the corresponding Nyquist frequency limit. The improvement made by the 20-second data was highlighted by Huber et al. (2022).

4.4.2 Asteroseismic Target List

To construct the set of stars used to establish the performance of the detection algorithm in N22, a manual inspection of the 11,220 spectra discussed in Sect. 4.2 was performed. On the construction of the the sets of 400 oscillators and 400 ‘non-oscillators’, several stars fell into the category of targets for which, although some excess power was present in the spectrum, we were unable to unambiguously classify the target as a solar-like oscillator. Since that work was done, new sectors of data had become available, which could facilitate unambiguous classification. We therefore reran the algorithm on the full set of 11,220 spectra. With the testing set of oscillators from N22 removed, 2651 stars were flagged in just one module and 490 in two. Of the single-module detections, the vast majority were false positives, presenting some large non-solar-type signal rather than solar-like oscillations (e.g. periodic dips caused by a transit, eclipse, or classical oscillations). These stars were not included in the metrics stated in N22. Including these stars in the false-positive metric for a single-module response increases the percentage to $\approx 20\%$. In total (with the testing set included), we detected 494 solar-like oscillators with responses in both modules, and another 258 with a single-module response.

4.4.3 Large Sample

For the 255,089 stars for which we analysed light curves, we expect a false-positive rate of 8.2%. Assuming the majority are not solar-like oscillators, this would equate to false positives in the range of $\approx 20,000$. We found 37,250 flagged in at least one module, therefore we took the more conservative approach and performed a manual inspection of stars that produced a flag in both modules. Of the 5,781 stars that produced flags in both modules, we found 2,927 clear solar-like oscillators. We have retained the list of single-module responses, but reserve releasing it until they have been manually vetted, to avoid confusion. Unlike the ATL sample, we have relaxed the requirement that ν_{max} exceeds $240 \mu\text{Hz}$. This gives a set of targets that are cooler on average, and more strongly peaked in magnitude (see Fig. 4.2).

Sample	Double	Single	Total
Literature	11	1	12
ATL	494	258	752
Large	2927	-	2927
20-sec	288	198	486
Total	3720	457	4177

Table 4.3: Detection counts in each sample. ‘Double’ refers to cases where the star flagged a detection in both the power excess and repeating pattern modules. ‘Single’ refers to cases where the star flagged in one module only.

4.4.4 20-second cadence

Of the 6157 stars in this set, the algorithm produced a single-module response for 1585, and a double-module response for 421. Upon visual inspection of these targets, we were able to clearly identify 490 solar-like oscillators.

4.5 Global asteroseismic parameters

Alongside enabling detection, the probability distributions calculated in the detection process allow us to measure the global asteroseismic parameters $\Delta\nu$ and ν_{\max} . There are already a number of pipelines dedicated to measuring these parameters via different methods (Huber et al., 2009; Hekker et al., 2010; Kallinger et al., 2010; Mathur et al., 2010; García et al., 2014; Elsworth et al., 2017; Zinn et al., 2019). However, as the main aim of this work is the construction of a list of solar-like oscillators, a full comparison between our method and these alternatives is reserved for future work.

The probability distribution as a function of frequency calculated by the frequency spacing method (see Sect. 4.4) was normalized to unit integral over the spectrum, producing a probability density. The 50th percentile of this was used to measure ν_{\max} , with the 16th and 84th percentiles giving the confidence interval.

N22 only required the ACF collapsed along the lag (τ) axis to perform a detection. To determine $\Delta\nu$, we instead collapsed along the test frequency. Rather than summing the ACF for all test frequencies at a given lag, we exploited the approximate relation between ν_{\max} and $\Delta\nu$

(Stello et al., 2009),

$$\frac{\tilde{\nu}_{\max}}{\nu_{\max,\odot}} = \left(\frac{\Delta\nu}{\Delta\nu_{\odot}} \right)^a, \quad (4.1)$$

where we took the value $a = 0.791$ as in N22. This estimate of ν_{\max} at a given $\Delta\nu$ ($\tilde{\nu}_{\max}$) allowed us to restrict the range of frequencies summed. Accordingly, we only summed bins in the range $|\nu_{\max} - \tilde{\nu}_{\max}| < 0.2\tilde{\nu}_{\max}$.

To calculate the expectation from a spectrum devoid of oscillations, we used 10^3 white-noise realizations. Similarly to N22, we found that for filtered white noise, the noise statistics can be well approximated by a Γ distribution in lag. The mean of this distribution can be described by the empirical relation

$$\mu(\tau) = A(B + \tau^{\alpha}/N_{\nu}^{\beta}), \quad (4.2)$$

where N_{ν} is the number of frequency bins included in the calculation of the ACF at a given τ . Using the `emcee` package (Foreman-Mackey et al., 2013a), we fitted for the parameters B , α , and β , the results of which can be found in Table 4.4. Parameter A is a calibration constant that depends on the time-series length and was determined on a star-by-star basis. Using Eq. 4.1 to estimate the value of $\Delta\nu$ ($\widetilde{\Delta\nu}$) given the measured value of ν_{\max} , we masked the ACF in the range $0.7\widetilde{\Delta\nu} < \Delta\nu < 1.3\widetilde{\Delta\nu}$. The calibration factor A was then estimated by the ratio of the modelled to observed ACF in the first 5 μ Hz and final 50 μ Hz (with the latter range accounting for the decrease in frequency resolution at small lag).

We found that the variance in the collapsed ACF can be approximated by

$$\sigma(\tau)^2 = c\mu(\tau)^2, \quad (4.3)$$

with the value of c determined by a fit to the white-noise simulations (see Table 4.4). A comparison of the predictions from Eq. 4.2 and 4.3 to simulations of different time-series lengths is shown in Fig. 4.3. We also tested the model on data binned to different effective lengths. The net effect of the binning is an additional multiplicative factor, which is accounted for in the calibration.

Parameter	Value
B	1.54
α	0.65
β	0.36
c	0.34

Table 4.4: Parameters for Eq. 4.2 and 4.3.

We used Eq. 4.2 and 4.3 to establish the probability ($P_{\Delta\nu}$) that the collapsed ACF (r) at a given value of τ is inconsistent with noise. Logarithmic probabilities were used for numerical stability. Given that the envelope will cause an excess above the mean, we can label any divergences below the mean as noise. Therefore, the natural choice is the survival function,

$$\log P_{\Delta\nu} = -\log \left(\int_r^\infty \frac{\beta^\alpha}{\gamma(\alpha)} r'^{\alpha-1} \exp(-\beta r') dr' \right), \quad (4.4)$$

where the shape parameter is $\alpha(\tau) = (\mu(\tau)/\sigma(\tau))^2$ and the scale parameter $\beta(\tau) = \mu(\tau)/\sigma(\tau)^2$. Normalizing $P_{\Delta\nu}$ to unit integral over the $\Delta\nu$ axis produces a probability density. The 50th percentile of this was used to measure $\Delta\nu$, with the 16th and 84th percentiles giving the confidence interval.

In the following sections, we discuss the values of $\Delta\nu$ and ν_{\max} in each of our samples. We use our Literature Sample to briefly comment on the robustness of our methods in TESS data compared to results produced largely from a bespoke analysis of individual stars. We then proceed to discuss the results in the remaining new detections. A summary of the catalogue is shown in Fig. 4.4. We note that in some targets, values of $\Delta\nu$ may be reported even though the star does not produce a flag in the repeating-pattern module. To report a detection, we require that the repeating-pattern merit function exceed a threshold that was chosen as the best balance between the false positives and false negatives. Therefore, a star could produce a measurable response in the collapsed ACF, while the merit function peaks just below the selected threshold. Accordingly, we only removed measurements from the final catalogue that were manually identified as clear outliers in the ν_{\max} - $\Delta\nu$ plane. The values that have been removed are shown in Fig 4.A.1 of the appendix.

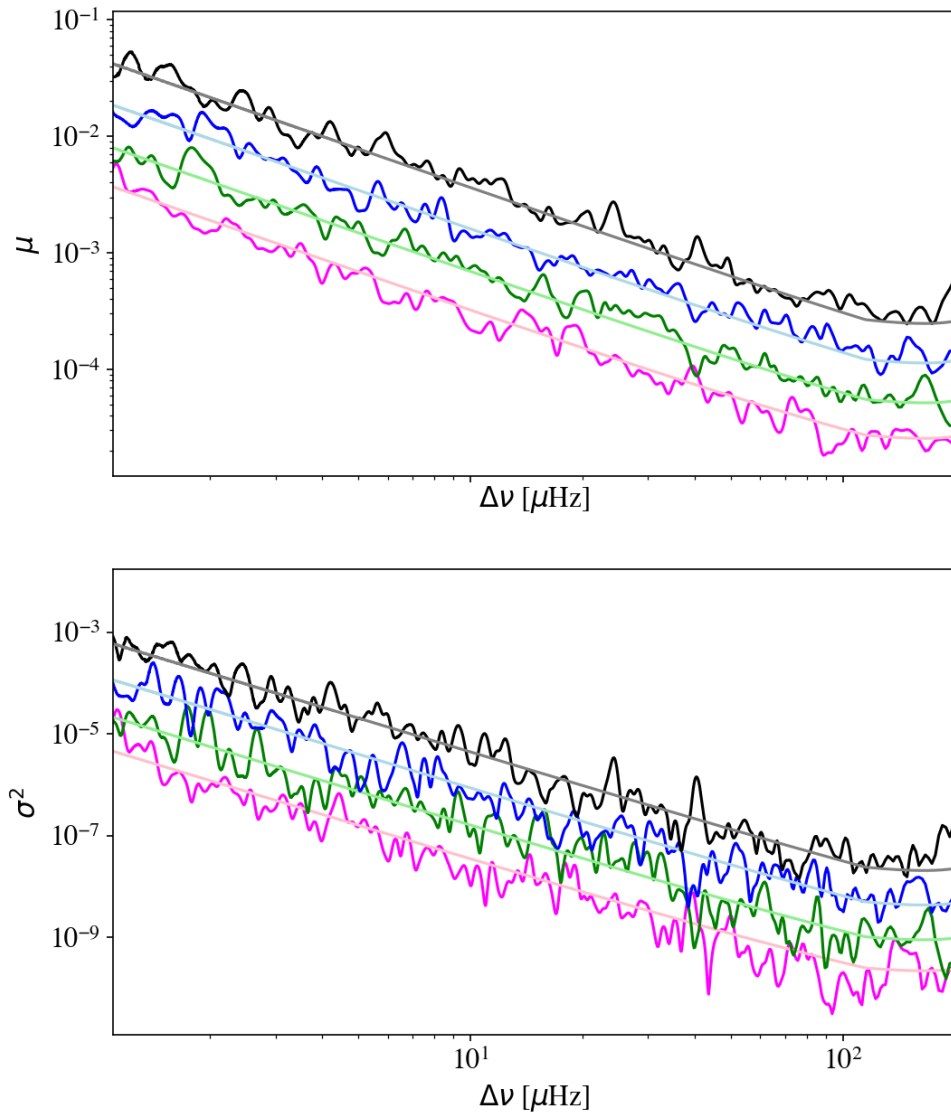


Figure 4.3: Mean simulated collapsed ACF as a function of $\Delta\nu$ for filtered white noise (top panel). Colours represent time series of different lengths, with one sector in black, four in blue, nine in green, and twelve in magenta. Pale lines show the predictions for each length according to Eq. 4.2. Variance on the simulated collapsed ACF presented in the top panel (bottom panel).

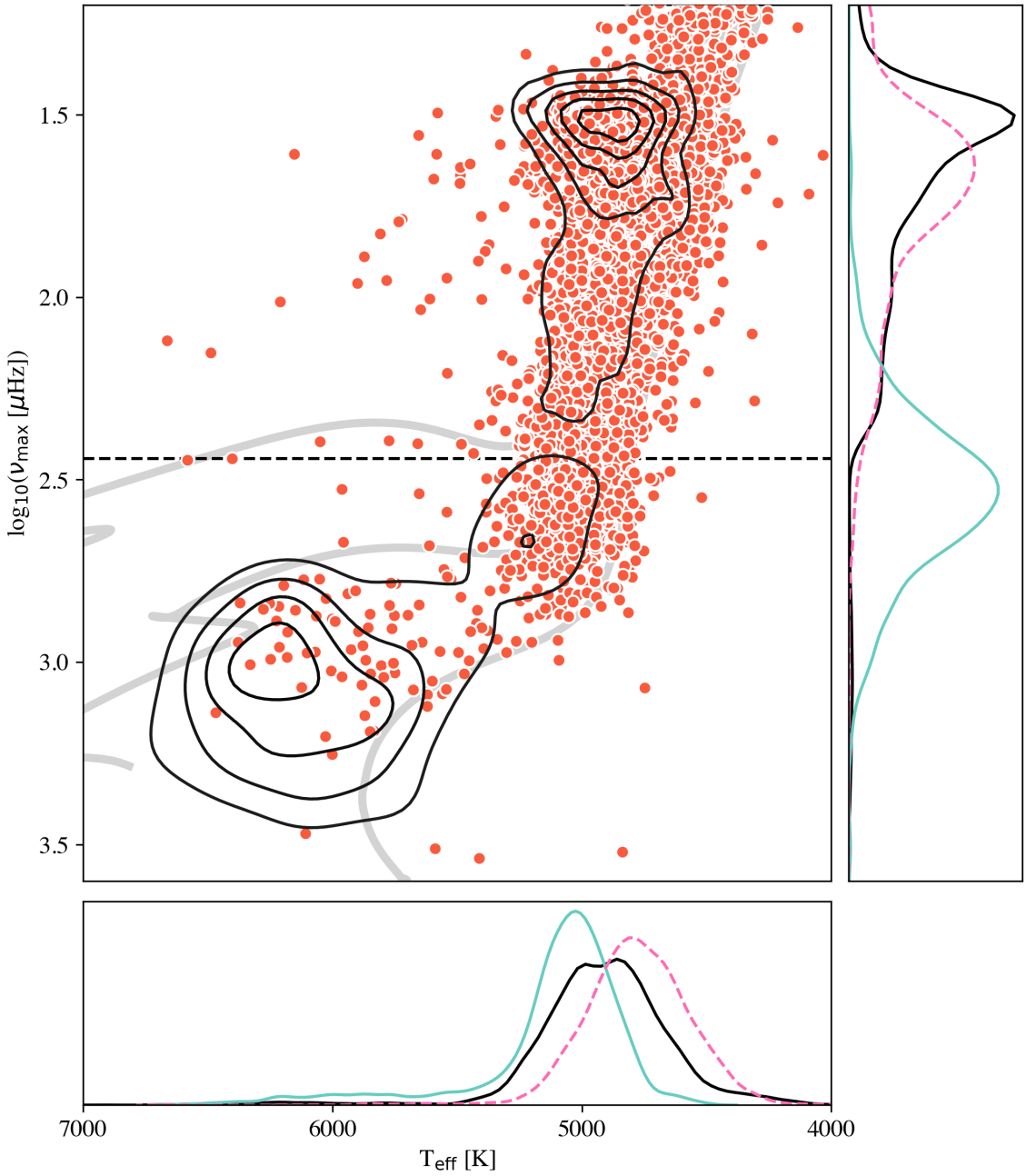


Figure 4.4: Asteroseismic HR diagram for stars in all samples (main panel, orange circles). Effective temperatures have been drawn from the TIC in all cases, to maintain consistency. Contour lines represent measurements from *Kepler* data reported in Yu et al. (2018b), Lund et al. (2017), and Serenelli et al. (2017), with effective temperatures from GDR2. The horizontal dashed line represents the *Kepler* long-cadence Nyquist frequency. Three stellar tracks at masses 1.0, 1.5, and 2.0 M_{\odot} generated by MIST (Choi et al., 2016) are shown in grey. The distributions in T_{eff} and ν_{\max} are shown in the bottom and right panels, respectively. Here, the catalogue is split into the ATL set in turquoise and the Large Sample in pink (dashed), with the *Kepler* distribution shown in black.

4.5.1 Literature Sample

Of the 13 targets making up the sample, 9 have published ν_{\max} values with uncertainties. In the remaining stars, the authors focussed on determining individual frequencies rather than global parameters, and so estimates of ν_{\max} without uncertainties were published. A comparison of the literature values to those measured by our method is shown in Fig. 4.5. On average, the measured values of ν_{\max} are higher than those reported in the literature by $\approx 2.5\%$. The star with largest fractional difference is HD 212771, where our value of ν_{\max} is higher by $\approx 9\%$. The literature value was measured using FFI data processed by the TESS Asteroseismic Science Operations Center (TASOC) pipeline (Handberg et al., 2021). From visual inspection of the signal-to-noise ratio spectrum of HD 212717, we found that the envelope extended beyond the FFI Nyquist frequency. The attenuation caused by the sampling integration causes a decrease in power near the Nyquist frequency, which could have caused an underestimate on ν_{\max} in Silva Aguirre et al. (2020). Visual inspection of the power spectra confirms that our higher value is more accurate.

In total, 11 stars have measurements of $\Delta\nu$ in the literature. In the case of ν Ind, the most recent asteroseismic study was made in Chaplin et al., 2020, where the authors used a single sector of TESS data to fit individual modes. We measured $\Delta\nu$ from the gradient of a linear fit to the radial mode frequencies as a function of order (White et al., 2011b). We took the same approach for λ^2 For, where similarly the authors did not provide estimates of $\Delta\nu$ (Nielsen et al., 2020). A comparison of the values with those from the algorithm is shown in the right panel of Fig. 4.5. The agreement is better than for ν_{\max} , with a mean fractional difference on $\Delta\nu$ of 0.24%.

4.5.2 Asteroseismic Target List

Of the 752 validated solar-like oscillators, we report both $\Delta\nu$ and ν_{\max} for 739. In the majority of cases, the determination is linked: both come from the autocorrelation function collapsed along the relevant axis. However, it is possible to detect the envelope without a signal from the

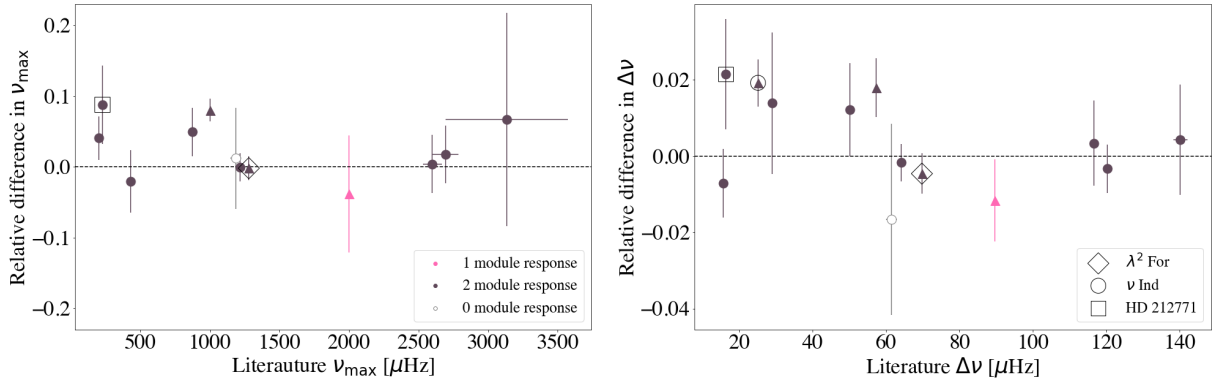


Figure 4.5: Comparison of the global astroseismic parameters measured by our algorithm to those reported in the literature. Stars are coloured by the number of modules in which they produce a flag; pink for a single module, brown for two modules, and an open grey marker for none. Triangles represent stars for which no uncertainty on ν_{\max} was reported in the literature. Targets λ^2 For, ν Ind, and HD212771, which are discussed in the text, are marked with a diamond, circle, and square, respectively. The left and right panels show the fractional difference between the values of ν_{\max} and $\Delta\nu$ as measured by the algorithm vs literature value, respectively.

frequency spacing.

In order to assess the quality of the measured ν_{\max} and $\Delta\nu$ values, we exploited the approximate scaling relation between the two (Eq. 4.1). Although there is a slight mass dependence in exponent a (Stello et al., 2009), the general trend remains such that stars disagreeing significantly with the rest of the population may indicate an error in one (or both) of the measured values.

Fig. 4.6 shows the relation between the values of ν_{\max} and $\Delta\nu$ for the targets in the ATL sample. The majority of the stars with detections in both modules follow Eq. 4.1. We highlight TIC 381975502 (CD-56 1110), in which a background eclipsing binary introduced several harmonic peaks in the power spectral density at low frequency. These peaks appear in the ACF as a large response at a test frequency corresponding to the frequency of the orbital harmonics, resulting in the algorithm incorrectly assigning both $\Delta\nu$ and ν_{\max} . This is also the case for TIC 271701447 (HR 4749; HD 108570). The values of ν_{\max} and $\Delta\nu$ for these targets have been removed from the final catalogue, while IDs have been retained.

For targets detected in just one module, there is a larger scatter about the scaling relation, as shown on Fig. 4.6. Using an exponent on Eq. 4.1 of $a = 0.791$ as calculated in N22, $\Delta\nu$ for 13 targets differs by more than 30% from the value predicted by the scaling relation and measured value of ν_{\max} . We performed a manual inspection of these stars and found that four are likely

misclassifications. A further two passed the detection threshold, both at the envelope and at a much lower frequency, biasing the resulting parameters. In three stars, the estimated ν_{\max} used in the prior was significantly higher than the observed value. They are overestimated by factors of three, five, and two. In these cases, the parallaxes reported in the ATL were drawn from XHIP rather than GDR2. The ν_{\max} predicted using GDR2 parallaxes produced a prior more consistent with the measured ν_{\max} . The remaining stars could be divided into two sets: Targets with less than one full sector of data, and high- ν_{\max} targets with low-mode amplitudes. The resulting low signal-to-noise ratio could impact the determination of $\Delta\nu$. Values of ν_{\max} and $\Delta\nu$ for these outliers have been removed.

In Fig. 4.4 the stars in the ATL sample cluster about the base of the red giant branch and extend toward the main sequence. The peak of the distribution falls just above the *Kepler* long-cadence Nyquist frequency, populating the previously sparsely sampled region. The density falls off toward higher ν_{\max} , which is likely a result of the decreasing mode amplitude.

4.5.3 Large Sample

Here, we report both ν_{\max} and $\Delta\nu$ for all but 62 stars. For these outliers, we found similar issues to those discussed in the ATL. Additionally, we noted 16 stars for which the probability distributions in ν_{\max} were multi-modal. The remaining targets vastly outnumber those from the ATL, and span the red giant branch (as shown in Fig. 4.4). The density increases with decreasing ν_{\max} until it peaks at $\approx 49 \mu\text{Hz}$. At the high- ν_{\max} tail, we note an overlap between the ATL and Large Sample. There are 119 stars that did not appear in the ATL even though they show oscillations at frequencies above $240 \mu\text{Hz}$. Of these, just under half lie near the ATL cutoff, with $240 < \nu_{\max} < 300 \mu\text{Hz}$. A total of 63 stars, however, are above $300 \mu\text{Hz}$ in a region that should be included in the ATL. There are several reasons why these targets could have been omitted. The estimate of ν_{\max} in the ATL was a function of T_{eff} , such that a significant underestimate on the latter could have pushed the former beyond the enforced $240 \mu\text{Hz}$ cut. Calculating T_{eff} for the additional targets using the methods stated in the ATL, we did not find a systematic underestimate compared to GDR2, with values agreeing to within 10%

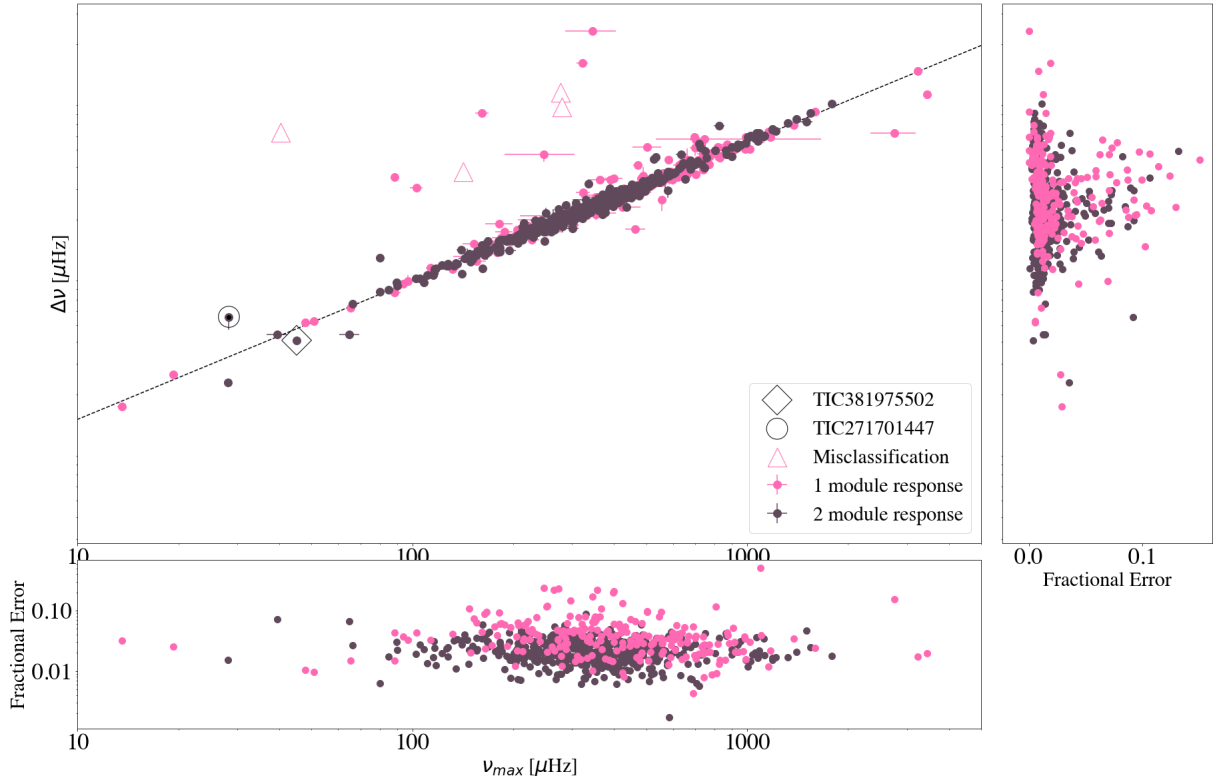


Figure 4.6: $\Delta\nu$ as a function of ν_{\max} measured by the algorithm for validated solar-like oscillators from the ATL set (main panel). Stars producing flags in only one module are shown in pink, and those producing flags in both modules are shown in brown. Triangles mark stars that were likely misclassified as solar-like oscillators. Targets TIC381975502 and TIC271701447, which are discussed in the text, have been marked with a diamond and circle. The dotted black line shows Eq. 4.1. Additional panels show the fractional uncertainties on $\Delta\nu$ and ν_{\max} .

in over 90% of the targets. The other possibility is that the detection probabilities for these targets were underestimated. This could be the result of an overestimated noise level caused by, for example, an underestimation of the size of the predicted pixel mask or a greater degree of contamination from background sources. A full comparison between the predictions in the ATL and the observed yield is reserved for future work.

According to the main aim of the TESS mission (Ricker et al., 2014), we expected that targets proposed for 120-second cadence would be less evolved than the giants presented here. Although targets were also selected when they were brighter than $T_{\text{mag}} = 6$ (where T_{mag} is the magnitude of the star for the TESS instrument response), which would preferentially select bright giants, we found that $\approx 80\%$ of the giants in which we detected solar-like oscillations were fainter than this limiting magnitude. We therefore checked that the oscillations occur in the star associated with the TIC number being searched, rather than in another star in the mask, by comparing the ν_{max} value predicted by the prior to the detected value (see Fig. 4.7). In general, the ratio of the two was close to unity, indicating that the detected envelope belongs to the target in question.

4.5.4 20-second cadence

The measured values of $\Delta\nu$ and ν_{max} are shown in Fig. 4.8. A total of 16 stars were removed by manual identification. We note that the uncertainties on $\Delta\nu$ presented in Fig. 4.8 appear larger than those presented in Fig. 4.6 (the ATL sample), which is likely due to the population of targets at $\nu_{\text{max}} < 100 \mu\text{Hz}$. The mean fractional uncertainty on the measured $\Delta\nu$ in the 20-second-cadence sample is 2.1%, approximately consistent with 1.9% in the ATL sample. Again, we find that the population is dominated by evolved stars, with the distribution peaking at a ν_{max} value of 50 μHz .

We note a detection in an oscillator observed by *Kepler* (KIC 6106415; HD 177153; ‘Perky’), which is a clear outlier in Fig. 4.8. The algorithm reports a $\Delta\nu$ of 131 μHz despite reporting a ν_{max} of 127 μHz . Using *Kepler* data, oscillations were identified at $\nu_{\text{max}} = 2249 \mu\text{Hz}$ (Lund et al., 2017). The envelope we detected at 127 μHz (which can be visually identified) appears

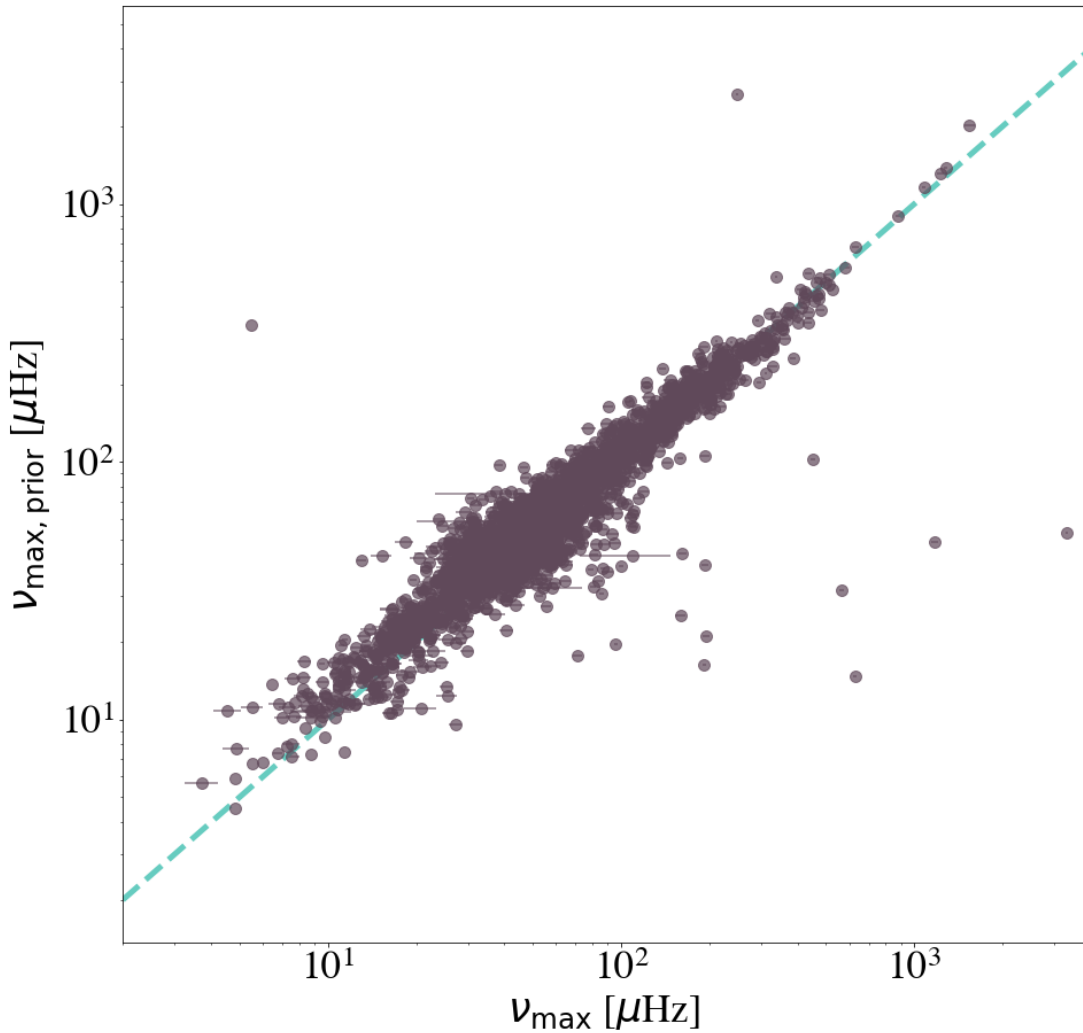


Figure 4.7: Prior ν_{max} ($\nu_{\text{max,prior}}$) vs measured values in short cadence targets. The dashed blue line represents the 1-1 line.

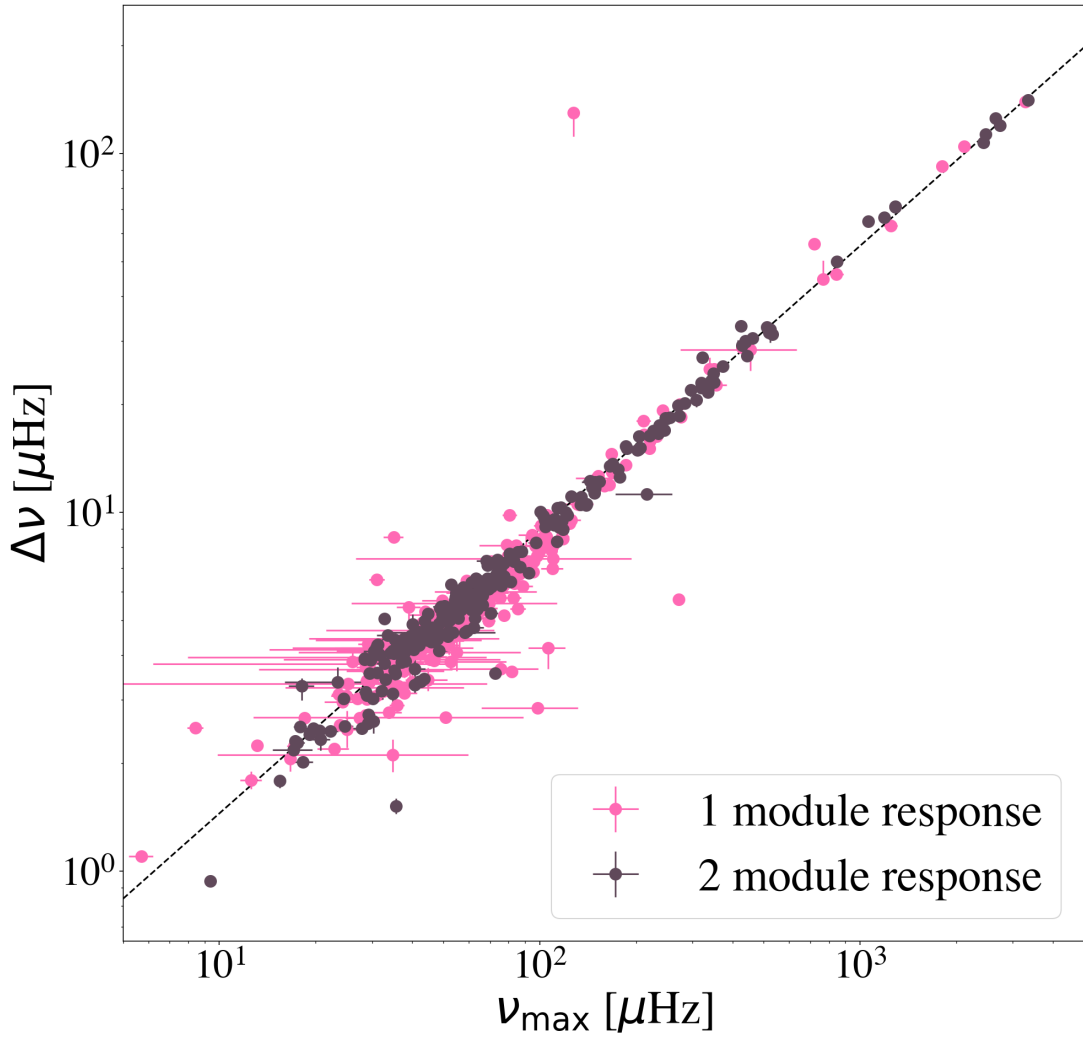


Figure 4.8: $\Delta\nu$ vs ν_{\max} for validated solar-like oscillators from the 20-second cadence set. Stars producing flags in only one module are shown in pink, and those producing flags in both are in brown.

to be on another red giant in the pixel mask. Therefore, the prior has caused an erroneous measurement of $\Delta\nu$.

4.6 Conclusions

Applying the algorithm introduced by Nielsen et al. (2022a) to 120-second- and 20-second-cadence observations from the TESS mission spanning Sectors 1 to 46, we have detected solar-like oscillations in a total of 4177 targets. Of these, 12 belong to a set of previously reported solar-like oscillators, 752 to stars that appeared in the ATL, and 486 were detected

using 20-second-cadence data. The remaining are targets brighter than 11th magnitude in 2MASS K_S , with temperatures in the range $4500\text{K} < T_{\text{eff}} < 6500\text{K}$, observed in 120-second cadence. Since Sector 46, data for additional sectors have been released. We leave the analysis of these and the data collected in upcoming sectors as we approach the end of the first extended mission for future work.

All catalogued targets have been manually vetted to confirm the presence of oscillations. We note that signals from eclipsing binaries, classical pulsators, or transiting planetary bodies can cause false-positive detections. Therefore, we highlight that when using the algorithm presented in N22 with very large data sets, the more conservative approach (asking for responses in both modules) is the most effective at reducing the amount of manual vetting required.

We have extended the work of N22 to include methods for measuring the global asteroseismic parameters, ν_{max} and $\Delta\nu$. We introduced a new model for parameterizing the collapsed ACF to produce a probability density for $\Delta\nu$. Applying this technique to the catalogue of detections, we measured the global asteroseismic parameters for 98% of the targets. Overlaying these stars on the asteroseismic HR diagram (ν_{max} and T_{eff}) allowed us to confirm the ATL successfully identified the least evolved stars, with little overlap in the remaining detections. The small set of stars that appear to have been missed by the ATL cluster about $K_S = 6$ mag, which is a region where the GDR2 astrometric solutions are known to have inferior astrometry (Lindegren et al., 2018), suggesting an issue in the parallaxes.

This catalogue demonstrates the significant contribution that the TESS mission can make to the field of asteroseismology. When targets from the ATL are isolated, the increase in the number of detections between the $280\ \mu\text{Hz}$ cutoff enforced by the 30-minute FFI observations and the upper edge of our catalogue at around $1000\ \mu\text{Hz}$ is at least twofold on the detections made in *Kepler* data. With the inclusion of the stars detected in 120-second cadence that did not appear in the ATL, we were able to use a homogeneous data set to measure asteroseismic values in solar-like oscillators from the subgiant regime through the red giant branch.

Funding for the TESS mission is provided by the NASA’s Science Mission Directorate. E.J.H., W.J.B. and G.R.D. acknowledge the support of Science and Technology Facilities Coun-

cil. T.R.B. acknowledges support from the Australian Research Council (Discovery Project DP210103119). M.B.N. acknowledges support from the UK Space Agency. C.K. is supported by Erciyes University Scientific Research Projects Coordination Unit under grant number DOSAP MAP-2020-9749. D.B. acknowledges support from NASA through the Living With A Star Program (NNX16AB76G) and from the TESS GI Program under awards 80NSSC18K1585 and 80NSSC19K0385. D.H. acknowledges support from the Alfred P. Sloan Foundation and the National Aeronautics and Space Administration (80NSSC21K0652). T.S.M. acknowledges support from NASA grant 80NSSC22K0475. The authors acknowledge use of the Blue-BEAR HPC service at the University of Birmingham. This paper includes data collected by the Kepler mission and obtained from the MAST data archive at the Space Telescope Science Institute (STScI). Funding for the Kepler mission is provided by the NASA Science Mission Directorate. This work has made use of data from the European Space Agency (ESA) mission Gaia (<https://www.cosmos.esa.int/web/gaia>), processed by the Gaia Data Processing and Analysis Consortium (DPAC, <https://www.cosmos.esa.int/web/gaia/dpac/consortium>). Funding for the DPAC has been provided by national institutions, in particular the institutions participating in the Gaia Multilateral Agreement. This publication makes use of data products from the Two Micron All Sky Survey, which is a joint project of the University of Massachusetts and the Infrared Processing and Analysis Center/California Institute of Technology, funded by the National Aeronautics and Space Administration and the National Science Foundation.

4.A Additional plots

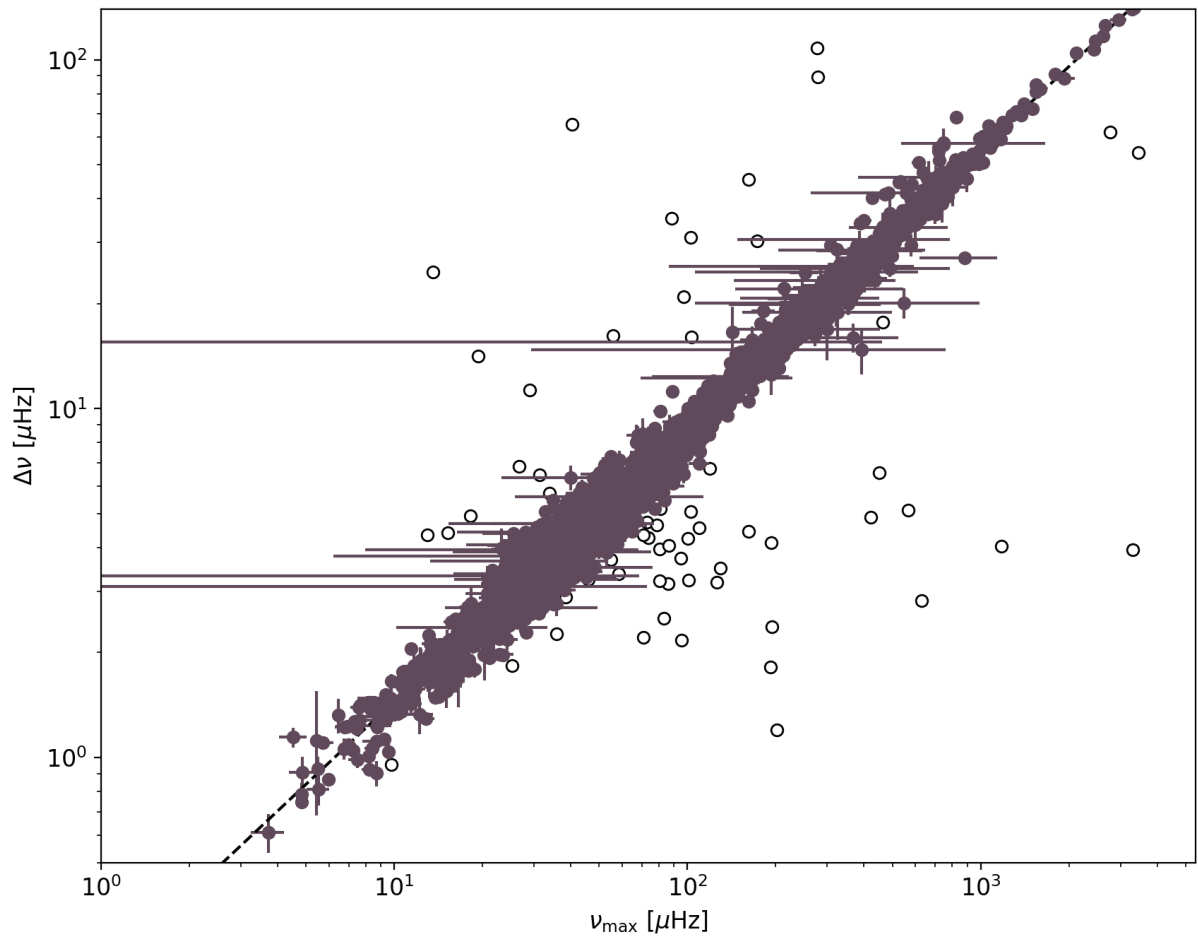


Figure 4.A.1: $\Delta\nu$ as a function of ν_{\max} for targets in the final catalogue in brown. Values that were removed after manual identification are shown as open circles.

Chapter 5

Predictions for HAYDN

Asteroseismology is uniquely suited to probe the internal mechanisms governing stellar evolution, many of which are still not yet well understood. However, these processes depend on the fundamental properties of stars, like mass and metallicity. To comprehensively sample the evolution of stellar interiors we require observations of stars sharing similar fundamental properties at different evolutionary states. Although numbering thousands of stars, *Kepler* asteroseismic catalogues are lacking in subgiants (see Section 2.3.1) and consist of stars that are broadly spread in metallicity. TESS observations have been used to close this subgiant gap (see section 4), but lightcurves are generally not of the required quality to enable well constrained measurements of individual mode frequencies, which are necessary for the most detailed asteroseismic analysis. To fully exploit the power of asteroseismology we require a new mission, designed to output the highest quality asteroseismic data for populations of solar-like oscillators.

If all stars of different fundamental properties were randomly distributed in space, isolating similar solar-like oscillators would require observations of large regions of the sky. Fortunately, nature does locally generate collections of similar stars. Stellar clusters consist of stars that have formed out of the same gas cloud, at roughly the same time, such that they share common chemical compositions and ages. The High-precision AsteroseismologY in DeNse stellar fields (HAYDN) space telescope was proposed to exploit these properties observing stellar clusters in, if it were to be accepted, the first mission dedicated primarily to asteroseismology (Miglio

et al., 2021). HAYDN went through its first proposal submission in 2023, responding to the ESA Voyage 2050 call for proposals. During the process, predictions for the seismic yield were required to determine the optimal observing strategy. I was involved in this process, producing simulated lightcurves for stars in clusters of interest and using these to determine the amount of asteroseismic information we could recover. Ultimately, HAYDN was not accepted. However, there is still a large amount of scientific interest in the mission, and it is expected that it will be proposed again in the future.

Among the processes HAYDN could provide crucial insight into is stellar rotation. Although classical techniques have enabled measurements of surface rotation in thousands of stars (e.g. Glebocki et al., 2005), rotation below the photosphere can only be measured using asteroseismology. Asteroseismic analysis of core rotation in red giants observed by *Kepler* has shown that our current modelling of the transport of angular momentum over-predicts core rotation rates by orders of magnitude. Which mechanism drives the required additional angular momentum transport, and its efficiency as stars evolve has not yet been identified. A magnetic field could be the cause (Mestel et al., 1987; Charbonneau et al., 1993; Maeder et al., 2005), but to explain the observations those fields would have to impact radiative zones, which is not expected for the types of surface fields we currently observe in stars. Fortunately, asteroseismology can also reveal the presence of magnetic fields buried deep below the outer convection zone in evolved stars. HAYDN could provide insight into the prevalence of such fields, and whether they correlate with internal rotation for stars sharing similar age and chemical composition.

Inference on both rotation and magnetism requires precise measurements of individual mode frequencies; The associated signatures can cause shifts that are on the order of 0.1% of the unperturbed frequency. Alongside investigating the total number of stars in which we could detect solar-like oscillations, I also quantified the detectability of the signatures of core rotation and magnetism on $\ell = 1$ modes.

The following chapter is adapted from a draft for publication, as such there is some repetition of Chapter 3 in Section 5.4. The work is in collaboration with the HAYDN science team lead by Prof. Andrea Miglio, who provided the population simulation of NGC 6397 (thanks to Dr. Léo Girardi and Dr. Diego Bossini) and predictions for the instrumental noise for each simulated star (thanks to Dr. Reza Samadi). The remaining work is all my own, as is all of the text.

5.1 NGC 6397; Asteroseismic Potential for Investigations of Core Magnetism and Rotation.

5.2 Introduction

As the only observational probe sensitive to the physical conditions below the photosphere of a star, asteroseismology has made significant contributions to our understanding of stellar physics (see Kurtz 2022 for a recent review). The combined observational power of NASA’s TESS (Ricker, 2014) and *Kepler* missions (Borucki et al., 2010) has provided asteroseismic data for stars from the pre-main sequence to the red giant branch. However, these targets span a wide range in metallicity, age and mass (see the catalogues of Silva Aguirre et al. 2017; Yu et al. 2018c; Hatt et al. 2023). This has the unfortunate consequence that we are restricted in our ability to study the dependence of various physical mechanisms on any one stellar parameter. Additionally, the most detailed asteroseismic analysis requires the accurate recovery of individual mode frequencies. Data of the quality required to facilitate such studies make up only a fraction of the available set.

Stellar clusters consist of populations of stars with similar age, initial chemical composition and distance. These shared properties make the stars in such associations excellent candidates for both testing current stellar models, and studying the evolution of stellar properties using asteroseismology. The *Kepler* mission (Borucki et al., 2010) observed four clusters, which have

been the subject of a number asteroseismic analyses. The scientific output of the works ranges from measurements of mass loss along the red giant branch to tests of asteroseismic scaling relations (Stello et al., 2007; Stello et al., 2010; Miglio et al., 2012; Brogaard et al., 2016; Arentoft et al., 2017; McKeever et al., 2019; Tailo et al., 2021; Tailo et al., 2022). However, *Kepler* was not designed for peak performance in dense stellar fields. Pixel sizes were set to capture the flux from field stars, and are too large to isolate single stars in stellar clusters. As a result, flux from nearby stars contaminates measurements of the target star, which affects the detectability of solar-like oscillations. Accordingly, although inference could be made using asteroseismology on global stellar parameters for numerous stars in stellar clusters, accessing detailed information about the stellar interior via individual mode frequencies has only been possible in a small number of targets (Handberg et al., 2017; Brogaard et al., 2021; Brogaard et al., 2023).

Asteroseismic analysis of solar-like oscillators in stellar clusters would provide key insights into the evolution of stellar rotation. In evolved stars, such techniques can be used to probe rotation deep below the photosphere. This is possible via the exploitation of mixed-modes, the result of coupling between modes propagating close to the stellar core and in the outer convective envelope. Measurements of rotationally perturbed mixed-modes in red giants observed by *Kepler* have highlighted a major shortcoming in the current modelling of angular momentum transport. Core rotation rates as inferred by asteroseismology are orders of magnitude slower than those predicted by stellar models (Eggenberger et al., 2012; Eggenberger et al., 2017; Ceillier et al., 2013; Marques et al., 2013; Spada et al., 2016; Ouazzani et al., 2017; Fuller et al., 2019; Mombarg, 2023). Additionally, the average core rotation rate appears broadly consistent from the base of the red-giant branch to near its tip (Gehan et al., 2018a), seemingly at odds with the ongoing contraction occurring in the core. Given this contraction should imply a spin up of the core, to locally conserve angular momentum, the efficiency of the mechanism of angular momentum transport must evolve with the contraction. Unfortunately, catalogues of core rotation rates inferred using asteroseismology are lacking in subgiants, such that it is not possible to observationally constrain the epoch in the stellar lifecycle at which models of stellar

rotation begin to break down. Stellar clusters could provide the first complete view of the evolution of core rotation from the first emergence of mixed modes on the subgiant branch to the red giant branch.

Several mechanisms have been presented as potential solutions to the missing angular momentum problem, including the presence of a magnetic field (Cantiello et al., 2014; Spada et al., 2016; Eggenberger et al., 2019; Fuller et al., 2019; Gouhier et al., 2022; Eggenberger et al., 2022; Moyano et al., 2023). While the magnetic fields we currently have observed in stars using traditional techniques are driven in convection zones, those capable of producing the observed core rotation rates in red giants would have to act in radiative interiors. Such fields are detectable using asteroseismology, and thus far have been measured in a small number of stars (Li et al., 2022a; Li et al., 2023; Deheuvels et al., 2023). The current leading theory explaining the presence of core magnetic fields in red giants is that they are the fossil remnants of magnetic fields driven by convection while the star was on the main sequence. Convectively driven fields are dependent on the gas properties, and as such the metallicity (Amard et al., 2020; Witzke et al., 2023). Therefore, following the evolution of the fossil remnants of a convectively driven magnetic field requires observations of stars of different evolutionary status sharing the same initial chemical composition. These conditions would be met by stars in stellar clusters.

The HAYDN space telescope (Miglio et al., 2021) was proposed in 2023 as the first, if it were to be accepted, asteroseismic mission aimed at observing clusters. In the following work we will provide insight on the amount of asteroseismic information that could be gathered for a stellar cluster identified as a potential target for HAYDN. To that end, we produced realistic synthetic lightcurves for thousands of solar-like oscillators in the cluster NGC 6397, and used these to identify whether oscillations were detectable. For those stars in which we made detections, we determined whether the frequencies of $\ell = 0$ and 2 modes were recoverable using currently available tools. Finally we introduced perturbations due to core rotation and magnetic fields to the $\ell = 1$ modes of a test star at the base of the red giant branch. Varying the scale of the two perturbations, we identified the ranges in magnetic and core rotational splitting which would have a measureable impact on oscillations.

Parameter	Unit	Value
Equivalent pupil diameter	cm	120
Focal length	mm	4125
PSF diameter	μm	26
Pointing Error	$\text{mas}/\text{Hz}^{1/2}$	70
Integration time	s	1.3
Readout time	s	0.1209
Pixel size	μm	10
Pixel scale	arcsec	0.5
Readout noise	e-	30
PRNU	-	1%
ADC	bits	14
Full Well Capacity	ke-	140
Gain	e-/ADU	10

Table 5.1: Proposed set of specifications for the HAYDN mission, used to generate expected noise levels.

5.3 Simulations

5.3.1 Stellar Parameters

During the proposal process for HAYDN, population simulations were performed for a number of stellar clusters (including NGC 6397) using the TRILEGAL code (see Miglio et al., 2021). In short, TRILEGAL functions by drawing fundamental parameters from a selected initial mass function, age-metallicity relation and star formation rate (Girardi et al., 2005). Stars of a given age, mass or metallicity are then recovered from a database of stellar tracks. NGC 6397 was simulated with a metallicity of $[\text{Fe}/\text{H}] = -1.8$ and age of 13.4 Gyrs (see Harris, 1996).

In total, the cluster simulation consisted of 22,248 stars. We identified candidate solar-like oscillators, which included stars from the main-sequence to the horizontal branch. Stars with luminosities exceeding the red edge of the δ Scuti instability strip (according to their effective temperature) were removed. We calculated the associated limiting luminosity according to,

$$L_{\text{red}} = L_{\odot} \left(\frac{T_{\text{red}}}{T_{\text{red},\odot}} \right)^{-1/0.093}, \quad (5.1)$$

with $T_{\text{red},\odot} = 8907\text{K}$ (Houdek et al., 1999; Chaplin et al., 2011b). Taking $T_{\text{red}} = T_{\text{eff}}$ in Equation

[5.1](#) for each star in the simulation, we calculated the associated L_{red} . If the star had luminosity above this limit, we removed it from the sample. This resulted in the removal of 190 stars (see Figure [5.1](#)). The density of mixed modes increases as a star evolves, such that calculating mode frequencies becomes increasingly computationally expensive. Accordingly, we removed stars that had evolved beyond the tip of the red giant branch. This resulted in the removal of an additional 30 stars. There were also a large number of low luminosity, low mass main-sequence stars which were highly unlikely to produce detectable oscillations. To reduce the total number of lightcurves in need of simulation, we set a faint limit on the apparent V-band magnitude for the considered solar-like oscillators at $m_V = 17$, informed by the yields predicted in [Miglio et al. \(2021\)](#). As a result, an additional 15,256 stars were removed, making the final count 6771 stars, with magnitudes ranging from the enforced maxima at 17 to the brightest star at 10.8 (see Figure [5.1](#)).

To simulate the lightcurve of a solar-like oscillator we required the frequencies of the pulsations, alongside other properties such as amplitudes and lifetimes. These are dependent on internal structure, meaning we required a stellar model for every star in the simulated population. To that end, we used Modules for Experiments in Stellar Astrophysics (MESA, [Paxton et al., 2011](#); [Paxton et al., 2013](#)) to calculate a grid of models with a metallicity of $[\text{Fe}/\text{H}] = -1.8 \text{dex}$, and initial masses in the range $0.72\text{M}_\odot < M < 0.77\text{M}_\odot$, according to the stars selected from the TRILEGAL simulation. The input physics was consistent with that in [Rodrigues et al. \(2017\)](#). This included the [Grevesse et al. \(1993\)](#) heavy elements partition. Equations of state and opacities were those of [Rogers et al. \(2002\)](#) and [Iglesias et al. \(1996\)](#) respectively, with low-temperature opacities augmented according to [Ferguson et al. \(2005\)](#). The atmosphere was a [Krishna Swamy \(1966\)](#) model. Convection was treating using mixing-length theory with a mixing length of $\alpha_{\text{MLT}} = 1.9657$. We used $Z = Z_\odot \cdot 10^{[\text{Fe}/\text{H}]}$ to convert between metallicity and mass fraction. The initial helium mass fraction was described by a linear enrichment law with a primordial helium abundance of 0.2485 and a slope of 1.007. Finally, mass loss along the red giant branch was included via Reimers law ([Reimers, 1975](#)), with $\eta = 0.2$.

For the purpose of the detection of solar-like oscillations, the crucial property of the oscilla-

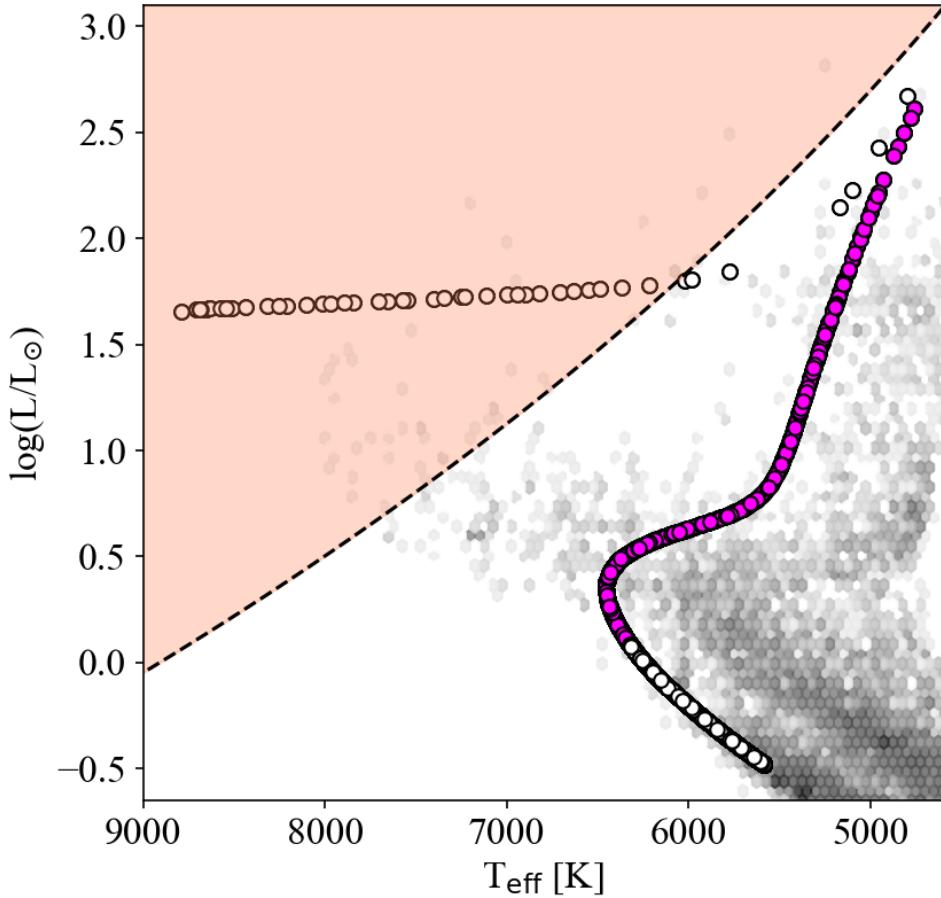


Figure 5.1: HR diagram for selected stars from simulation. The full set of stars output from TRILEGAL is shown in the empty scatter points. Filled points are the solar-like oscillators selected for this work. The black dotted line marks the location of the red-edge of the δ Scuti instability strip. Accordingly, stars in the red shaded region are unlikely to host solar-like oscillations. The background colour shows the distribution of luminosity and temperature in a random draw from Gaia.

tions is their amplitude. These scale with luminosity, mass and effective temperature. The stars in our selection vary in luminosity by $\approx 300 L_\odot$, in T_{eff} by $\approx 2000\text{K}$ and in mass by $\approx 0.05M_\odot$. Accordingly, we matched each star in the TRILEGAL simulation to one of our stellar models by minimizing,

$$\chi^2 = \sqrt{(L_{\text{MESA}} - L_{\text{TRILEGAL}})^2 + (T_{\text{eff,MESA}} - T_{\text{eff,TRILEGAL}})^2}. \quad (5.2)$$

On average the MESA models and the TRILEGAL simulations differed in T_{eff} and L_\odot by less than 0.01%. This would propagate to a difference in mode amplitude of the same order.

5.3.2 Simulated Lightcurves

We calculated the lightcurves using The AsteroFLAG Artificial Dataset Generator 3 (AADG3) which simulates relative flux data for solar-like oscillators (see Howe et al., 2015, for full details). Lightcurves were calculated using the same cadence as the *Kepler* short-cadence data (58.85s), which is suitable for the detection of oscillations in main sequence stars. Star-specific inputs required by AADG3 include the properties of the modes alongside additional background terms required to describe the signal from granulation. To calculate these properties, we followed the general method of Ball et al. (2018), with some adjustments that will be addressed in the following section (Section 5.3.3).

Once the lightcurve based on the intrinsic properties of the star had been calculated, we added white noise consistent with the specifications proposed for HAYDN (as detailed in Table 5.1, see Section 5.3.4). As no telescope is capable of truly uninterrupted observations we introduce gaps in the lightcurves, informing the number and length of these gaps with the distribution of such quantities in *Kepler* long-cadence observations (see Section 5.3.5).

The following analysis splits into two domains. Firstly, we used all 6771 simulated lightcurves to determine in which stars oscillations are detectable, and whether the frequencies of individual $\ell = 0, 2$ modes were recoverable using tools that are currently available. Secondly, we took a test star from the set in which $\ell = 0$ and 2 modes were recovered and inves-

tigated the detectability of seismic signatures of core rotation and magnetism on $\ell = 1$ (dipole) mode frequencies. Magnetism and rotation were only added to this star, and not included in the first step in analysis, given for dipole modes they triple the number of profiles that AADG3 has to simulate (adding $m = \pm 1$). We expect this should not impact the total detection yield, as the total power in the envelope associated with modes remains the same regardless of perturbations to the individual mode frequencies.

5.3.3 Properties of The Unperturbed Oscillations

Unperturbed Mode Frequencies

We computed unperturbed frequencies using GYRE (Townsend et al., 2013), simulating modes of angular degree $\ell = 0$ to 2. Modes with $\ell = 3$ were not included, given they are computationally expensive to calculate in stars near the tip of the red giant branch. Although such modes have been detected in the spectra of red giants observed by *Kepler*, they are rarely used in seismic analysis given their low signal-to-noise. As such, they are unlikely to be of use in the large scale population analysis for which the HAYDN mission is being proposed. GYRE solves the oscillation equations by searching in a grid of possible eigenfrequencies. As in Ball et al. (2018) we varied the number of points in these grids of frequencies according to ℓ . These were set to 800 points for $\ell = 0$, 1000 for $\ell = 1$ and 3000 for $\ell = 2$.

Our simulations included both evolved stars and stars on the main sequence. For the former, using frequency grids with values spaced inversely in frequency is more appropriate (given the presence of mixed modes which repeat at regular intervals in period), whereas for the latter a linear spacing in frequency is more appropriate (as modes repeat at regular intervals in frequency). To determine in which stars we should grid inversely in frequency, we calculated the mixed mode density, $\mathcal{N} = \Delta\nu / (\nu_{\max}^2 \Delta\Pi_1)$, where $\Delta\nu$ is the large frequency spacing, ν_{\max} is the frequency at maximum power and $\Delta\Pi_1$ is the period spacing for dipole modes. The mixed mode density approximates the number of g-modes we should expect per $\Delta\nu$. For stars with $\mathcal{N} > 1$, we used inverse gridding for non-radial modes. Radial modes are never mixed, and thus we

Star Type	γ	α	β
Main Sequence	1	-1	1.5
Red Giant Branch	$0.83^{+0.03}_{-0.03}$	$-0.62^{+0.01}_{-0.01}$	$-4.77^{+0.28}_{-0.27}$

Table 5.2: Exponents used in Equation 5.3 for stars on the red giant branch and the main sequence. Exponents for stars on the main sequence are from a manipulation of the equations in Kjeldsen et al. (1995). These are the result of a combination of theoretically derived scaling relations and fits to model stars and observational data. There-in error bars are not listed on the exponents of the fits. Exponents for red giants were determined via a fit to measurements from the Yu et al. (2018c) catalogue.

always use linear gridding.

Mode linewidths, amplitudes

One of the detection modules that we apply to the data (see Section 5.4) functions using predictions for mode amplitudes as a function of v_{\max} and T_{eff} . The relation used is a manipulation of that given by Kjeldsen et al. (1995), where the luminosity and mass dependence has been replaced by v_{\max} (see Nielsen et al., 2022b). We use the same equation to generate mode amplitudes for the main sequence stars in our simulation (see Table 5.2). However, as stars evolve the scaling relation for mode amplitude given in Kjeldsen et al. (1995) becomes increasingly inaccurate (Stello et al., 2011; Huber et al., 2011). Therefore for the red giants in our population we refit a relation of the form,

$$A_{\max} = A_{\max,\text{bol}} \gamma \left(\frac{v_{\max}}{3090} \right)^{\alpha} \left(\frac{T_{\text{eff}}}{5777} \right)^{\beta}, \quad (5.3)$$

to the observed amplitudes of red giant branch stars reported in Yu et al. (2018c) using the `emcee` package (Foreman-Mackey et al., 2013a). The best fitting exponents are in Table 5.2, alongside the exponents we used for main sequence stars. We did not fit a separate relation to observations of solar-like oscillations in subgiants, given the small number of measurements available. To determine which exponents to use for a given simulated star, we labelled models with central hydrogen abundance less than 10^{-12} as main sequence (Dotter, 2016), the remaining stars were labelled as red giants.

x	a_x	b_x	c_x
α	-3.710×10^0	1.073×10^{-3}	1.883×10^{-4}
Γ_α	-7.209×10^1	1.543×10^{-2}	9.101×10^{-4}
$\Delta\Gamma_{\text{dip}}$	-2.266×10^{-1}	5.083×10^{-5}	2.715×10^{-6}
ν_{dip}	-2.190×10^3	4.302×10^{-1}	8.427×10^{-1}
W_{dip}	-5.639×10^{-1}	1.138×10^{-4}	1.312×10^{-4}

Table 5.3: Parameters for Equation 5.5, according to Ball et al. (2018).

Linewidths were calculated according to Equations (13) and (14) in Ball et al. (2018), in which the linewidth of a mode at frequency ν is calculated via,

$$\ln \Gamma = \alpha \ln \frac{\nu}{\nu_{\max}} + \ln \Gamma_\alpha + \frac{\ln \Delta\Gamma_{\text{dip}}}{1 + \left(\frac{2 \ln \frac{\nu}{\nu_{\text{dip}}}}{\ln \frac{W_{\text{dip}}}{\nu_{\max}}} \right)^2}, \quad (5.4)$$

where α , Γ_α , $\Delta\Gamma_{\text{dip}}$, ν_{dip} and W_{dip} are determined according to the T_{eff} and ν_{\max} of the star in question. That-is, each parameter (taken in the following as x) is approximated as,

$$x = a_x + b_x T_{\text{eff}} + c_x \nu_{\max}, \quad (5.5)$$

where a_x , b_x and c_x were determined via a fit to 92 stars. These are listed in Table 5.3, which is a reproduction of Table 1 in Ball et al. (2018).

As in Ball et al. (2018), to account for the observed reduction in linewidth and mode amplitude with increasing mode inertia ($\mathcal{I}_{n,\ell}$), we divided these values by the parameter $Q_{n,\ell}$,

$$Q_{n,\ell} = \frac{\mathcal{I}_{n,\ell}}{\mathcal{I}_0(\nu_{n,\ell})}. \quad (5.6)$$

Here, $\mathcal{I}_0(\nu_{n,\ell})$ is the mode inertia of a hypothetical radial mode evaluated at a given mode frequency ($\nu_{n,\ell}$). The inertia $\mathcal{I}_{n,\ell}$ is output directly from GYRE. We then calculated $\mathcal{I}_0(\nu_{n,\ell})$ by interpolating the $\ell = 0$ mode inertia as a function of frequency and evaluating at $\nu_{n,\ell}$.

5.3.4 Properties of the noise

The catalogues of stellar parameters generated prior to this work included predictions for the expected noise levels in lightcurves collected by HAYDN, using the telescope specifications detailed in Table 5.1. The associated noise levels were generated using the methodology described in Samadi et al. (2019), which calculates the expected standard deviation on the lightcurve in ppm/hr^{1/2}. This required the effective temperature and magnitude of the stars, which were taken from the catalogues described in Section 5.3.1. Contributions to the noise budget included photon noise, readout noise, quantization noise, background noise and various jitter noise components due to the pointing error (satellite jitter). Finally, the contribution of the flux from nearby stars to the aperture of the target star was added, using the point spread function given in Table 5.1. This required stellar positions, which were drawn according to the observed cluster position (Harris, 1996) and an empirical log(density)-log(radius) relation (see Ferraro et al, in prep). The distance was set at 2.4 kpc (Harris, 1996).

We transformed the predicted noise from ppm/hr^{1/2} to ppm/cadence (σ [ppm/cadence]) and added it to the lightcurves output from AADG3 by a random draw from a normal distribution with zero mean and variance σ [ppm/cadence].

5.3.5 Observation duration and Gaps

Gaps are expected to occur in lightcurves for various reasons, including downlinking data, repointing the telescope and more anomalous causes like issues with detector electronics. These gaps alter the properties of the power spectrum, and can reduce the signal-to-noise of solar-like oscillations (see for example García et al., 2014; Bedding et al., 2022a). The longest uninterrupted observations we currently have access to are those of the nominal *Kepler* mission, which released observations in 90-day long quarters. To simulate realistic gaps to modify our lightcurves we drew 100 random stars from the seismic catalogue of Yu et al. (2018c). For each star, we calculated the average number and duration of the gaps in each available quarter. For each star in our simulation we then drew the total number of gaps and their length from the

resulting distribution across the *Kepler* stars.

The total duration of the lightcurve also has a significant impact on the detectability of solar-like oscillations. A shorter lightcurve will result in a power spectrum with a reduced signal-to-noise and frequency resolution. These impact both the detection of the power excess associated with modes, and the identification of individual mode frequencies (when not properly resolved). To investigate the impact of observation length on the detectability of oscillations in NGC 6397 we calculated lightcurves with four different lengths. The minimum was set at 90 days (the length of a single *Kepler* quarter) and the maximum at one year. For a small subset of stars we calculated lightcurves that were four years in length (these will be discussed in Section 5.6), providing the required resolution to detect the small frequency perturbations associated with magnetic fields and rotation.

5.4 Detection Metrics

5.4.1 The Presence of Oscillations

Given HAYDN would observe thousands of stars, the mission would likely have to employ an automated approach to identify stars in which solar-like oscillations are detectable. Various pipelines have been produced to automate detection, optimized for use primarily with *Kepler* and TESS data (Stello et al., 2017; Hon et al., 2019; Kuszlewicz et al., 2020). In the following we use the pipeline presented in Hatt et al. (2023). This is able to both perform detection and give initial estimates of the global parameters ν_{\max} and $\Delta\nu$.

The pipeline consists of two modules searching for different identifying features present in the spectra of solar-like oscillators. These are;

1. **Power Excess (PE) Module:** This searches for excess power present in the spectrum that is consistent with expectations for a solar-like oscillator and inconsistent with white noise. The module outputs a merit function (the PE merit), identified with the probability that a solar-like envelope is present, as a function of ν_{\max} . This function is normalized such that

it varies between zero (no significant evidence of solar-like oscillations) and unity (clear evidence of solar-like oscillations).

2. Repeating Pattern (RP) Module: This searches for correlations in the lightcurve that can be identified with sound waves crossing the star. Like the PE module, it also outputs a merit function as a function of ν_{\max} . The period of the correlations that occur in lightcurves due to solar-like oscillations is a proxy for $\Delta\nu$. Accordingly, alongside outputting the merit function, the module exploits the associated likelihoods to produce probability densities for ν_{\max} and $\Delta\nu$.

The thresholds on PE and RP merit that were found to maximise the accuracy of the pipeline are 0.77 and 0.73 respectively (Hatt et al., 2023). As such, any star with a PE merit exceeding 0.77 or a RP merit exceeding 0.73 is labelled as a positive detection.

5.4.2 $\ell = 0, 2$ Mode Frequency Recovery

Before fitting mode frequencies we removed the signature of granulation by applying a moving-median filter to the power spectrum. We divided the observed power by this approximate spectrum, which defined the signal-to-noise ratio (SNR). The resulting SNR spectrum of a solar-like oscillator can be approximated as the sum of Lorentzian profiles centered on the mode frequencies. That is,

$$\text{SNR} = \sum_n \sum_\ell \frac{h_{n,\ell} V_\ell}{1 + \frac{4}{\Gamma_{n,\ell}^2} (\nu_{n,\ell} - \nu_{\max})^2}, \quad (5.7)$$

where V_ℓ is the mode visibility, $h_{n,\ell}$ is the mode height, $\Gamma_{n,\ell}$ is the linewidth and $\nu_{n,\ell}$ the mode frequency. We fit Equation 5.7 to the spectra of our simulated oscillators in two steps. For all of the targets in which we detected oscillations we fit the profiles of modes with $\ell = 0$ and 2 using the `pbjam` package (Nielsen et al., 2021). The $\ell = 1$ modes were only fit a test star, drawn from the set in which we could measure the $\ell = 0, 2$ mode frequencies, in which we explored varying rotational and magnetic signatures.

The `pjam` package enables automated fitting of modes with $\ell = 0$ and 2 by setting priors on the locations of mode frequencies informed by the p-mode asymptotic relation,

$$\nu_{n,\ell} \approx \Delta\nu(n + \ell/2 + \epsilon_p) - \delta\nu_{0,\ell}. \quad (5.8)$$

Fitting is divided into two steps; Firstly Equation 5.7 for $\ell = 0$ and 2 is fit to the data, with $\nu_{n,\ell}$ replaced by Equation 5.8. This fit only includes one quadrupole mode per radial mode, which will be preferentially the most pressure dominant. The number of radial orders over which to perform the sum is provided as input by the user. In the following we chose to fit for 12 radial orders per star¹. Mode visibilities are set at $V_{\ell=0} = 1$, $V_{\ell=2} = 0.62$ (Lund et al., 2017). In this step $h_{n,\ell}$ and $\Gamma_{n,\ell}$ are replaced by a single mode width and height, such that the parameters of the model are $\Delta\nu$, ν_{\max} , ϵ_p , $\delta\nu_{0,2}$, H_{env} (the envelope height), Γ_{env} (the envelope width) and Γ_{mode} (the mode width). To perform this fit in a computationally efficient manner, `pjam` takes as input estimates of ν_{\max} , $\Delta\nu$ and T_{eff} , which are used to construct priors. We supplied ν_{\max} and $\Delta\nu$ (and associated uncertainties) from the detection pipeline, alongside the model value of T_{eff} with an uncertainty of 250K. After the spectrum has been fitted using Equations 5.8 and 5.7, the resulting parameters are used to inform priors of a second fit where mode frequencies, heights and widths are allowed to vary.

The `pjam` package can fit $\ell = 0$ and 2 modes even in evolved stars as radial modes cannot be mixed (and so always follow Equation 5.8), and quadrupole modes are expected to be heavily p-dominated. Dipole modes are not included, as they quickly become mixed as stars evolve off of the main sequence, meaning Equation 5.8 could not be used as a prior.

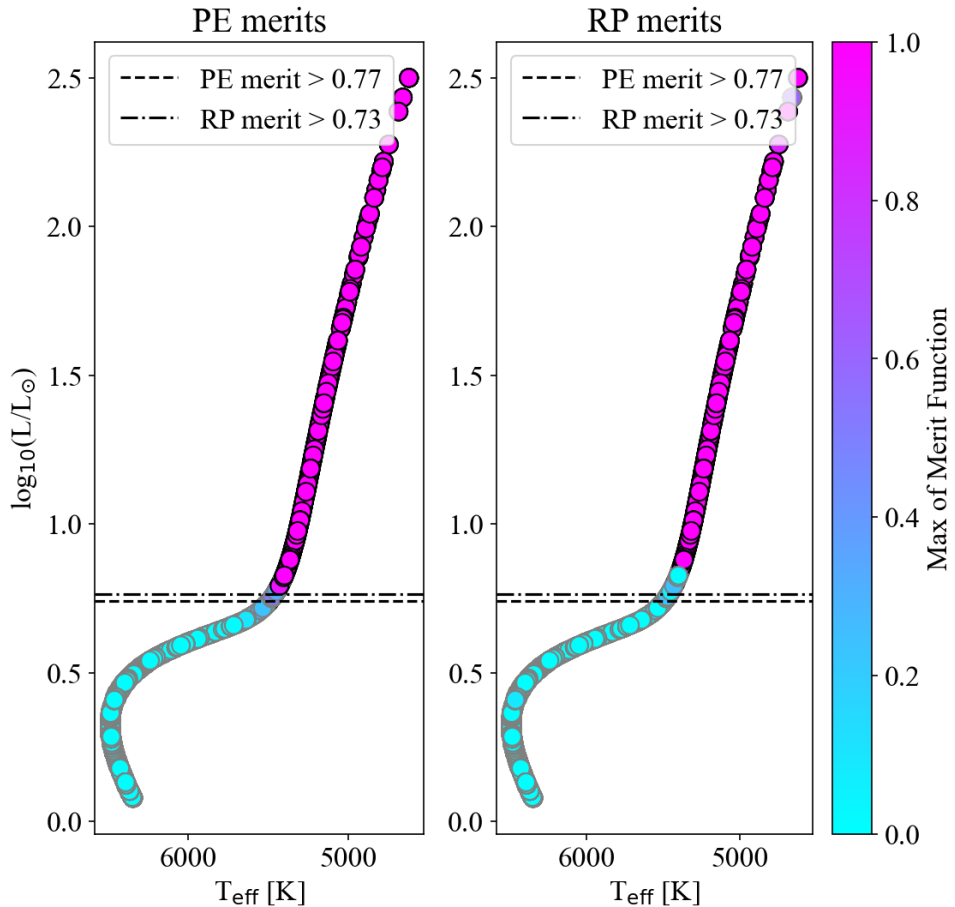


Figure 5.2: HR diagram for the simulated population of NGC 6397 showing detection results made with year-long lightcurves. Right: Points coloured by the maximum of the PE merit function in a given spectrum. Left: Points coloured by the maximum of the RP merit function in a given spectrum. Dashed horizontal line marks the maximum v_{\max} of stars reliably recovered by the PE module. The dotted dashed line is the same for the RP module.

5.5 Results in Unperturbed Spectra

5.5.1 Detection of Oscillations

With a years worth of observations, we found we could detect the solar-like oscillations in a total of 740 targets. The faintest magnitude of the stars in which we made detections was $m_V = 15.4$. This corresponds to a maximum detected ν_{\max} of $363 \mu\text{Hz}$, which for stars in this mass range is at the base of the red giant branch (see Figure 5.2). This maximum is far below the Nyquist frequency for observations made at a 60-second cadence, instead implying the theoretical limit on cadence could be as long as 45 minutes. Detections made in the PE module extended to higher ν_{\max} than those made in the RP module ($363 \mu\text{Hz}$ and $336 \mu\text{Hz}$ respectively). A total of 90 stars have detectable power excess, but do not pass the threshold for identification of $\Delta\nu$.

As expected, the total number of detections increased with observing length. Counts for lightcurves of length 3, 6 and 9 months are shown in Table 5.4 and shown in Figure 5.3. We made an additional 137 detections when increasing the lightcurve length from 3 months to 12 months. The largest increase in number of detections occurred between 3 and 6 months. Although the number of detections in the RP module levels off once the length reaches 12 months (see Figure 5.3), it appears the detections in the PE module still continue to increase. This suggests observations longer than 12-months could result in additional detections, albeit the lack of a response in the RP module means they are unlikely to be high enough SNR to allow measurement of $\Delta\nu$. Surprisingly, a small number of main sequence stars did pass the PE merit threshold in the 9 month, 6 month and 3 month data. There were 9, 3 and 9 stars with $\nu_{\max} > 500 \mu\text{Hz}$ in these sets respectively. For these stars we calculated another 100 realisations of the lightcurves and re-ran the detection pipeline. We found that none of the detections were made again, and so the positive detections were likely the result of chance realisation of the noise. Therefore, to determine the maximum value of ν_{\max} in which HAYDN would perform well in NGC 6397, we do not use these stars. Instead, we sort the detections by ν_{\max} and locate the value below which the difference in successive ν_{\max} values is less than $10 \mu\text{Hz}$. This essentially marks

¹Although this is a larger number than will likely be identifiable in any given spectrum, modes which have very low SNR will not contribute significantly to the likelihood ad thus will not influence the result.

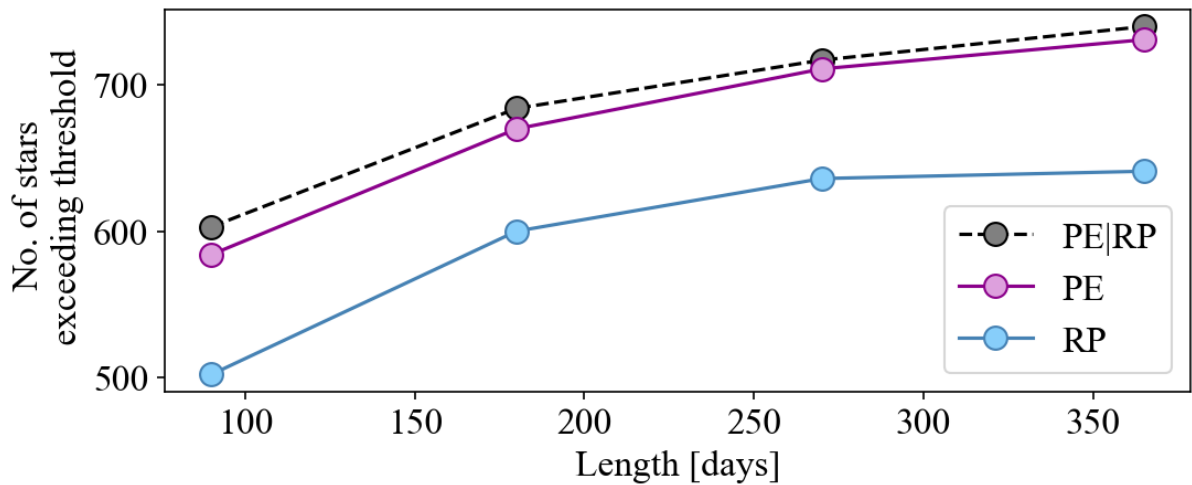


Figure 5.3: Number of stars with PE or RP merit functions exceeding thresholds as a function of observation length.

Observing strategy	PE	RP	Total Unique	Maximum ν_{\max}
1 year	731	641	740	363 μ Hz
9 months	711	636	717	352 μ Hz
6 months	670	600	684	329 μ Hz
3 months	584	502	603	270 μ Hz

Table 5.4: Number of stars exceeding detection thresholds in the PE and RP modules for various lightcurve lengths.

the location on the HR diagram at which oscillations become readily detectable, regardless of noise realisation. The resulting limits are listed in Table 5.4.

We used the values of $\Delta\nu$ and ν_{\max} from the detection pipeline to inform priors when performing the analysis of individual modes. Therefore, if they are inaccurate, we may expect biases in the recovery of mode frequencies. In Figure 5.4 we show the value of the global parameters measured by the detection pipeline against the values from the stellar models. For ν_{\max} , the value measured by the pipeline is within 1σ of the model value for all but one star. The uncertainties reported by the pipeline decrease with ν_{\max} , a result of the increasing SNR. For $\Delta\nu$, the pipeline reports values that are more than 1σ from the model value in 6 stars. As was the case for ν_{\max} , these are at high values of $\Delta\nu$ ($> 20 \mu$ Hz), reflecting the decreased SNR. Indeed, the mean apparent V-band magnitude in the 6 discrepant stars is 15.26, compared to the mean in the remaining stars at 14.04.

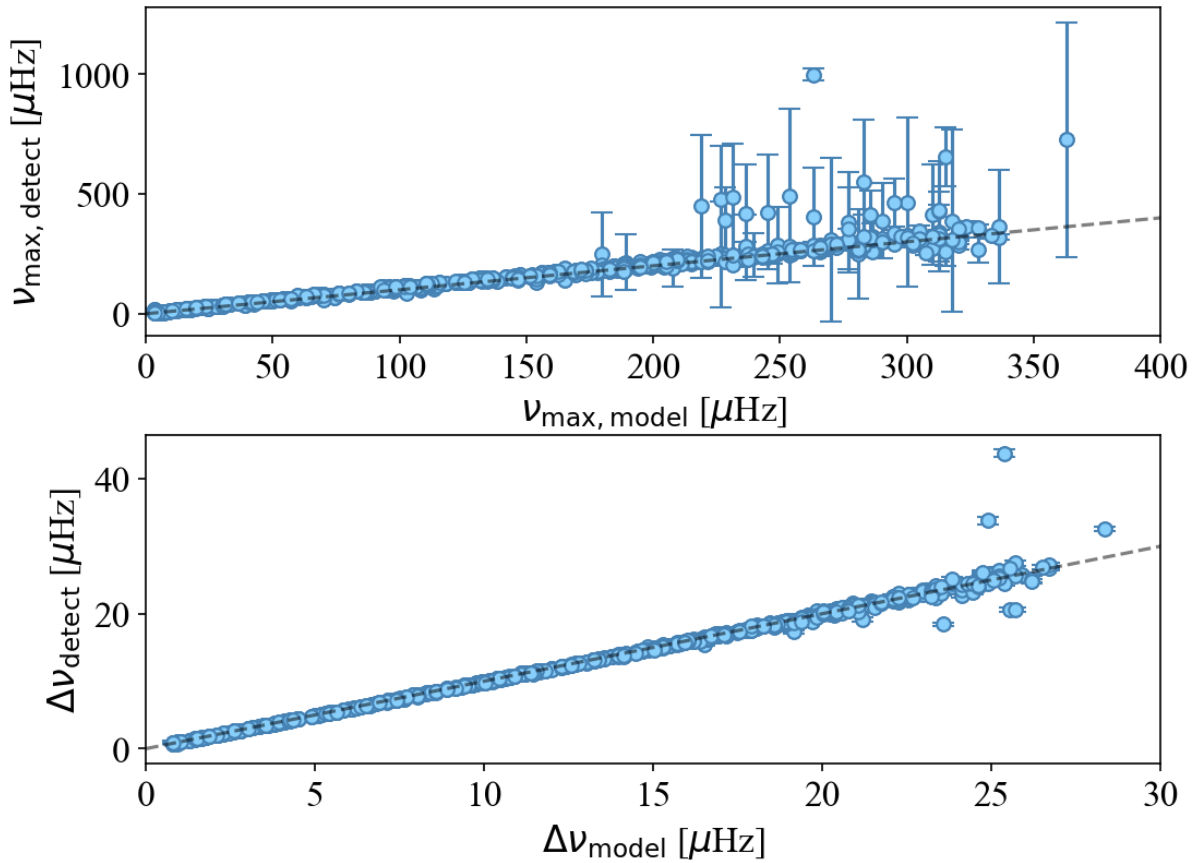


Figure 5.4: Global asteroseismic parameters v_{\max} (top panel) and $\Delta\nu$ (bottom panel) measured by the detection pipeline as a function of the values from the stellar models. Black dotted line is the one-to-one line.

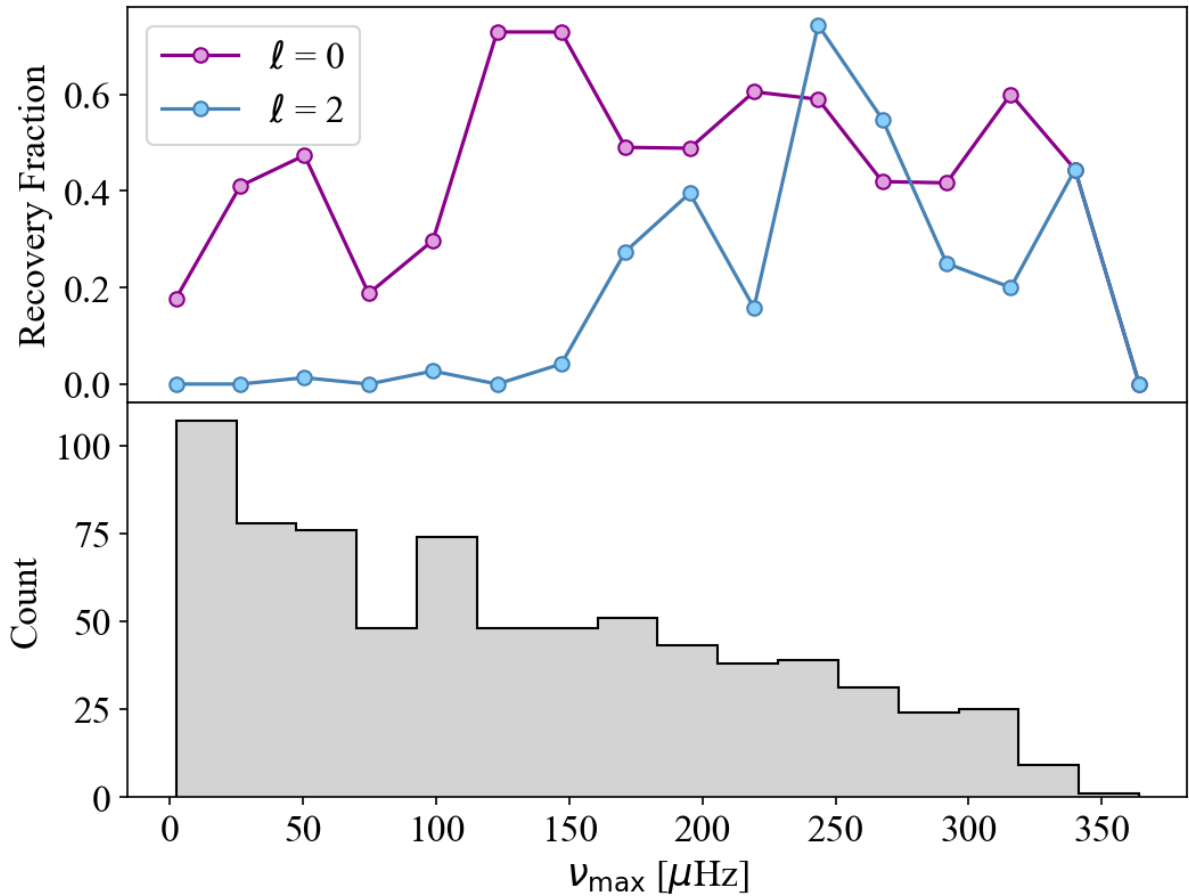


Figure 5.5: Recovery of $\ell = 0$ and 2 frequencies according to the mean difference between model and measured frequencies. Successful recoveries are defined as those in which the average difference between the model and measured mode frequencies is less than the average uncertainty reported by `pbjam`. The top panel shows the fraction of stars in which $\ell = 0$ or 2 modes are recovered as a function of v_{\max} . Fractions are calculated in bins in v_{\max} with a width of 20 μHz . For reference, the distribution in v_{\max} of all of the stars in which we detect the presence of oscillations is included in the bottom panel.

5.5.2 Results: $\ell=0, 2$ Mode Frequency Recovery

We quantified the number of stars in which we correctly recovered the $\ell = 0, 2$ mode frequencies according to the mean difference between the model and measured mode frequencies² ($\langle \nu_{n,\ell,\text{model}} - \nu_{n,\ell,\text{measure}} \rangle$). For radial modes, we found this difference was less than three times the average error as reported by `pbjam`³ (σ) in 322 stars, which have $12 \mu\text{Hz} < v_{\max} < 336 \mu\text{Hz}$. There was no clear dependence between the fraction of stars in which we recovered radial mode

²measured mode frequencies are identified as the mean of the posterior distribution of the mode frequencies from `pbjam`

³This is taken as the standard deviation on the posterior distributions of the individual mode frequencies

frequencies and ν_{\max} , as is shown in Figure 5.5. For the quadrupole modes the difference was less than 3σ in 103 stars, with $70 \mu\text{Hz} < \nu_{\max} < 328 \mu\text{Hz}$. The recovery of $\ell = 2$ mode frequencies does depend on ν_{\max} , as can be seen in Figure 5.5. There-in we find the fraction of stars in which the average difference in model and measured frequency is less than 3σ is consistently below 5% for $\nu_{\max} \lesssim 150 \mu\text{Hz}$. The decrease in the fraction of stars in which we recovered quadrupole mode frequencies with decreasing ν_{\max} is a result of the increased mode mixing in the $\ell = 2$ modes. This both makes the asymptotic p-mode relation used by `pbjam` to inform a prior on mode frequencies less appropriate and reduces the linewidths and mode amplitudes according to the increase in the mode inertia. We note here that the reduction in amplitudes via $Q_{n,\ell}$ (see Equation 5.6) assumes that damping in the envelope dominates over radiative damping in the core. However, for the most evolved giants in this cluster it is likely the radiative damping is dominant. The inclusion of the effect of radiative damping in the cores of these evolved stars may influence conclusions on the detectability of quadrupole modes (Grosjean et al., 2014; and see the review of Belkacem, 2019).

5.6 Detectability of Rotational and Magnetic Signatures

For non-radial modes, rotation and magnetism break the degeneracy between modes of different m for a given n and ℓ , resulting in the appearance of multiplets in the power spectrum. For the rotation rates observed in solar-like oscillators (which are relatively slow), rotation shifts modes proportionally to m , producing multiplets that have a symmetric appearance. For dipole modes, stellar rotation rates are recovered by measuring the separation between components with $m = +1$ and -1 , with the degree of separation increasing with more rapid rotation (see Section 5.6.1). Magnetism, on the other hand, does not generally produce shifts that are proportional to m (see Section 5.6.2). This can result in multiplets with an asymmetric distribution in frequency. The asymmetry of a multiplet is defined as $\delta_{\text{asym}} = \nu_{m=-1} + \nu_{m=+1} - 2\nu_{m=0}$, and has been previously used to identify the presence of magnetic splitting (Li et al., 2022a; Li et al., 2023).

There are four primary features impacting the detectability of rotational perturbations for a

spectrum in which the signal-to-noise is high enough to permit the measurement of individual mode frequencies. Firstly, measurement using dipole frequencies requires identification of modes with $m = \pm 1$, which implies the star must have an inclination $i \gtrapprox 30^\circ$. Assuming an isotropic distribution of stellar inclination angles, this would be the case for 90% of stars in a randomly drawn sample. The rotational splitting must then be large enough that the single Lorentzian profile is no longer a good descriptor of the data. The associated minimum detectable rotational splitting will be dependent on mode linewidth and so will vary on a star-by-star basis. The data must also be collected for long enough that the frequency resolution is finer than the rotational splitting. Finally, rotational splitting which is large enough to be on the scale of the separation between adjacent mixed modes introduces additional difficulty in the mode identification process and can lead to the incorrect assignment of a given mode to a multiplet. The density of mixed modes increases as a star evolves, such that the maximum recoverable rotation rate may decrease as stars climb the red giant branch.

Magnetic perturbations recovered via the asymmetry of multiplet components are subject to similar requirements. For dipole modes, measuring the asymmetry parameter (δ_{asym}) requires constraints on the frequencies of all three azimuthal orders in a multiplet. This is only possible for stars with $30^\circ \lesssim i \lesssim 60^\circ$. Again assuming an isotropic distribution of stellar inclination angles, this condition would be met for $\approx 40\%$ of the observed stars. A significant detection in a single multiplet requires that the asymmetry is larger than the uncertainty on individual mode frequencies. Therefore, detectability is also impacted by the frequency resolution of the data and the linewidth.

We investigated the range of magnetic and rotational perturbation for which we could accurately recover perturbed dipole mode frequencies. To make the recovery of perturbations below the $0.1 \mu\text{Hz}$ level possible, lightcurves exceeding a year in length are preferable. We extended our baseline to four years, matching that of the nominal *Kepler* mission. We selected a test star in which the $\ell = 0$ and 2 modes were recoverable, prioritizing a target near the base of the red giant branch where the mode amplitudes are lowest. The effects of varying the rotation and magnetic parameters were investigated independently. That is, we tested recovering different

rotational signatures in the absence of magnetism before setting a representative rotation rate and exploring the magnetic parameter space.

5.6.1 Simulated Mode Frequencies with Core Rotation

We re-ran AADG3 to calculate 4-year lightcurves for the selected star. Aside from the addition of rotational perturbations, all other inputs were the same as those described in Section 5.3.2. AADG3 includes rotation by augmenting the unperturbed frequencies according to,

$$\nu_{n,\ell,m} = \nu_{n,\ell} + m\delta\nu_{\text{rot},n,\ell}, \quad (5.9)$$

where $\delta\nu_{\text{rot},n,\ell}$ is taken as an input. The selected target is on the red giant branch. The radial rotation profile in such stars can be approximated by considering two domains, informed by the contraction of the core and expansion of the envelope. Therefore, we approximate $\delta\nu_{\text{rot},n,\ell}$ according to,

$$\delta\nu_{\text{rot},n,\ell} = \zeta_{n,\ell}\delta\nu_{\text{core}} + (1 - \zeta_{n,\ell})\delta\nu_{\text{env}}, \quad (5.10)$$

where $\zeta_{n,\ell}$ is dependent on mode inertia as,

$$\zeta_{n,\ell} = \frac{\mathcal{I}_{\text{core},n,\ell}}{\mathcal{I}_{n,\ell}}, \quad (5.11)$$

describing the extent to which a mode is mixed, with $\zeta_{n,\ell} = 1$ as a pure g-mode and $\zeta_{n,\ell} = 0$ a pure p-mode.

We informed the ranges in $\delta\nu_{\text{core}}$ and $\delta\nu_{\text{env}}$ to test using observations from three catalogues (Deheuvels et al., 2014; Triana et al., 2017; Gehan et al., 2018a, see Figure 5.6). These catalogues had a minimum value of $\delta\nu_{\text{core}} \approx 0.1 \mu\text{Hz}$, which we set as our minimum. We were interested in testing whether the maximum recoverable value of $\delta\nu_{\text{core}}$ would be limited by the mixed mode density. Therefore we set the maximum value at the predicted separation between mixed modes at the base of the red giant branch, $\delta\nu_{\text{core}} = 3 \mu\text{Hz}$.

The envelopes of evolved stars rotate far slower than the cores, given the expansion of the

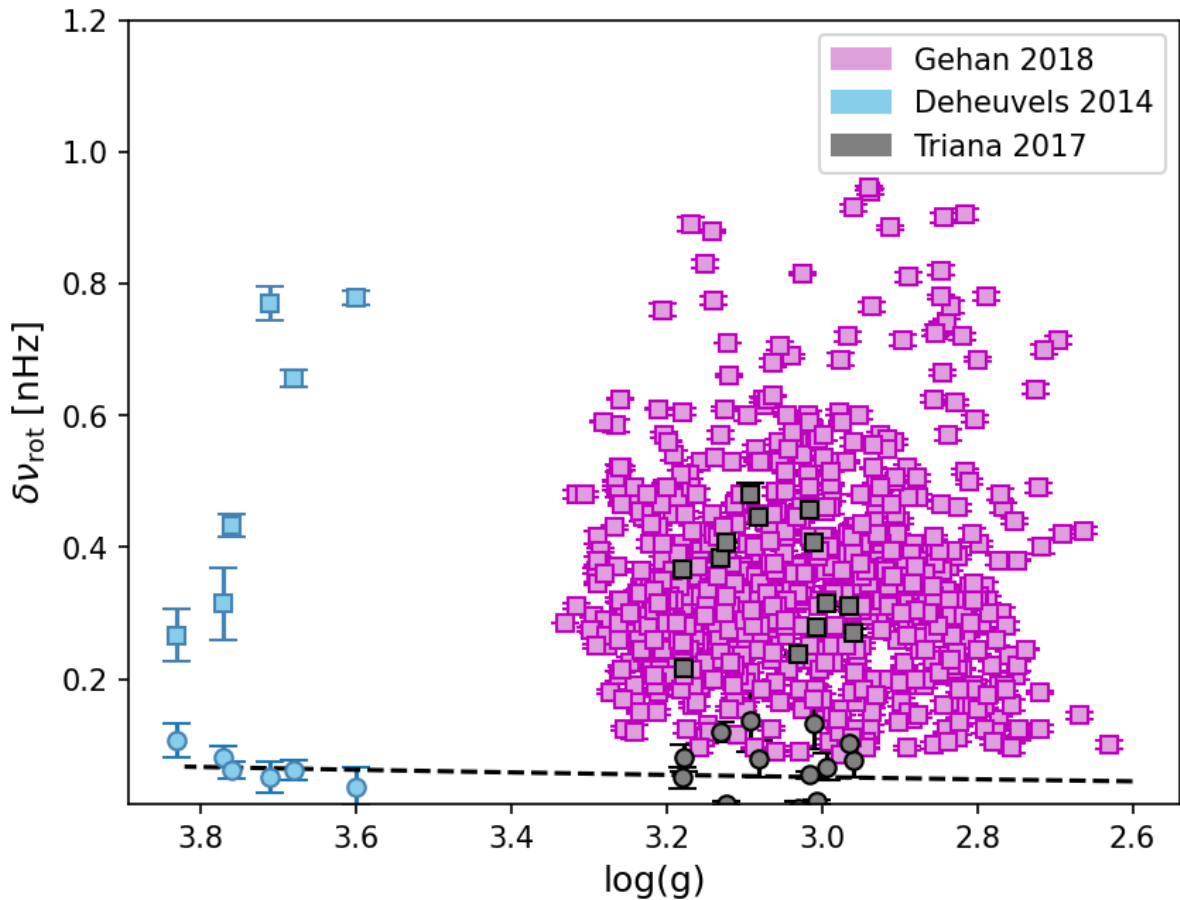


Figure 5.6: Rotational splitting as a function of surface gravity for stars reported in Deheuvels et al. (2014) and Gehan et al. (2018a) and Triana et al. (2017). Squares represent core rotation rates, circles for envelope rotation rates. Line shows the log-linear fit to the data of Deheuvels et al. (2014) and Triana et al. (2017).

outer layers. As such, $\delta\nu_{\text{env}}$ is a difficult quantity to measure, even with four years of *Kepler* data. The only catalogues to report envelope rotation rates in evolved stars are Deheuvels et al. (2014) and Triana et al. (2017). Despite the difference in evolutionary phase, the distribution of envelope rotation is very similar in both works (see Figure 5.6), with a mean of $\delta\nu_{\text{env}} = 0.1 \mu\text{Hz}$ and $0.08 \mu\text{Hz}$ respectively. Accordingly, we gave all models the same envelope rotation rate at $\delta\nu_{\text{env}} = 0.09 \mu\text{Hz}$.

5.6.2 Simulated Mode Frequencies with Core Magnetism

We recalculated lightcurves for the selected star with a 4-year baseline, but set a constant rotational profile and varied the magnetic signature. The value of $\delta\nu_{\text{core}}$ for the test star was

taken as the mean value from Gehan et al. (2018a) for targets with measured ν_{\max} within 20 μHz of the simulated value. The envelope splitting, $\delta\nu_{\text{env}}$, was again set to 0.09 μHz .

The public version of AADG3 does not yet include the option of providing magnetic perturbations. Therefore, we altered the package to allow the user to provide such shifts as input. In the presence of a magnetic field modes are perturbed according to,

$$\nu_{n,\ell,m} = \nu_{n,\ell} + m\delta\nu_{\text{rot},n,\ell} + \delta\nu_{\text{mag},n,\ell,m}. \quad (5.12)$$

Assuming this field is axisymmetric, $\delta\nu_{\text{mag},n,\ell=1,m}$ can be parameterized as (Li et al., 2022a),

$$\delta\nu_{\text{mag},n,\ell=1,m=0} = (1 - a)\delta\nu_{\text{mag}} \left(\frac{\nu_{\max}}{\nu} \right)^3 \quad (5.13)$$

and

$$\delta\nu_{\text{mag},n,\ell=1,m=\pm 1} = (1 + a/2)\delta\nu_{\text{mag}} \left(\frac{\nu_{\max}}{\nu} \right)^3, \quad (5.14)$$

where a is a parameter controlled by the topology of the field and $\delta\nu_{\text{mag}}$ by a radial average of the field strength. The topology parameter can take values in the range $-0.5 < a < 1.0$. We sample three representative values, -0.5 , 0.0 and 1.0 . Observational evidence for a sensible range in $\delta\nu_{\text{mag}}$ is sparse compared to that for $\delta\nu_{\text{core}}$. At time of writing, values have been reported in the range $0.05 \mu\text{Hz}$ to $0.2 \mu\text{Hz}$. We tested 10 values from $0.05 \mu\text{Hz}$ to $0.5 \mu\text{Hz}$ (Li et al., 2022a; Li et al., 2023).

5.6.3 $\ell = 1$ Mode Recovery

To recover the properties of the dipole modes, we used the `pbjam` results to mask regions of the spectrum with frequency within $3\Gamma_{\text{mode}}$ of a $\ell = 0$ or 2 mode. We then fit the remaining spectrum using a sum of Lorentzians. Each radial order consists of three modes with frequencies $\nu_{n,m=0}$, $\nu_{n,m=+1}$ and $\nu_{n,m=-1}$ (I have dropped the $\ell = 1$ subscript as these are all dipole modes). The spectrum is thus,

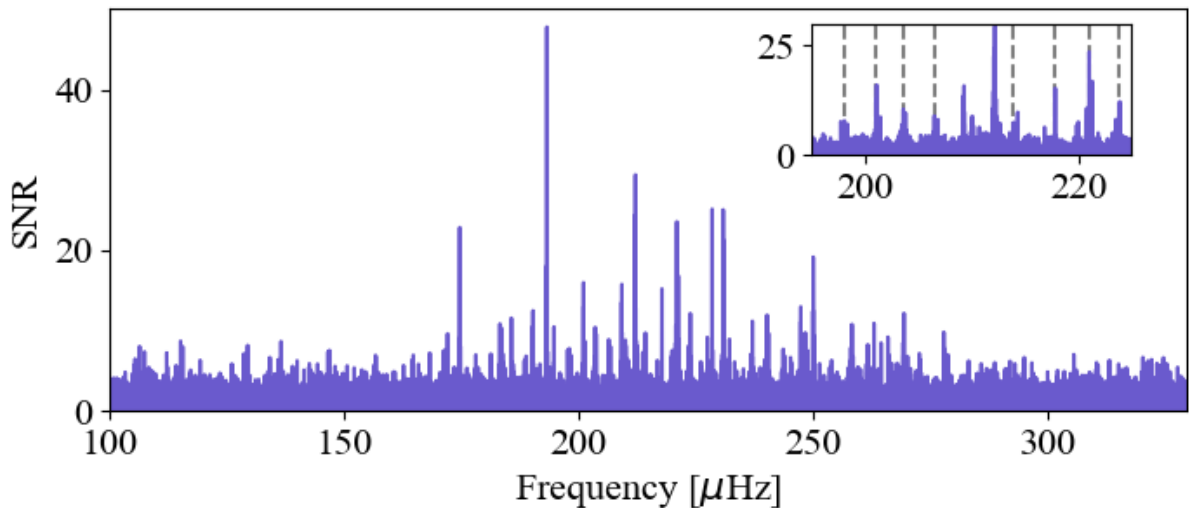


Figure 5.7: Spectrum of the star used to test fitting perturbed $\ell = 1$ modes. Insert is the region in which we fit the perturbed dipole modes. Grey dotted lines show the true values of the $m = 0$ frequencies.

$$\text{SNR} = \sum_n \sum_{m=-1,0,+1} \frac{h_n \mathcal{E}_m(i)}{1 + \frac{4}{\Gamma_n^2} (\nu_{n,m} - \nu_{\max})^2}, \quad (5.15)$$

where $\mathcal{E}_m(i)$ describes the dependence of the relative heights of the modes in a multiplet on the stellar inclination (i). Modes with $m = 0$ have $\mathcal{E}_{m=0}(i) = \cos^2(i)$ and modes with $m = \pm 1$ have $\mathcal{E}_{m=\pm 1}(i) = 1/2 \sin^2(i)$. We parameterise the mode frequencies ($\nu_{n,m}$) according to Equations 5.9 and 5.10 or 5.12 - 5.14 depending on whether we are investigating rotation or magnetism. In either case, the priors on the mode heights, widths and the stellar inclination are the same. These are detailed in Table 5.5 alongside the priors used for parameters associated with mode frequencies. The mean values used to define priors on the unperturbed mode frequencies were set via a visual inspection of the spectra. We set a conservative prior on the unperturbed frequencies with a width of 5% of $\Delta\nu$. This was to account for the fact that magnetic fields may impact the $m = 0$ frequency, such that we can no longer identify the central frequency of a multiplet as the unperturbed frequency, $\nu_{n,\ell=1}$.

Parameter	Prior
Γ_n	$\log \mathcal{N}(\mu = \log(\Gamma_{n,\ell=0,2}), \sigma = 1.0)$
ν_n	$\mathcal{N}(\mu = \nu_{n,\text{guess}}, \sigma = 0.05\Delta\nu)$
$h_{n,\ell=1}$	$\log \mathcal{N}(\mu = \log(h_{\text{gauss},n}), \sigma = 0.4)$
i	$\mathcal{U}(0, \pi/2)$
$\delta\nu_{\text{core},n}$	$\mathcal{U}(0, 3.0)$
$\delta\nu_{\text{mag},n}$	$\mathcal{U}(0, 0.5)$
a	$\mathcal{U}(-0.5, 1.0)$

Table 5.5: Priors used in the fit of the perturbed dipole mode frequencies.

5.6.4 Results: Rotation Recovery

We selected the test star with $\nu_{\max} = 216.8 \mu\text{Hz}$, $T_{\text{eff}} = 5344\text{K}$, $M = 0.77M_{\odot}$ and $i = 45^\circ$. The model used to fit the rotationally perturbed spectrum has five parameters per mode, meaning the computational expense of the fit quickly increases as more modes are included. Therefore, we fit only a selection of modes in the spectrum with the highest signal-to-noise. We identified eight multiplets in the range $\nu_{\max} - \Delta\nu < \nu < \nu_{\max} + \Delta\nu$. The full spectrum and associated window in which the fitting was performed is shown in Figure 5.7.

Figures 5.8 - 5.10 show the recovery of the rotational splitting. A successful recovery for the rotational splitting on a given mode is defined as cases in which the mean of the posterior on $\delta\nu_{\text{rot},n}$ ($\delta\nu_{\text{rot},n,\text{measure}}$) is within three standard deviations of the model value ($\delta\nu_{\text{rot},n,\text{model}}$). Additionally, we require that the standard deviation on the posterior is less than 50% of the mean, which removes cases which are just a replica of the prior. According to these conditions, on average we recover the rotational splitting on five modes per spectrum. We recovered the rotational splitting on all eight modes for four values of $\delta\nu_{\text{core}}$ ($0.85 \mu\text{Hz}$, $1.1 \mu\text{Hz}$, $1.4 \mu\text{Hz}$ and $2.55 \mu\text{Hz}$). We did not correctly measure any of the rotationally split modes in spectra with $\delta\nu_{\text{core}} < 0.4 \mu\text{Hz}$. For these spectra, the posteriors on the rotational splitting for each mode are just a replica of the uniform prior. The sampler has converged on a model with larger linewidth and low inclination, such that the $m = \pm 1$ modes are not contributing significantly to the observed power. Generally, the number of modes that are recovered increases from $\delta\nu_{\text{core}} = 0.1 \mu\text{Hz}$ to $1.0 \mu\text{Hz}$, before levelling out between $1.0 \mu\text{Hz}$ and $2.0 \mu\text{Hz}$, and finally decreasing at values

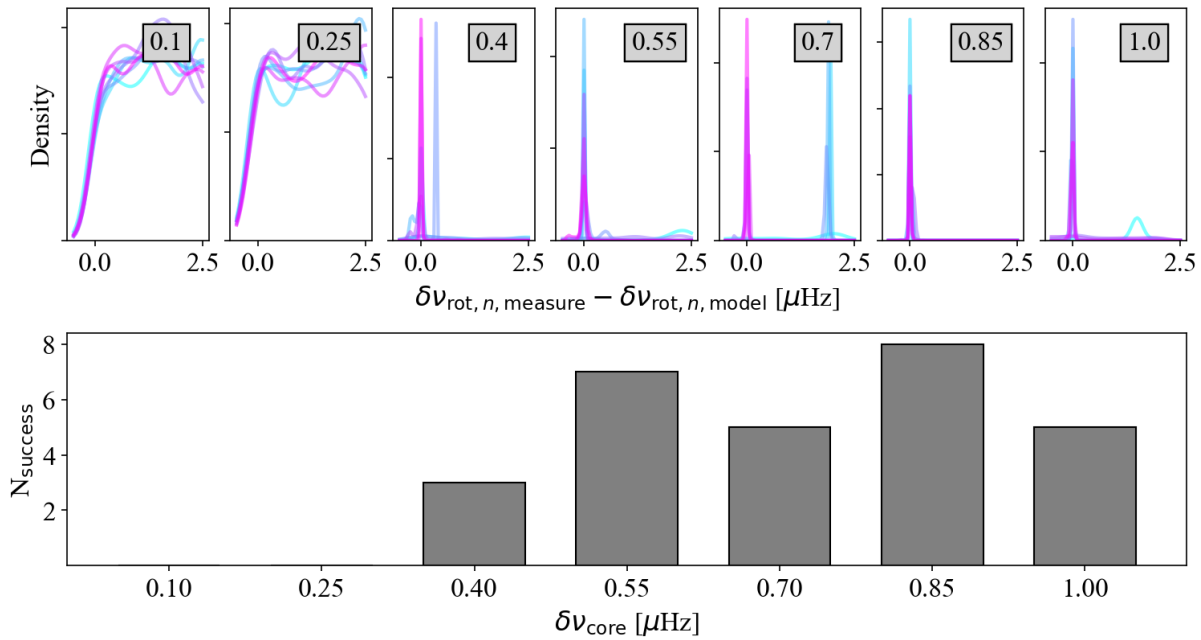


Figure 5.8: Recovery of rotational splitting for $0.1 \mu\text{Hz} < \delta\nu_{\text{core}} < 1.0 \mu\text{Hz}$. Panels in the top row show the posterior on the difference between the model and measured values of $\delta\nu_{\text{rot},n}$ for each value of $\delta\nu_{\text{core}}$. Annotations are included with the value of $\delta\nu_{\text{core}}$ in μHz . Panels on the bottom row show the number of modes in which we measure $|\delta\nu_{\text{rot},n,\text{measure}} - \delta\nu_{\text{rot},n,\text{model}}| < 3\sigma$.

in excess of $2.0 \mu\text{Hz}$. The mode that is the most frequently unsuccessfully recovered is the most mixed of the set, and has the smallest linewidth at $0.01 \mu\text{Hz}$ (the average in the remaining modes is $0.04 \mu\text{Hz}$). Whereas at $\delta\nu_{\text{core}} < 2.0 \mu\text{Hz}$ unsuccessful recovery of rotational splitting is associated with overestimating $\delta\nu_{\text{rot},n,\text{model}}$, at $\delta\nu_{\text{core}} > 2.0 \mu\text{Hz}$ the splitting is more frequently underestimated.

The missing angular momentum problem has that stellar models imply the rotation rates of the cores of red giants should be more rapid than those which we have thus far observed. For this test star we have found that rotation rates both in the range of those previously observed ($< 0.4 \mu\text{Hz}$), and in the more rapid ranges which are predicted by stellar models ($> 2 \mu\text{Hz}$) were not consistently accurately recovered. This implies that care must be taken to establish accurate detection thresholds when exploiting observations of populations of stars to make inference on the distribution of core rotation rates, and its relation to model predictions.

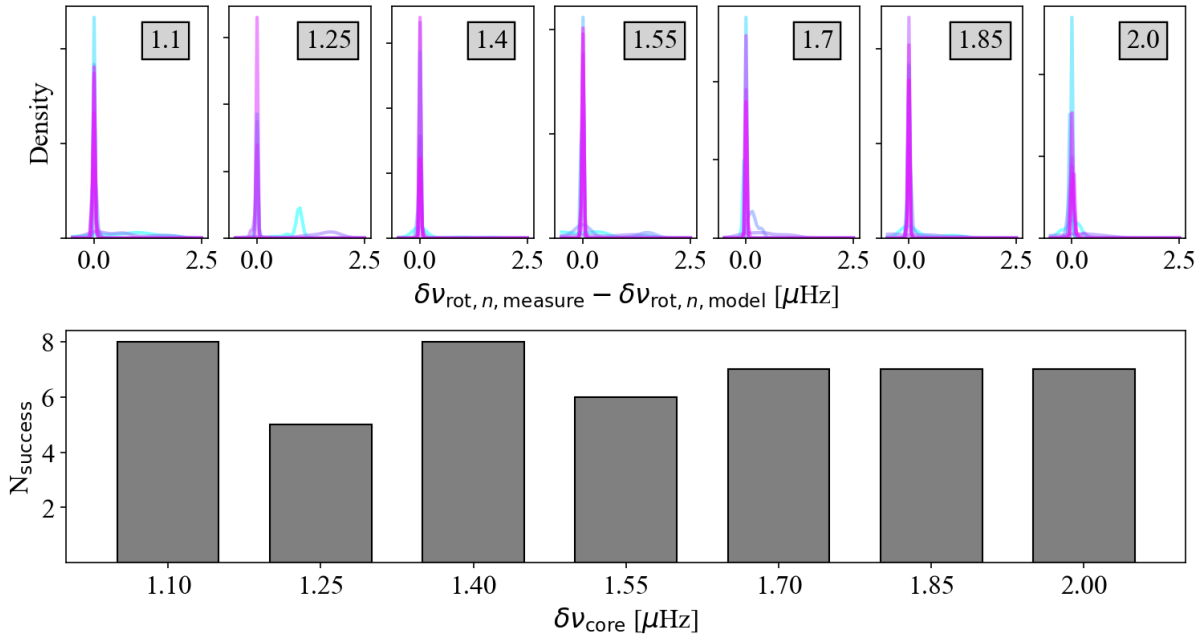


Figure 5.9: As in Figure 5.8, but with $1.1 \mu\text{Hz} < \delta\nu_{\text{core}} < 2.0 \mu\text{Hz}$

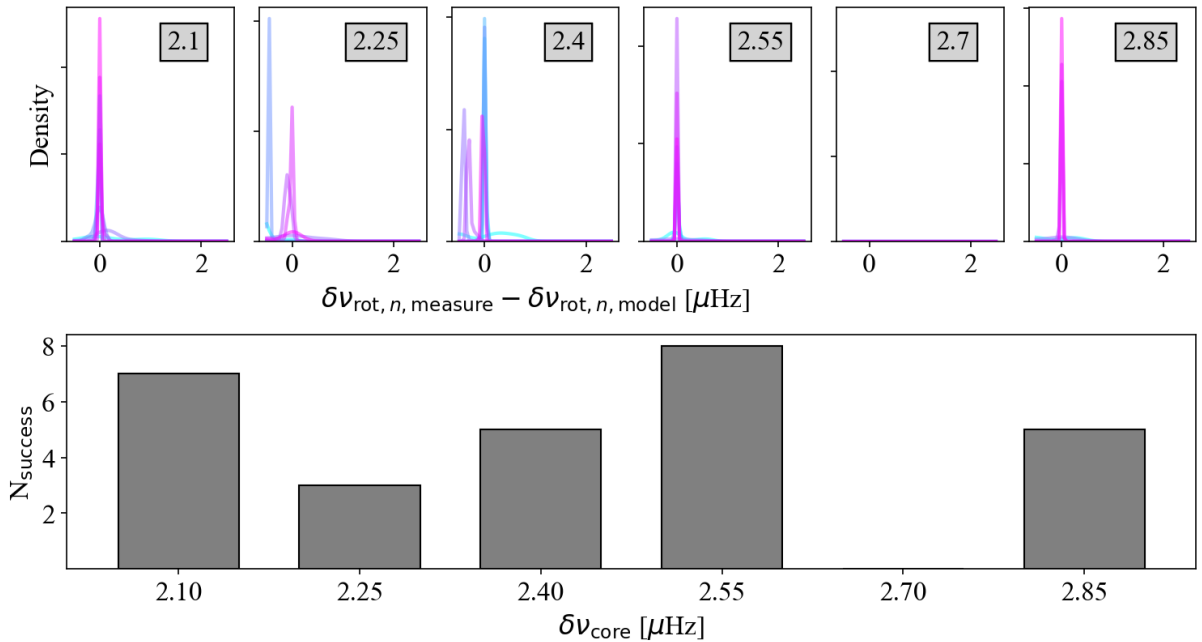


Figure 5.10: As in Figure 5.8, but with $2.1 \mu\text{Hz} < \delta\nu_{\text{core}} < 3.0 \mu\text{Hz}$

5.6.5 Results: Magnetic Recovery

For the test star selected in the previous section, we applied a core rotational splitting of $\delta\nu_{\text{core}} = 0.34\mu\text{Hz}$. Given the degeneracy between $\delta\nu_{\text{mag}}$ and a , we define a successful recovery of the magnetic signature via the frequencies of the individual components of each multiplet ($\nu_{n,m=0,\pm 1}$). That-is, we identify the success of a recovery with the difference between $\nu_{n,m,\text{model}}$ and $\nu_{n,m,\text{measured}}$. For the selected test star, magnetically perturbed mode frequencies were recovered to within 1σ for all of the combinations of $\delta\nu_{\text{mag}}$ and a that we tested. This is shown in the left panel of Figure 5.11. This is true even when the magnetic splitting is larger than the rotational splitting, and the asymmetry is maximised. Although below the scale of the uncertainty on an individual measurement, the measured mode frequencies appear to be systematically overestimated.

We calculated the asymmetry parameter, δ_{asym} , using the posteriors on the parameters defining $\nu_{m=-1}$, $\nu_{m=+1}$ and $\nu_{m=0}$. The mean of the resulting distribution was taken as the measured value of δ_{asym} , with error bars as the standard deviation on the distribution. The right panel of Figure 5.11 shows the recovered and true values of the asymmetry parameter for the most asymmetrically split multiplet in each realisation of the spectrum. We found that in all cases the measured values of δ_{asym} agreed with the true values to better than 1σ . The best agreement between the true asymmetry and the measured asymmetry is achieved with $a = 1$. However, the error bars estimated via the standard deviation on the posterior for δ_{asym} are substantial enough that no measurement is more than 2σ from zero.

Should we accurately measure the dipole mode frequencies for all 322 stars for which we could recover radial mode frequencies, ≈ 130 would be in the correct inclination range to permit measurement of the magnetic asymmetry (assuming an isotropic distribution on i). As we could not make a measurement of asymmetry that was more than 2σ from zero in this test star, the signatures tested here may not appear as significant outliers in this population.

5.7 Conclusions

We generated 6771 realistic simulated lightcurves for solar-like oscillators in the cluster NGC 6397 as they would be observed by the proposed HAYDN mission. We found that if these stars were observed for a year we could detect solar-like oscillations in 740. This was reduced to 603 when only observing for 3 months. In all data sets we were only able to reliably detect oscillations on the red giant branch, in stars with $3 \mu\text{Hz} < \nu_{\max} < 363 \mu\text{Hz}$.

For the lightcurves that were a year in length, we quantified the number of stars in which we could recover the frequencies of the $\ell = 0$ and 2 modes. We measured radial mode frequencies that were less than 3σ from the model values in 322 stars, with $12 \mu\text{Hz} < \nu_{\max} < 336 \mu\text{Hz}$. Quadrupole modes were accurately recovered in fewer stars, for a total of 103 stars with $70 \mu\text{Hz} < \nu_{\max} < 328 \mu\text{Hz}$. These were preferentially the least evolved; For stars with $\nu_{\max} \lesssim 150 \mu\text{Hz}$, the fraction of stars in which the average difference between model and measured mode frequencies was less than 3σ was consistently less than 5%.

We then tested whether rotational and magnetic perturbations to $\ell = 1$ modes would be detectable in a test star in which we could recover $\ell = 0$ and 2 frequencies. We selected a star at the base of the red giant branch, with $\nu_{\max} = 216.8 \mu\text{Hz}$, fitting the rotational splitting in 8 modes. We found that rotational splitting could not be accurately recovered for any modes in spectra with $\delta\nu_{\text{core}} < 0.4 \mu\text{Hz}$. This is surprising, given the average mode linewidth for these modes is a factor of ≈ 10 smaller than $\delta\nu_{\text{core}}$, at $0.03 \mu\text{Hz}$. For $\delta\nu_{\text{core}}$ from $0.4 \mu\text{Hz}$ to $2.0 \mu\text{Hz}$ the number of modes with accurately recovered rotational splitting increased. Beyond this the number of modes in which we could accurately measure the rotation decreased on average.

We tested whether the frequencies of magnetically perturbed modes could be recovered in the test star, when setting a rotational splitting consistent with that reported in the literature. We applied perturbations with values of a of -0.5, 0.0 and 1.0, and $\delta\nu_{\text{mag}}$ in the range $0.05 \mu\text{Hz} < \delta\nu_{\text{mag}} < 0.5 \mu\text{Hz}$. To quantify how well the perturbations could be recovered, we fit the same eight modes as were considered for the investigation of the signature of rotation. We found that we could measure the resulting perturbed mode frequencies to within 1σ in all the cases tested. The asymmetry between modes in multiplets has been used to identify spectra in which

a core magnetic field may be altering mode frequencies. Therefore, we identified whether the associated asymmetry parameter, δ_{asym} , was correctly measured in the spectra. We found that although it was recovered to within 1σ of the model value, the measured value was less than 2σ from zero in all cases. This implies that although we could infer whether a magnetic feature was present in this test star, should this signal be buried in a population of hundreds of stars it may not be flagged as significant enough to warrant further investigation.

The HAYDN mission marks the next big step in our understanding of stellar evolution. In this work we have shown how observations of just one cluster (NGC 6397) will provide information rich spectra for hundreds of solar-like oscillators. We achieved this using tools that are currently readily available, such as the open-source mode recovery code `pbjam`. In future, we should expect such packages and the methods they exploit to progress even further, enabling the recovery of mode frequencies in even more stars. Additionally, NGC 6397 is far from the brightest of the candidate clusters suggested as good targets for observation. Therefore we can expect future work to confirm HAYDN as capable of having an asteroseismic yield rivalling current missions, with stars selected specifically to enable inference on the evolution of various stellar internal properties.

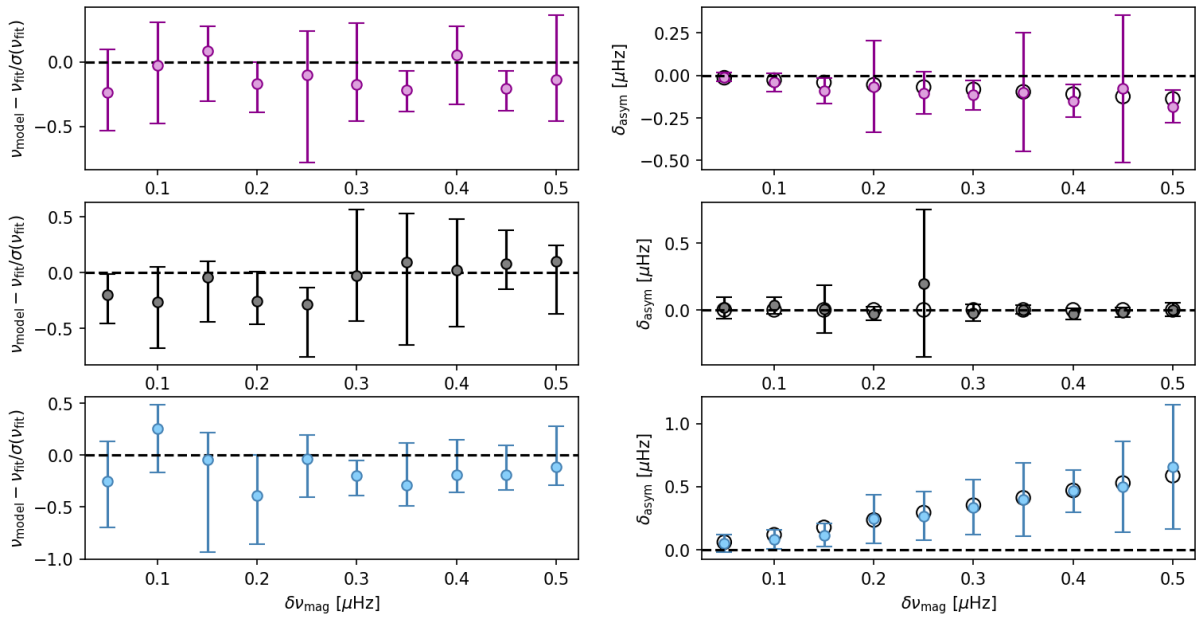


Figure 5.11: Diagnostic plots for the recovery of magnetically perturbed modes. Plots in the left-hand column are the average difference in the model and measured frequencies as a fraction of the measurement uncertainty, $\sigma(\nu_{\text{fit}})$. From top to bottom these are for perturbations with $a = -0.5, 0$ and 1 . Plots in the right hand panel are in the same order in a . These panels show the recovery of the asymmetry parameter, δ_{asym} . Empty circles are the true value.

Chapter 6

Rotation and Magnetism

This chapter is a reformatted version of a draft for publication that was submitted to the journal Monthly Notices of the Royal Astronomical Society and is currently pending reviewer comments. Section 6.2.2 was written by Dr. Martin Nielsen, and Dr. Joel Ong provided the first paragraph of text under the subheading ‘Priors on $\Delta\Pi_1$, p_L , p_D , ϵ_g and $\delta\nu_{01}$ ’ in Section 6.2.3. The code used to generate the stretched échelles used in the following was provided by Dr. Joel Ong.

6.1 Introduction

Magnetic fields play a critical role in stellar evolution. The prevailing theory regarding those which are observed in the Sun and other main-sequence solar-type stars is that they are generated by a dynamo process. This mechanism is, crucially, dependent on the interplay between turbulent convection and differential rotation (Noyes et al., 1984). Convection is supported at various phases in the lifecycle of low to intermediate mass stars, providing several avenues for the formation of a magnetic field. Magnetic fields have been invoked as a possible solution to many open problems in stellar evolution (see Brun et al. 2017 for a review). Notably, a magnetic field could transport angular momentum from the core to the outer envelope, reducing the degree of differential rotation occurring in evolved stars (Cantiello et al., 2014; Spada et al., 2016;

Eggenberger et al., 2019; Fuller et al., 2019; Gouhier et al., 2022; Eggenberger et al., 2022; Moyano et al., 2023). This could resolve the observed discrepancy between predicted rotation rates in the cores of evolved stars and those observed, the latter being (at best) two orders of magnitude too small (Eggenberger et al., 2012; Marques et al., 2013; Ceillier et al., 2013).

Given magnetic fields in the outer layers of stars can be detected in light curves due to the manifestation of this field as star-spots, most detected stellar magnetic fields in convection zones are sun-like in nature. However, a magnetic field capable of producing observed red giant branch (RGB) rotation rates would need to operate near the stellar core (Maeder et al., 2014). Core convection is expected in stars with masses above $\approx 1.1M_{\odot}$ during the main sequence (MS) (Kippenhahn et al., 1990). It is possible for these fields to remain stable as the star evolves off of the main-sequence, where the interior becomes radiative (Emeriau-Viard et al., 2017; Villebrun et al., 2019; Becerra et al., 2022). Even without the presence of a convective core on the main sequence, it is possible to create a magnetic field in stably-stratified zones via a Taylor-Spruit dynamo or related processes (Spruit, 2002; Fuller et al., 2019; Eggenberger et al., 2022; Petitdemange et al., 2023).

Asteroseismology, the study of stellar pulsations, offers the only probe sensitive to near core regions. Solar-like oscillations come in two types, propagating in two largely distinct regions. In the surface convection zones, turbulent motion drives acoustic oscillations known as pressure or p-modes. Closer to the core, strong density stratification supports buoyancy oscillations, gravity or g-modes. When the frequencies of p and g-modes approach each other, the two types of modes can couple forming what is known as a mixed-mode (Unno et al., 1989). Sharing properties of both the pure p and g modes, mixed-modes are both sensitive to conditions near the stellar core and the surface. Mode amplitudes reach a maximum about a characteristic oscillation frequency (ν_{\max}) that scales with the acoustic cut off. On the main sequence, the maximum g-mode frequency is significantly lower than ν_{\max} , such that mixed modes are not excited to observable amplitudes. As a star evolves off of the MS onto the RGB, ν_{\max} decreases in response to the expansion of the outer layers. Concurrently the core contracts, increasing the density of g-modes. As ν_{\max} approaches the maximum frequency of the g-modes, mixed modes

become increasingly observable. The *Kepler* telescope (Borucki et al., 2010) observed a large number of evolved stars with high-precision photometry, such that we are able to measure mixed modes in thousands of stars (Mosser et al., 2014; Vrard et al., 2016; Kuszlewicz et al., 2023).

The presence of a magnetic field within the region where modes propagate has been shown to perturb mode frequencies (Gough et al., 1990; Goode et al., 1992; Takata et al., 1994; Hasan et al., 2005; Mathis et al., 2021; Bugnet et al., 2021; Li et al., 2022a; Mathis et al., 2023). This owes both directly to the introduction of the Lorentz force into the equations of stellar oscillation and indirectly by impacting the properties of mode cavities. Unlike rotation, magnetic fields are not, in general, azimuthally symmetric. As such, the degree to which a mode is perturbed is dependent both on field strength and its geometry and topology (Gomes et al., 2020; Mathis et al., 2021; Bugnet et al., 2021; Loi, 2021). Alongside identifying the presence of a magnetic field, asteroseismology can put key constraints on field strength and structure. The theoretical tools required to exploit the spectra of evolved stars in such a way have only just been established. Furthermore, the size of the parameter space involved with fitting even unperturbed mixed modes makes the problem computationally expensive and contingent on well-informed priors (Kuszlewicz et al., 2023). Even more free parameters are required when considering perturbations, amplifying the issue. As such, only the cases with the strongest magnetic signatures have thus far been analysed. Accordingly current catalogues of core magnetic fields are very limited, numbering 24 stars at time of writing (Li et al., 2022a; Li et al., 2023; Deheuvels et al., 2023).

In this work we will investigate the perturbations caused by core rotation and magnetic fields using a sample of 302 low luminosity RGB stars observed by *Kepler*. In section 6.2 we describe how the sample is selected from the > 16000 RGB stars in Yu et al., 2018a (hereafter Y18). We then go on to fit a perturbed asymptotic expression to the power spectra. To enable a large scale fitting without the problem becoming computationally intractable, we construct priors on the perturbed quantities. This is done via a novel method of exploiting stretched period échelle diagrams calculated using the spectrum directly, a tool so far only used on previously measured mode frequencies. In section 6.3 we detail the resulting measurements, before discussing

correlations with fundamental stellar properties in section 6.4.

6.2 Survey Methodology

6.2.1 Target Selection

We used *Kepler* long-cadence light curves, calculating the power spectral density via a Lomb-Scargle periodogram (Lomb, 1976; Scargle, 1982) using the `lightkurve` package (Lightkurve Collaboration et al., 2018).

Of the observable mixed modes present in a given spectrum, those which are gravity-dominated are the most sensitive to core conditions. As the widths of these modes are smaller than their pressure-dominated counterparts (Mosser et al., 2011; Mosser et al., 2015; Mosser et al., 2018; Vrard et al., 2016), they set an upper limit on the frequency resolution we required. For such modes, the linewidths are on the order of $0.01\mu\text{Hz}$ (Yu et al., 2018a; Li et al., 2020) necessitating time series that exceed three years in length. Therefore we restrict ourselves to stars that were observed by *Kepler* for a full 4-years.

For a given radial order and ℓ , rotation breaks the degeneracy between modes of differing azimuthal order, m . To leading order in perturbation theory (i.e. for slow rotation), the degree to which a mode is perturbed by rotation is proportional to m , such that modes of order $m = 0$ are not affected, remaining at the unperturbed frequency. For modes with non-zero m , the magnitude of the perturbation is shared between two modes having azimuthal orders m and m' if $|m| = |m'|$. The sign of m then determines whether the mode increases or decreases in frequency.

Magnetic fields will perturb all components of a multiplet, with (generally) a different shift for all $|m|$ components. The resulting asymmetry in the spectrum of a magnetically perturbed multiplet is distinct, and as such is commonly used to establish a detection. However, the degree to which the shift differs among components is dependent on the topology of the field (see section 6.2.3) and certain configurations result in zero asymmetry regardless of field strength (Loi, 2021; Mathis et al., 2023; Li et al., 2022a). Therefore, we make no selection based on asymmetry but rather focus on the average shift of the multiplet. In the following we used

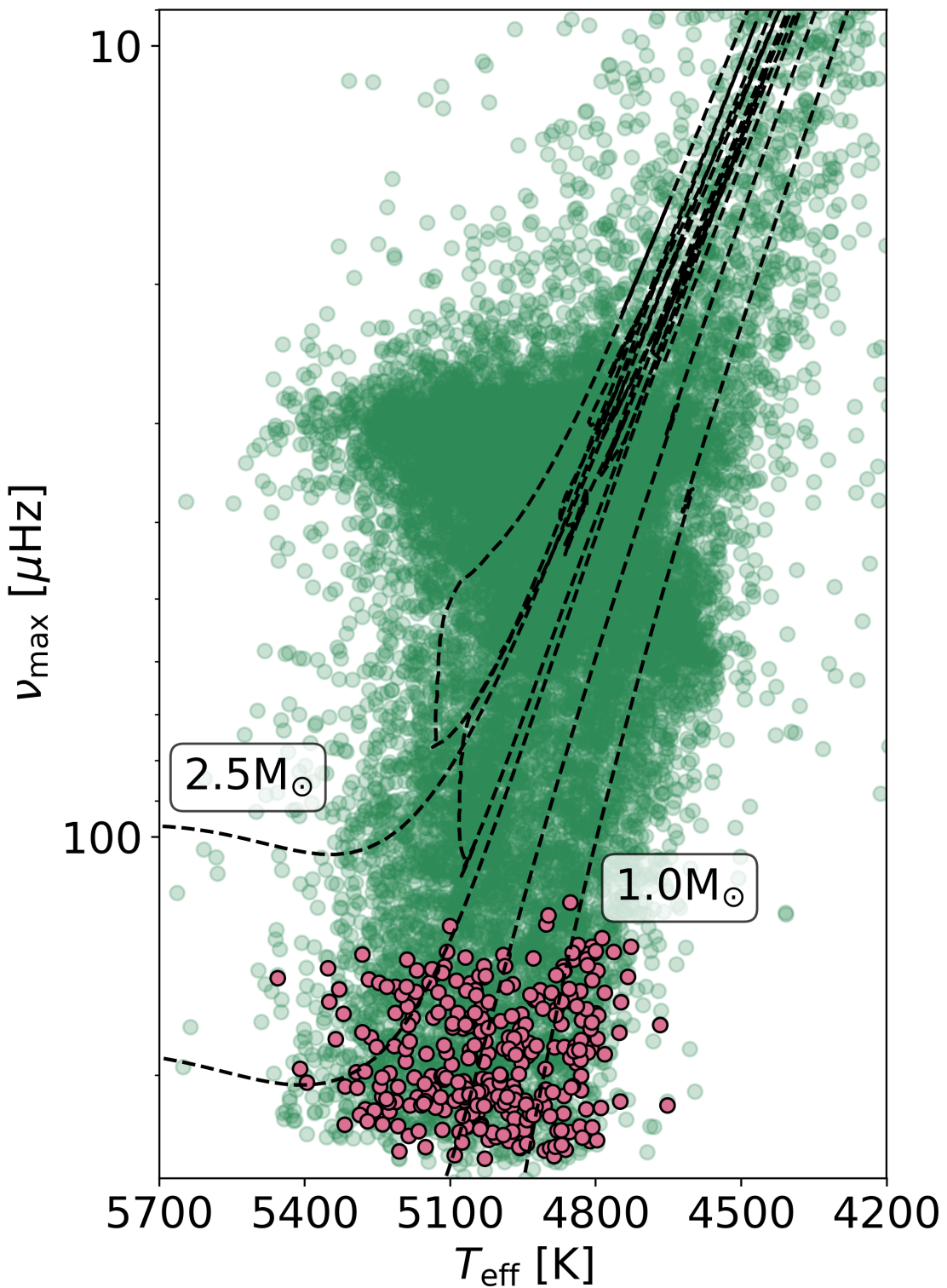


Figure 6.1: ν_{max} and T_{eff} values for the selected sample (pink) compared to those from the catalogue by Yu et al. (2018a) (green). For reference we show the MIST (Choi et al., 2016; Dotter, 2016) evolutionary tracks for $1 M_{\odot}$, $1.5 M_{\odot}$, $2 M_{\odot}$, and $2.5 M_{\odot}$ stars at $[\text{Fe}/\text{H}] = -0.25$ which approximately corresponds to the median metallicity of the selected sample, as reported in table 2 of Yu et al. (2018a).

modes of angular degree $\ell = 1$ (dipole modes, see section 6.2.3), such that multiplets consist of 3 components ($m = 0, \pm 1$). Given all components of the multiplet contain information about the magnetism, we restricted ourselves to targets where-in we could visually identify all three peaks for a given $\ell = 1$ mode. This occurs at intermediate inclination, approximately in the range $30^\circ < i < 60^\circ$.

Finally, as a star evolves along the RGB, the mixed mode density ($\mathcal{N} = \Delta\nu/\Delta\Pi_1\nu_{\max}^2$) increases. Once the rotational splitting is of the order of the separation between adjacent mixed modes, identification of multiplet components becomes difficult. Therefore we restrict ourselves to targets with $\nu_{\max} > 100 \mu\text{Hz}$ (implying mixed mode densities in the region of $\mathcal{N} < 10$). The upper limit on ν_{\max} is set by the Nyquist limit in the data at $277 \mu\text{Hz}$. Applying these constraints to the > 16000 targets identified in Y18, we construct a list of 334 stars (see Fig. 6.1).

6.2.2 Data pre-processing

Rather than measuring mode frequencies prior to fitting for the perturbed quantities, we fit the power spectra directly. Given p-modes of angular degree $\ell = 0$ do not couple to g-modes, they will not provide information about core magnetism or rotation. Additionally, mode coupling in modes of angular degree $\ell = 2$ is orders of magnitude smaller than that in $\ell = 1$ modes. As such, we removed the additional power from the $\ell = 0$ and 2 modes (see sections 6.2.2, 6.2.2) prior to fitting a perturbed expression to the spectrum of the dipole modes (section 6.2.3).

Computing the S/N spectrum

The first step in the process is to estimate the background noise level. Here we define the background noise as any power that is not directly attributed to the oscillation modes. For stars on the red giant branch (RGB) the background typically consists of a frequency independent term due to photon noise, two frequency dependent terms due to granulation on the stellar surface, and finally a third frequency dependent term which accounts for any residual, long-term, instrumental variability (see, e.g, Kallinger et al., 2014b).

Here we model the photon noise as a frequency independent, random, variable. Three

frequency-dependent terms as Harvey-like profiles (Harvey, 1985b), following Kallinger et al. (2014b), are introduced to model the signature of granulation. All the terms in the background noise model vary slowly with frequency, and so we bin the spectrum in log-frequency, after which the model parameters are sampled.

We evaluate a set of 100 draws from the model posterior distribution to compute a mean background level on the unbinned frequency grid. We divide the power spectral density (PSD) by the mean background model to obtain a residual S/N spectrum which now only contains the oscillation envelope.

Establishing a mean $\ell = 2, 0$ model

The next step is to remove the contribution of the $\ell = 0$ and $\ell = 2$ modes to the S/N spectrum. This is done by computing a mean $\ell = 2, 0$ model which is then used to obtain a residual S/N spectrum which notionally only contains the $\ell = 1$ modes. The $\ell = 2, 0$ model that we use is consistent with that of Nielsen et al. (2022a) which, to summarize, consists of a set of mode frequencies determined by the asymptotic p-mode relation for the $\ell = 0$ and $\ell = 2$ modes. The spectrum is then approximated as a sum of Lorentzian profiles at these frequencies, modulated by a Gaussian envelope in power setting the mode heights. For simplicity, we set a single width for all modes. To construct the mean $\ell = 2, 0$ model we draw 50 samples from the model posterior distribution, and average the resulting model spectra. The sampling is performed using a principal component based dimensionality reduction method presented in Nielsen et al. (2023).

Dividing the S/N spectrum by the mean $\ell = 2, 0$ model leaves us with a residual spectrum which consists primarily of power due to the $\ell = 1$ modes, any potential $\ell = 3$ modes, and to a lesser extent any residual power remaining due to errors in the $\ell = 2, 0$ model. While this simplifies the sampling of the $\ell = 1$ model posterior distribution, the inference on the core rotation and magnetism is now conditional on the background and $\ell = 2, 0$ models. This means that in the following we neglect any errors due to uncertainty in these models. However, for high S/N red giant stars where the background and $\ell = 2, 0$ model parameters can be precisely

estimated, this is not expected to be a significant contribution to uncertainty on the rotation and magnetic field terms. We also cannot capture correlations between perturbed quantities and the background.

6.2.3 Estimating the $\ell = 1$ model parameters

We then used the remaining S/N spectrum to estimate the posterior distribution of the $\ell = 1$ model parameters. At high radial order, the frequencies of pure g -modes (ν_g) approximately satisfy an asymptotic eigenvalue equation,

$$1/\nu_g \approx \Delta\Pi_1(n_g + \epsilon_g), \quad (6.1)$$

where $\Delta\Pi_1$ is the period spacing for $\ell = 1$ modes, n_g is the g -mode radial order and ϵ_g is the phase offset. To calculate the frequencies of mixed-modes, these pure g -modes must be coupled to the pure p-modes. For this purpose we used the matrix construction of Ong et al., 2021a (see also Deheuvels et al., 2010). That is, mixed modes emerge as the eigenvalues (ω) of the following,

$$\left(\begin{bmatrix} -\Omega_p^2 & \mathbf{L} \\ \mathbf{L}^\dagger & -\Omega_g^2 \end{bmatrix} + \omega^2 \begin{bmatrix} \mathbb{I} & \mathbf{D} \\ \mathbf{D}^\dagger & \mathbb{I} \end{bmatrix} \right) \mathbf{v} = 0, \quad (6.2)$$

where $\Omega_p = 2\pi\nu_p$ and $\Omega_g = 2\pi\nu_g$ are diagonal matrices containing the angular frequencies of the pure p- and g-mode frequencies (ν_p and ν_g), \mathbf{v} is the eigenvector specifying mixed-modes as a combination of pure p- and g-modes, \mathbf{L} and \mathbf{D} are coupling matrices (with elements L_{ij} and D_{ij} respectively). In general, the elements of these coupling matrices vary with their associated p- and g-mode frequencies. We parameterised this frequency dependence as $L_{ij} \sim \omega_{g,j}^2 \cdot p_L$, where p_L is a scalar, and similarly $D_{ij} \sim \omega_{g,j}/\omega_{p_i} \cdot p_D$, where p_D is a scalar. A full motivation for this parameterisation will be provided in Nielsen et al. (in prep.). Therefore, for a given set of pure p- and g-mode frequencies, mixed mode frequencies can be described using the introduction of two parameters, p_L and p_D . For each star we sample these as random, independent variables.

The parameters $\Delta\Pi_1$, ϵ_g , p_L and p_D were used to provide unperturbed $m = 0$ mode frequencies, to which we introduced the perturbations due to core rotation and a core magnetic field. In the presence of slow rotation, as is the case in these red giants, modes are perturbed linearly. Here, we approximate the rotation as happening in the core, ignoring the much slower envelope rotation (Goupil et al., 2013). Under such assumptions, pure g-modes are perturbed according to,

$$\nu'_{m,g} = \bar{\nu}_g + m\delta\nu_{\text{rot},g}, \quad (6.3)$$

where $\bar{\nu}_g$ is the unperturbed frequency and $\delta\nu_{\text{rot},g}$ is the rotational splitting of the pure g-modes. In the following we will drop the subscript g for simplicity.

A magnetic field in the core will also perturb the pure g-mode frequencies. In the following we used models consistent with those established in Li et al., 2022a, which are subject to the constraint that effects of non-axisymmetry of the magnetic field are negligible. Unlike the case of rotation, a magnetic field will also impact the $m=0$ modes, such that we have,

$$\delta\nu_{\text{mag},m=0} = (1 - a)\delta\nu_{\text{mag}}\left(\frac{\nu_{\text{max}}}{\nu}\right)^3, \quad (6.4)$$

$$\delta\nu_{\text{mag},m=\pm 1} = (1 + a/2)\delta\nu_{\text{mag}}\left(\frac{\nu_{\text{max}}}{\nu}\right)^3, \quad (6.5)$$

where a is a parameter dependent on the field topology, dependent on an average of the radial field strength weighted by a second order Legendre polynomial. As such, the value ranges between $-0.5 < a < 1$, with the maximum negative value corresponding to a field concentrated about the equator and maximum positive values corresponding to a field concentrated at the poles. A full inversion for the structure of the field is not possible, given the degeneracy between fields of different spatial scales (see Loi, 2021; Mathis et al., 2023). The parameter $\delta\nu_{\text{mag}}$ is dependent on an average of the radial field strength (see section 6.4.2). It should be noted that the assumption of non-axisymmetry are met only when the ratio of the magnetic to the rotational splitting is less than one.

Our total model for the perturbed pure g-mode frequencies is thus,

$$\nu'_m = \bar{\nu} + m\delta\nu_{\text{rot}} + \delta\nu_{\text{mag},m}. \quad (6.6)$$

Given values for the parameters $\Delta\Pi_1$, ϵ_g , p_L and p_D , we may then calculate the resulting mixed-mode frequencies by performing mode-coupling calculations via equation 6.2 for each m separately, linearly perturbing the pure g-mode frequencies as above to describe core rotation and a core magnetic field. For this purpose, we neglect the effects of rotation and magnetism on the pure p-modes, which are largely insensitive to the core.

The final additional parameter required to describe the mode frequencies is the $\ell = 1$ small frequency spacing ($\delta\nu_{01}$), which describes the deviation between the pure p-mode $\ell = 1$ frequencies and the midpoint of the adjacent $\ell = 0$ mode frequencies. The complete set of parameters required to describe the frequencies numbers 8 ($\Delta\Pi_1$, p_L , p_D , ϵ_g , $\delta\nu_{01}$, $\delta\nu_{\text{mag}}$, a , $\delta\nu_{\text{rot}}$).

Similar to the analysis in section 6.2.2, we used these frequencies to fit a forward model to the power spectrum, described by a sum of Lorentzian profiles. Linewidths are fixed at the value of the $\ell = 0$ linewidth modified by the ζ function, $\Gamma_{\ell=1} = \Gamma_{\ell=0}(1 - \zeta)$. This accounts for the reduction in linewidth for g-dominated mixed modes, where the mode inertia is large. We assume mode heights can be approximated by the product of the envelope height from the $\ell = 0, 2$ model with the relative mode visibility of $\ell = 1$ modes ($V_{\ell=1}$), which for *Kepler* is $V_{\ell=1} = 1.505$ (Mosser et al., 2012a; Lund et al., 2017). Additionally, the relative power between modes in a multiplet depends on stellar inclination, i . This is frequently accounted for by multiplying mode heights by the factor $\mathcal{E}_{\ell,|m|}(i)$. For dipole modes with $m = 0$ this is given by $\mathcal{E}_{1,0}(i) = \cos^2(i)$, and for $m = \pm 1$ by $\mathcal{E}_{1,|\pm 1|}(i) = 1/2 \sin^2(i)$. We included this in our model, allowing i to vary as a free parameter, setting a uniform prior in the range 0° to 90° .

To estimate the posterior distribution on the parameters of the $\ell = 1$ model we use the `Dynesty` nested sampling package (Speagle, 2020). This relies on establishing a set of prior distributions for each of the model parameters.

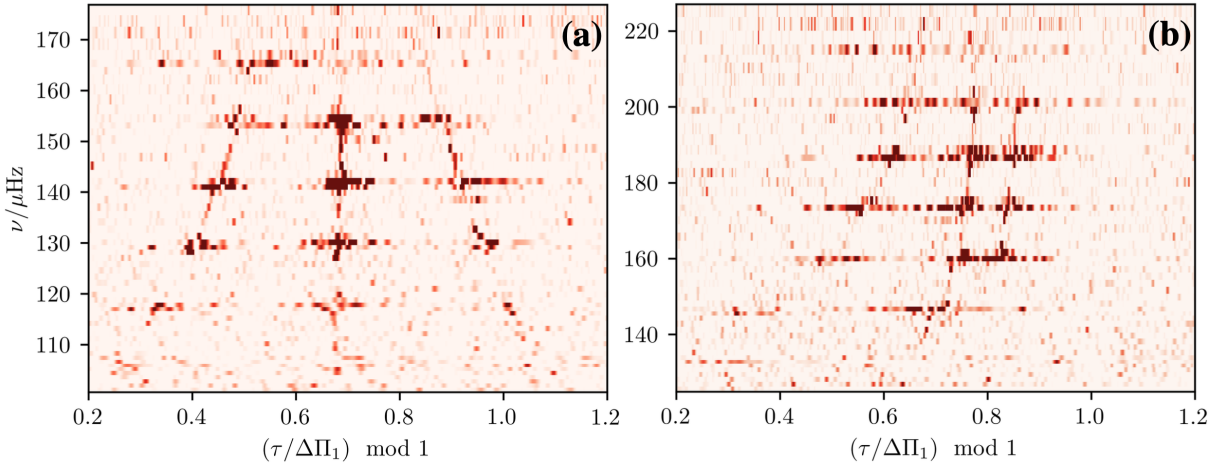


Figure 6.2: Stretched échelle power diagrams for two red giants showing characteristic features of rotation and magnetism. (a): KIC 10006097, showing symmetric rotational splitting. (b): KIC 8684542, from the sample of Li et al. (2022a), showing pronounced asymmetric rotational splitting indicative of core magnetism. The power spectrum indicates excess power along the g-mode ridges that do not correspond to identified and fitted modes in, e.g., their Fig. 3.

Priors on $\Delta\Pi_1, p_L, p_D, \epsilon_g, \delta\nu_{01}$

To construct priors on these parameters, we exploited the so-called ‘stretched’ échelle diagram construction (Vrard et al., 2016). In the asymptotic approximation, mixed modes are the roots of the characteristic equation

$$\tan \theta_p(\nu) \tan \theta_g(\nu) - q(\nu) = 0, \quad (6.7)$$

where q is a coupling strength (in most cases approximated as a constant), and θ_p, θ_g are smooth functions of frequency constructed such that at pure p- and g-mode frequencies ν_p and ν_g ,

$$\theta_p(\nu_p) = \pi n_p; \text{ and } \theta_g(\nu_g) = \pi n_g. \quad (6.8)$$

Given observational access to only mixed modes, but also inferences of notional p-mode frequencies, g-mode period spacings, and coupling strengths consistent with Eqs. (6.1), (6.7) and (6.8), one may invert Eq (6.7) to produce “stretched” frequencies ν_g associated with each mixed mode ν . While several numerical formulations for doing this exist (e.g. Mosser et al. 2012b; Mosser et al. 2015; Mosser et al. 2017; Mosser et al. 2018; Gehan et al. 2018b; Gehan et al.

2021), Ong et al., 2023b prescribe an analytic expression,

$$\frac{1}{\nu_g} \equiv \tau(\nu) \sim \frac{1}{\nu} + \frac{\Delta\Pi_l}{\pi} \arctan\left(\frac{q}{\tan\theta_p}\right), \quad (6.9)$$

assuming that the pure p-modes are affected by neither rotation nor magnetism. Traditionally, these stretching functions are applied to mixed-mode frequencies fitted in advance from the power spectrum. In this work, we instead apply the stretching directly to the frequency coordinate of the power spectrum. Having done so, the morphology of the resulting stretched period-échelle power diagrams correspond directly to the linear expressions Eqs (6.3) to (6.5).

To exploit this diagram to construct priors we note two features:

1. If the correct values of $\Delta\Pi_1$ and q are used to construct the diagram, modes of given azimuthal order should sit in distinct ridges. Therefore, by varying these parameters manually and identifying those which return the most well defined ridges we arrive at initial estimates of $\Delta\Pi_1$ and q .
2. In the absence of a magnetic field, $m = 0$ modes would align vertically in a ridge at the value of ϵ_g . As such, once we have settled on the combination $\Delta\Pi$ and q , we can use the central ridge as an estimate of ϵ_g .

We varied these parameters by hand using the interactive tool introduced in Ong et al. (2023a).

We show examples of the resulting power diagrams in figure 6.2.

Priors on $\Delta\Pi_1$ and ϵ_g were set according to a normal distribution centered on our estimate from the stretched échelle. Uncertainties on $\Delta\Pi_1$ from methods exploiting stretched échelles are on the order of a few percent (Vrard et al., 2016). The only literature work using stretched échelles to measure ϵ_g is Mosser et al. (2018). There-in the mean uncertainty on ϵ_g is $\approx 30\%$. We also note that previous uncertainty estimates do not account for the presence of magnetic asymmetry. For cases where $m = 0$ components have been significantly perturbed by a magnetic field, the combination of parameters constructing the most vertical $m = 0$ ridge will not be an accurate representation of the true values. In an attempt to quantify this effect, we constructed a mock spectrum with values of $\delta\nu_{\text{mag}}$ and a consistent with those reported for KIC8684542 by Li

et al. (2023) (the full set of asymptotic values used can be found in the appendix). We found that the difference between the injected and recovered $\Delta\Pi_1$ was below the 1% level. The difference between the input $\epsilon_{g,\text{input}}$ and that from the hand tuned stretched échelle was more significant, at approximately 10%, but remained below the mean uncertainty reported in Mosser et al. (2018).

We set the width of the prior on $\Delta\Pi_1$ as 10% of the mean. As previously discussed, the average fractional uncertainty on ϵ_g reported in the literature is $\approx 30\%$ (Mosser et al., 2018). The computational expense associated with nested sampling scales with the volume of prior space, such that setting a very wide prior leads to the calculation becoming infeasible. As such, the width of the prior on ϵ_g was set to 30% of the mean. To ensure our results are not prior dominated, we visually inspected the posterior versus prior distributions on ϵ_g .

Exploiting the stretched period échelles required us to use the asymptotic expression for mixed modes, rather than the matrix formalism used in the sampling. Following Ong et al. (2023b) the value of q evaluated at ν_{\max} can be determined from the matrix coupling parameters as

$$q \approx \frac{1}{\Delta\nu\Delta\Pi_1} \left(\frac{L + \omega^2 D}{8\pi\nu^2} \right)^2 = \frac{1}{\Delta\nu\Delta\Pi_1} \left(\frac{\pi}{2} (p_L + p_D) \right)^2, \quad (6.10)$$

with all frequencies evaluated at ν_{\max} . This expression indicates that, from a single value of q alone, it is not possible to uniquely identify p_L and p_D . However, given they are informed by the internal profile of the star, certain values will be more physically motivated. To identify characteristic values of p_L and p_D for our stars we exploited the grid of stellar models used in Ong et al. (2021b). For a given model star in this grid, values of p_L and p_D were subsequently calculated from the corresponding coupling matrices. Stellar tracks were calculated with masses from $0.8 M_\odot$ to $2 M_\odot$, and Fe/H from -1.0 dex to 0.5 dex.

For a given star, we select stellar model tracks in a mass range consistent with those reported in Y18. We then located models with ν_{\max} in the range $\nu_{\max,\text{obs}} \pm \sigma(\nu_{\max,\text{obs}})$, $\Delta\Pi_1$ in the range $\Delta\Pi_{1,\text{prior}} \pm 0.1\Delta\Pi_{1,\text{prior}}$ and a value of q consistent with that derived from the stretched échelle (to within 10%). The means of the distributions of p_L and p_D in the selected models were taken as the means of the normal distributions we used as priors on p_L and p_D . The widths of these priors were set at 10% of the mean, informed by the average standard deviation on the values in

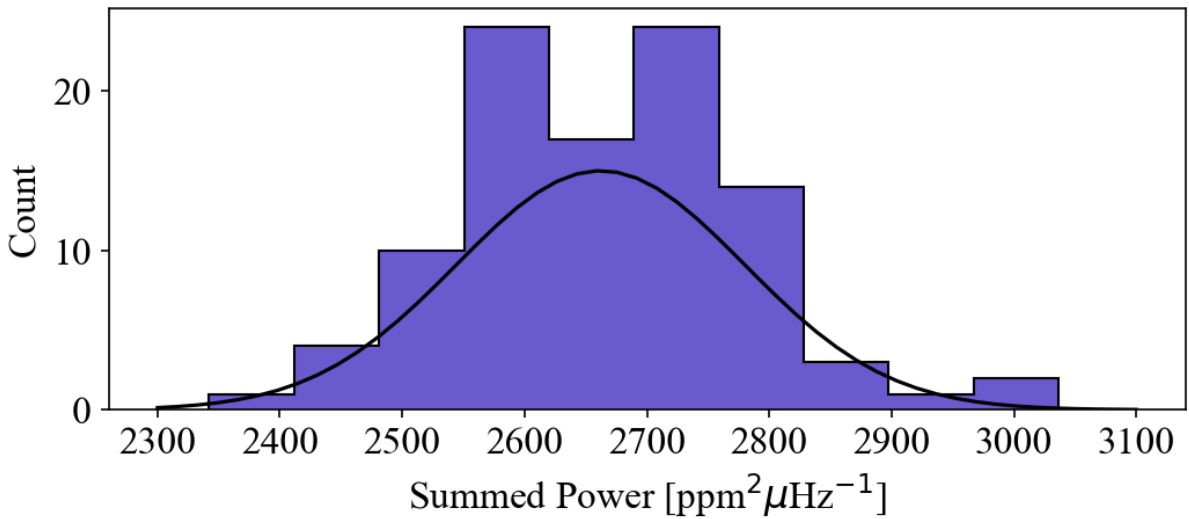


Figure 6.3: Distribution of summed power across ridges defined by $\delta\nu_{\text{rot}} = 0$, $\delta\nu_{\text{mag}} = 0$ and $a = -0.5$ for a white noise spectrum stretched according to the asymptotic parameters of KIC10006097

the selected models.

Priors on $\delta\nu_{\text{mag}}$, a , $\delta\nu_{\text{rot}}$

Once $\Delta\Pi_1$, q and ϵ_g have been set, ridges in the stretched échelle can be approximated using the three remaining parameters in our mixed mode model. Therefore, for each star we constructed a grid of templates describing possible ridges given test values of $\delta\nu_{\text{mag}}$, a and $\delta\nu_{\text{rot}}$. We uniformly sample $\delta\nu_{\text{mag}}$ in the range 0 to $0.2\mu\text{Hz}$, $\delta\nu_{\text{rot}}$ in the range 0.0 to $0.8\mu\text{Hz}$ and a from -0.5 to 1. Our grid had 50 points in each direction, such that the resolution on the magnetic splitting is $0.004\mu\text{Hz}$, on the rotation it is $0.02\mu\text{Hz}$ and on a is 0.03.

To establish the parameter values required to best describe the data we performed a null hypothesis test (H0 test). For a given star, we summed the total observed power in these ridges, and established the likelihood that we would observe the resulting power just due to white noise (the H0 likelihood). If we were summing power in N bins without performing the stretching, this would simply amount to the likelihood of drawing a given value of summed power from a χ^2 distribution with $2N$ degrees of freedom. However, the stretching introduces correlation between bins, such that the number of degrees of freedom in the stretched spectrum is no longer $2N$. An analytical definition of the correct number of degrees of freedom required to describe a

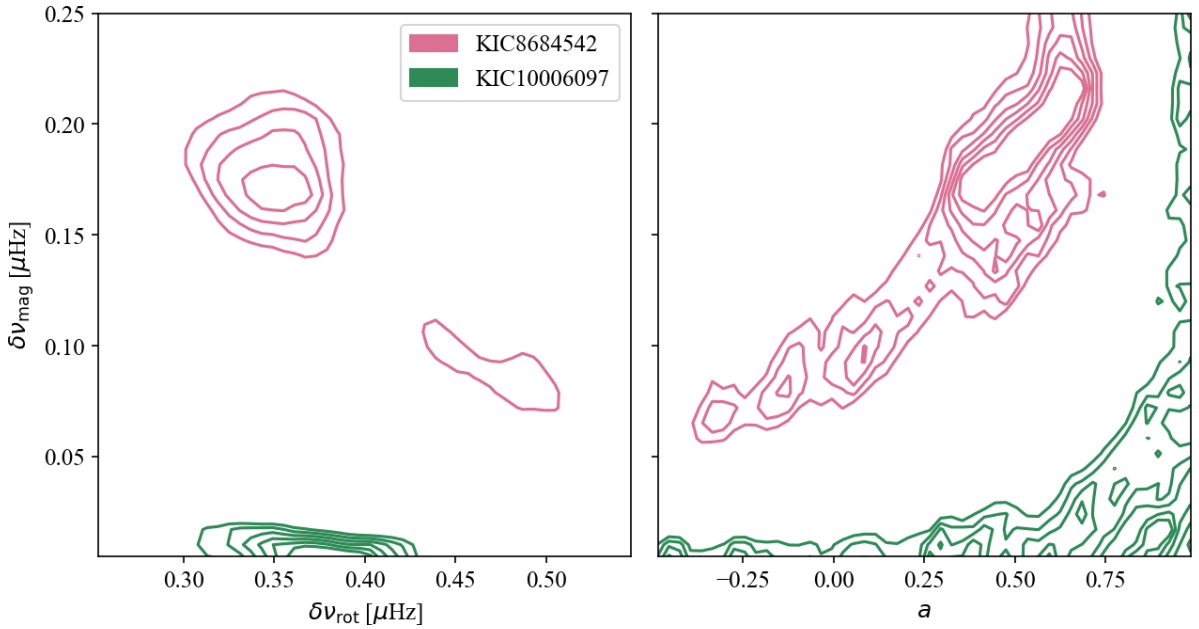


Figure 6.4: Left panel: Inverse of the 2-dimensional H0 likelihood space for $\delta\nu_{\text{mag}}$ and $\delta\nu_{\text{rot}}$. Two stars are shown, KIC 8684542 and KIC 10006097. Right panel: Inverse of the 2-dimensional H0 likelihood space for $\delta\nu_{\text{mag}}$ and a for KIC 8684542 and KIC 10006097.

stretched spectrum is yet to be established. Given the degree of stretching depends on $\Delta\Pi_1$ and q , this will vary on a star-by-star basis.

To approximate the statistics for the summed stretched power we therefore used white noise simulations. For each target we performed 50 realisations of a white noise spectrum evaluated on the same frequency grid as the real data. We then stretched this spectrum according to the value of $\Delta\Pi_1$ and q used in the prior and processed the stretched échelle as if it were real data. This resulted in 50 realisations of a 3 dimensional summed power array for a given star. Given each point corresponds to the sum of a large number of χ^2 distributed parameters, the resulting sum should be distributed according to a Gaussian (according to the central limit theorem). Accordingly, we calculated the H0 likelihood of the real data for a combination of $\delta\nu_{\text{mag}}$, a , $\delta\nu_{\text{rot}}$ via,

$$\mathcal{L}(\Theta|H0) \approx \mathcal{N}(\mu_{\Theta,WN}, \sigma_{\Theta,WN}), \quad (6.11)$$

where $\mu_{\Theta,WN}$ and $\sigma_{\Theta,WN}$ are the mean and standard deviation of the white noise realisations.

The parameters are $\Theta = (\delta\nu_{\text{mag}}, a, \delta\nu_{\text{rot}})$. Figure 6.3 shows the distribution of summed power in a single cell of the 3-d array for a white noise spectrum stretched according to the asymptotic parameters of KIC10006097. Therein we increased the number of realisations to 100 for illustrative purposes.

The width over which we summed the power about the predicted ridge was informed by the expected (stretched) line-width for g-dominated modes. At the base of the RGB, the distribution of radial mode linewidths peaks at $\approx 0.15\mu\text{Hz}$ (Yu et al., 2018a). The dipole mode linewidth for a given mixed mode then scales as $\Gamma_1(\nu) = \Gamma_0(1 - \zeta(\nu))$. For a mode ν_i with $\zeta(\nu_i) = 0.9$, this implies $\Gamma_1(\nu) \approx 0.015\mu\text{Hz}$. Therefore, we sum power in a width of $0.03\mu\text{Hz}$. Given this definition was set using an arbitrary selection of ζ , we tested 10 different widths up to a maximum of $0.15\mu\text{Hz}$. For KIC10006097 we found the resulting value of $\delta\nu_{\text{rot}}$ was consistent across widths from 0.015 to $0.084\mu\text{Hz}$. At widths larger than $0.084\mu\text{Hz}$, the measured value of $\delta\nu_{\text{rot}}$ was consistently smaller by $\approx 0.1\mu\text{Hz}$.

Examples of the 2-d distributions in likelihood for the échelle diagrams shown in figure 6.2 can be seen in figure 6.4. The H0 likelihood was then marginalised over each axis, and the minima of the 1D distributions used to inform the mean of the prior used in the sampling.

In a handful of cases the likelihood space was multimodal. To identify which mode best described the data, we manually vetted the associated ridges and subsequently reduced the range to exclude the spurious peak. This multimodality was a by-product of the use of H0 likelihood, as a model that is not necessarily the best descriptor of the signal can still capture power that is very unlikely to be the result of noise (for example residual power from $\ell = 0, 2$ modes).

Given these likelihoods are conditional on the combination of $\Delta\Pi_1$, q and ϵ_g , we did not use the width of the minima in the H0 likelihood to establish the width of the prior. To establish the most appropriate width to set on the prior on rotational splitting, we compared our values to those from Gehan et al., 2018b (henceforth G18). The resulting differences in measured rotation rates give a better estimate of the uncertainty associated with varying asymptotic parameters. Of the 334 stars in our target list, 142 are also in G18. The differences between the values in that catalogue and those we measured can be well approximated using a normal distribution with μ

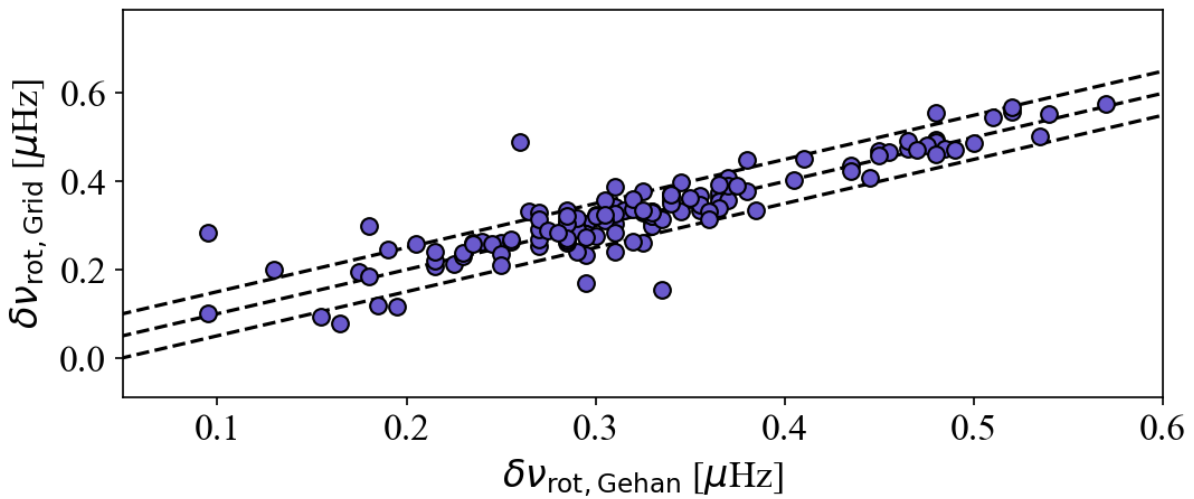


Figure 6.5: Core rotational splitting from the template matching technique versus those reported in G18. Black dotted lines show the 1-1 relation $\pm 0.05 \mu\text{Hz}$

$= 0.00 \mu\text{Hz}$ and $\sigma = 0.05 \mu\text{Hz}$ (see figure 6.5). As such our prior was $\mathcal{N}(\delta\nu_{\text{rot, echelle}}, 0.05 \mu\text{Hz})$.

The largest catalogue of magnetic parameters is that of Li et al., 2023 (henceforth L23, see also Li et al., 2022a, henceforth L22). Of the 13 stars listed there, 8 appear in our target list. We found our values of a differed substantially (see figure 6.6), with a preference for large values, which could be a consequence of the correlation with $\Delta\Pi_1$ (noted in L23). As such we ignore the result from the summed stretched power and set a uniform prior on a between -0.5 and 1 for all stars.

Our values of $\delta\nu_{\text{mag}}$ are in better agreement (see figure 6.6), with a standard deviation of $0.05 \mu\text{Hz}$. We set the prior as uniform, allowing values in the range $[\delta\nu_{\text{mag, echelle}} - 0.15 \mu\text{Hz}, \delta\nu_{\text{mag, echelle}} + 0.15 \mu\text{Hz}]$. For cases where this width would cause the prior to allow negative values of $\delta\nu_{\text{mag}}$, we set the lower limit on the prior at 0. In one outlier, the grid method has a $\delta\nu_{\text{mag}}$ which is smaller than that in L23 by $0.13 \mu\text{Hz}$. This is likely a consequence of selecting the value of $\Delta\Pi_1$ that made the $m = 0$ ridge appear most vertical (see section 6.2). Given setting a wider prior on $\delta\nu_{\text{mag}}$ for all stars would result in significant additional computational expense, we manually vetted posteriors and best fit models and only expanded the prior ranges where necessary. This amounted to expanding the prior range on $\delta\nu_{\text{mag}}$ for KIC8684542.

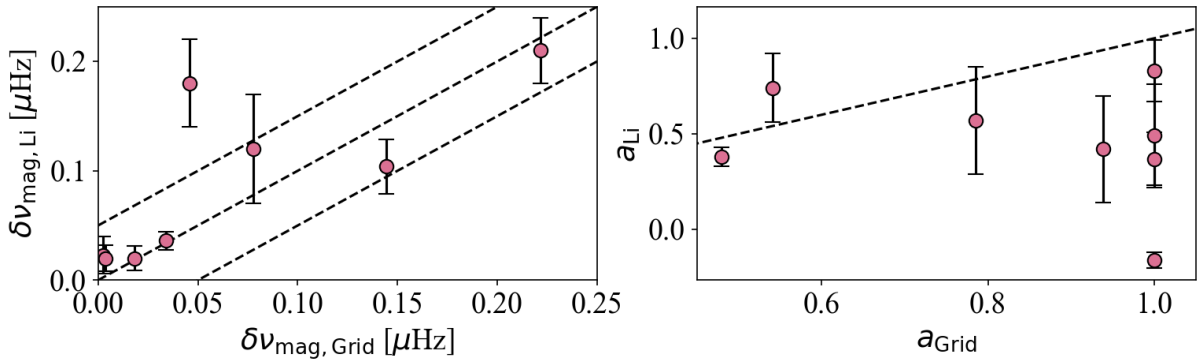


Figure 6.6: Left panel: Magnetic splitting, $\delta\nu_{\text{mag}}$, measured using summed power versus that reported in L23. Black dotted lines are the 1-1 relation $\pm 0.05\mu\text{Hz}$. Right panel: Topology parameter, a , measured using summed power versus that reported in L23. Black dotted line is the 1-1 relation.

6.3 Results

Of the 334 targets we report the magnetic and rotational parameters in 302 stars. Those which we do not report are cases where the posterior distribution was simply a replica of the prior. Such cases were the result of either low SNR or low inclination such that the rotational splitting was not well constrained. For a comparison of our values of $\Delta\Pi_1$, q and literature values, see appendix 6.B. Example corner plots for the parameters in the $\ell = 1$ model in two stars of the 302 are shown in the appendix (figures 6.C.1 and 6.C.2).

6.3.1 Rotational splitting

The distribution of core rotational splitting is shown in the top panel of figure 6.7, and is bimodal. The more populous peak is located at $\approx 0.32\mu\text{Hz}$ with the secondary peak at $\approx 0.47\mu\text{Hz}$. There does not appear to be any strong correlation between the rotational splitting (or associated bimodality) and the remaining asymptotic parameters (see figure 6.B.1, which shows a corner plot of the distribution of asymptotic parameters across the whole population). Notably the distributions of $\delta\nu_{\text{mag}}$ and a with $\delta\nu_{\text{rot}} > 0.4\mu\text{Hz}$ are consistent with those in the remaining catalogue.

Revisiting the 142 stars which appear in G18 which we used to inform the width of the prior on $\delta\nu_{\text{rot}}$, we found general agreement, with $\approx 80\%$ agreeing to 10% or better. As can be seen in

figure 6.8, we found a correlation between the difference in $\delta\nu_{\text{rot}}$ with $\delta\nu_{\text{mag}}$. For the star with the largest value of $\delta\nu_{\text{mag}}$ (KIC8684542), the difference in $\delta\nu_{\text{rot}}$ is of order $0.23 \mu\text{Hz}$. This was also noted in L23. Given the small values of magnetic splitting present in the vast majority of our targets, the offset in $\delta\nu_{\text{rot}}$ is below the scale of the uncertainties. As such, this is unlikely to impact previous conclusions regarding the distribution of rotational splittings on a population scale. We note a small number of stars (9) with differences in $\delta\nu_{\text{rot}}$ exceeding 0.1 despite having $\delta\nu_{\text{mag}}$ values below 0.001. This is a symptom of low SNR on the $m = \pm 1$ components of multiplets due to low stellar inclination, the average in the 9 cases being 45° .

6.3.2 Magnetic Parameters

The distribution in magnetic splittings peaks about $\log_{10}(\delta\nu_{\text{mag}}) = -2.54$, with a standard deviation of $\sigma(\log_{10}(\delta\nu_{\text{mag}})) = 0.45$ (see figure 6.9). This indicates that, from an observational perspective, perturbations to mode frequencies due to a core magnetic field of the scales reported in L22 and L23 are uncommon regardless of asymmetry. In total we find the mean on the posterior of the magnetic splitting is at least 2σ from zero in 24 stars, approximately 8% of the total sample.

The measurements of the topology parameter a span the full range in values allowed by the prior, with a peak at zero - the value which minimizes the asymmetry (see figure 6.9). For stars in which the mean value of the posterior on $\delta\nu_{\text{mag}}$ is at least 2σ from zero, 42% have values of a exceeding 0.5. These are inconsistent with a dipolar field, and must be identified with an architecture having the field concentrated more towards the poles than the equator. Values of a below -0.2 occur in 30% of the stars with significant $\delta\nu_{\text{mag}}$. These also cannot be the result of a dipolar field, instead being consistent with a field concentrated near the equator.

The asymmetry between modes in a multiplet is often used as an identifier of the presence of a magnetic perturbation. L22 and L23 quantify this using an additional parameter, $\delta_{\text{asym}} = 3a\delta\nu_{\text{mag}}$. In our catalogue δ_{asym} also peaks near zero, the distribution having a mean value $\log_{10}(\delta_{\text{asym}}) = -2.78$ with a standard deviation of $\sigma(\log_{10}(\delta_{\text{asym}})) = 0.67$ (see figure 6.9). Only 12 stars have asymmetry parameters that are at least 2σ from zero, making them easily identifiable

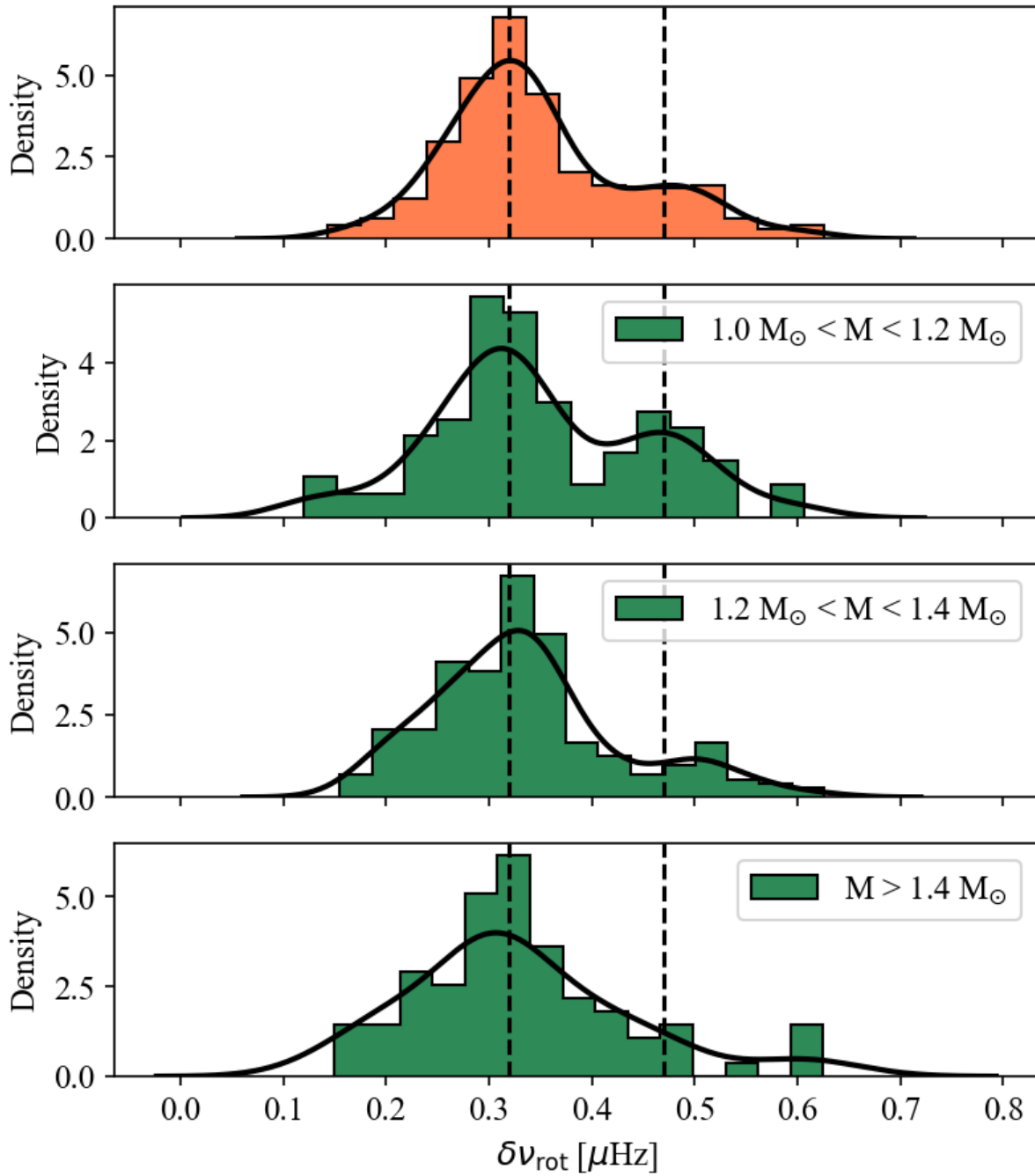


Figure 6.7: Distribution of $\delta\nu_{\text{rot}}$ in three mass ranges. Values of $\delta\nu_{\text{rot}}$ are those reported here, supplemented by values from G18 with $\nu_{\text{max}} < 150 \mu\text{Hz}$. The black curves show are a KDE of the distribution. Black dotted lines mark the locations of the two peaks identified in the lowest mass set to guide the eye.

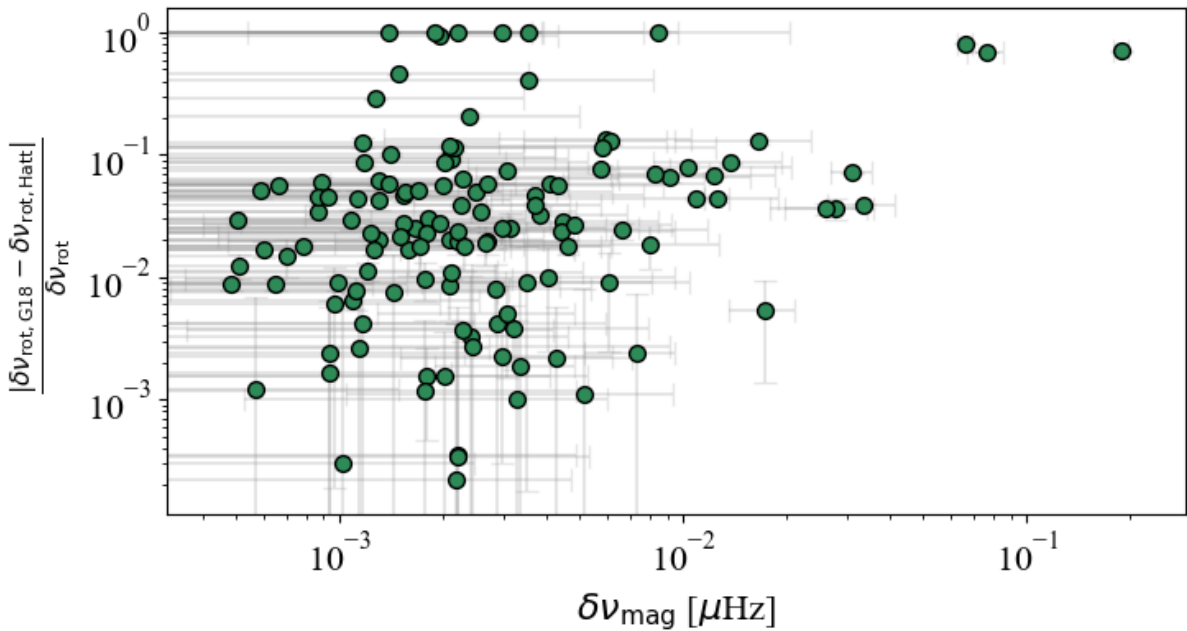


Figure 6.8: Fractional difference in $\delta\nu_{\text{rot}}$ measured here and reported in G18 as a function of $\delta\nu_{\text{mag}}$.

by eye. All 8 of the stars that we have in common with L23 appear in this set. The remaining targets identified as having significant $\delta\nu_{\text{mag}}$ values but little asymmetry have not been previously identified.

We find no obvious correlation between $\delta\nu_{\text{mag}}$ and any other asymptotic parameter, including the topology. This was also noted in L23. Bugnet, 2022 noted that not accounting for a magnetic perturbation could produce a systematic underestimate of $\Delta\Pi_1$ when using the techniques presented in Vrard et al., 2016. They simulated a star with a magnetic splitting of $0.4 \mu\text{Hz}$, which is much larger than those reported in L22 and L23, and found this would cause a 1% difference in the measured period spacing. We do not find a clear trend between the difference in our period spacing and that recorded in Vrard et al., 2016 with the magnetic splitting. As such, for stars with the magnitudes of magnetic perturbation reported here, discrepant $\Delta\Pi_1$ alone cannot be used as an identifier.

For the 8 stars we have in common with Li et al. (2023), our values of $\delta\nu_{\text{mag}}$ are in broad agreement, with the mean absolute difference being 1.09σ . Agreement on a is slightly worse, with a mean absolute difference of 1.5σ . Our methods do differ, Li et al. (2023) fit the

asymptotic expression to mode frequencies rather than directly fitting a forward model to the spectrum. Additionally we differ in our method of coupling modes, where we used the matrix construction discussed in Ong et al. (2021a) and Deheuvels et al. (2010), Li et al. (2023) use the JWKB construction of Unno et al. (1989). Finally, our priors on asymptotic parameters differ (see Li et al. 2023 for details).

6.4 Discussion

6.4.1 Rotation and stellar mass

As previously noted, the distribution of core rotational splitting appears bimodal. We show the dependence of this distribution with stellar mass in the left-most panel of figure 6.10. Masses are from Y18, where-in they are calculated via scaling relations with ν_{\max} , $\Delta\nu$ and T_{eff} . It appears the divide between the two populations in rotation is mass dependent, with the more rapidly rotating peak preferentially populated with less massive stars. To better sample the underlying distribution, we expand our sample to include stars from the G18 catalogue with $\nu_{\max} > 100\mu\text{Hz}$, giving us 492 stars. We show these data in the middle panel of figure 6.10. The trend with stellar mass remains.

We divided the combined catalogue into stars in ranges $1.0M_{\odot} < M_{*} < 1.2M_{\odot}$, $1.2M_{\odot} < M_{*} < 1.4M_{\odot}$ and $M_{*} > 1.4M_{\odot}$. The resulting distributions in $\delta\nu_{\text{rot}}$ can be seen in figure 6.7. In the lowest mass range, the secondary peak is identifiable at $\delta\nu_{\text{rot}} 0.47 \mu\text{Hz}$. In the mid range, the peak shifts upwards in $\delta\nu_{\text{rot}}$ to $0.50 \mu\text{Hz}$ and is less well populated. The set with the highest masses contains the fewest total stars and it is unclear whether a secondary peak is present. In total 25% of the population have $\delta\nu_{\text{rot}} > 0.40\mu\text{Hz}$.

Although it was not reported in G18, a bimodality in core rotation is present in their measurements for stars with $\nu_{\max} > 100\mu\text{Hz}$. In figure 6.11 we show our measurements of $\delta\nu_{\text{rot}}$ and those from G18 as a function of stellar mass in three ranges of \mathcal{N} . The left-hand panel is a reproduction of figure 6.10. The following panels show this distribution with increasing mixed mode density, \mathcal{N} . As such, for a given mass, stars go from least to most evolved from

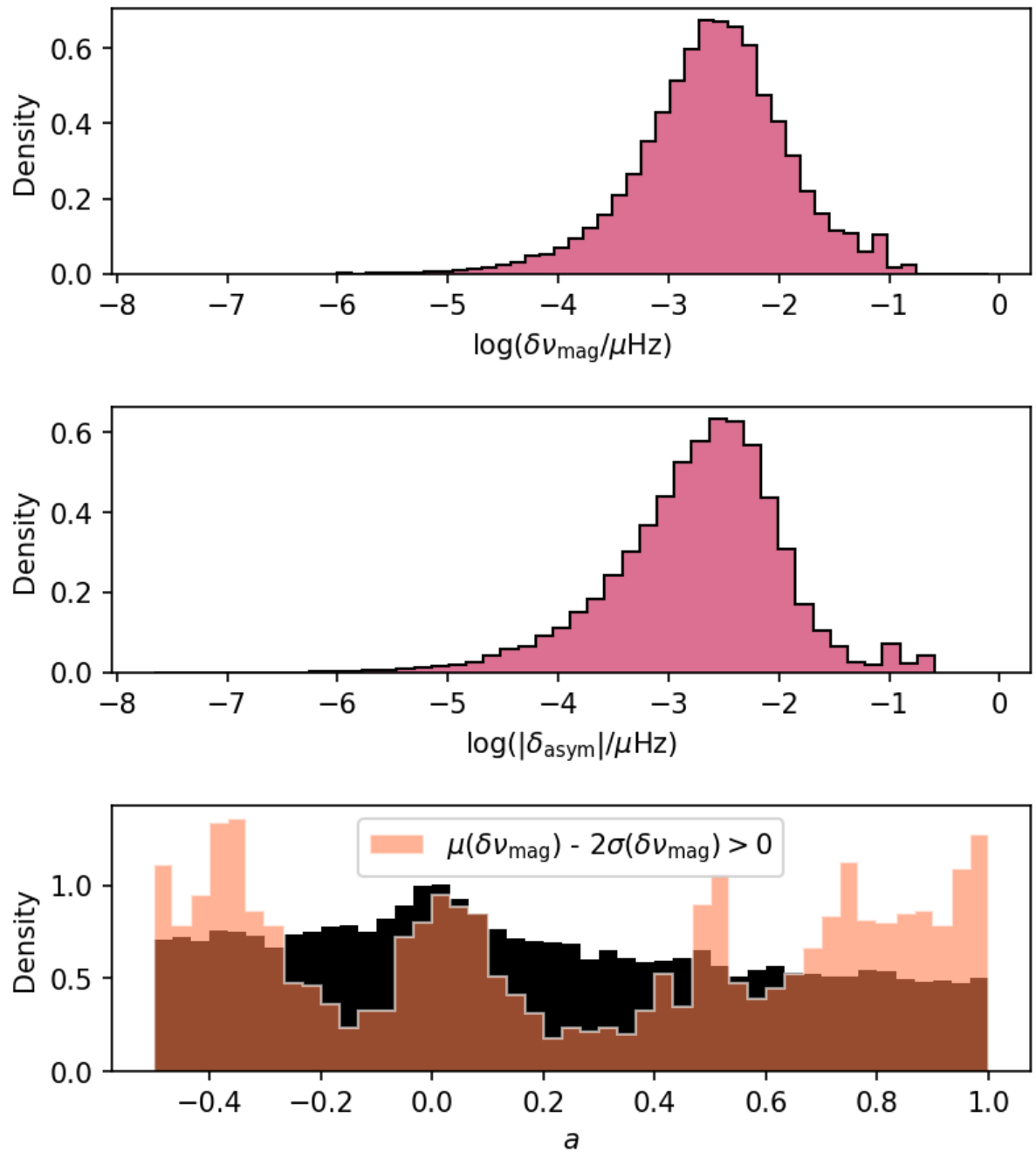


Figure 6.9: Distributions of magnetic parameters. Histograms are built using 100 draws from the posterior for each of the 302 stars. Top panel: Distribution of $\delta\nu_{\text{mag}}$. Middle panel: Distribution of δ_{asym} . Bottom panel: Distribution of a .

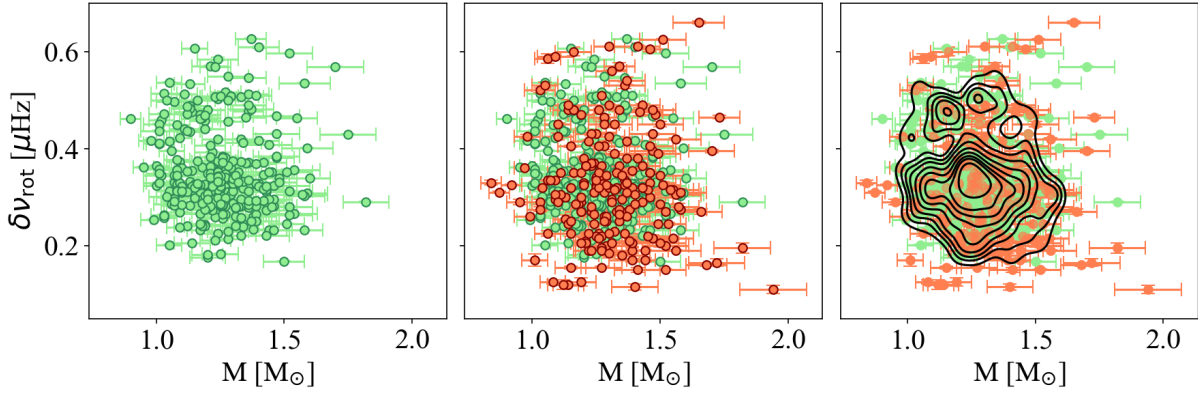


Figure 6.10: Distribution of $\delta\nu_{\text{rot}}$ as a function of stellar mass for the combined set of stars reported here and in G18. The left-most panel shows just the measurements reported in this work. In the center panel we fold in measurements from G18. The Black contours in the right hand panel are a kernel density estimate (KDE) highlighting the bimodality.

the left-most to the right-most panel. G18 and Mosser et al., 2012b concluded that core rotation rates in red giants decrease slightly as stars evolve, but only slightly. Indeed, the highest density of stars is at $\approx 0.3 \mu\text{Hz}$ in all three subsets. However, the spread in the distribution increases, such that the secondary peak identified at $0.47 \mu\text{Hz}$ appears to migrate to larger values with increasing N . For stars with $N < 7$, 2.4% of the population have $\delta\nu_{\text{rot}} > 0.6 \mu\text{Hz}$, this increases to 6.1% for stars with $N > 11$.

Red Clump stars are expected to have core rotation rates that differ from those on the RGB. However, given the cores are undergoing expansion due to the onset of helium burning, rotation rates are expected to decrease. This was observed to be the case in Mosser et al., 2012b. There-in the authors reported splittings ranging from 0.01 to $0.1 \mu\text{Hz}$. Therefore, it is unlikely the subset of rapid rotators are misclassified clump stars.

One interpretation of this result is that the stars in the more rapidly rotating population in each range in N belong to a single population with a weaker rotational coupling between core and envelope, such that the efficiency of angular momentum transport has been reduced. Accordingly their cores would be able to more effectively spin up as they contract. As the core contracts, the envelope is undergoing expansion, such that we can use the evolution of core rotation with stellar radius to infer the sign of the dependence on core contraction. Cantiello et al. (2014) found that the increase in core rotation should scale with stellar radius as $\Omega_{\text{core}} \propto R_*^\alpha$, with

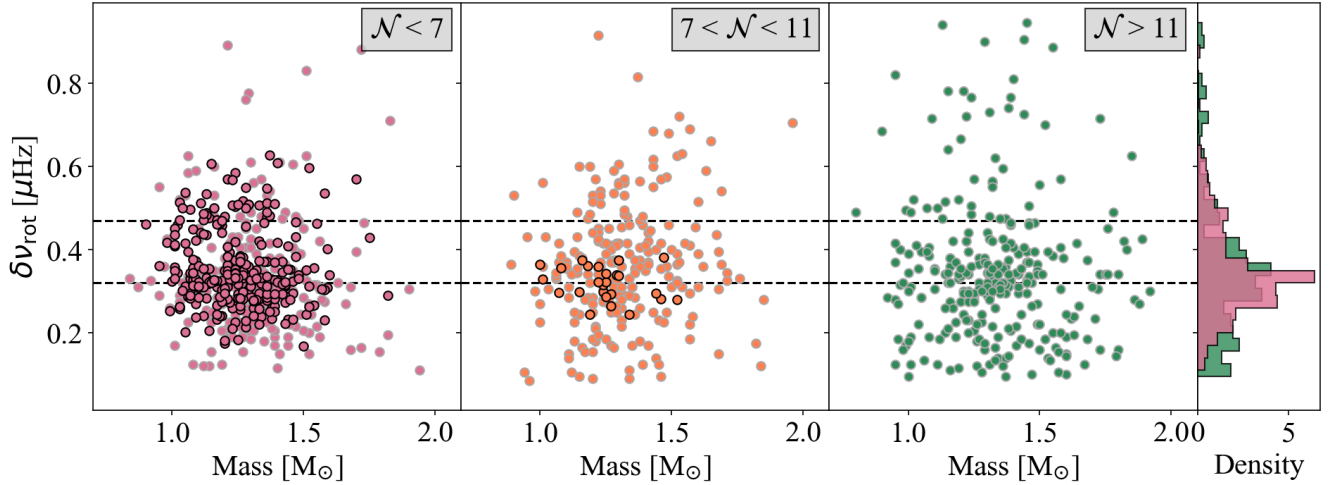


Figure 6.11: Distribution of $\delta\nu_{\text{rot}}$ reported in G18 (grey edgecolor) and here (black edgecolor) for stars in 3 different N ranges. The left-most panel is targets with $N < 7$, the middle panel has targets in the range $7 < N < 11$. The right-most is stars with $N > 11$. Black dotted lines are at $\delta\nu_{\text{rot}} = 0.32 \mu\text{Hz}$ and $0.47 \mu\text{Hz}$. Histograms on the right show the distribution in the stars with $N < 7$ in pink and with $N > 11$ in green.

α taking a value of 1.32 or 0.58, depending on whether they include just rotational instabilities or fold in those due to magnetic torques in radiative regions. That is, the cores should spin up as the star evolves. This is in clear disagreement with the core rotation rates measured by Mosser et al. (2012b), who found exponents of -0.5 for stars on the RGB and -1.3 in the RC. The mean values of stellar radius in the stars with $N < 7$ and $N > 11$ are $4.89 R_\odot$ and $7.14 R_\odot$ respectively. For representative stars at these radii to spin up from $\approx 0.5 \mu\text{Hz}$ to $\approx 0.7 \mu\text{Hz}$ would imply a relation of the form $\Omega_{\text{core}} \propto R_*^{0.8}$. This exponent sits in between those predicted by Cantiello et al. (2014).

6.4.2 Magnetic Perturbations and Stellar Properties

As noted in section 6.1, a core magnetic field could impact the transport of angular momentum within a star. We found no clear correlation between the bimodality in $\delta\nu_{\text{rot}}$ and $\delta\nu_{\text{mag}}$ or a . However, given a strong core magnetic field is frequently hypothesised as a solution to the discrepancy between modelled and observed core rotation rates, constraints on the average field strength in a large sample of stars remain in demand. In the following sections we invert the observed magnetic splitting to constrain the average core magnetic field strength.

Stellar Models

According to L22, the root-mean-square (rms) of the radial field strength scales with the magnetic splitting as

$$\langle B_r^2 \rangle = \int_{r_i}^{r_o} K(r) \overline{B_r^2} dr = \frac{16\pi^4 \mu_0 v_{\max}^3 \delta\nu_{\text{mag}}}{I}, \quad (6.12)$$

where I is a factor determined by the internal structure of the star. This is given by,

$$I = \frac{\int_{r_i}^{r_o} \left(\frac{N}{r}\right)^3 \frac{dr}{\rho}}{\int_{r_i}^{r_o} \frac{N}{r} dr}, \quad (6.13)$$

where N is the Brunt-Väisällä frequency, r is radius and ρ the stellar density. Therefore, we require models of the internal profile of our targets to invert our measured $\delta\nu_{\text{mag}}$ to give an estimate of the radial field strength.

To that end, we used Modules for Experiments in Stellar Astrophysics (MESA, Paxton et al., 2011; Paxton et al., 2013) to calculate a grid of stellar models with varying mass and metallicity. We calculated stellar evolution tracks with masses varying in the range of those reported in Y18 for our targets, spanning from $1M_\odot$ to $2M_\odot$ in increments of $0.05M_\odot$. Metallicities ranged from -1.0dex to +1.0dex with a spacing of 0.25dex. We used a mixing length of $\alpha_{\text{MLT}} = 2.29$, which was found via calibration of a solar model. Overshoot was treated using the exponential formalism with $f_1 = 0.015$ and $f_0 = 0.004$. Mode frequencies were then calculated using GYRE. To avoid too much computational expense, we restricted the grid to just radial modes.

A suitable model from this grid was selected for each star using the AIMS package (Astero-seismic Inference on a Massive Scale, Rendle et al., 2019). To do this AIMS searches the grid for the region with the highest posterior probability given the observed parameters, then explores the surrounding space using an MCMC sampler (emcee, Foreman-Mackey et al., 2013b). For general use in fitting global properties, AIMS interpolates between grid points. However, we require internal profiles and are, therefore, restricted to selecting models in the grid. We choose the model with the highest posterior probability, but note this is naturally restricted by the grid

resolution. AIMS provides several methods to apply surface corrections to model frequencies, of which we selected the method of Ball et al. (2014). We provided T_{eff} , [Fe/H], $\log(g)$, mass (from Y18) alongside $\Delta\Pi_1$, ν_{max} , $\Delta\nu$ and radial mode frequencies from the $\ell = 2, 0$ model (see section 6.2.2) as observables.

The only model parameter which could induce additional uncertainty in equation 6.12 is \mathcal{I} . Across all of the best fitting models, the variation in this parameter is well approximated by a Gaussian with a spread which is 30% of the mean. If we take this as a conservative proxy for the model uncertainty on this parameter (given our stars share similar observable properties), we would expect a modeling error on the inferred field strength of order 30%. We took this value forward as the model error, stating it in addition to the statistical error from the measurement of $\delta\nu_{\text{mag}}$, noting this is a very conservative estimate.

Mass

The presence of core convection during the main sequence is dependent on stellar mass, requiring the star to have a mass greater than $\approx 1.1 M_{\odot}$ (Kippenhahn et al., 1990). A magnetic field could then be driven in this convection zone and remain on the RGB in fossil form. Should significant magnetic perturbations only be measured in stars of mass $> 1.1 M_{\odot}$, we may take this as evidence that core magnetic fields in red giants are the remains of those generated in a convection zone on the main sequence. However, as shown in Li et al. (2022a) and Li et al., 2023, stars with masses below $1.1 M_{\odot}$ can still develop small convective cores on the main sequence, due to the burning of ^3He and ^{12}C outside of equilibrium. There-in the authors find that the core sizes are not large enough to reach the hydrogen burning shell on the red giant branch. As such, modes would be less sensitive to the presence of the field and therefore require a larger field strength to produce a shift of similar scale. Assuming field strength does not depend on stellar mass, we should then find that measurable magnetic perturbations in stars with $M < 1.1 M_{\odot}$ are broadly smaller in magnitude.

Figure 6.12 shows $\delta\nu_{\text{mag}}$ as a function of stellar mass (mass values from Y18). We note that $\delta\nu_{\text{mag}}$ values in excess of $0.04 \mu\text{Hz}$ only begin to appear at masses larger than $\approx 1.1 M_{\odot}$. However,

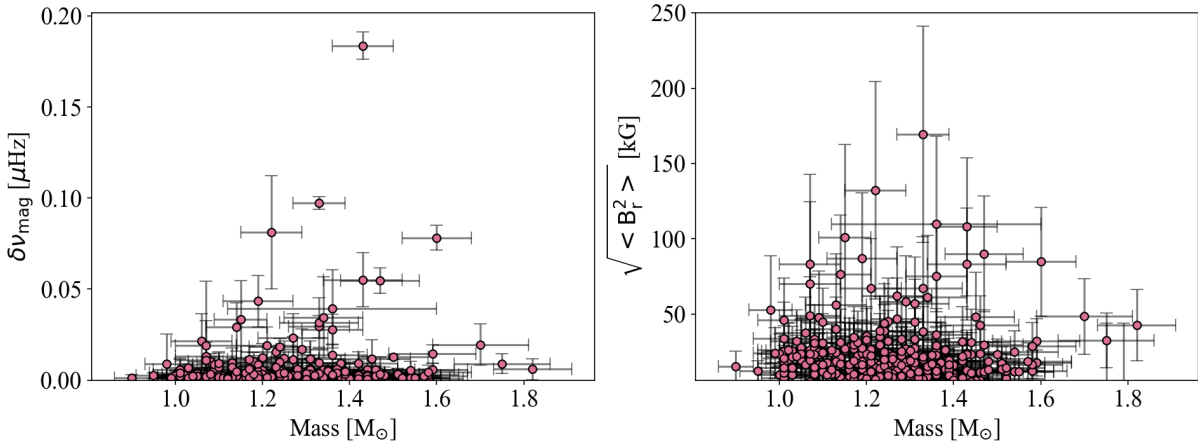


Figure 6.12: Left panel: $\delta\nu_{\text{mag}}$ as a function of stellar mass. Right panel: Best fitting $\sqrt{\langle B_r^2 \rangle}$ as a function of stellar mass.

this is not the case for small but significant magnetic splittings at values below $0.04\mu\text{Hz}$. In this regime stars span the full range in stellar mass present in our population. This could be consistent with a field driven in the small main sequence convection zone caused by the burning of ${}^3\text{He}$ and ${}^{12}\text{C}$ outside of equilibrium. Given that these targets have not previously been published due to the lack of asymmetry, this highlights a potential detection bias when manually selecting targets. This result could also be the signature of a systematic underestimate on stellar mass for the stars with significant $\delta\nu_{\text{mag}}$ at $M < 1.1M_{\odot}$. However, comparisons to masses derived from eclipsing binaries have shown masses from asteroseismic scaling relations are likely to be systematically overestimated rather than underestimated (Gaulme et al., 2016; Brogaard et al., 2018; Themeßl et al., 2018; Li et al., 2022b).

Magnetic Field Strengths

To determine the value of $\langle B_r^2 \rangle$ that would reproduce the magnetic splitting we measured, we utilized the best fitting models from the grid outlined in section 6.4.2. From these models we calculated the value of \mathcal{I} for each star. We then drew 1000 samples from the posterior distributions on $\delta\nu_{\text{mag}}$ and ν_{max} and calculated the mean field strength, $\langle B^2 \rangle$, according to equation 6.12. The reported field strength for each star is taken as the mean of the resulting distribution on $\langle B^2 \rangle$. Uncertainties are the standard deviation on this distribution plus the

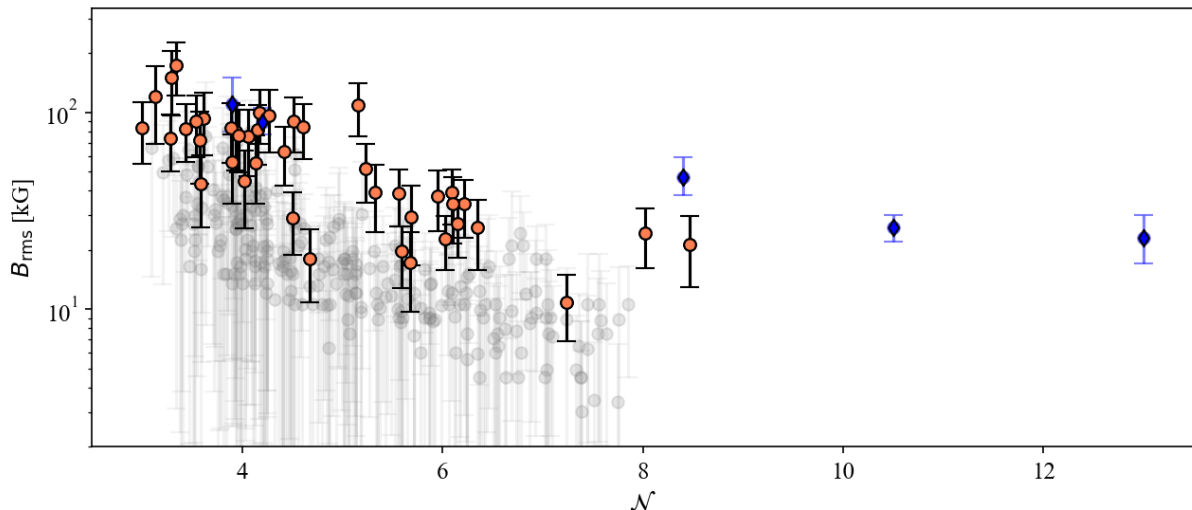


Figure 6.13: Best fitting $\sqrt{\langle B_r^2 \rangle}$ as a function of mixed mode density, \mathcal{N} . Stars with $\delta\nu_{\text{mag}} - 2\sigma(\delta\nu_{\text{mag}}) > 0$ are shown in orange. The remaining measurements are in grey. Blue diamonds show values reported in L23 for stars that do not appear in this work.

expected uncertainty from the models (see section 6.4.2) added in quadrature.

The distribution of $\langle B_r^2 \rangle$ peaks at zero, reflecting the measured magnetic splitting. For the stars with a field value at least 2σ from zero, 30% of the population have $\langle B_r^2 \rangle < 30$ kG. The distribution then tails with increasing field strength to the maximum at 169.4 ± 51 kG, occurring in KIC5696081.

There is no significant correlation between the measured core field strengths and stellar mass (see figure 6.12). At the low mass end of the distribution, the scale of the spread appears larger in $\langle B_r^2 \rangle$ than $\delta\nu_{\text{mag}}$. This is a consequence of the ν_{max}^{-3} dependence on $\delta\nu_{\text{mag}}$. For a given field strength, a larger ν_{max} (preferentially occurring in lower mass stars) implies a smaller magnetic splitting.

L23 identified a decrease in the core field strength as stars evolve along the RGB, but caveat this with a note that there is significant scatter. We observe the same dependence in our larger set of stars, as is shown in figure 6.13. There-in the authors identified the decrease follows the decrease in the critical field strength, which sets an upper limit on the observable field strength.

6.5 Limitations

Although the aim of this work was to catalogue a large number of stars such that we could start exploring population statistics, we were still subject to various detection biases. Firstly, we restricted ourselves to spectra where-in we could clearly identify all three components of the $\ell = 1$ multiplets. Therefore, we are restricted to inclination in the approximate range $20^\circ < i < 80^\circ$. With the assumption that stellar inclination is isotropically distributed this limits us to $\approx 70\%$ of the possible sample of stars.

Secondly, targets were selected by manual identification of rotational splitting. This meant that we required spectra where-in the separation between mixed modes was significantly larger than the rotational splitting. This defined both the lower limit on ν_{\max} ($100 \mu\text{Hz}$) and sets an upper limit on the $\delta\nu_{\text{rot}}$ for a given star. For a target with $\nu_{\max} = 150 \mu\text{Hz}$, $\Delta\Pi_1 = 80$ secs, the expected separation between adjacent mixed modes is approximately $3\mu\text{Hz}$. Currently, the maximum recorded core rotation rate for a red giant is $0.95 \mu\text{Hz}$ (Gehan et al., 2018b). Therefore, while our method is well suited to the range in core rotation previously reported in the literature, stars with rotation rates exceeding a few μHz would not have appeared in our initial sample selection.

Finally, We do not treat envelope rotation, which would introduce additional splitting in the p-dominated modes. Should the envelope rotation be significant, this could lead to an overestimate in our measurement of core rotational splitting. However, surface rotation rates in red giants are observed to be orders of magnitude smaller than the core rotation (Goupil et al., 2013), such that they are unlikely to cause significant error. Non-standard stellar evolution (e.g. mergers) can cause rapid envelope rotation in red giants. However, best estimates for the prevalence of such non-standard rotators is on the order of 8% (Gaulme et al., 2020). In our catalogue, $\approx 25\%$ of stars have core rotational splitting larger than $0.4\mu\text{Hz}$. A study of the relation between envelope rotational splitting, core rotational splitting and magnetic parameters is reserved for future work.

6.6 Conclusions

Exploiting the stretched period échelle, we have demonstrated how template matching can be used to construct initial estimates of the perturbations to dipole mode frequencies caused by core rotation and a magnetic field. We parameterise these using the magnetic splitting ($\delta\nu_{\text{mag}}$), a parameter dependent on field topology (a) and core rotational splitting ($\delta\nu_{\text{rot}}$). This allowed us to establish well-motivated priors for $\delta\nu_{\text{mag}}$ and $\delta\nu_{\text{rot}}$ in 334 low luminosity red giants.

Utilizing the information gained from the stretched échelles, we performed a full fit of the perturbed asymptotic expression to the power spectrum. This allowed us to jointly constrain $\Delta\Pi_1$, q , ϵ_g , $\delta\nu_{01}$, $\delta\nu_{\text{rot}}$, a and $\delta\nu_{\text{mag}}$ in 302 targets. We found that not accounting for the magnetic perturbation when measuring the rotational splitting can lead to biased measurements when the magnetic perturbation is large ($\delta\nu_{\text{mag}}$ on the scale of $0.1\mu\text{Hz}$). For the star with the largest value of $\delta\nu_{\text{mag}}$ the value of $\delta\nu_{\text{rot}}$ reported in G18 is 70% smaller than the value we measured.

We identified a bimodality in the core rotation rates of the stars in our sample. The more populous peak is at $\delta\nu_{\text{rot}} = 0.32 \mu\text{Hz}$, with the secondary at $0.47 \mu\text{Hz}$. The location and size of this secondary peak appears to be mass dependent. We found the distribution also evolves with N , with the upper limit on core rotation increasing with increasing N . Assuming that in each N range the most rapidly rotating stars belong to a secondary population, the observed increase in core rotation rate would imply a relation of the form $\Omega_{\text{core}} \propto R_*^{0.8}$. This is much closer to the predictions in Cantiello et al. (2014), suggesting in these stars the evolution of core rotation could be reproduced using a combination of rotational and magnetic instabilities.

We measured a magnetic splitting that is at least 2σ from zero in 8% of the total sample. Strong asymmetry was only present in 50% of these targets (4% of the full catalogue). For the stars with a clear detection of magnetic splitting, the topology parameter is not uniformly populated. A large percentage (42%) have values of a exceeding 0.5, identifiable with an architecture with the field more concentrated at the poles than the equator. Another large group (30% of stars with significant magnetic splitting) have values of a below -0.2, consistent with a field concentrated near the equator.

We did not observe any correlation between magnetic and rotational parameters, and so are

$\Delta\Pi_1$ (s)	ϵ_g	q	$\delta\nu_{\text{mag}}$ (μHz)	a	$\delta\nu_{\text{rot}}$ (μHz)
80.39	0.8	0.124	0.195	0.47	0.33

Table 6.A.1: Values of the asymptotic parameters used to construct a mock spectrum for KIC8684542.

unable to comment on whether the additional angular momentum transport is directly related to the magnetic fields we measured.

Although the largest magnetic splittings we measured were in stars with masses greater than $1.1 M_\odot$, magnetic splittings inconsistent with zero were measured in stars with masses from $1.03M_\odot$ to $1.6M_\odot$. This suggests that a main sequence convective core may not be the only channel for generating stable magnetic fields that are observed in fossil form on the red giant branch.

For the targets in which we measured significant magnetic splittings, the field strengths are on the order of tens of kG, with the number of detections decreasing with increasing field strength. The maximum value we measured was 169.4kG in KIC5696081. We confirm the tentative conclusion made in L23 that measurable field strengths decrease as stars evolve.

6.A Parameters for Injection Recovery Test

6.B Comparisons to Literature Values

6.B.1 G-mode asymptotics

Vrard et al., 2016 (V16) published measurements of g-mode asymptotics in 6100 red giants. Mosser et al., 2017 (M17) built on this catalogue to include the mode coupling parameter, q . In figure 6.B.2 we show comparisons between our measurements of period spacing and coupling parameter (which we derive from equation 6.10) and those from the aforementioned catalogues. The strong gridding in q is a result of the methods used in M17. On average, the values of q reported here are higher, with the mean offset being 10%. This is below the average uncertainty

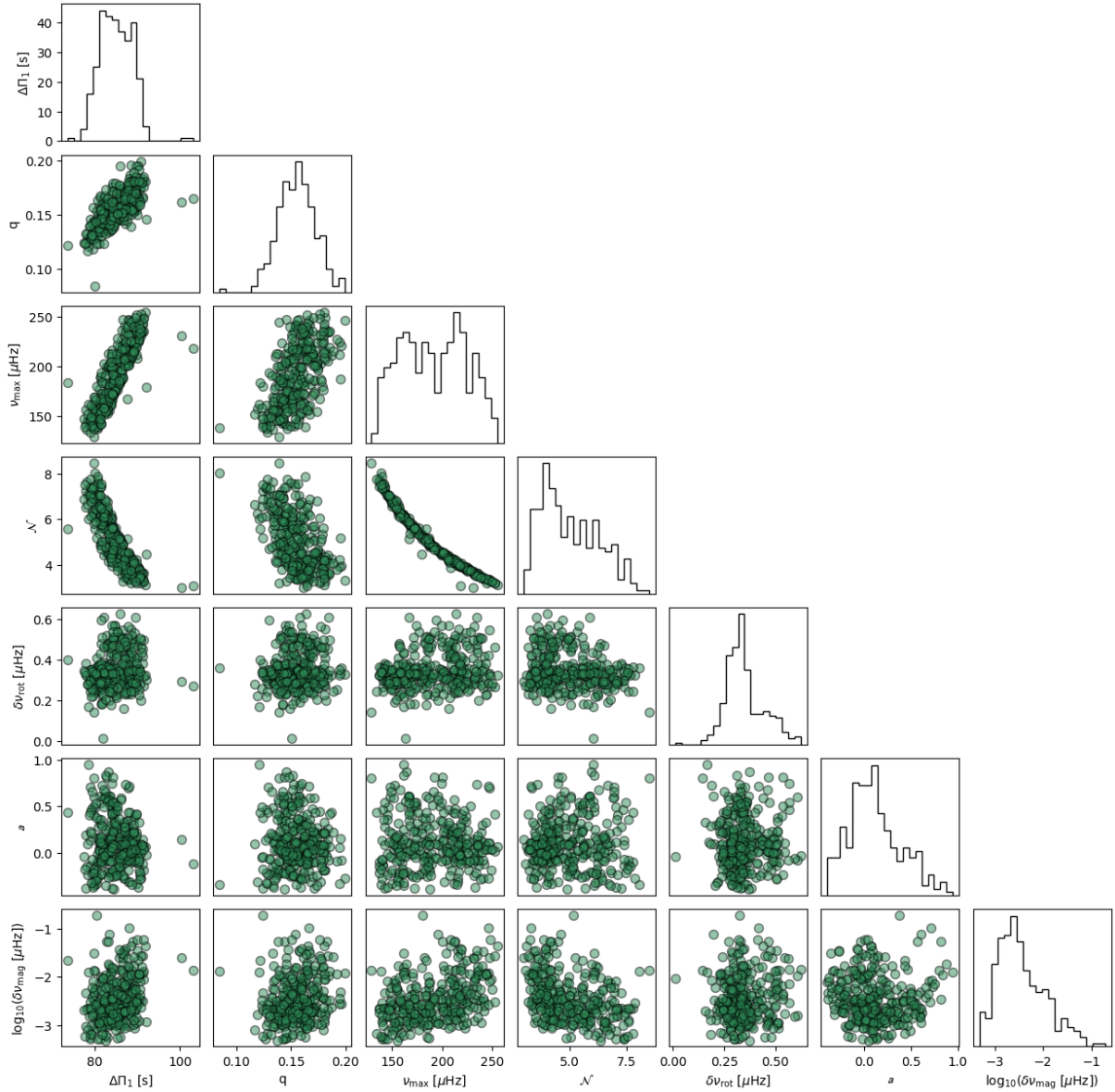


Figure 6.B.1: Corner plot showing the distribution of the asymptotic parameters, rotational splitting and magnetic parameters across all 302 stars.

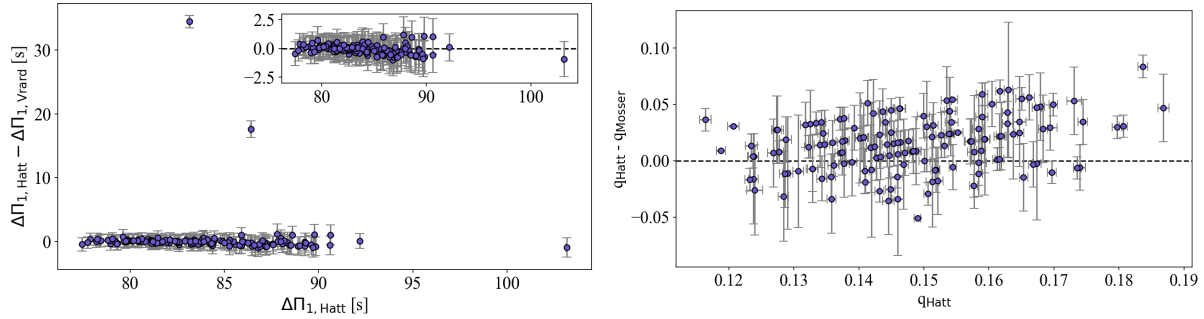


Figure 6.B.2: Left: Difference in period spacing measured here and reported in V16. Right: Difference in q measured here and reported in M17.

reported in M17, which is 16%. Dhanpal et al. (2023) measured q using .

Our period spacing measurements are consistent with those reported in V16. We note the uncertainties reported here are smaller than those in V16 by two orders of magnitude. They are, however, consistent with those reported in more recent studies exploiting similar fitting methods (Li et al., 2022a; Kuszlewicz et al., 2023; Li et al., 2023).

6.C Example Corner Plots

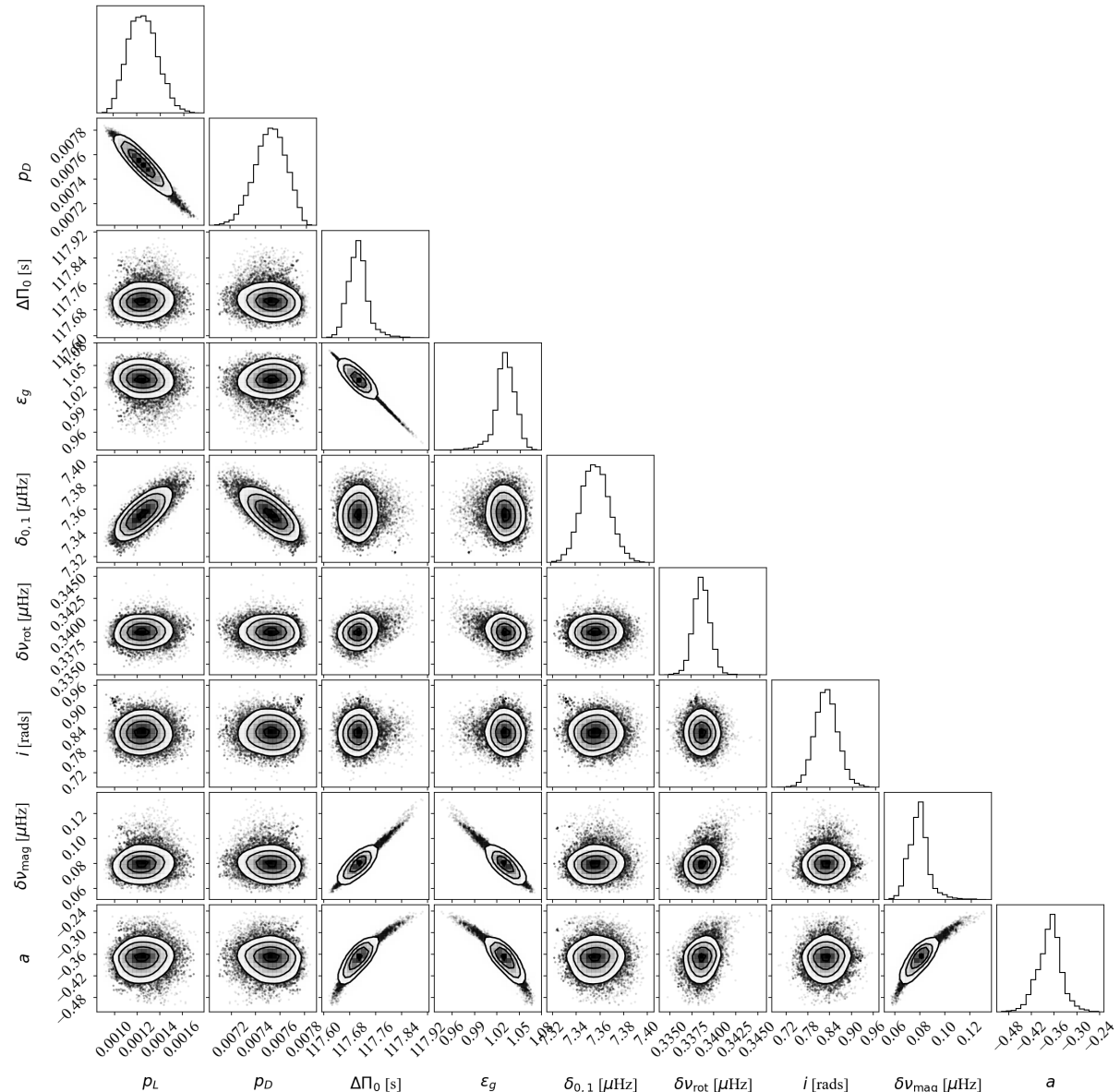


Figure 6.C.1: Corner plot of the asymptotic parameters of KIC11515377.

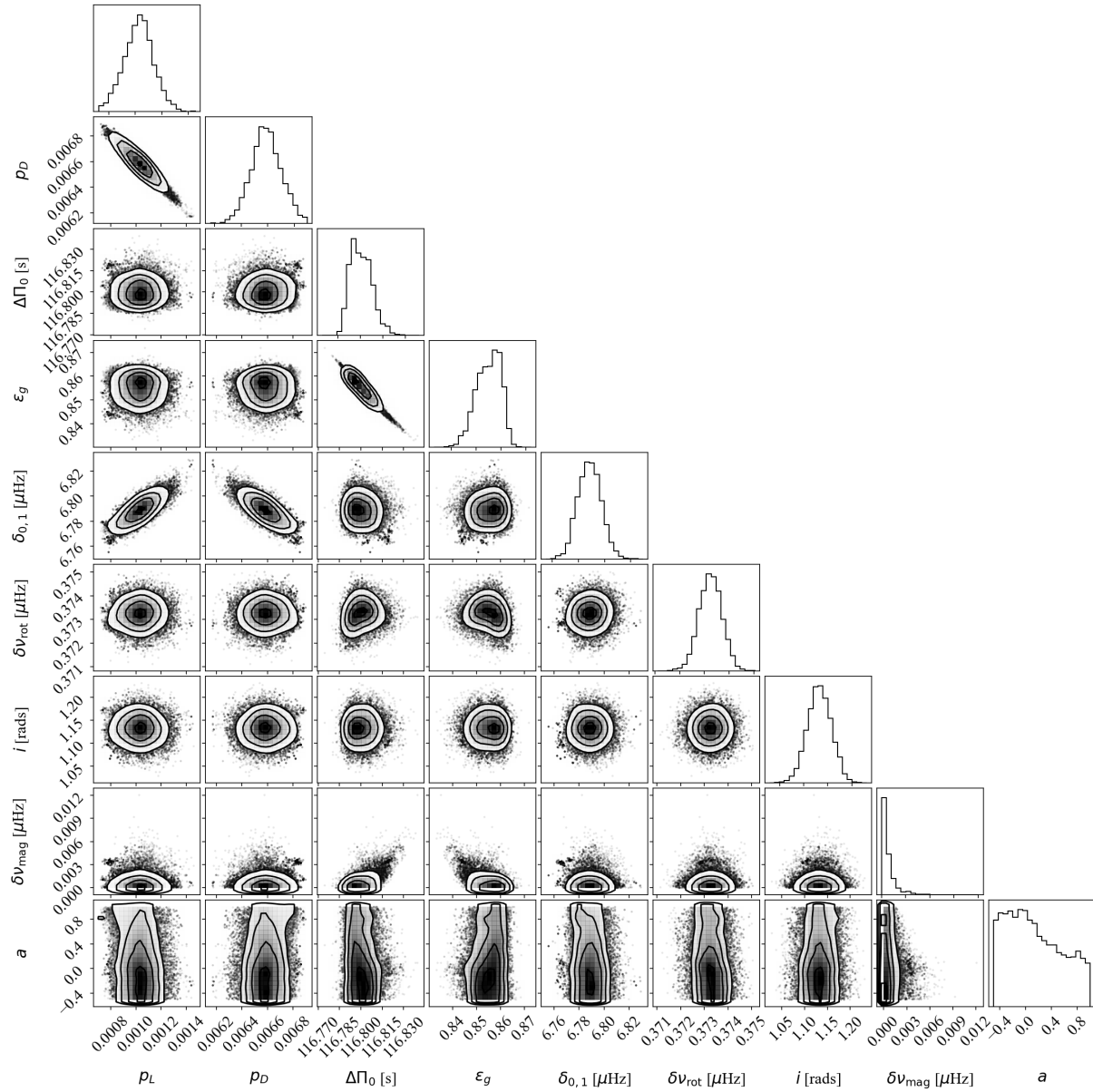


Figure 6.C.2: Corner plot of the asymptotic parameters of KIC7018212.

Chapter 7

Conclusions and Future Work

This thesis was dedicated to developing and applying asteroseismic analysis methods to both identify solar-like oscillations and measure stellar internal properties in large numbers of stars. I made measurements in increasing levels of detail, beginning with detecting the presence of oscillations and ending with measuring small perturbations to mode frequencies due to core magnetism and rotation. Additionally, I used the methods generated for use on real data to quantify the asteroseismic potential of the proposed HAYDN observing mission.

In Chapters 1 and 2, I covered the basics of the evolution of the solar-like oscillator and how we exploit measurements of their oscillations to reveal stellar fundamental properties. In Chapter 3, I used this basis to introduce the pipeline I worked on to detect solar-like oscillations in large datasets. In doing so, I covered the basics of Bayesian analysis, describing how we determine the probability that a hypothesis is supported by observations of some type. These mechanisms were used to develop two modules searching for signatures in the power spectrum that can be used to identify solar like oscillations. In the first, we determined whether the observed power in the spectrum was consistent with expectations for a mode envelope. In the second we utilized the autocorrelation of the lightcurve to identify signatures of sound waves crossing the stellar radius. We validated the method on a test set of stars observed by NASA's TESS mission, determining the pipeline could function to an accuracy of 93.2%.

In Chapter 4 we extended the pipeline to include methods to measure the global asteroseismic

parameters, $\Delta\nu$ and ν_{\max} . In doing so, I introduced a new parameterization of the statistics of a collapsed auto-correlation function. After demonstrating the method could reproduce literature values of $\Delta\nu$ and ν_{\max} , I applied the pipeline to over 200,000 lightcurves. This resulted in the first catalogue of solar-like oscillators identified using TESS short cadence data, numbering 4,177 stars. At time of writing, the catalogue has doubled the number of stars detected with ν_{\max} between $280\mu\text{Hz}$ and $1000\mu\text{Hz}$. These stars populate the subgiant branch, which marks a significant transitional period where-in core hydrogen burning has ceased and the star is undergoing structural change.

We constructed the TESS catalogue using data taken from sectors 1-46. The majority of the lightcurves were collected in 120 second cadence, as 20 second cadence was only introduced during the first extended mission (starting with sector 27). We found in a number of main-sequence stars observed at both cadences, oscillations were only detectable in 20 second data, where-in the signal-to-noise was larger. Another 30 sectors have passed since the completion of our catalogue, meaning the amount of 20 second data available has more than doubled. In future, we will be rerunning the pipeline on this new data, with the aim of increasing the number of main sequence stars in which we have detected solar-like oscillations using TESS.

In Chapter 5, I introduced the asteroseismic potential of stellar clusters. I discussed the HAYDN mission, a space mission proposed to observe stellar clusters with the main aim being the study of solar-like oscillations. To establish the expected yield of such a mission, I generated realistic lightcurves for a population of stars that were simulated to mimic the characteristics of the cluster NGC 6397. I then applied the detection pipeline to this data, determining the detection limits in lightcurves of various lengths. For year-long lightcurves, oscillations were detected in 740 of the 6771 stars. Reducing the observing period to 3 months resulted in a net loss of 137 detections. Regardless of length tested, we only detected oscillations in stars on the red giant branch. For those stars in which oscillations were detectable, I used the `pbjam` package to fit the $\ell = 0$ and 2 modes. We reliably measured $\ell = 0$ mode frequencies in 322 stars. Those stars in which we systematically could not recover the frequencies were the most evolved in the set, having $3.4 \mu\text{Hz} < \nu_{\max} < 12 \mu\text{Hz}$. Quadrupole mode frequencies ($\ell = 2$) were

recovered in 103 stars, preferentially in the least evolved ($70\mu\text{Hz} < \nu_{\text{max}} < 328\ \mu\text{hz}$). Finally, I experimented with rotation and magnetism, identifying the ranges in these parameters which produce measurable perturbations to dipole mode frequencies. For a test star at the base of the red giant branch, I found that rotational splitting could be reliably measured in the range $0.4\mu\text{Hz} < \delta\nu_{\text{rot}} < 2.0\mu\text{Hz}$. At splitting below $0.4\mu\text{Hz}$ we could not recover the splitting in any modes, while above $2.0\ \mu\text{Hz}$ the number of modes for which we could accurately recover the splitting varied significantly for each test value of $\delta\nu_{\text{rot}}$. The magnetic asymmetry (a parameter frequently used to identify magnetic signatures) was recovered in all test cases, however the measured value was never more than 2σ from zero. This work demonstrated the wealth of asteroseismic information that could be captured by a mission like HAYDN.

At time of writing, stellar models of NGC 6397 with self consistent mode frequencies had not been generated. Accordingly, we had to assign frequencies by matching a new set of stellar models to stars in the simulated population. The team that produced the population synthesis for candidate clusters are currently working on a new simulation where stars are drawn from grids including asteroseismic parameters. These will replace our models in the published version of Chapter 5. Additionally, I identified the ranges in which signatures of rotation and magnetism could be recovered in the spectrum of a test star at the base of the red giant branch. In future, this will be extended to the more evolved stars in which we could detect oscillations, to determine how detection limits vary with evolutionary status. This will have important implications for the use of these measurements in exploring the missing angular momentum problem.

Finally, in Chapter 6 I reported the largest catalogue of measurements of magnetic and rotational perturbations to mode frequencies made to date. In doing so I introduced a new method to make first estimates of the magnetic and rotational parameters for an observed star. We used these measurements as a prior on a full fit of the spectrum of the perturbed dipole modes in 312 stars. We identified a clear bimodality in core rotation rate, which had not yet been reported. We found the more populous primary peak had $\delta\nu_{\text{rot}} = 0.32\ \mu\text{Hz}$ (consistent with previous catalogues), while the secondary peak had $\delta\nu_{\text{rot}} = 0.47\ \mu\text{Hz}$. The secondary peak appears to migrate to larger $\delta\nu_{\text{rot}}$ and become less populous as stellar mass increases.

This introduces another feature which our current models of stellar rotation cannot account for, opening a new chapter in our investigation of the angular momentum transport in stars. A magnetic splitting that was more than 2σ from zero was identified in just 24 stars, which were not uniformly distributed in the topology parameter, a . This could indicate the magnetic fields in the cores of red giants are generated with some preferential topology.

The cause of the bimodality we identified in core rotation rates is yet to be established. Our current models for rotation in red giants produce core rotation rates that are much more rapid than those identified with the primary peak in our distribution. Future work will include identifying whether the stars in the more rapidly rotating secondary peak are compatible with current models, which would provide further insight into the missing angular momentum problem. Additionally, the magnetic parameters catalogued in the final sections of Chapter 6 constitute the largest set ever measured. The current leading theory concerning the origins of core magnetic fields in red giants is that they are the fossil remains of a field generated in the convective core on the main sequence. However, such a convective core is traditionally assumed to only occur in stars with mass greater than $1.1M_{\odot}$. We measured a significant magnetic signature in a number of stars with masses below this limit. It has been shown that small convective cores can be generated in stars with masses below this limit. A more complete modelling of our observed stars would allow us to identify whether this is likely the case in these stars.

Catalogues of measurements of solar-like oscillations are providing insight into stellar processes that have previously been observationally inaccessible. Techniques learned using *Kepler* data can now be applied to the hundreds of thousands of stars observed by TESS, enabling large-scale population studies of the internal properties of stars. An asteroseismic specific observing mission seems inevitable, and will likely answer a number of open questions in the field of stellar physics.

References

- Addison, B. C. et al. (Apr. 2021). “TOI-257b (HD 19916b): a warm sub-saturn orbiting an evolved F-type star”. In: *MNRAS* 502.3, pp. 3704–3722. doi: [10.1093/mnras/staa3960](https://doi.org/10.1093/mnras/staa3960). arXiv: [2001.07345 \[astro-ph.EP\]](https://arxiv.org/abs/2001.07345).
- Amard, L. et al. (Nov. 2019). “First grids of low-mass stellar models and isochrones with self-consistent treatment of rotation. From 0.2 to 1.5 M_{\odot} at seven metallicities from PMS to TAMS”. In: *A&A* 631, A77, A77. doi: [10.1051/0004-6361/201935160](https://doi.org/10.1051/0004-6361/201935160). arXiv: [1905.08516 \[astro-ph.SR\]](https://arxiv.org/abs/1905.08516).
- Amard, L. et al. (Feb. 2020). “The Impact of Metallicity on the Evolution of the Rotation and Magnetic Activity of Sun-like Stars”. In: *ApJ* 889.2, 108, p. 108. doi: [10.3847/1538-4357/ab6173](https://doi.org/10.3847/1538-4357/ab6173). arXiv: [2001.10404 \[astro-ph.SR\]](https://arxiv.org/abs/2001.10404).
- Anderson, E. et al. (May 2012). “XHIP: An extended hipparcos compilation”. In: *Astronomy Letters* 38.5, pp. 331–346. ISSN: 1562-6873. doi: [10.1134/S1063773712050015](https://doi.org/10.1134/S1063773712050015). URL: <http://dx.doi.org/10.1134/S1063773712050015>.
- Appourchaux, T. et al. (Oct. 1998). “The art of fitting p-mode spectra. I. Maximum likelihood estimation”. In: *A&AS* 132, pp. 107–119. doi: [10.1051/aas:1998441](https://doi.org/10.1051/aas:1998441). arXiv: [astro-ph/9710082 \[astro-ph\]](https://arxiv.org/abs/astro-ph/9710082).
- Appourchaux, T. et al. (July 2012a). “Oscillation mode frequencies of 61 main-sequence and subgiant stars observed by Kepler”. In: *A&A* 543, A54, A54. doi: [10.1051/0004-6361/201218948](https://doi.org/10.1051/0004-6361/201218948). arXiv: [1204.3147 \[astro-ph.SR\]](https://arxiv.org/abs/1204.3147).

- Appourchaux, T. et al. (Jan. 2012b). “Oscillation mode linewidths of main-sequence and subgiant stars observed by Kepler”. In: *A&A* 537, A134, A134. doi: [10.1051/0004-6361/201118496](https://doi.org/10.1051/0004-6361/201118496). arXiv: [1112.3295 \[astro-ph.SR\]](https://arxiv.org/abs/1112.3295).
- Arentoft, T. et al. (Apr. 2017). “Convective-core Overshoot and Suppression of Oscillations: Constraints from Red Giants in NGC 6811”. In: *ApJ* 838.2, 115, p. 115. doi: [10.3847/1538-4357/aa63f7](https://doi.org/10.3847/1538-4357/aa63f7). arXiv: [1703.01097 \[astro-ph.SR\]](https://arxiv.org/abs/1703.01097).
- Babcock, H. W. (Mar. 1961). “The Topology of the Sun’s Magnetic Field and the 22-Year Cycle.” In: *ApJ* 133, p. 572. doi: [10.1086/147060](https://doi.org/10.1086/147060).
- Baglin, A. et al. (Jan. 2006). “CoRoT: a high precision photometer for stellar evolution and exoplanet finding”. In: *36th COSPAR Scientific Assembly*. Vol. 36, p. 3749.
- Ball, W. H. et al. (Aug. 2014). “A new correction of stellar oscillation frequencies for near-surface effects”. In: *A&A* 568, A123, A123. doi: [10.1051/0004-6361/201424325](https://doi.org/10.1051/0004-6361/201424325). arXiv: [1408.0986 \[astro-ph.SR\]](https://arxiv.org/abs/1408.0986).
- Ball, W. H. et al. (Dec. 2018). “A Synthetic Sample of Short-cadence Solar-like Oscillators for TESS”. In: *ApJS* 239.2, 34, p. 34. doi: [10.3847/1538-4365/aaedbc](https://doi.org/10.3847/1538-4365/aaedbc). arXiv: [1809.09108 \[astro-ph.SR\]](https://arxiv.org/abs/1809.09108).
- Ballot, J. et al. (July 2011). “Visibilities and bolometric corrections for stellar oscillation modes observed by Kepler”. In: *A&A* 531, A124, A124. doi: [10.1051/0004-6361/201016230](https://doi.org/10.1051/0004-6361/201016230). arXiv: [1105.4557 \[astro-ph.SR\]](https://arxiv.org/abs/1105.4557).
- Barnes, S. A. (Mar. 2003). “On the Rotational Evolution of Solar- and Late-Type Stars, Its Magnetic Origins, and the Possibility of Stellar Gyrochronology”. In: *ApJ* 586.1, pp. 464–479. doi: [10.1086/367639](https://doi.org/10.1086/367639). arXiv: [astro-ph/0303631 \[astro-ph\]](https://arxiv.org/abs/astro-ph/0303631).
- (Nov. 2007). “Ages for Illustrative Field Stars Using Gyrochronology: Viability, Limitations, and Errors”. In: *ApJ* 669.2, pp. 1167–1189. doi: [10.1086/519295](https://doi.org/10.1086/519295). arXiv: [0704.3068 \[astro-ph\]](https://arxiv.org/abs/0704.3068).
- Basu, S. (Aug. 2016). “Global seismology of the Sun”. In: *Living Reviews in Solar Physics* 13.1, 2, p. 2. doi: [10.1007/s41116-016-0003-4](https://doi.org/10.1007/s41116-016-0003-4). arXiv: [1606.07071 \[astro-ph.SR\]](https://arxiv.org/abs/1606.07071).

- Basu, S. et al. (2017a). *Asteroseismic data analysis : foundations and techniques / Sarbani Basu and William J. Chaplin.* eng. Princeton series in modern observational astronomy. ISBN: 9781400888207.
- Basu, S. et al. (2017b). *Asteroseismic Data Analysis: Foundations and Techniques.*
- Batalha, N. M. et al. (Apr. 2010). “Selection, Prioritization, and Characteristics of Kepler Target Stars”. In: *ApJS* 713.2, pp. L109–L114. doi: [10.1088/2041-8205/713/2/L109](https://doi.org/10.1088/2041-8205/713/2/L109). arXiv: [1001.0349 \[astro-ph.SR\]](https://arxiv.org/abs/1001.0349).
- Bayes, M. et al. (Jan. 1763). “An Essay towards Solving a Problem in the Doctrine of Chances. By the Late Rev. Mr. Bayes, F. R. S. Communicated by Mr. Price, in a Letter to John Canton, A. M. F. R. S.” In: *Philosophical Transactions of the Royal Society of London Series I* 53, pp. 370–418.
- Becerra, L. et al. (Mar. 2022). “Evolution of random initial magnetic fields in stably stratified and barotropic stars”. In: *MNRAS* 511.1, pp. 732–745. doi: [10.1093/mnras/stac102](https://doi.org/10.1093/mnras/stac102). arXiv: [2111.10673 \[astro-ph.SR\]](https://arxiv.org/abs/2111.10673).
- Bedding, T. R. et al. (Apr. 2010). “Solar-like Oscillations in Low-luminosity Red Giants: First Results from Kepler”. In: *ApJS* 713.2, pp. L176–L181. doi: [10.1088/2041-8205/713/2/L176](https://doi.org/10.1088/2041-8205/713/2/L176). arXiv: [1001.0229 \[astro-ph.SR\]](https://arxiv.org/abs/1001.0229).
- Bedding, T. R. et al. (July 2007). “Solar-like Oscillations in the G2 Subgiant β Hydri from Dual-Site Observations”. In: *ApJ* 663.2, pp. 1315–1324. doi: [10.1086/518593](https://doi.org/10.1086/518593). arXiv: [astro-ph/0703747 \[astro-ph\]](https://arxiv.org/abs/astro-ph/0703747).
- Bedding, T. R. et al. (Sept. 2022a). “Dealing with Large Gaps in Asteroseismic Time Series”. In: *Research Notes of the American Astronomical Society* 6.9, 202, p. 202. doi: [10.3847/2515-5172/ac8f94](https://doi.org/10.3847/2515-5172/ac8f94). arXiv: [2303.15584 \[astro-ph.IM\]](https://arxiv.org/abs/2303.15584).
- (Sept. 2022b). “Dealing with Large Gaps in Asteroseismic Time Series”. In: *Research Notes of the AAS* 6.9, p. 179. doi: [10.3847/2515-5172/ac8f94](https://doi.org/10.3847/2515-5172/ac8f94). URL: <https://doi.org/10.3847/2515-5172/ac8f94>.

- Belkacem, K. (June 2019). “Red giant stars: from mixed modes to angular momentum”. In: *EAS Publications Series*. Vol. 82. EAS Publications Series, pp. 189–211. doi: [10.1051/eas/1982019](https://doi.org/10.1051/eas/1982019).
- Borucki, W. J. et al. (Feb. 2010). “Kepler Planet-Detection Mission: Introduction and First Results”. In: *Science* 327.5968, p. 977. doi: [10.1126/science.1185402](https://doi.org/10.1126/science.1185402).
- Bouchy, F. et al. (Sept. 2005). “Asteroseismology of the planet-hosting star μ Arae. I. The acoustic spectrum”. In: *A&A* 440.2, pp. 609–614. doi: [10.1051/0004-6361:20052697](https://doi.org/10.1051/0004-6361:20052697). arXiv: [astro-ph/0504043 \[astro-ph\]](https://arxiv.org/abs/astro-ph/0504043).
- Bouvier, J. (Sept. 2013). “Observational studies of stellar rotation”. In: *EAS Publications Series*. Ed. by P. Hennebelle et al. Vol. 62. EAS Publications Series, pp. 143–168. doi: [10.1051/eas/1362005](https://doi.org/10.1051/eas/1362005). arXiv: [1307.2891 \[astro-ph.SR\]](https://arxiv.org/abs/1307.2891).
- Brogaard, K. et al. (Sept. 2016). “Testing asteroseismic scaling relations using eclipsing binaries in star clusters and the field”. In: *Astronomische Nachrichten* 337.8-9, p. 793. doi: [10.1002/asna.201612374](https://doi.org/10.1002/asna.201612374). arXiv: [1601.01412 \[astro-ph.SR\]](https://arxiv.org/abs/1601.01412).
- Brogaard, K. et al. (May 2018). “Establishing the accuracy of asteroseismic mass and radius estimates of giant stars - I. Three eclipsing systems at $[Fe/H] \sim -0.3$ and the need for a large high-precision sample”. In: *MNRAS* 476.3, pp. 3729–3743. doi: [10.1093/mnras/sty268](https://doi.org/10.1093/mnras/sty268). arXiv: [1801.08167 \[astro-ph.SR\]](https://arxiv.org/abs/1801.08167).
- Brogaard, K. et al. (Oct. 2021). “Asteroseismology of overmassive, undermassive, and potential past members of the open cluster NGC 6791”. In: *MNRAS* 507.1, pp. 496–509. doi: [10.1093/mnras/stab2183](https://doi.org/10.1093/mnras/stab2183). arXiv: [2108.03869 \[astro-ph.SR\]](https://arxiv.org/abs/2108.03869).
- Brogaard, K. et al. (Nov. 2023). “Asteroseismic age estimate of the open cluster NGC 6866 using Kepler and Gaia”. In: *A&A* 679, A23, A23. doi: [10.1051/0004-6361/202347330](https://doi.org/10.1051/0004-6361/202347330). arXiv: [2308.12731 \[astro-ph.SR\]](https://arxiv.org/abs/2308.12731).
- Brown, T. M. et al. (Feb. 1991). “Detection of Possible p-Mode Oscillations on Procyon”. In: *ApJ* 368, p. 599. doi: [10.1086/169725](https://doi.org/10.1086/169725).
- Brun, A. S. et al. (Sept. 2017). “Magnetism, dynamo action and the solar-stellar connection”. In: *Living Reviews in Solar Physics* 14.1, 4, p. 4. doi: [10.1007/s41116-017-0007-8](https://doi.org/10.1007/s41116-017-0007-8).

- Bugnet, L. (Nov. 2022). “Magnetic signatures on mixed-mode frequencies. II. Period spacings as a probe of the internal magnetism of red giants”. In: A&A 667, A68, A68. doi: [10.1051/0004-6361/202243167](https://doi.org/10.1051/0004-6361/202243167). arXiv: [2208.14954 \[astro-ph.SR\]](https://arxiv.org/abs/2208.14954).
- Bugnet, L. et al. (June 2021). “Magnetic signatures on mixed-mode frequencies. I. An axisymmetric fossil field inside the core of red giants”. In: A&A 650, A53, A53. doi: [10.1051/0004-6361/202039159](https://doi.org/10.1051/0004-6361/202039159). arXiv: [2102.01216 \[astro-ph.SR\]](https://arxiv.org/abs/2102.01216).
- Bulgen, G. et al. (July 2019). “Progress in global helioseismology: a new light on the solar modelling problem and its implications for solar-like stars”. In: *Frontiers in Astronomy and Space Sciences* 6, 42, p. 42. doi: [10.3389/fspas.2019.00042](https://doi.org/10.3389/fspas.2019.00042). arXiv: [1906.08213 \[astro-ph.SR\]](https://arxiv.org/abs/1906.08213).
- Campante, T. L. et al. (Oct. 2016). “The Asteroseismic Potential of TESS: Exoplanet-host Stars”. In: ApJ 830.2, 138, p. 138. doi: [10.3847/0004-637X/830/2/138](https://doi.org/10.3847/0004-637X/830/2/138). arXiv: [1608.01138 \[astro-ph.SR\]](https://arxiv.org/abs/1608.01138).
- Campante, T. L. et al. (Nov. 2019). “TESS Asteroseismology of the Known Red-giant Host Stars HD 212771 and HD 203949”. In: ApJ 885.1, 31, p. 31. doi: [10.3847/1538-4357/ab44a8](https://doi.org/10.3847/1538-4357/ab44a8). arXiv: [1909.05961 \[astro-ph.SR\]](https://arxiv.org/abs/1909.05961).
- Cantiello, M. et al. (June 2014). “Angular Momentum Transport within Evolved Low-mass Stars”. In: ApJ 788.1, 93, p. 93. doi: [10.1088/0004-637X/788/1/93](https://doi.org/10.1088/0004-637X/788/1/93). arXiv: [1405.1419 \[astro-ph.SR\]](https://arxiv.org/abs/1405.1419).
- Ceillier, T. et al. (July 2013). “Understanding angular momentum transport in red giants: the case of KIC 7341231”. In: A&A 555, A54, A54. doi: [10.1051/0004-6361/201321473](https://doi.org/10.1051/0004-6361/201321473). arXiv: [1305.5630 \[astro-ph.SR\]](https://arxiv.org/abs/1305.5630).
- Çelik Orhan, Z. et al. (May 2021). “Asteroseismic analysis of 15 solar-like oscillating evolved stars”. In: MNRAS 503.3, pp. 4529–4536. doi: [10.1093/mnras/stab757](https://doi.org/10.1093/mnras/stab757). arXiv: [2105.03776 \[astro-ph.SR\]](https://arxiv.org/abs/2105.03776).
- Chaplin, W. J. et al. (Apr. 2011a). “Ensemble Asteroseismology of Solar-Type Stars with the NASA Kepler Mission”. In: Science 332.6026, p. 213. doi: [10.1126/science.1201827](https://doi.org/10.1126/science.1201827). arXiv: [1109.4723 \[astro-ph.SR\]](https://arxiv.org/abs/1109.4723).

- Chaplin, W. J. et al. (May 2011b). “Predicting the Detectability of Oscillations in Solar-type Stars Observed by Kepler”. In: *ApJ* 732.1, 54, p. 54. doi: [10.1088/0004-637X/732/1/54](https://doi.org/10.1088/0004-637X/732/1/54). arXiv: [1103.0702 \[astro-ph.SR\]](https://arxiv.org/abs/1103.0702).
- Chaplin, W. J. et al. (Jan. 2014). “Asteroseismic Fundamental Properties of Solar-type Stars Observed by the NASA Kepler Mission”. In: *ApJS* 210.1, 1, p. 1. doi: [10.1088/0067-0049/210/1/1](https://doi.org/10.1088/0067-0049/210/1/1). arXiv: [1310.4001 \[astro-ph.SR\]](https://arxiv.org/abs/1310.4001).
- Chaplin, W. J. et al. (Jan. 2020). “Age dating of an early Milky Way merger via asteroseismology of the naked-eye star ν Indi”. In: *Nature Astronomy* 4.4, pp. 382–389. ISSN: 2397-3366. doi: [10.1038/s41550-019-0975-9](https://doi.org/10.1038/s41550-019-0975-9). URL: <http://dx.doi.org/10.1038/s41550-019-0975-9>.
- Charbonneau, P. et al. (Nov. 1993). “Angular Momentum Transport in Magnetized Stellar Radiative Zones. II. The Solar Spin-down”. In: *ApJ* 417, p. 762. doi: [10.1086/173357](https://doi.org/10.1086/173357).
- Choi, J. et al. (June 2016). “Mesa Isochrones and Stellar Tracks (MIST). I. Solar-scaled Models”. In: *ApJ* 823.2, 102, p. 102. doi: [10.3847/0004-637X/823/2/102](https://doi.org/10.3847/0004-637X/823/2/102). arXiv: [1604.08592 \[astro-ph.SR\]](https://arxiv.org/abs/1604.08592).
- Chontos, A. et al. (Dec. 2021). “TESS Asteroseismology of α Mensae: Benchmark Ages for a G7 Dwarf and Its M Dwarf Companion”. In: *ApJ* 922.2, 229, p. 229. doi: [10.3847/1538-4357/ac1269](https://doi.org/10.3847/1538-4357/ac1269). arXiv: [2012.10797 \[astro-ph.SR\]](https://arxiv.org/abs/2012.10797).
- Claverie, A. et al. (Dec. 1979). “Solar structure from global studies of the 5-minute oscillation”. In: *Nature* 282, pp. 591–594. doi: [10.1038/282591a0](https://doi.org/10.1038/282591a0).
- Coelho, H. R. et al. (Aug. 2015). “A test of the asteroseismic ν_{max} scaling relation for solar-like oscillations in main-sequence and subgiant stars”. In: *MNRAS* 451.3, pp. 3011–3020. doi: [10.1093/mnras/stv1175](https://doi.org/10.1093/mnras/stv1175). arXiv: [1505.06087 \[astro-ph.SR\]](https://arxiv.org/abs/1505.06087).
- Deheuvels, S. et al. (July 2010). “New insights on the interior of solar-like pulsators thanks to CoRoT: the case of HD 49385”. In: *Ap&SS* 328.1-2, pp. 259–263. doi: [10.1007/s10509-009-0216-2](https://doi.org/10.1007/s10509-009-0216-2). arXiv: [0912.2834 \[astro-ph.SR\]](https://arxiv.org/abs/0912.2834).
- Deheuvels, S. et al. (Apr. 2014). “Seismic constraints on the radial dependence of the internal rotation profiles of six Kepler subgiants and young red giants”. In: *A&A* 564, A27, A27. doi: [10.1051/0004-6361/201322779](https://doi.org/10.1051/0004-6361/201322779). arXiv: [1401.3096 \[astro-ph.SR\]](https://arxiv.org/abs/1401.3096).

- Deheuvels, S. et al. (Feb. 2023). “Strong magnetic fields detected in the cores of 11 red giant stars using gravity-mode period spacings”. In: A&A 670, L16, p. L16. doi: [10.1051/0004-6361/202245282](https://doi.org/10.1051/0004-6361/202245282). arXiv: [2301.01308 \[astro-ph.SR\]](https://arxiv.org/abs/2301.01308).
- Dhanpal, S. et al. (Sept. 2023). “Inferring coupling strengths of mixed-mode oscillations in red-giant stars using deep learning”. In: *arXiv e-prints*, arXiv:2309.17372, arXiv:2309.17372. doi: [10.48550/arXiv.2309.17372](https://doi.org/10.48550/arXiv.2309.17372). arXiv: [2309.17372 \[astro-ph.SR\]](https://arxiv.org/abs/2309.17372).
- Dotter, A. (Jan. 2016). “MESA Isochrones and Stellar Tracks (MIST) 0: Methods for the Construction of Stellar Isochrones”. In: ApJS 222.1, 8, p. 8. doi: [10.3847/0067-0049/222/1/8](https://doi.org/10.3847/0067-0049/222/1/8). arXiv: [1601.05144 \[astro-ph.SR\]](https://arxiv.org/abs/1601.05144).
- Dziembowski, W. (Jan. 1977). “Light and radial velocity variations in a nonradially oscillating star.” In: Acta Astron. 27, pp. 203–211.
- Eddington, A. S. (1926). *The Internal Constitution of the Stars*.
- Eggenberger, P. et al. (Aug. 2012). “Angular momentum transport in stellar interiors constrained by rotational splittings of mixed modes in red giants”. In: A&A 544, L4, p. L4. doi: [10.1051/0004-6361/201219729](https://doi.org/10.1051/0004-6361/201219729). arXiv: [1207.1023 \[astro-ph.SR\]](https://arxiv.org/abs/1207.1023).
- Eggenberger, P. et al. (Mar. 2017). “Constraining the efficiency of angular momentum transport with asteroseismology of red giants: the effect of stellar mass”. In: A&A 599, A18, A18. doi: [10.1051/0004-6361/201629459](https://doi.org/10.1051/0004-6361/201629459). arXiv: [1612.04258 \[astro-ph.SR\]](https://arxiv.org/abs/1612.04258).
- Eggenberger, P. et al. (Nov. 2019). “Asteroseismology of evolved stars to constrain the internal transport of angular momentum. II. Test of a revised prescription for transport by the Tayler instability”. In: A&A 631, L6, p. L6. doi: [10.1051/0004-6361/201936348](https://doi.org/10.1051/0004-6361/201936348). arXiv: [2001.11525 \[astro-ph.SR\]](https://arxiv.org/abs/2001.11525).
- Eggenberger, P. et al. (Aug. 2022). “Rotation in stellar interiors: General formulation and an asteroseismic-calibrated transport by the Tayler instability”. In: A&A 664, L16, p. L16. doi: [10.1051/0004-6361/202243781](https://doi.org/10.1051/0004-6361/202243781). arXiv: [2309.17396 \[astro-ph.SR\]](https://arxiv.org/abs/2309.17396).
- Eggenberger, P. et al. (Aug. 2021). “Grids of stellar models with rotation. VI. Models from 0.8 to 120 M_⊙ at a metallicity Z = 0.006”. In: A&A 652, A137, A137. doi: [10.1051/0004-6361/202141222](https://doi.org/10.1051/0004-6361/202141222). arXiv: [2201.12262 \[astro-ph.GA\]](https://arxiv.org/abs/2201.12262).

- Elsworth, Y. et al. (Apr. 2017). “A new method for the asteroseismic determination of the evolutionary state of red-giant stars”. In: *MNRAS* 466.3, pp. 3344–3352. doi: [10.1093/mnras/stw3288](https://doi.org/10.1093/mnras/stw3288). arXiv: [1612.04751 \[astro-ph.SR\]](https://arxiv.org/abs/1612.04751).
- Emeriau-Viard, C. et al. (Sept. 2017). “Origin and Evolution of Magnetic Field in PMS Stars: Influence of Rotation and Structural Changes”. In: *ApJ* 846.1, 8, p. 8. doi: [10.3847/1538-4357/aa7b33](https://doi.org/10.3847/1538-4357/aa7b33). arXiv: [1709.04667 \[astro-ph.SR\]](https://arxiv.org/abs/1709.04667).
- Fausnaugh, M. M. et al. (Feb. 2019). *TESS Data Release Notes: Sector 5, DR7*. https://tasoc.dk/docs/release_notes/tess_sector_05_drn07_v02.pdf.
- Fausnaugh, M. et al. (Sept. 2021). “The TESS Mission Target Selection Procedure”. In: *PASP* 133.1027, 095002, p. 095002. doi: [10.1088/1538-3873/ac1d3f](https://doi.org/10.1088/1538-3873/ac1d3f). arXiv: [2109.02665 \[astro-ph.IM\]](https://arxiv.org/abs/2109.02665).
- Ferguson, J. W. et al. (Apr. 2005). “Low-Temperature Opacities”. In: *ApJ* 623.1, pp. 585–596. doi: [10.1086/428642](https://doi.org/10.1086/428642). arXiv: [astro-ph/0502045 \[astro-ph\]](https://arxiv.org/abs/astro-ph/0502045).
- Foreman-Mackey, D. et al. (Mar. 2013a). “emcee: The MCMC Hammer”. In: *PASP* 125.925, p. 306. doi: [10.1086/670067](https://doi.org/10.1086/670067). arXiv: [1202.3665 \[astro-ph.IM\]](https://arxiv.org/abs/1202.3665).
- (Feb. 2013b). “emcee: The MCMC Hammer”. In: *Publications of the Astronomical Society of the Pacific* 125.925, p. 306. doi: [10.1086/670067](https://doi.org/10.1086/670067). URL: <https://dx.doi.org/10.1086/670067>.
- Fuller, J. et al. (May 2019). “Slowing the spins of stellar cores”. In: *MNRAS* 485.3, pp. 3661–3680. doi: [10.1093/mnras/stz514](https://doi.org/10.1093/mnras/stz514). arXiv: [1902.08227 \[astro-ph.SR\]](https://arxiv.org/abs/1902.08227).
- Gaia Collaboration et al. (2018). “Gaia Data Release 2 - Summary of the contents and survey properties”. In: *A&A* 616, A1. doi: [10.1051/0004-6361/201833051](https://doi.org/10.1051/0004-6361/201833051). URL: <https://doi.org/10.1051/0004-6361/201833051>.
- García, R. A. et al. (Aug. 2014). “Impact on asteroseismic analyses of regular gaps in Kepler data”. In: *A&A* 568, A10, A10. doi: [10.1051/0004-6361/201323326](https://doi.org/10.1051/0004-6361/201323326). arXiv: [1405.5374 \[astro-ph.SR\]](https://arxiv.org/abs/1405.5374).
- Gaulme, P. et al. (Dec. 2016). “Testing the Asteroseismic Scaling Relations for Red Giants with Eclipsing Binaries Observed by Kepler”. In: *ApJ* 832.2, 121, p. 121. doi: [10.3847/0004-637X/832/2/121](https://doi.org/10.3847/0004-637X/832/2/121). arXiv: [1609.06645 \[astro-ph.SR\]](https://arxiv.org/abs/1609.06645).

- Gaulme, P. et al. (July 2020). “Active red giants: Close binaries versus single rapid rotators”. In: A&A 639, A63, A63. doi: [10.1051/0004-6361/202037781](https://doi.org/10.1051/0004-6361/202037781). arXiv: [2004.13792](https://arxiv.org/abs/2004.13792) [astro-ph.SR].
- Gehan, C. et al. (Aug. 2018a). “Core rotation braking on the red giant branch for various mass ranges”. In: A&A 616, A24, A24. doi: [10.1051/0004-6361/201832822](https://doi.org/10.1051/0004-6361/201832822). arXiv: [1802.04558](https://arxiv.org/abs/1802.04558) [astro-ph.SR].
- (Aug. 2018b). “Core rotation braking on the red giant branch for various mass ranges”. In: A&A 616, A24, A24. doi: [10.1051/0004-6361/201832822](https://doi.org/10.1051/0004-6361/201832822). arXiv: [1802.04558](https://arxiv.org/abs/1802.04558) [astro-ph.SR].
- Gehan, C. et al. (Jan. 2021). “Automated approach to measure stellar inclinations: validation through large-scale measurements on the red giant branch”. In: A&A 645, A124, A124. doi: [10.1051/0004-6361/202039285](https://doi.org/10.1051/0004-6361/202039285). arXiv: [2011.02502](https://arxiv.org/abs/2011.02502) [astro-ph.SR].
- Girardi, L. et al. (June 2005). “Star counts in the Galaxy. Simulating from very deep to very shallow photometric surveys with the TRILEGAL code”. In: A&A 436.3, pp. 895–915. doi: [10.1051/0004-6361:20042352](https://doi.org/10.1051/0004-6361:20042352). arXiv: [astro-ph/0504047](https://arxiv.org/abs/astro-ph/0504047) [astro-ph].
- Gizon, L. et al. (June 2003). “Determining the Inclination of the Rotation Axis of a Sun-like Star”. In: ApJ 589.2, pp. 1009–1019. doi: [10.1086/374715](https://doi.org/10.1086/374715).
- Glebocki, R. et al. (Mar. 2005). *VizieR Online Data Catalog: Catalog of Stellar Rotational Velocities (Glebocki+ 2005)*.
- Godoy-Rivera, D. et al. (July 2021). “Testing the Limits of Precise Subgiant Characterization with APOGEE and Gaia: Opening a Window to Unprecedented Astrophysical Studies”. In: ApJ 915.1, 19, p. 19. doi: [10.3847/1538-4357/abf8ba](https://doi.org/10.3847/1538-4357/abf8ba). arXiv: [2104.07679](https://arxiv.org/abs/2104.07679) [astro-ph.SR].
- Gomes, P. et al. (July 2020). “Core magnetic field imprint in the non-radial oscillations of red giant stars”. In: MNRAS 496.1, pp. 620–628. doi: [10.1093/mnras/staa1585](https://doi.org/10.1093/mnras/staa1585). arXiv: [2007.09632](https://arxiv.org/abs/2007.09632) [astro-ph.SR].
- Goode, P. R. et al. (Aug. 1992). “The Effect of an Inclined Magnetic Field on Solar Oscillation Frequencies”. In: ApJ 395, p. 307. doi: [10.1086/171653](https://doi.org/10.1086/171653).

- Gough, D. O. et al. (Jan. 1990). “The effect of rotation and a buried magnetic field on stellar oscillations”. In: MNRAS 242, pp. 25–55. doi: [10.1093/mnras/242.1.25](https://doi.org/10.1093/mnras/242.1.25).
- Gouhier, B. et al. (May 2022). “Angular momentum transport in a contracting stellar radiative zone embedded in a large-scale magnetic field”. In: A&A 661, A119, A119. doi: [10.1051/0004-6361/202141613](https://doi.org/10.1051/0004-6361/202141613). arXiv: [2201.02645 \[astro-ph.SR\]](https://arxiv.org/abs/2201.02645).
- Goupil, M. J. et al. (Jan. 2013). “Seismic diagnostics for transport of angular momentum in stars. II. Interpreting observed rotational splittings of slowly rotating red giant stars”. In: A&A 549, A75, A75. doi: [10.1051/0004-6361/201220266](https://doi.org/10.1051/0004-6361/201220266). arXiv: [1211.1546 \[astro-ph.SR\]](https://arxiv.org/abs/1211.1546).
- Grevesse, N. et al. (Jan. 1993). “Atomic data and the spectrum of the solar photosphere.” In: *Physica Scripta Volume T* 47, pp. 133–138. doi: [10.1088/0031-8949/1993/T47/021](https://doi.org/10.1088/0031-8949/1993/T47/021).
- Grosjean, M. et al. (Dec. 2014). “Theoretical power spectra of mixed modes in low-mass red giant stars”. In: A&A 572, A11, A11. doi: [10.1051/0004-6361/201423827](https://doi.org/10.1051/0004-6361/201423827). arXiv: [1409.6121 \[astro-ph.SR\]](https://arxiv.org/abs/1409.6121).
- Grundahl, F. et al. (Feb. 2017). “First Results from the Hertzsprung SONG Telescope: Asteroseismology of the G5 Subgiant Star μ Herculis”. In: ApJ 836.1, 142, p. 142. doi: [10.3847/1538-4357/836/1/142](https://doi.org/10.3847/1538-4357/836/1/142). arXiv: [1701.03365 \[astro-ph.SR\]](https://arxiv.org/abs/1701.03365).
- Guggenberger, E. et al. (Aug. 2016). “Significantly improving stellar mass and radius estimates: a new reference function for the $\Delta\nu$ scaling relation”. In: MNRAS 460.4, pp. 4277–4281. doi: [10.1093/mnras/stw1326](https://doi.org/10.1093/mnras/stw1326). arXiv: [1606.01917 \[astro-ph.SR\]](https://arxiv.org/abs/1606.01917).
- Guggenberger, E. et al. (Sept. 2017). “Mitigating the mass dependence in the $\Delta\nu$ scaling relation of red giant stars”. In: MNRAS 470.2, pp. 2069–2078. doi: [10.1093/mnras/stx1253](https://doi.org/10.1093/mnras/stx1253). arXiv: [1705.07886 \[astro-ph.SR\]](https://arxiv.org/abs/1705.07886).
- Handberg, R. et al. (Nov. 2017). “NGC 6819: testing the asteroseismic mass scale, mass loss and evidence for products of non-standard evolution”. In: MNRAS 472.1, pp. 979–997. doi: [10.1093/mnras/stx1929](https://doi.org/10.1093/mnras/stx1929). arXiv: [1707.08223 \[astro-ph.SR\]](https://arxiv.org/abs/1707.08223).
- Handberg, R. et al. (Oct. 2021). “TESS Data for Asteroseismology: Photometry”. In: ApJ 162.4, 170, p. 170. doi: [10.3847/1538-3881/ac09f1](https://doi.org/10.3847/1538-3881/ac09f1). arXiv: [2106.08341 \[astro-ph.IM\]](https://arxiv.org/abs/2106.08341).

- Harris, W. E. (Oct. 1996). “A Catalog of Parameters for Globular Clusters in the Milky Way”. In: AJ 112, p. 1487. doi: [10.1086/118116](https://doi.org/10.1086/118116).
- Harvey, J. (June 1985a). “High-Resolution Helioseismology”. In: *Future Missions in Solar, Heliospheric & Space Plasma Physics*. Ed. by E. Rolfe et al. Vol. 235. ESA Special Publication, p. 199.
- (June 1985b). “High-resolution helioseismology”. In: *Future Missions in Solar, Heliospheric & Space Plasma Physics*. Ed. by E. Rolfe et al. Vol. 235. ESA Special Publication, pp. 199–208.
- Hasan, S. S. et al. (Dec. 2005). “Probing the internal magnetic field of slowly pulsating B-stars through g modes”. In: A&A 444.2, pp. L29–L32. doi: [10.1051/0004-6361:200500203](https://doi.org/10.1051/0004-6361:200500203). arXiv: [astro-ph/0511472 \[astro-ph\]](https://arxiv.org/abs/astro-ph/0511472).
- Hatt, E. et al. (Jan. 2023). “Catalogue of solar-like oscillators observed by TESS in 120-s and 20-s cadence”. In: A&A 669, A67, A67. doi: [10.1051/0004-6361/202244579](https://doi.org/10.1051/0004-6361/202244579). arXiv: [2210.09109 \[astro-ph.SR\]](https://arxiv.org/abs/2210.09109).
- Hekker, S. et al. (Oct. 2009). “Characteristics of solar-like oscillations in red giants observed in the CoRoT exoplanet field”. In: A&A 506.1, pp. 465–469. doi: [10.1051/0004-6361/200911858](https://doi.org/10.1051/0004-6361/200911858). arXiv: [0906.5002 \[astro-ph.SR\]](https://arxiv.org/abs/0906.5002).
- Hekker, S. et al. (Mar. 2010). “The Octave (Birmingham-Sheffield Hallam) automated pipeline for extracting oscillation parameters of solar-like main-sequence stars”. In: MNRAS 402.3, pp. 2049–2059. doi: [10.1111/j.1365-2966.2009.16030.x](https://doi.org/10.1111/j.1365-2966.2009.16030.x). arXiv: [0911.2612 \[astro-ph.SR\]](https://arxiv.org/abs/0911.2612).
- Hekker, S. et al. (Jan. 2011). “Solar-like oscillations in red giants observed with Kepler: comparison of global oscillation parameters from different methods”. In: A&A 525, A131, A131. doi: [10.1051/0004-6361/201015185](https://doi.org/10.1051/0004-6361/201015185). arXiv: [1008.2959 \[astro-ph.SR\]](https://arxiv.org/abs/1008.2959).
- Hon, M. et al. (June 2019). “A search for red giant solar-like oscillations in all Kepler data”. In: MNRAS 485.4, pp. 5616–5630. doi: [10.1093/mnras/stz622](https://doi.org/10.1093/mnras/stz622). arXiv: [1903.00115 \[astro-ph.SR\]](https://arxiv.org/abs/1903.00115).
- Hon, M. et al. (2021). *A ‘Quick Look’ at All-Sky Galactic Archeology with TESS: 158,000 Oscillating Red Giants from the MIT Quick-Look Pipeline*. arXiv: [2108.01241 \[astro-ph.SR\]](https://arxiv.org/abs/2108.01241).

- Houdek, G. (Dec. 2006). “Stochastic excitation and damping of solar-type oscillations”. In: *arXiv e-prints*, astro-ph/0612024, astro-ph/0612024. doi: [10.48550/arXiv.astro-ph/0612024](https://doi.org/10.48550/arXiv.astro-ph/0612024). arXiv: [astro-ph/0612024 \[astro-ph\]](https://arxiv.org/abs/astro-ph/0612024).
- Houdek, G. et al. (Jan. 1999). “On the Location of the Instability Strip”. In: *Stellar Structure: Theory and Test of Connective Energy Transport*. Ed. by A. Gimenez et al. Vol. 173. Astronomical Society of the Pacific Conference Series, p. 317.
- Howe, R. et al. (Mar. 2000). “Dynamic Variations at the Base of the Solar Convection Zone”. In: *Science* 287.5462, pp. 2456–2460. doi: [10.1126/science.287.5462.2456](https://doi.org/10.1126/science.287.5462.2456).
- Howe, R. et al. (Dec. 2015). “Validation of solar-cycle changes in low-degree helioseismic parameters from the Birmingham Solar-Oscillations Network”. In: *MNRAS* 454.4, pp. 4120–4141. doi: [10.1093/mnras/stv2210](https://doi.org/10.1093/mnras/stv2210). arXiv: [1509.06894 \[astro-ph.SR\]](https://arxiv.org/abs/1509.06894).
- Howe, R. (Dec. 2009). “Solar Interior Rotation and its Variation”. In: *Living Reviews in Solar Physics* 6.1, 1, p. 1. doi: [10.12942/lrsp-2009-1](https://doi.org/10.12942/lrsp-2009-1). arXiv: [0902.2406 \[astro-ph.SR\]](https://arxiv.org/abs/0902.2406).
- Hubble, E. P. (Jan. 1925). “Cepheids in Spiral Nebulae”. In: *Popular Astronomy* 33, pp. 252–255.
- (May 1926). “A spiral nebula as a stellar system: Messier 33.” In: *ApJ* 63, pp. 236–274. doi: [10.1086/142976](https://doi.org/10.1086/142976).
- Huber, D. et al. (Oct. 2009). “Automated extraction of oscillation parameters for Kepler observations of solar-type stars”. In: *Communications in Asteroseismology* 160, p. 74. arXiv: [0910.2764 \[astro-ph.SR\]](https://arxiv.org/abs/0910.2764).
- Huber, D. et al. (Dec. 2011). “Testing Scaling Relations for Solar-like Oscillations from the Main Sequence to Red Giants Using Kepler Data”. In: *ApJ* 743.2, 143, p. 143. doi: [10.1088/0004-637X/743/2/143](https://doi.org/10.1088/0004-637X/743/2/143). arXiv: [1109.3460 \[astro-ph.SR\]](https://arxiv.org/abs/1109.3460).
- Huber, D. et al. (Nov. 2012). “Fundamental Properties of Stars Using Asteroseismology from Kepler and CoRoT and Interferometry from the CHARA Array”. In: *ApJ* 760.1, 32, p. 32. doi: [10.1088/0004-637X/760/1/32](https://doi.org/10.1088/0004-637X/760/1/32). arXiv: [1210.0012 \[astro-ph.SR\]](https://arxiv.org/abs/1210.0012).
- Huber, D. et al. (Mar. 2014). “Revised Stellar Properties of Kepler Targets for the Quarter 1–16 Transit Detection Run”. In: *ApJS* 211.1, 2, p. 2. doi: [10.1088/0067-0049/211/1/2](https://doi.org/10.1088/0067-0049/211/1/2). arXiv: [1312.0662 \[astro-ph.EP\]](https://arxiv.org/abs/1312.0662).

- Huber, D. et al. (June 2019). “A Hot Saturn Orbiting an Oscillating Late Subgiant Discovered by TESS”. In: *ApJ* 157.6, 245, p. 245. doi: [10.3847/1538-3881/ab1488](https://doi.org/10.3847/1538-3881/ab1488). arXiv: [1901.01643 \[astro-ph.EP\]](https://arxiv.org/abs/1901.01643).
- Huber, D. et al. (Feb. 2022). “A 20 Second Cadence View of Solar-type Stars and Their Planets with TESS: Asteroseismology of Solar Analogs and a Recharacterization of π Men c”. In: *ApJ* 163.2, 79, p. 79. doi: [10.3847/1538-3881/ac3000](https://doi.org/10.3847/1538-3881/ac3000). arXiv: [2108.09109 \[astro-ph.SR\]](https://arxiv.org/abs/2108.09109).
- Iglesias, C. A. et al. (June 1996). “Updated Opal Opacities”. In: *ApJ* 464, p. 943. doi: [10.1086/177381](https://doi.org/10.1086/177381).
- Irwin, J. et al. (June 2009). “The rotational evolution of low-mass stars”. In: *The Ages of Stars*. Ed. by E. E. Mamajek et al. Vol. 258, pp. 363–374. doi: [10.1017/S1743921309032025](https://doi.org/10.1017/S1743921309032025). arXiv: [0901.3342 \[astro-ph.SR\]](https://arxiv.org/abs/0901.3342).
- Jenkins, J. M. et al. (Aug. 2016). “The TESS science processing operations center”. In: *Software and Cyberinfrastructure for Astronomy IV*. Ed. by G. Chiozzi et al. Vol. 9913. Society of Photo-Optical Instrumentation Engineers (SPIE) Conference Series, 99133E, 99133E. doi: [10.1117/12.2233418](https://doi.org/10.1117/12.2233418).
- Jiang, C. et al. (June 2020). “TESS Asteroseismic Analysis of the Known Exoplanet Host Star HD 222076”. In: *ApJ* 896.1, 65, p. 65. doi: [10.3847/1538-4357/ab8f29](https://doi.org/10.3847/1538-4357/ab8f29). arXiv: [2005.00272 \[astro-ph.SR\]](https://arxiv.org/abs/2005.00272).
- Kallinger, T. et al. (Nov. 2010). “Asteroseismology of red giants from the first four months of Kepler data: Fundamental stellar parameters”. In: *A&A* 522, A1, A1. doi: [10.1051/0004-6361/201015263](https://doi.org/10.1051/0004-6361/201015263). arXiv: [1010.4589 \[astro-ph.SR\]](https://arxiv.org/abs/1010.4589).
- Kallinger, T. et al. (Oct. 2014a). “The connection between stellar granulation and oscillation as seen by the Kepler mission”. In: *A&A* 570, A41, A41. doi: [10.1051/0004-6361/201424313](https://doi.org/10.1051/0004-6361/201424313). arXiv: [1408.0817 \[astro-ph.SR\]](https://arxiv.org/abs/1408.0817).
- (Oct. 2014b). “The connection between stellar granulation and oscillation as seen by the Kepler mission”. In: *A&A* 570, A41, A41. doi: [10.1051/0004-6361/201424313](https://doi.org/10.1051/0004-6361/201424313). arXiv: [1408.0817 \[astro-ph.SR\]](https://arxiv.org/abs/1408.0817).

- Karoff, C. et al. (June 2007). “Detection of p-mode oscillations in β Hydri from photometric observations with WIRE”. In: *Communications in Asteroseismology* 150, p. 147. doi: [10.1553/cia150s147](https://doi.org/10.1553/cia150s147).
- Kippenhahn, R. et al. (1990). *Stellar Structure and Evolution*.
- (1994). *Stellar Structure and Evolution*.
- Kjeldsen, H. et al. (Jan. 1995). “Amplitudes of stellar oscillations: the implications for asteroseismology.” In: A&A 293, pp. 87–106. doi: [10.48550/arXiv.astro-ph/9403015](https://doi.org/10.48550/arXiv.astro-ph/9403015). arXiv: [astro-ph/9403015 \[astro-ph\]](https://arxiv.org/abs/astro-ph/9403015).
- (May 2011). “Amplitudes of solar-like oscillations: a new scaling relation”. In: A&A 529, L8, p. L8. doi: [10.1051/0004-6361/201116789](https://doi.org/10.1051/0004-6361/201116789). arXiv: [1104.1659 \[astro-ph.SR\]](https://arxiv.org/abs/1104.1659).
- Kraft, R. P. (Nov. 1967). “Studies of Stellar Rotation. V. The Dependence of Rotation on Age among Solar-Type Stars”. In: ApJ 150, p. 551. doi: [10.1086/149359](https://doi.org/10.1086/149359).
- Krishna Swamy, K. S. (July 1966). “Profiles of Strong Lines in K-Dwarfs”. In: ApJ 145, p. 174. doi: [10.1086/148752](https://doi.org/10.1086/148752).
- Kurtz, D. (Mar. 2022). “Asteroseismology across the HR diagram”. In: *Annual Conference and General Assembly of the*, 1, p. 1. doi: [10.48550/arXiv.2201.11629](https://doi.org/10.48550/arXiv.2201.11629). arXiv: [2201.11629 \[astro-ph.SR\]](https://arxiv.org/abs/2201.11629).
- Kuszlewicz, J. S. et al. (Oct. 2020). “Clumpiness: time-domain classification of red giant evolutionary states”. In: MNRAS 497.4, pp. 4843–4856. doi: [10.1093/mnras/staa2155](https://doi.org/10.1093/mnras/staa2155). arXiv: [2007.10921 \[astro-ph.SR\]](https://arxiv.org/abs/2007.10921).
- Kuszlewicz, J. S. et al. (Sept. 2023). “Mixed-mode Ensemble Asteroseismology of Low-luminosity Kepler Red Giants”. In: ApJ 954.2, 152, p. 152. doi: [10.3847/1538-4357/ace598](https://doi.org/10.3847/1538-4357/ace598). arXiv: [2307.06482 \[astro-ph.SR\]](https://arxiv.org/abs/2307.06482).
- Lagarde, N. et al. (Aug. 2015). “Models of red giants in the CoRoT asteroseismology fields combining asteroseismic and spectroscopic constraints”. In: A&A 580, A141, A141. doi: [10.1051/0004-6361/201525856](https://doi.org/10.1051/0004-6361/201525856). arXiv: [1505.01529 \[astro-ph.SR\]](https://arxiv.org/abs/1505.01529).

- Lebreton, Y. et al. (Sept. 2014). “Asteroseismology for “à la carte” stellar age-dating and weighing. Age and mass of the CoRoT exoplanet host HD 52265”. In: *A&A* 569, A21, A21. doi: [10.1051/0004-6361/201423797](https://doi.org/10.1051/0004-6361/201423797). arXiv: [1406.0652 \[astro-ph.SR\]](https://arxiv.org/abs/1406.0652).
- Lefebvre, S. et al. (Nov. 2008). “Variations of the solar granulation motions with height using the GOLF/SoHO experiment”. In: *A&A* 490.3, pp. 1143–1149. doi: [10.1051/0004-6361:200810344](https://doi.org/10.1051/0004-6361:200810344). arXiv: [0808.0422 \[astro-ph\]](https://arxiv.org/abs/0808.0422).
- Leighton, R. B. et al. (Mar. 1962). “Velocity Fields in the Solar Atmosphere. I. Preliminary Report.” In: *ApJ* 135, p. 474. doi: [10.1086/147285](https://doi.org/10.1086/147285).
- Li, G. et al. (Oct. 2022a). “Magnetic fields of 30 to 100 kG in the cores of red giant stars”. In: *Nature* 610.7930, pp. 43–46. doi: [10.1038/s41586-022-05176-0](https://doi.org/10.1038/s41586-022-05176-0). arXiv: [2208.09487 \[astro-ph.SR\]](https://arxiv.org/abs/2208.09487).
- Li, G. et al. (Sept. 2023). “Internal magnetic fields in 13 red giants detected by asteroseismology”. In: *arXiv e-prints*, arXiv:2309.13756, arXiv:2309.13756. doi: [10.48550/arXiv.2309.13756](https://doi.org/10.48550/arXiv.2309.13756). arXiv: [2309.13756 \[astro-ph.SR\]](https://arxiv.org/abs/2309.13756).
- Li, T. et al. (Mar. 2022b). “Asteroseismology of 3642 Kepler Red Giants: Correcting the Scaling Relations Based on Detailed Modeling”. In: *ApJ* 927.2, 167, p. 167. doi: [10.3847/1538-4357/ac4fbf](https://doi.org/10.3847/1538-4357/ac4fbf). arXiv: [2201.09577 \[astro-ph.SR\]](https://arxiv.org/abs/2201.09577).
- Li, Y. et al. (June 2020). “Asteroseismology of 36 Kepler subgiants - I. Oscillation frequencies, linewidths, and amplitudes”. In: *MNRAS* 495.2, pp. 2363–2386. doi: [10.1093/mnras/staa1335](https://doi.org/10.1093/mnras/staa1335). arXiv: [2005.06460 \[astro-ph.SR\]](https://arxiv.org/abs/2005.06460).
- Li, Y. et al. (Mar. 2021). “Testing the intrinsic scatter of the asteroseismic scaling relations with Kepler red giants”. In: *MNRAS* 501.3, pp. 3162–3172. doi: [10.1093/mnras/staa3932](https://doi.org/10.1093/mnras/staa3932). arXiv: [2012.10038 \[astro-ph.SR\]](https://arxiv.org/abs/2012.10038).
- Liebert, J. et al. (Jan. 2003). “The True Incidence of Magnetism Among Field White Dwarfs”. In: *AJ* 125.1, pp. 348–353. doi: [10.1086/345573](https://doi.org/10.1086/345573). arXiv: [astro-ph/0210319 \[astro-ph\]](https://arxiv.org/abs/astro-ph/0210319).
- Lightkurve Collaboration et al. (Dec. 2018). *Lightkurve: Kepler and TESS time series analysis in Python*. Astrophysics Source Code Library. ascl: [1812.013](https://ascl.net/1812.013).

- Lindegren, L. et al. (Aug. 2018). “Gaia Data Release 2. The astrometric solution”. In: *A&A* 616, A2, A2. doi: [10.1051/0004-6361/201832727](https://doi.org/10.1051/0004-6361/201832727). arXiv: [1804.09366 \[astro-ph.IM\]](https://arxiv.org/abs/1804.09366).
- Loi, S. T. (July 2021). “Topology and obliquity of core magnetic fields in shaping seismic properties of slowly rotating evolved stars”. In: *MNRAS* 504.3, pp. 3711–3729. doi: [10.1093/mnras/stab991](https://doi.org/10.1093/mnras/stab991). arXiv: [2104.03112 \[astro-ph.SR\]](https://arxiv.org/abs/2104.03112).
- Lomb, N. R. (Feb. 1976). “Least-Squares Frequency Analysis of Unequally Spaced Data”. In: *Ap&SS* 39.2, pp. 447–462. doi: [10.1007/BF00648343](https://doi.org/10.1007/BF00648343).
- Lund, M. N. et al. (Feb. 2017). “Standing on the Shoulders of Dwarfs: the Kepler Asteroseismic LEGACY Sample. I. Oscillation Mode Parameters”. In: *ApJ* 835.2, 172, p. 172. doi: [10.3847/1538-4357/835/2/172](https://doi.org/10.3847/1538-4357/835/2/172). arXiv: [1612.00436 \[astro-ph.SR\]](https://arxiv.org/abs/1612.00436).
- Mackereth, J. T. et al. (Apr. 2021). “Prospects for Galactic and stellar astrophysics with asteroseismology of giant stars in the TESS continuous viewing zones and beyond”. In: *MNRAS* 502.2, pp. 1947–1966. doi: [10.1093/mnras/stab098](https://doi.org/10.1093/mnras/stab098). arXiv: [2012.00140 \[astro-ph.GA\]](https://arxiv.org/abs/2012.00140).
- Maeder, A. et al. (Sept. 2005). “Stellar evolution with rotation and magnetic fields. III. The interplay of circulation and dynamo”. In: *A&A* 440.3, pp. 1041–1049. doi: [10.1051/0004-6361:20053261](https://doi.org/10.1051/0004-6361:20053261). arXiv: [astro-ph/0506347 \[astro-ph\]](https://arxiv.org/abs/astro-ph/0506347).
- Maeder, A. et al. (Mar. 2010). “Evolution of massive stars with mass loss and rotation”. In: *New A Rev.* 54.3-6, pp. 32–38. doi: [10.1016/j.newar.2010.09.017](https://doi.org/10.1016/j.newar.2010.09.017).
- (Jan. 2012). “Rotating massive stars: From first stars to gamma ray bursts”. In: *Reviews of Modern Physics* 84.1, pp. 25–63. doi: [10.1103/RevModPhys.84.25](https://doi.org/10.1103/RevModPhys.84.25).
- (Oct. 2014). “Magnetic Braking of Stellar Cores in Red Giants and Supergiants”. In: *ApJ* 793.2, 123, p. 123. doi: [10.1088/0004-637X/793/2/123](https://doi.org/10.1088/0004-637X/793/2/123). arXiv: [1408.1192 \[astro-ph.SR\]](https://arxiv.org/abs/1408.1192).
- Magic, Z. et al. (Sept. 2013). “The Stagger-grid: A grid of 3D stellar atmosphere models. I. Methods and general properties”. In: *A&A* 557, A26, A26. doi: [10.1051/0004-6361/201321274](https://doi.org/10.1051/0004-6361/201321274). arXiv: [1302.2621 \[astro-ph.SR\]](https://arxiv.org/abs/1302.2621).
- Marques, J. P. et al. (Jan. 2013). “Seismic diagnostics for transport of angular momentum in stars. I. Rotational splittings from the pre-main sequence to the red-giant branch”. In: *A&A* 549, A74, A74. doi: [10.1051/0004-6361/201220211](https://doi.org/10.1051/0004-6361/201220211). arXiv: [1211.1271 \[astro-ph.SR\]](https://arxiv.org/abs/1211.1271).

- Mathis, S. et al. (Mar. 2021). “Probing the internal magnetism of stars using asymptotic magneto-asteroseismology”. In: A&A 647, A122, A122. doi: [10.1051/0004-6361/202039180](https://doi.org/10.1051/0004-6361/202039180). arXiv: [2012.11050 \[astro-ph.SR\]](https://arxiv.org/abs/2012.11050).
- Mathis, S. et al. (Aug. 2023). “Asymmetries of frequency splittings of dipolar mixed modes: A window on the topology of deep magnetic fields”. In: A&A 676, L9, p. L9. doi: [10.1051/0004-6361/202346832](https://doi.org/10.1051/0004-6361/202346832). arXiv: [2306.11587 \[astro-ph.SR\]](https://arxiv.org/abs/2306.11587).
- Mathur, S. et al. (Feb. 2010). “Determining global parameters of the oscillations of solar-like stars”. In: A&A 511, A46, A46. doi: [10.1051/0004-6361/200913266](https://doi.org/10.1051/0004-6361/200913266). arXiv: [0912.3367 \[astro-ph.SR\]](https://arxiv.org/abs/0912.3367).
- Mathur, S. et al. (Nov. 2011). “Granulation in Red Giants: Observations by the Kepler Mission and Three-dimensional Convection Simulations”. In: ApJ 741.2, 119, p. 119. doi: [10.1088/0004-637X/741/2/119](https://doi.org/10.1088/0004-637X/741/2/119). arXiv: [1109.1194 \[astro-ph.SR\]](https://arxiv.org/abs/1109.1194).
- Mathur, S. et al. (Apr. 2012). “A Uniform Asteroseismic Analysis of 22 Solar-type Stars Observed by Kepler”. In: ApJ 749.2, 152, p. 152. doi: [10.1088/0004-637X/749/2/152](https://doi.org/10.1088/0004-637X/749/2/152). arXiv: [1202.2844 \[astro-ph.SR\]](https://arxiv.org/abs/1202.2844).
- Mathur, S. et al. (Jan. 2022). “Detections of solar-like oscillations in dwarfs and subgiants with Kepler DR25 short-cadence data”. In: A&A 657, A31, A31. doi: [10.1051/0004-6361/202141168](https://doi.org/10.1051/0004-6361/202141168). arXiv: [2109.14058 \[astro-ph.SR\]](https://arxiv.org/abs/2109.14058).
- McKeever, J. et al. (Apr. 2019). “The Helium Abundance of NGC 6791 from Modeling of Stellar Oscillations”. In: ApJ 874.2, 180, p. 180. doi: [10.3847/1538-4357/ab0c04](https://doi.org/10.3847/1538-4357/ab0c04). arXiv: [1903.00497 \[astro-ph.SR\]](https://arxiv.org/abs/1903.00497).
- Mestel, L. et al. (May 1987). “Magnetic fields and non-uniform rotation in stellar radiative zones.” In: MNRAS 226, pp. 123–135. doi: [10.1093/mnras/226.1.123](https://doi.org/10.1093/mnras/226.1.123).
- Metcalfe, T. S. et al. (Oct. 2014). “Properties of 42 Solar-type Kepler Targets from the Asteroseismic Modeling Portal”. In: ApJS 214.2, 27, p. 27. doi: [10.1088/0067-0049/214/2/27](https://doi.org/10.1088/0067-0049/214/2/27). arXiv: [1402.3614 \[astro-ph.SR\]](https://arxiv.org/abs/1402.3614).

- Metcalfe, T. S. et al. (Sept. 2020). “The Evolution of Rotation and Magnetic Activity in 94 Aqr Aa from Asteroseismology with TESS”. In: *ApJ* 900.2, 154, p. 154. doi: [10.3847/1538-4357/aba963](https://doi.org/10.3847/1538-4357/aba963). arXiv: [2007.12755 \[astro-ph.SR\]](https://arxiv.org/abs/2007.12755).
- Metropolis, N. et al. (June 1953). “Equation of State Calculations by Fast Computing Machines”. In: *J. Chem. Phys.* 21.6, pp. 1087–1092. doi: [10.1063/1.1699114](https://doi.org/10.1063/1.1699114).
- Meynet, G. et al. (Sept. 2000). “Stellar evolution with rotation. V. Changes in all the outputs of massive star models”. In: *A&A* 361, pp. 101–120. doi: [10.48550/arXiv.astro-ph/0006404](https://doi.org/10.48550/arXiv.astro-ph/0006404). arXiv: [astro-ph/0006404 \[astro-ph\]](https://arxiv.org/abs/astro-ph/0006404).
- Miglio, A. et al. (Jan. 2012). “Asteroseismology of old open clusters with Kepler: direct estimate of the integrated red giant branch mass-loss in NGC 6791 and 6819”. In: *MNRAS* 419.3, pp. 2077–2088. doi: [10.1111/j.1365-2966.2011.19859.x](https://doi.org/10.1111/j.1365-2966.2011.19859.x). arXiv: [1109.4376 \[astro-ph.SR\]](https://arxiv.org/abs/1109.4376).
- Miglio, A. et al. (June 2021). “Haydn”. In: *Experimental Astronomy* 51.3, pp. 963–1001. doi: [10.1007/s10686-021-09711-1](https://doi.org/10.1007/s10686-021-09711-1). arXiv: [1908.05129 \[astro-ph.SR\]](https://arxiv.org/abs/1908.05129).
- Mombarg, J. S. G. (Sept. 2023). “Calibrating angular momentum transport in intermediate-mass stars from gravity-mode asteroseismology”. In: *A&A* 677, A63, A63. doi: [10.1051/0004-6361/202345956](https://doi.org/10.1051/0004-6361/202345956). arXiv: [2306.17211 \[astro-ph.SR\]](https://arxiv.org/abs/2306.17211).
- Mosser, B. et al. (Dec. 2009a). “On detecting the large separation in the autocorrelation of stellar oscillation times series”. In: *A&A* 508.2, pp. 877–887. doi: [10.1051/0004-6361/200912944](https://doi.org/10.1051/0004-6361/200912944). arXiv: [0909.0782 \[astro-ph.SR\]](https://arxiv.org/abs/0909.0782).
- Mosser, B. et al. (Oct. 2009b). “The CoRoT target HD 175726: an active star with weak solar-like oscillations”. In: *A&A* 506.1, pp. 33–40. doi: [10.1051/0004-6361/200911917](https://doi.org/10.1051/0004-6361/200911917). arXiv: [0908.2244 \[astro-ph.SR\]](https://arxiv.org/abs/0908.2244).
- Mosser, B. et al. (July 2010). “Red-giant seismic properties analyzed with CoRoT”. In: *A&A* 517, A22, A22. doi: [10.1051/0004-6361/201014036](https://doi.org/10.1051/0004-6361/201014036). arXiv: [1004.0449 \[astro-ph.SR\]](https://arxiv.org/abs/1004.0449).
- Mosser, B. et al. (Jan. 2011). “The universal red-giant oscillation pattern. An automated determination with CoRoT data”. In: *A&A* 525, L9, p. L9. doi: [10.1051/0004-6361/201015440](https://doi.org/10.1051/0004-6361/201015440). arXiv: [1011.1928 \[astro-ph.SR\]](https://arxiv.org/abs/1011.1928).

- Mosser, B. et al. (Jan. 2012a). “Characterization of the power excess of solar-like oscillations in red giants with Kepler”. In: A&A 537, A30, A30. doi: [10.1051/0004-6361/20111735210](https://doi.org/10.1051/0004-6361/20111735210). arXiv: [1110.0980 \[astro-ph.SR\]](https://arxiv.org/abs/1110.0980).
- Mosser, B. et al. (Apr. 2012b). “Probing the core structure and evolution of red giants using gravity-dominated mixed modes observed with Kepler”. In: A&A 540, A143, A143. doi: [10.1051/0004-6361/201118519](https://doi.org/10.1051/0004-6361/201118519). arXiv: [1203.0689 \[astro-ph.SR\]](https://arxiv.org/abs/1203.0689).
- Mosser, B. et al. (Feb. 2013). “Asymptotic and measured large frequency separations”. In: A&A 550, A126, A126. doi: [10.1051/0004-6361/201220435](https://doi.org/10.1051/0004-6361/201220435). arXiv: [1212.1687 \[astro-ph.SR\]](https://arxiv.org/abs/1212.1687).
- Mosser, B. et al. (Dec. 2014). “Mixed modes in red giants: a window on stellar evolution”. In: A&A 572, L5, p. L5. doi: [10.1051/0004-6361/201425039](https://doi.org/10.1051/0004-6361/201425039). arXiv: [1411.1082 \[astro-ph.SR\]](https://arxiv.org/abs/1411.1082).
- Mosser, B. et al. (Dec. 2015). “Period spacings in red giants. I. Disentangling rotation and revealing core structure discontinuities”. In: A&A 584, A50, A50. doi: [10.1051/0004-6361/201527075](https://doi.org/10.1051/0004-6361/201527075). arXiv: [1509.06193 \[astro-ph.SR\]](https://arxiv.org/abs/1509.06193).
- Mosser, B. et al. (Apr. 2017). “Period spacings in red giants. III. Coupling factors of mixed modes”. In: A&A 600, A1, A1. doi: [10.1051/0004-6361/201630053](https://doi.org/10.1051/0004-6361/201630053). arXiv: [1612.08453 \[astro-ph.SR\]](https://arxiv.org/abs/1612.08453).
- Mosser, B. et al. (Oct. 2018). “Period spacings in red giants. IV. Toward a complete description of the mixed-mode pattern”. In: A&A 618, A109, A109. doi: [10.1051/0004-6361/201832777](https://doi.org/10.1051/0004-6361/201832777).
- Moyano, F. D. et al. (May 2023). “Asteroseismology of evolved stars to constrain the internal transport of angular momentum. VI. Testing a parametric formulation for the azimuthal magneto-rotational instability”. In: A&A 673, A110, A110. doi: [10.1051/0004-6361/202245519](https://doi.org/10.1051/0004-6361/202245519). arXiv: [2302.07811 \[astro-ph.SR\]](https://arxiv.org/abs/2302.07811).
- Nielsen, M. B. et al. (Sept. 2020). “TESS asteroseismology of the known planet host star λ^2 Fornacis”. In: A&A 641, A25, A25. doi: [10.1051/0004-6361/202037461](https://doi.org/10.1051/0004-6361/202037461). arXiv: [2007.00497 \[astro-ph.SR\]](https://arxiv.org/abs/2007.00497).

- Nielsen, M. B. et al. (Feb. 2021). “PBjam: A Python Package for Automating Asteroseismology of Solar-like Oscillators”. In: *ApJ* 161.2, 62, p. 62. doi: [10.3847/1538-3881/abcd39](https://doi.org/10.3847/1538-3881/abcd39). arXiv: [2012.00580 \[astro-ph.SR\]](https://arxiv.org/abs/2012.00580).
- Nielsen, M. B. et al. (Mar. 2022a). “A probabilistic method for detecting solar-like oscillations using meaningful prior information”. In: *arXiv e-prints*, arXiv:2203.09404, arXiv:2203.09404. arXiv: [2203.09404 \[astro-ph.SR\]](https://arxiv.org/abs/2203.09404).
- (July 2022b). “A probabilistic method for detecting solar-like oscillations using meaningful prior information. Application to TESS 2-minute photometry”. In: *A&A* 663, A51, A51. doi: [10.1051/0004-6361/202243064](https://doi.org/10.1051/0004-6361/202243064). arXiv: [2203.09404 \[astro-ph.SR\]](https://arxiv.org/abs/2203.09404).
- Nielsen, M. B. et al. (June 2023). “Simplifying asteroseismic analysis of solar-like oscillators: An application of principal component analysis for dimensionality reduction”. In: *arXiv e-prints*, arXiv:2306.13577, arXiv:2306.13577. doi: [10.48550/arXiv.2306.13577](https://doi.org/10.48550/arXiv.2306.13577). arXiv: [2306.13577 \[astro-ph.SR\]](https://arxiv.org/abs/2306.13577).
- Noyes, R. W. et al. (Apr. 1984). “Rotation, convection, and magnetic activity in lower main-sequence stars.” In: *ApJ* 279, pp. 763–777. doi: [10.1086/161945](https://doi.org/10.1086/161945).
- Ong, J. M. et al. (2023a). “Reggae: A Parametric Tuner for PBJam, and a Visualization Tool for Red Giant Oscillation Spectra”. In: *Journal of Open Source Software*.
- Ong, J. M. J. et al. (Oct. 2021a). “Mixed Modes and Asteroseismic Surface Effects. I. Analytic Treatment”. In: *ApJ* 920.1, 8, p. 8. doi: [10.3847/1538-4357/ac12ca](https://doi.org/10.3847/1538-4357/ac12ca). arXiv: [2107.03405 \[astro-ph.SR\]](https://arxiv.org/abs/2107.03405).
- Ong, J. M. J. et al. (Nov. 2021b). “Mixed Modes and Asteroseismic Surface Effects. II. Subgiant Systematics”. In: *ApJ* 922.1, 18, p. 18. doi: [10.3847/1538-4357/ac1e8b](https://doi.org/10.3847/1538-4357/ac1e8b). arXiv: [2108.07370 \[astro-ph.SR\]](https://arxiv.org/abs/2108.07370).
- Ong, J. M. J. et al. (Apr. 2023b). “Mode Mixing and Rotational Splittings. II. Reconciling Different Approaches to Mode Coupling”. In: *ApJ* 946.1, 92, p. 92. doi: [10.3847/1538-4357/acbf2f](https://doi.org/10.3847/1538-4357/acbf2f). arXiv: [2302.12402 \[astro-ph.SR\]](https://arxiv.org/abs/2302.12402).

- Ouazzani, R.-M. et al. (Feb. 2017). “A new asteroseismic diagnostic for internal rotation in γ Doradus stars”. In: MNRAS 465.2, pp. 2294–2309. doi: [10.1093/mnras/stw2717](https://doi.org/10.1093/mnras/stw2717). arXiv: [1610.06184 \[astro-ph.SR\]](https://arxiv.org/abs/1610.06184).
- Parker, E. N. (Sept. 1955). “Hydromagnetic Dynamo Models.” In: ApJ 122, p. 293. doi: [10.1086/146087](https://doi.org/10.1086/146087).
- Paxton, B. et al. (Jan. 2011). “Modules for Experiments in Stellar Astrophysics (MESA)”. In: ApJS 192.1, 3, p. 3. doi: [10.1088/0067-0049/192/1/3](https://doi.org/10.1088/0067-0049/192/1/3). arXiv: [1009.1622 \[astro-ph.SR\]](https://arxiv.org/abs/1009.1622).
- Paxton, B. et al. (Sept. 2013). “Modules for Experiments in Stellar Astrophysics (MESA): Planets, Oscillations, Rotation, and Massive Stars”. In: ApJS 208.1, 4, p. 4. doi: [10.1088/0067-0049/208/1/4](https://doi.org/10.1088/0067-0049/208/1/4). arXiv: [1301.0319 \[astro-ph.SR\]](https://arxiv.org/abs/1301.0319).
- Perryman, M. A. C. et al. (Apr. 2001). “GAIA: Composition, formation and evolution of the Galaxy”. In: A&A 369, pp. 339–363. doi: [10.1051/0004-6361:20010085](https://doi.org/10.1051/0004-6361:20010085). arXiv: [astro-ph/0101235 \[astro-ph\]](https://arxiv.org/abs/astro-ph/0101235).
- Petitdemange, L. et al. (Jan. 2023). “Spin-down by dynamo action in simulated radiative stellar layers”. In: Science 379.6629, pp. 300–303. doi: [10.1126/science.abk2169](https://doi.org/10.1126/science.abk2169). arXiv: [2206.13819 \[astro-ph.SR\]](https://arxiv.org/abs/2206.13819).
- Pourbaix, D. et al. (Sept. 2004). “ S_B^9 : The ninth catalogue of spectroscopic binary orbits”. In: A&A 424, pp. 727–732. doi: [10.1051/0004-6361:20041213](https://doi.org/10.1051/0004-6361:20041213). arXiv: [astro-ph/0406573 \[astro-ph\]](https://arxiv.org/abs/astro-ph/0406573).
- Power, J. et al. (Apr. 2008). “Properties of a volume-limited sample of Ap-stars”. In: Contributions of the Astronomical Observatory Skalnaté Pleso 38.2, pp. 443–444.
- Prat, V. et al. (July 2019). “Period spacings of gravity modes in rapidly rotating magnetic stars. I. Axisymmetric fossil field with poloidal and toroidal components”. In: A&A 627, A64, A64. doi: [10.1051/0004-6361/201935462](https://doi.org/10.1051/0004-6361/201935462). arXiv: [1903.05620 \[astro-ph.SR\]](https://arxiv.org/abs/1903.05620).
- Press, W. H. et al. (Mar. 1989). “Fast Algorithm for Spectral Analysis of Unevenly Sampled Data”. In: ApJ 338, p. 277. doi: [10.1086/167197](https://doi.org/10.1086/167197).
- Rauer, H. et al. (Nov. 2014). “The PLATO 2.0 mission”. In: Experimental Astronomy 38.1-2, pp. 249–330. doi: [10.1007/s10686-014-9383-4](https://doi.org/10.1007/s10686-014-9383-4). arXiv: [1310.0696 \[astro-ph.EP\]](https://arxiv.org/abs/1310.0696).

- Reimers, D. (Jan. 1975). “Circumstellar absorption lines and mass loss from red giants.” In: *Memoires of the Societe Royale des Sciences de Liege* 8, pp. 369–382.
- Reiners, A. et al. (June 2022). “Magnetism, rotation, and nonthermal emission in cool stars. Average magnetic field measurements in 292 M dwarfs”. In: A&A 662, A41, A41. doi: [10.1051/0004-6361/202243251](https://doi.org/10.1051/0004-6361/202243251). arXiv: [2204.00342 \[astro-ph.SR\]](https://arxiv.org/abs/2204.00342).
- Rendle, B. M. et al. (Mar. 2019). “AIMS - a new tool for stellar parameter determinations using asteroseismic constraints”. In: MNRAS 484.1, pp. 771–786. doi: [10.1093/mnras/stz031](https://doi.org/10.1093/mnras/stz031). arXiv: [1901.02663 \[astro-ph.SR\]](https://arxiv.org/abs/1901.02663).
- Ricker, G. R. (Mar. 2014). “The Transiting Exoplanet Survey Satellite Mission”. In: *Search for Life Beyond the Solar System. Exoplanets, Biosignatures & Instruments*. Ed. by D. Apai et al., 3.10, p. 3.10.
- Ricker, G. R. et al. (Aug. 2014). “Transiting Exoplanet Survey Satellite (TESS)”. In: *Space Telescopes and Instrumentation 2014: Optical, Infrared, and Millimeter Wave*. Ed. by J. Oschmann Jacobus M. et al. Vol. 9143. Society of Photo-Optical Instrumentation Engineers (SPIE) Conference Series, 914320, p. 914320. doi: [10.1117/12.2063489](https://doi.org/10.1117/12.2063489). arXiv: [1406.0151 \[astro-ph.EP\]](https://arxiv.org/abs/1406.0151).
- Rodrigues, T. S. et al. (May 2017). “Determining stellar parameters of asteroseismic targets: going beyond the use of scaling relations”. In: MNRAS 467.2, pp. 1433–1448. doi: [10.1093/mnras/stx120](https://doi.org/10.1093/mnras/stx120). arXiv: [1701.04791 \[astro-ph.SR\]](https://arxiv.org/abs/1701.04791).
- Rogers, F. J. et al. (Sept. 2002). “Updated and Expanded OPAL Equation-of-State Tables: Implications for Helioseismology”. In: ApJ 576.2, pp. 1064–1074. doi: [10.1086/341894](https://doi.org/10.1086/341894).
- Roxburgh, I. W. et al. (July 2006). “The autocorrelation function of stellar p-mode measurements and its diagnostic properties”. In: MNRAS 369.3, pp. 1491–1496. doi: [10.1111/j.1365-2966.2006.10396.x](https://doi.org/10.1111/j.1365-2966.2006.10396.x).
- Samadi, R. et al. (June 2005). “Excitation of Solar-like Oscillations: From PMS to MS Stellar Models”. In: *Journal of Astrophysics and Astronomy* 26.2-3, p. 171. doi: [10.1007/BF02702325](https://doi.org/10.1007/BF02702325).

- Samadi, R. et al. (Feb. 2007). “Excitation of solar-like oscillations across the HR diagram”. In: A&A 463.1, pp. 297–308. doi: [10.1051/0004-6361:20041953](https://doi.org/10.1051/0004-6361:20041953). arXiv: [astro-ph/0611762](https://arxiv.org/abs/astro-ph/0611762) [astro-ph].
- Samadi, R. et al. (Apr. 2019). “The PLATO Solar-like Light-curve Simulator. A tool to generate realistic stellar light-curves with instrumental effects representative of the PLATO mission”. In: A&A 624, A117, A117. doi: [10.1051/0004-6361/201834822](https://doi.org/10.1051/0004-6361/201834822). arXiv: [1903.02747](https://arxiv.org/abs/1903.02747) [astro-ph.IM].
- Scargle, J. D. (Dec. 1982). “Studies in astronomical time series analysis. II. Statistical aspects of spectral analysis of unevenly spaced data.” In: ApJ 263, pp. 835–853. doi: [10.1086/160554](https://doi.org/10.1086/160554).
- Schofield, M. et al. (Mar. 2019). “The Asteroseismic Target List for Solar-like Oscillators Observed in 2 minute Cadence with the Transiting Exoplanet Survey Satellite”. In: ApJS 241.1, 12, p. 12. doi: [10.3847/1538-4365/ab04f5](https://doi.org/10.3847/1538-4365/ab04f5). arXiv: [1901.10148](https://arxiv.org/abs/1901.10148) [astro-ph.SR].
- Serenelli, A. et al. (Dec. 2017). “The First APOKASC Catalog of Kepler Dwarf and Subgiant Stars”. In: ApJS 233.2, 23, p. 23. doi: [10.3847/1538-4365/aa97df](https://doi.org/10.3847/1538-4365/aa97df). arXiv: [1710.06858](https://arxiv.org/abs/1710.06858) [astro-ph.SR].
- Sharma, S. et al. (Sept. 2016). “Modelling the Milky Way with Galaxia and making use of asteroseismology”. In: *Astronomische Nachrichten* 337.8-9, p. 875. doi: [10.1002/asna.201612389](https://doi.org/10.1002/asna.201612389).
- Silva Aguirre, V. et al. (Sept. 2012). “Verifying Asteroseismically Determined Parameters of Kepler Stars Using Hipparcos Parallaxes: Self-consistent Stellar Properties and Distances”. In: ApJ 757.1, 99, p. 99. doi: [10.1088/0004-637X/757/1/99](https://doi.org/10.1088/0004-637X/757/1/99). arXiv: [1208.6294](https://arxiv.org/abs/1208.6294) [astro-ph.SR].
- Silva Aguirre, V. et al. (Sept. 2015). “Ages and fundamental properties of Kepler exoplanet host stars from asteroseismology”. In: MNRAS 452.2, pp. 2127–2148. doi: [10.1093/mnras/stv1388](https://doi.org/10.1093/mnras/stv1388). arXiv: [1504.07992](https://arxiv.org/abs/1504.07992) [astro-ph.SR].
- Silva Aguirre, V. et al. (Feb. 2017). “Standing on the Shoulders of Dwarfs: the Kepler Asteroseismic LEGACY Sample. II.Radii, Masses, and Ages”. In: ApJ 835.2, 173, p. 173. doi: [10.3847/1538-4357/835/2/173](https://doi.org/10.3847/1538-4357/835/2/173). arXiv: [1611.08776](https://arxiv.org/abs/1611.08776) [astro-ph.SR].

- Silva Aguirre, V. et al. (Feb. 2020). “Detection and Characterization of Oscillating Red Giants: First Results from the TESS Satellite”. In: *ApJS* 889.2, L34, p. L34. doi: [10.3847/2041-8213/ab6443](https://doi.org/10.3847/2041-8213/ab6443). arXiv: [1912.07604 \[astro-ph.SR\]](https://arxiv.org/abs/1912.07604).
- Skumanich, A. (Feb. 1972). “Time Scales for Ca II Emission Decay, Rotational Braking, and Lithium Depletion”. In: *ApJ* 171, p. 565. doi: [10.1086/151310](https://doi.org/10.1086/151310).
- Spada, F. et al. (May 2016). “Angular momentum transport efficiency in post-main sequence low-mass stars”. In: *A&A* 589, A23, A23. doi: [10.1051/0004-6361/201527591](https://doi.org/10.1051/0004-6361/201527591). arXiv: [1603.01119 \[astro-ph.SR\]](https://arxiv.org/abs/1603.01119).
- Speagle, J. S. (Apr. 2020). “DYNESTY: a dynamic nested sampling package for estimating Bayesian posteriors and evidences”. In: *MNRAS* 493.3, pp. 3132–3158. doi: [10.1093/mnras/staa278](https://doi.org/10.1093/mnras/staa278). arXiv: [1904.02180 \[astro-ph.IM\]](https://arxiv.org/abs/1904.02180).
- Spruit, H. C. (Jan. 2002). “Dynamo action by differential rotation in a stably stratified stellar interior”. In: *A&A* 381, pp. 923–932. doi: [10.1051/0004-6361:20011465](https://doi.org/10.1051/0004-6361:20011465). arXiv: [astro-ph/0108207 \[astro-ph\]](https://arxiv.org/abs/astro-ph/0108207).
- Stassun, K. G. et al. (Sept. 2018). “The TESS Input Catalog and Candidate Target List”. In: *ApJ* 156.3, 102, p. 102. doi: [10.3847/1538-3881/aad050](https://doi.org/10.3847/1538-3881/aad050). arXiv: [1706.00495 \[astro-ph.EP\]](https://arxiv.org/abs/1706.00495).
- Stassun, K. G. et al. (Oct. 2019). “The Revised TESS Input Catalog and Candidate Target List”. In: *ApJ* 158.4, 138, p. 138. doi: [10.3847/1538-3881/ab3467](https://doi.org/10.3847/1538-3881/ab3467). arXiv: [1905.10694 \[astro-ph.SR\]](https://arxiv.org/abs/1905.10694).
- Stello, D. et al. (May 2007). “Multisite campaign on the open cluster M67 - II. Evidence for solar-like oscillations in red giant stars”. In: *MNRAS* 377.2, pp. 584–594. doi: [10.1111/j.1365-2966.2007.11585.x](https://doi.org/10.1111/j.1365-2966.2007.11585.x). arXiv: [astro-ph/0702092 \[astro-ph\]](https://arxiv.org/abs/astro-ph/0702092).
- Stello, D. et al. (Feb. 2008). “Oscillating K Giants with the WIRE Satellite: Determination of Their Asteroseismic Masses”. In: *ApJ* 674.1, p. L53. doi: [10.1086/528936](https://doi.org/10.1086/528936). arXiv: [0801.2155 \[astro-ph\]](https://arxiv.org/abs/0801.2155).
- Stello, D. et al. (Nov. 2009). “The relation between $\Delta\nu$ and ν_{max} for solar-like oscillations”. In: *MNRAS* 400.1, pp. L80–L84. doi: [10.1111/j.1745-3933.2009.00767.x](https://doi.org/10.1111/j.1745-3933.2009.00767.x). arXiv: [0909.5193 \[astro-ph.SR\]](https://arxiv.org/abs/0909.5193).

- Stello, D. et al. (Apr. 2010). “Detection of Solar-like Oscillations from Kepler Photometry of the Open Cluster NGC 6819”. In: *ApJ* 713.2, pp. L182–L186. doi: [10.1088/2041-8205/713/2/L182](https://doi.org/10.1088/2041-8205/713/2/L182). arXiv: [1001.0026 \[astro-ph.SR\]](https://arxiv.org/abs/1001.0026).
- Stello, D. et al. (Aug. 2011). “Amplitudes of Solar-like Oscillations: Constraints from Red Giants in Open Clusters Observed by Kepler”. In: *ApJ* 737.1, L10, p. L10. doi: [10.1088/2041-8205/737/1/L10](https://doi.org/10.1088/2041-8205/737/1/L10). arXiv: [1107.0490 \[astro-ph.SR\]](https://arxiv.org/abs/1107.0490).
- Stello, D. et al. (Mar. 2013). “Asteroseismic Classification of Stellar Populations among 13,000 Red Giants Observed by Kepler”. In: *ApJS* 765.2, L41, p. L41. doi: [10.1088/2041-8205/765/2/L41](https://doi.org/10.1088/2041-8205/765/2/L41). arXiv: [1302.0858 \[astro-ph.SR\]](https://arxiv.org/abs/1302.0858).
- Stello, D. et al. (Aug. 2015). “Oscillating Red Giants Observed during Campaign 1 of the Kepler K2 Mission: New Prospects for Galactic Archaeology”. In: *ApJS* 809.1, L3, p. L3. doi: [10.1088/2041-8205/809/1/L3](https://doi.org/10.1088/2041-8205/809/1/L3). arXiv: [1506.08931 \[astro-ph.GA\]](https://arxiv.org/abs/1506.08931).
- Stello, D. et al. (Jan. 2017). “The K2 Galactic Archaeology Program Data Release. I. Asteroseismic Results from Campaign 1”. In: *ApJ* 835.1, 83, p. 83. doi: [10.3847/1538-4357/835/1/83](https://doi.org/10.3847/1538-4357/835/1/83). arXiv: [1611.09852 \[astro-ph.SR\]](https://arxiv.org/abs/1611.09852).
- Stello, D. et al. (May 2022). “TESS asteroseismology of the Kepler red giants”. In: *MNRAS* 512.2, pp. 1677–1686. doi: [10.1093/mnras/stac414](https://doi.org/10.1093/mnras/stac414). arXiv: [2107.05831 \[astro-ph.SR\]](https://arxiv.org/abs/2107.05831).
- Tailo, M. et al. (May 2021). “Mass-loss law for red giant stars in simple population globular clusters”. In: *MNRAS* 503.1, pp. 694–703. doi: [10.1093/mnras/stab568](https://doi.org/10.1093/mnras/stab568). arXiv: [2102.12146 \[astro-ph.SR\]](https://arxiv.org/abs/2102.12146).
- Tailo, M. et al. (June 2022). “Asteroseismology of the multiple stellar populations in the globular cluster M4”. In: *A&A* 662, L7, p. L7. doi: [10.1051/0004-6361/202243721](https://doi.org/10.1051/0004-6361/202243721). arXiv: [2205.06645 \[astro-ph.SR\]](https://arxiv.org/abs/2205.06645).
- Takata, M. et al. (June 1994). “Selection Rules for Perturbations to the Eigenfunctions of the Pulsations of Stars due to the Rotation and Magnetic Field”. In: *PASJ* 46, pp. 301–314.
- Themeßl, N. et al. (Aug. 2018). “Oscillating red giants in eclipsing binary systems: empirical reference value for asteroseismic scaling relation”. In: *MNRAS* 478.4, pp. 4669–4696. doi: [10.1093/mnras/sty1113](https://doi.org/10.1093/mnras/sty1113). arXiv: [1804.11151 \[astro-ph.SR\]](https://arxiv.org/abs/1804.11151).

- Thompson, S. E. et al. (May 2016). *Kepler Archive Manual*. Kepler Science Document KDMC-10008-006.
- Tian, Z. J. et al. (Dec. 2014). “Astroseismic analysis of solar-like star KIC 6225718: constraints on stellar parameters and core overshooting”. In: MNRAS 445.3, pp. 2999–3008. doi: [10.1093/mnras/stu1768](https://doi.org/10.1093/mnras/stu1768).
- Torres, G. (Nov. 2010). “On the Use of Empirical Bolometric Corrections for Stars”. In: ApJ 140.5, pp. 1158–1162. doi: [10.1088/0004-6256/140/5/1158](https://doi.org/10.1088/0004-6256/140/5/1158). arXiv: [1008.3913 \[astro-ph.SR\]](https://arxiv.org/abs/1008.3913).
- Townsend, R. H. D. et al. (Nov. 2013). “GYRE: an open-source stellar oscillation code based on a new Magnus Multiple Shooting scheme”. In: MNRAS 435.4, pp. 3406–3418. doi: [10.1093/mnras/stt1533](https://doi.org/10.1093/mnras/stt1533). arXiv: [1308.2965 \[astro-ph.SR\]](https://arxiv.org/abs/1308.2965).
- Triana, S. A. et al. (June 2017). “Internal rotation of 13 low-mass low-luminosity red giants in the Kepler field”. In: A&A 602, A62, A62. doi: [10.1051/0004-6361/201629186](https://doi.org/10.1051/0004-6361/201629186). arXiv: [1702.07910 \[astro-ph.SR\]](https://arxiv.org/abs/1702.07910).
- Ulrich, R. K. (July 1986). “Determination of Stellar Ages from Asteroseismology”. In: ApJ 306, p. L37. doi: [10.1086/184700](https://doi.org/10.1086/184700).
- Unno, W. et al. (1989). *Nonradial oscillations of stars*.
- van Saders, J. L. et al. (Feb. 2012). “The Sensitivity of Convection Zone Depth to Stellar Abundances: An Absolute Stellar Abundance Scale from Asteroseismology”. In: ApJ 746.1, 16, p. 16. doi: [10.1088/0004-637X/746/1/16](https://doi.org/10.1088/0004-637X/746/1/16). arXiv: [1108.2273 \[astro-ph.SR\]](https://arxiv.org/abs/1108.2273).
- Villebrun, F. et al. (Feb. 2019). “Magnetic fields of intermediate-mass T Tauri stars. I. Magnetic detections and fundamental stellar parameters”. In: A&A 622, A72, A72. doi: [10.1051/0004-6361/201833545](https://doi.org/10.1051/0004-6361/201833545). arXiv: [1810.12803 \[astro-ph.SR\]](https://arxiv.org/abs/1810.12803).
- Vrard, M. et al. (Apr. 2016). “Period spacings in red giants. II. Automated measurement”. In: A&A 588, A87, A87. doi: [10.1051/0004-6361/201527259](https://doi.org/10.1051/0004-6361/201527259). arXiv: [1602.04940 \[astro-ph.SR\]](https://arxiv.org/abs/1602.04940).

- White, T. R. et al. (Nov. 2011a). “Astroseismic Diagrams from a Survey of Solar-like Oscillations with Kepler”. In: *ApJ* 742.1, L3, p. L3. doi: [10.1088/2041-8205/742/1/L3](https://doi.org/10.1088/2041-8205/742/1/L3). arXiv: [1110.1375 \[astro-ph.SR\]](https://arxiv.org/abs/1110.1375).
- White, T. R. et al. (Dec. 2011b). “Calculating Astroseismic Diagrams for Solar-like Oscillations”. In: *ApJ* 743.2, 161, p. 161. doi: [10.1088/0004-637X/743/2/161](https://doi.org/10.1088/0004-637X/743/2/161). arXiv: [1109.3455 \[astro-ph.SR\]](https://arxiv.org/abs/1109.3455).
- Witzke, V. et al. (Jan. 2023). “Small-scale dynamo in cool stars. II. The effect of metallicity”. In: *A&A* 669, A157, A157. doi: [10.1051/0004-6361/202244771](https://doi.org/10.1051/0004-6361/202244771). arXiv: [2211.02722 \[astro-ph.SR\]](https://arxiv.org/abs/2211.02722).
- Woodard, M. F. (Jan. 1984). “Short-Period Oscillations in the Total Solar Irradiance.” PhD thesis. University of California, San Diego.
- Yıldız, M. et al. (Oct. 2016). “Fundamental properties of Kepler and CoRoT targets - III. Tuning scaling relations using the first adiabatic exponent”. In: *MNRAS* 462.2, pp. 1577–1590. doi: [10.1093/mnras/stw1709](https://doi.org/10.1093/mnras/stw1709). arXiv: [1607.03768 \[astro-ph.SR\]](https://arxiv.org/abs/1607.03768).
- (Oct. 2019). “Fundamental properties of Kepler and CoRoT targets - IV. Masses and radii from frequencies of minimum $\Delta\nu$ and their implications”. In: *MNRAS* 489.2, pp. 1753–1769. doi: [10.1093/mnras/stz2223](https://doi.org/10.1093/mnras/stz2223). arXiv: [1909.09488 \[astro-ph.SR\]](https://arxiv.org/abs/1909.09488).
- Yu, J. et al. (June 2018a). “Astroseismology of 16,000 Kepler Red Giants: Global Oscillation Parameters, Masses, and Radii”. In: *ApJS* 236.2, 42, p. 42. doi: [10.3847/1538-4365/aaaf74](https://doi.org/10.3847/1538-4365/aaaf74). arXiv: [1802.04455 \[astro-ph.SR\]](https://arxiv.org/abs/1802.04455).
- (June 2018b). “Astroseismology of 16,000 Kepler Red Giants: Global Oscillation Parameters, Masses, and Radii”. In: *The Astrophysical Journal Supplement Series* 236.2, p. 42. ISSN: 1538-4365. doi: [10.3847/1538-4365/aaaf74](https://doi.org/10.3847/1538-4365/aaaf74). URL: <http://dx.doi.org/10.3847/1538-4365/aaaf74>.
- (June 2018c). “Astroseismology of 16,000 Kepler Red Giants: Global Oscillation Parameters, Masses, and Radii”. In: *ApJS* 236.2, 42, p. 42. doi: [10.3847/1538-4365/aaaf74](https://doi.org/10.3847/1538-4365/aaaf74). arXiv: [1802.04455 \[astro-ph.SR\]](https://arxiv.org/abs/1802.04455).

- Zinn, J. C. et al. (Oct. 2019). “The Bayesian Asteroseismology Data Modeling Pipeline and Its Application to K2 Data”. In: *ApJ* 884.2, 107, p. 107. doi: [10.3847/1538-4357/ab43c0](https://doi.org/10.3847/1538-4357/ab43c0). arXiv: [1909.11927 \[astro-ph.SR\]](https://arxiv.org/abs/1909.11927).